Chip designs for high efficiency III-nitride based ultraviolet light emitting diodes with enhanced light extraction

vorgelegt von
Master of Science in Physics
Neysha Lobo Ploch
geb. Mumbai, Indien

Von der Fakultät II–Mathematik und Naturwissenschaften
der Technischen Universität Berlin
zur Erlangung des akademischen Grades

Doktor der Naturwissenschaften
-Dr. rer. nat.-

genehmigte Dissertation

Promotionsausschuss:
Vorsitzender: Prof. Dr. rer. nat. Michael Lehmann
Gutachter: Prof. Dr. rer. nat. Michael Kneissl
Gutachter: Prof. Dr. rer. nat. Gottfried Döhler

Tag der wissenschaftlichen Aussprache: 20. July 2015

Berlin 2015

Contents

1 Introduction to ultraviolet light emitting diodes

Ultraviolet (UV) radiation has a broad range of commercial applications, ranging from disinfection of water, air and surfaces to health care and even industrial production (Fig. 1.1). In 2014 the UV lamp market was estimated to be a $815M business [1] and is expected to increase with the introduction of new applications. This large market has provided a tremendous push in the development of UV sources.

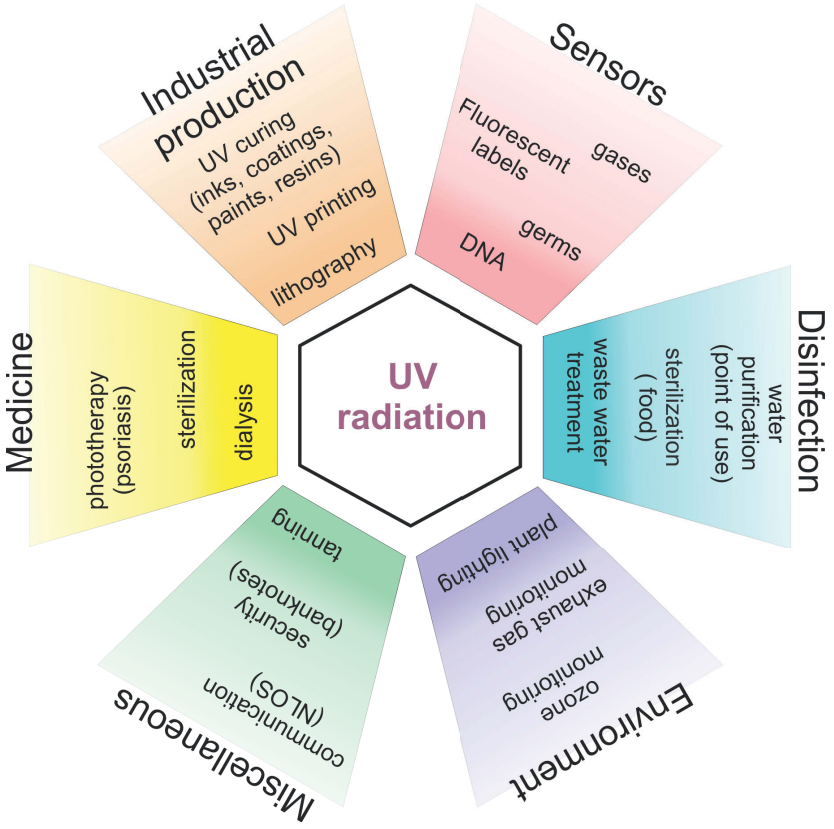

Figure 1.1: Applications of ultraviolet radiation.

The main factors influencing the choice of a UV source are a strong overlap between the spectral emission of the source and the required wavelength for the application, efficient production of the required intensity doses and finally lifetimes over a thousand hours and easy maintenance. The conventional sources of UV radiation are gas discharge lamps such

as low and medium pressure mercury lamps, xenon lamps and excimer lamps. In the last two decades many research efforts are being directed towards developing UV light emitting diodes (LEDs) due to their distinct advantages over conventional sources. For instance, LEDs have a pre-tunable and nearly monochromatic emission spectrum, high power conversion efficiencies, long lifetimes, no thermal heating, instant turn on of emission and are environmentally friendly. Furthermore, due to their low operating voltages, compact size and robustness, they are ideal sources for point of use applications.

Hexagonal wurtzite structure group III-nitride semiconductors, namely AlN, GaN and InN along with their ternary and quaternary alloys, have proven to be promising candidates for the production of LEDs emitting in the UV-A (320–400 nm), UV-B (290–320 nm) and UV-C (200–290 nm) wavelength regions because of their direct band gaps which span the range from 0.7 eV to 6.2 eV. Using this technology, UV LEDs captured 15 % of the complete UV lamp market in 2014 with an estimated market value of $122M [1]. The UV LED market is expected to continue growing by not only substituting conventional lamps but also by generating new application fields. Nevertheless, the efficiency of UV LEDs is much below that of their visible counterparts (Fig. 1.2) and their overall performance is still far below what is expected by the market. Hence, further research is required to improve the performance of UV LEDs in order for them to be a dominant player in the market.

Performance of III-nitride UV LEDs

The performance of an LED is best characterized by the external quantum efficiency (EQE or η_{EQE}) and the wall plug efficiency (WPE or η_{WPE}) of the device. The EQE is defined as the ratio of the number of photons emitted into free space per second to the number of carriers injected into the LED per second. The WPE describes the power conversion efficiency of the LED and is an important factor in determining the viability of an LED as a light source. It is defined as the ratio of the optical output power to the electrical input power. In the ideal case the LED should have an EQE and WPE of unity.

The EQE can be expressed as a product of two distinct components, i.e. the internal quantum efficiency (IQE or η_{int}) and the light extraction efficiency (LEE or $\eta_{extraction}$) as given below

$$\eta_{EQE} = \eta_{int} \times \eta_{extraction} = \eta_{inj} \times \eta_{rad} \times \eta_{extraction} \tag{1.1}$$

The IQE of an LED is the ratio of the number of electron-hole pairs that recombine radiatively in the active region per second to the total number of carriers injected into the LED per second. The IQE can be further divided into the radiative quantum efficiency (η_{rad}), i.e. the fraction of the total recombination in the active region that recombines radiatively, and the injection efficiency (η_{inj}), i.e. the fraction of the injected current that recombines, both radiatively and non-radiatively, in the active region [2]. The IQE is mainly dependent on the heterostucture design and the threading dislocation density (TDD) of the LED. The LEE is defined as the ratio of the number of photons emitted into free space per second to the number of photons emitted from the active region per second. The LEE is dependent on the geometry of the LED and the absorption of the emitted light by various materials

such as the metal contacts and the substrate. While UV-A LEDs emitting at around 400 nm are commercially available with EQEs as high as 60 % [3], the EQE decreases as the wavelength moves deeper into the UV region (Fig. 1.2). Recently UV Craftory demonstrated 280–300 nm LEDs with EQEs as high as 14.3 % [4]. However, the EQE of most UV-B and UV-C LEDs still remain below 10 %.

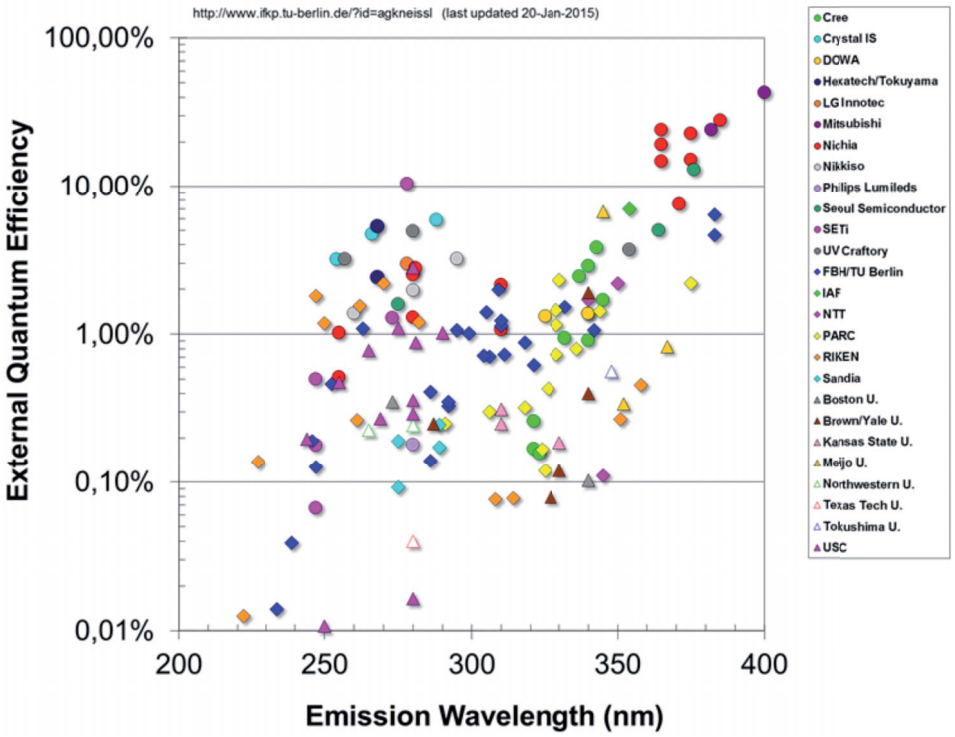

Figure 1.2: Reported values of the external quantum efficiencies of III-nitride LEDs emitting in the UV region [5, 6].

One of the main reasons for the low EQE of UV LEDs is the lack of a lattice matched substrate for epitaxial growth. The most commonly used substrate for metalorganic vapour phase epitaxy of UV LEDs is sapphire, which not only has a large lattice mismatch with the AlInGaN layers but also has a significantly different thermal expansion coefficient. Buffer layers of AlN [7] or GaN [8], grown at low temperatures, between the sapphire substrate and the active AlGaN layers result in defect densities in the order of $10^{10}\,\mathrm{cm}^{-2}$ in the active layers. The large threading dislocation densities (TDDs), which act as non-radiative recombination channels, significantly reduce the IQE of UV LEDs [9–11]. In order to get an IQE greater than 50 % it is necessary to reduce the TDD below $10^{9}\,\mathrm{cm}^{-2}$ [4, 12]. A number of techniques have been used to fabricate templates with low TDDs such as epitaxial

lateral-overgrowth (ELO) of GaN on sapphire using a SiO_2 mask [13], migration-enhanced metalorganic chemical vapour deposition (MEMOCVD) to grow low defect density AlN and AlN/AlGaN superlattice layers on sapphire [14], ELO of patterned AlN and sapphire templates to obtain low dislocation density AlN layers [15] and the use of an AlN/GaN multibuffer-layer structure to reduce the TDD [16]. Using these techniques TDDs in the order of 10^8 cm^{-2}–10^9 cm^{-2} have been achieved. In the recent years high quality free standing GaN substrates with defect densities from 10^6 cm^{-2} down to 10^4 cm^{-2} have also become commercially available which can be used for the fabrication of highly efficient LEDs emitting below 365 nm. While tremendous efforts are being made to realise free standing AlN substrates, the currently available substrates are highly absorbing in the UV region with defect densities in the range of 10^2 cm^{-2}–10^4 cm^{-2}.

Another factor that reduces the IQE of UV LEDs is the quantum confined Stark effect (QCSE). Due to the ionic nature of the group III metal–nitride bonds and the deviation of the lattice structure from the ideal wurtzite structure, III-nitrides suffer from the existence of a large spontaneous polarization field [17]. Furthermore, due to strain arising from the presence of non-relaxed heterojunctions in the active region, a piezoelectric polarization field in also present in the layers. This built in spontaneous and piezoelectric polarization results in a strong electrostatic field which separate the electrons and holes in the quantum well thus leading to a reduction in the radiative recombination efficiency. In order to reduce the QCSE, techniques such as the use of polarization matched barriers have resulted in UV LEDs with higher EQEs [18].

Efficient current injection is a critical issue for UV LEDs due to the leakage of electrons from the active region and their subsequent recombination in the p-doped regions. The electron leakage is mainly attributed to the problems in the p-doping of high Al content AlGaN layers and the resulting low hole concentrations. The ionization energy of Mg acceptors increases with the Al content in the layer from 187 meV for GaN [19] to 510 meV for AlN layers [20]. Due to these high ionization energies the concentration of holes in the p-doped regions is low (10^{17} cm^3) [21]. To increase the confinement of the electrons in the active region, single electron blocking layers (EBL) with high Al contents [22], multiple quantum barriers (MQB) [4] or thin Al interlayers [23] have been introduced between the multi quantum well (MQW) active region and the p-doped semiconductor region.

The high refractive index of III-nitride semiconductors gives rise to difficulties in extracting the light generated in the LED. The presence of absorbing contacts and TM polarization of the emitted light in deep UV LEDs further decreases the LEE of the devices.

For UV LEDs to be used commercially it is necessary that the devices have efficient power conversion and long lifetimes. Currently the voltage drop across the LEDs during operation is much greater than the band-gap. The high resistances of the n- and p-type current spreading layers due to challenges in doping layers with high Al contents, the difficulty in finding ohmic contacts due to the large band-gap of the semiconductor material and the presence of multiple heterojunctions in the device structure result in large operational voltages. Furthermore, the large series resistance combined with the low EQE of UV LEDs result in severe self heating of the devices which affects the lifetime of the devices [24]. At present the lifetime (L_{50}) of UV LEDs range from a few hundred hours for UV-C LEDs to a few thousand

hours for UV-B and UV-A LEDs [24–26]. Recently 310 nm LEDs with lifetimes greater than 10,000 h have been reported [5].

While most research efforts are being directed towards increasing the IQE of UV LEDs, a number of other areas of the device development still needs to be investigated. Currently standard chip technologies used for visible GaN LEDs are being applied to UV LEDs. In order to produce highly efficient UV LEDs it is necessary to develop new chip designs, packages and integrated optics aimed to solve the specific problems faced by UV emitters. Additionally, new techniques to increase the LEE of UV LEDs still need to be explored.

Outline of this work

This work has two main areas of focus in the development of III-nitride UV LEDs. Firstly, the design of LED chip geometries to improve the electrical performance and thermal management of the devices and secondly, the investigation of techniques to increase the light extraction efficiency of UV LEDs.

In Chapter 1, the growth and fabrication of LED chips emitting in the UV-A and UV-B region which have been investigated in this work is presented and the measurement techniques used to characterize the LEDs electrically, optically and thermally are described. The simulation models used to study the current spreading and thermal distribution in LED chips along with models used to determine the LEE are also explained in this chapter.

The designing of UV LED chips is presented in Chapters 2–3. The dependence of the IQE on the current density, the self heating of the LED and the problem of current crowding in lateral geometry LEDs is discussed in Chapter 2. These three factors must be taken into account when designing a UV LED chip. In Chapter 3, two UV LED chip layouts, namely the interdigitated finger contact geometry and micro-LED arrays, are presented. It is demonstrated that use of these geometries result in uniform current injection, reduced series resistance and improved thermal management in UV LED chips as compared to conventional large area square contacts.

Techniques to increase the LEE of UV LEDs are discussed in Chapters 4–6. The factors that limit the LEE of UV LEDs are presented in Chapter 4. In particular the origin and the influence of the optical polarization of the light, emitted from the active region, on the LEE is investigated. An overview of the different techniques used to extract light from nitride-based LEDs will also be presented and the possibility of their extension to UV LEDs is discussed. In Chapter 5, the texturing of the sapphire substrate back-surface to increase the LEE is studied. Simulations used to optimize the surface structures show that the best structures to increase the LEE are micro-frustums. Processing techniques to fabricate the optimized structures on sapphire substrates are presented. Finally in Chapter 6, a novel nanopixel contact LED design, consisting of an array of Pd nanopixels along with an Al reflector, which results in the enhanced extraction of light from UV LEDs is proposed. The methods to optimize and fabricate nanopixel contact LEDs are discussed. Using this design a two-fold increase in the optical power as compared to large area square contacts is demonstrated for UV-A LEDs.

This work was supported in part by the German Federal Ministry of Research and Education through the *Deep UV LED* research project (Grant Nos. 13N9933 and 13N9934) and the Innovative Regional Growth Core *Berlin WideBaSe* (Grant Nos. 03WKBT01C and 03WKBT01D) and the Deutsche Forschungsgemeinschaft within the *Sonderforschungsbereich 787*.

2 Fabrication, characterization and simulation of UV LEDs

An overview of the techniques used to grow and fabricate the III-nitride based UV LEDs, investigated in this work, will be presented in this chapter. The set-ups used to characterize the performance of the LEDs as well as the simulation models used to optimize the device parameters will also be discussed.

2.1 Growth of nitride-based UV LEDs

Metalorganic vapour phase epitaxy (MOVPE) is one of the most widely used epitaxial technique for the growth of nitride-based LEDs due to the higher throughput and superior material quality as compared to techniques such as molecular beam epitaxy [27]. In this process very thin layers are deposited on a hot substrate due to chemical reactions occurring between metalorganic precursors and hydrides. The typical group-III precursors used in MOVPE growth are Trimethylgallium (TMGa), Trimethylaluminium (TMAl) and Trimethylindium (TMIn) while Ammonia (NH_3) is used as a nitrogen source. For the controlled introduction of n- and p-type dopants in the AlInGaN layers, silane (SiH_4) or disilane (Si_2H_6) and cyclopentadienylmagnesium (Cp_2Mg) are used respectively. Hydrogen (H_2) and nitrogen (N_2) are the typically used carrier gases.

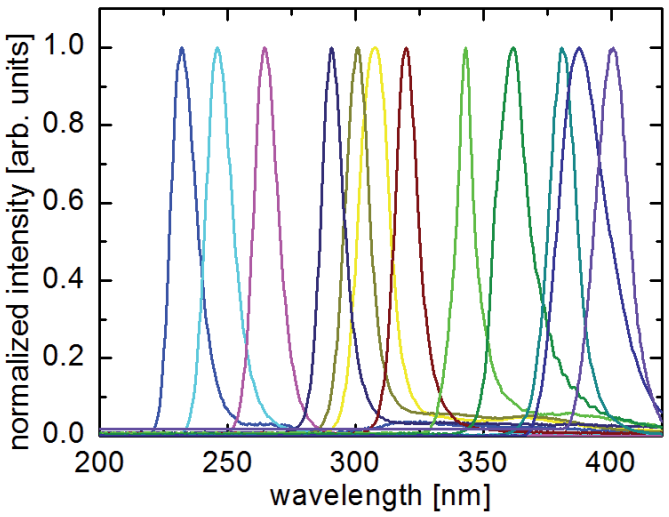

Figure 2.1: Normalized emission spectrum of III-nitride based UV LEDs fabricated at the Technische Universität Berlin and the Ferdinand-Braun-Institut Leibniz-Institut für Höchstfrequenztechnik [28]

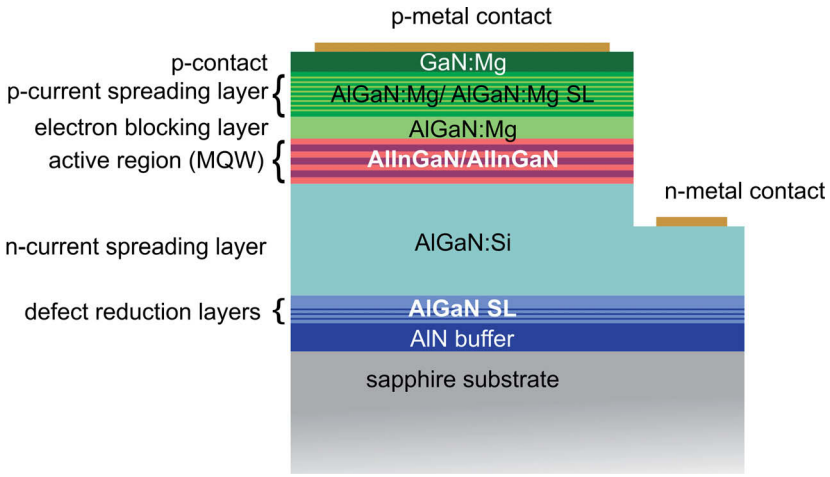

Figure 2.2: Schematic cross sectional view of a III-nitride based UV LED heterostructure.

The AlInGaN UV LEDs investigated in this work were grown by MOVPE on (0001) oriented sapphire substrates at the Technische Universität Berlin (Thomas Swan CCS MOVPE reactor) and the Ferdinand-Braun-Institut Leibniz-Institut für Höchstfrequenztechnik (Aix200HT and Aix2400G3HT MOVPE reactors). LEDs across the UV-A, UV-B and even in the UV-C region were successfully fabricated (Fig. 2.1). A schematic of the generic heterostructure design of the UV-B LEDs[1] is shown in Fig. 2.2. A 700 nm thick AlN buffer layer was grown in two steps on the sapphire substrate for the reduction of the defect density [29, 30]. First a low temperature (1000 °C) nucleation layer was grown followed by a smoothening layer grown at a high temperature (1500 °C) to improve the surface diffusion length of the Al adatoms. A 140 nm thick nominally undoped short-period AlGaN superlattice was deposited on the AlN buffer layer followed by an 600 nm undoped $Al_xGa_{1-x}N$ layer. The value of x varied from 35 % to 50 % to ensure that the layer was transparent at the emission wavelength. The n-current spreading layer consisted of a 4 μm thick Si-doped $Al_xGa_{1-x}N$ layer and a 500 nm thick Si-doped AlGaN short-period superlattice. The Si concentration of the layers was approximately 2×10^{18} cm^{-3}. The superlattice structures were used to compensate for the strain difference between the AlN/sapphire template and the $Al_xGa_{1-x}N$ layers allowing the growth of thick layers which are necessary for good current spreading. For $Al_{0.5}Ga_{0.5}N$:Si layers, threading dislocation densities of 10^{10} cm^{-2} were obtained.

Next the active region, consisting of AlInGaN multiple quantum wells (MQW), was deposited on the n-current spreading layer. In the case of 320 nm LEDs $Al_{0.20}In_{0.02}Ga_{0.78}N$/ $Al_{0.30}In_{0.02}Ga_{0.68}N$ MQWs were used. Quaternary AlInGaN MQW active regions were not only used to control the polarization fields in the MQWs [18] but also to improve the surface morphology and to reduce the defect density of the layers [31, 32]. To prevent the leakage of electrons into the p-current spreading layer and to confine them in the active region a 20 nm thick AlGaN:Mg electron blocking layer (EBL) was used. The Al content in the EBL varied from 35 % to 50 % depending on the wavelength.

[1] Detailed structures for other wavelengths are described in the corresponding chapters.

The p-current spreading layer, which followed the active region, consisted of a 150 nm thick Mg-doped AlGaN or AlGaN/GaN short-period superlattice. The Mg concentration of the layers was approximately $6\times10^{19}\,\mathrm{cm}^{-3}$. In order to form a low contact resistance p-ohmic contact, a 20 nm thick highly doped GaN:Mg layer was grown at the end of the LED structure. The LEDs were then annealed at 835 °C for 10 minutes in nitrogen ambient to activate the p-type carriers.

2.2 Fabrication of UV LEDs

The UV LED wafers were processed into lateral geometry LEDs due to the insulating sapphire substrate. Two kinds of LED structures were fabricated:

1. Flip-chip mountable UV LEDs for use in applications (Fig. 2.3 a).
2. LED test structures for measurements made on wafer (Fig. 2.3 b). These LEDs were used to obtain quick feedback on the opto-electrical characteristics of the UV LEDs and for the optimization of the processing technology.

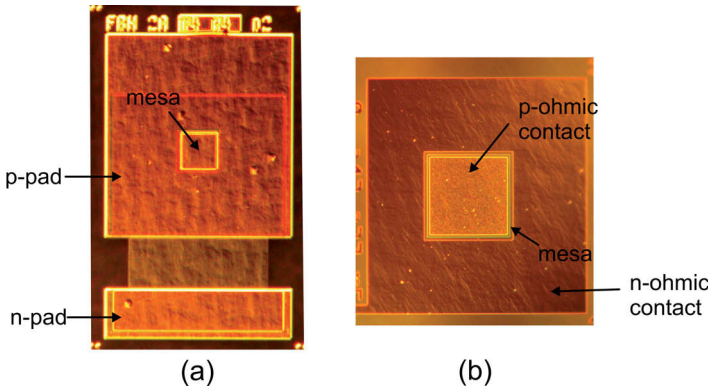

Figure 2.3: Microscope images of (a) a flip-chip mountable UV LED and (b) an LED test structure for on-wafer measurements.

2.2.1 Fabrication of flip-chip mountable UV LEDs

The fabrication of flip-chip mountable UV LED chips is a six level process using standard chip processing technologies (Fig. 2.4). The transfer of the geometrical patterns from the mask to the wafer was done using photolithography for all levels.

Level 1: Deposition of the p-ohmic contact

The first level in the fabrication of the LEDs is the deposition of the p-ohmic metal contact. A buffered oxide etch, with a solution of NH_4F(40 %)/HF(49 %)/H_2O (3:1:3), was used to clean the surface of the LED wafer before deposition of the p-ohmic contact. In this work three different p-ohmic contacts were used based on the wavelength of the LED and the application.

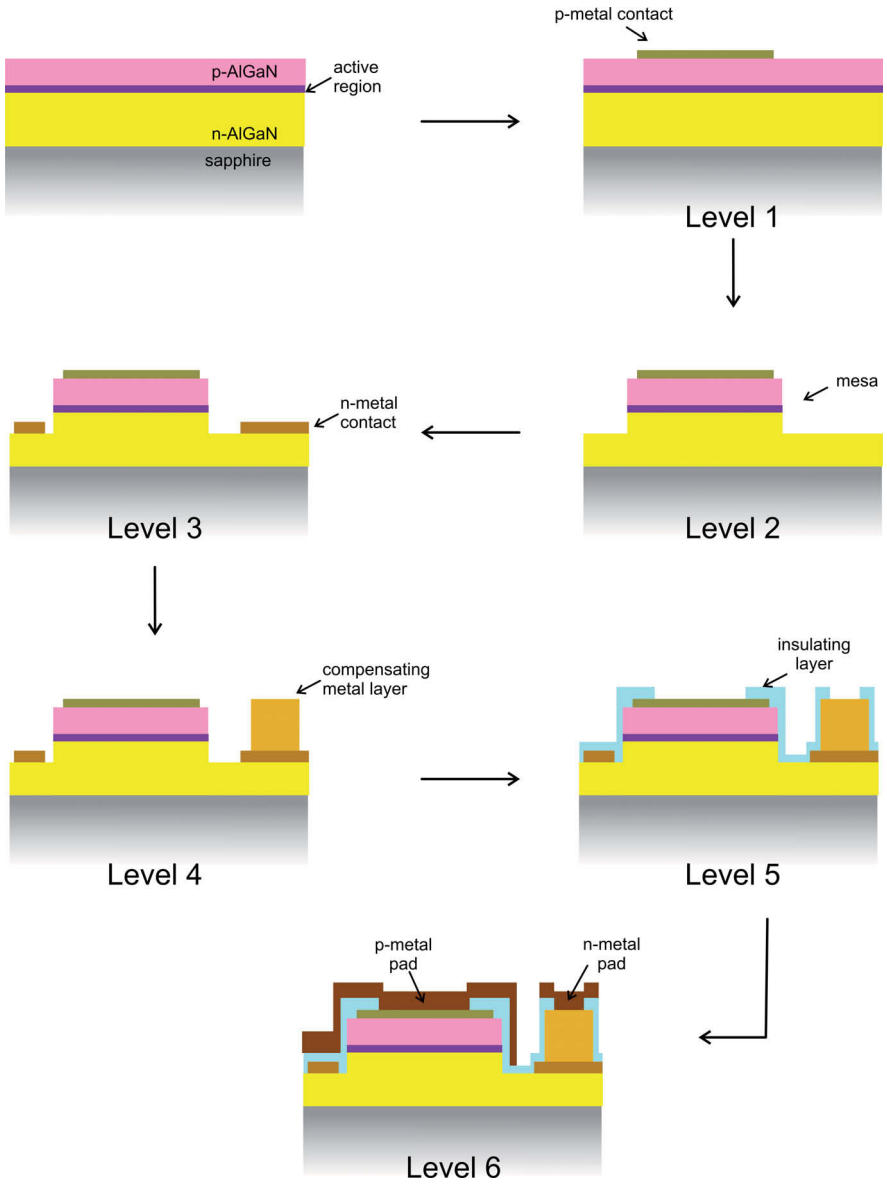

Figure 2.4: Schematic of the processing levels involved in the fabrication of a flip-chip mountable UV LED.

- Ni/Au contacts were used for bottom emitter LEDs emitting at wavelengths longer than 380 nm. A 20 nm thick layer of Ni followed by a 20 nm thick layer of Au was deposited on the complete LED wafer using electron beam physical vapour deposition. Sputter-etching through Ar+ ion bombardment was used for the patterning of the structures. To form an ohmic contact to the GaN:Mg layer, the wafer was annealed at 545 °C in oxygen ambient for 10 minutes. A specific contact resistivity of $2.1\times10^{-3}\ \Omega\text{cm}^2$ was obtained after annealing.

- Pd contacts were used for bottom emitter LEDs emitting at wavelengths shorter than 380 nm. 30 nm thick Pd contacts were fabricated in the same way as the Ni/Au contacts. The contacts were annealed at 530 °C in nitrogen ambient for 5 minutes to form an ohmic contact to the GaN:Mg layer with a specific contact resistivity of $6.5\times10^{-3}\ \Omega\text{cm}^2$.

- Indium tin oxide (ITO) contacts were used for top emitter LEDs emitting in the UV-A wavelength region. Using sputter deposition, a 300 nm thick layer of ITO was deposited on the complete LED wafer. The contact geometries were patterned using inductively coupled plasma etching (ICP-etching) with BCl_3 as a reagent. To increase the transparency of the ITO layer, the wafer was then annealed for 5 minutes at 600 °C in nitrogen ambient. A specific contact resistivity of $2\times10^{-3}\ \Omega\text{cm}^2$ was obtained after annealing.

Level 2: Definition of the mesa

After the deposition and formation of the p-ohmic contact, the LED wafers were etched down to the AlGaN:Si n-current spreading layer to form a n-ohmic contact. The mesa was patterned using negative resist photolithography and ICP-etching with BCl_3 and Cl_2 as reagents. During the etching process, heat is generated which results in elevated wafer temperatures. To prevent melting of the photoresist at these elevated temperatures, negative photoresist is used as a mask due to its higher temperature stability as compared to positive photoresist.

Level 3: Deposition of the n-ohmic contact

The n-ohmic contact was deposited on the exposed AlGaN:Si n-current spreading layer in lateral geometry UV LEDs. In this work a metal stack consisting of Ti/Al/Mo/Au with thickness 10 nm, 50 nm, 20 nm and 200 nm respectively was used as an n-ohmic contact. The metal stack was deposited using electron beam physical vapour deposition and patterned using the lift-off technique. For UV LEDs emitting at wavelengths ≥ 380 nm, an ohmic contact was formed to the GaN:Si n-current spreading layer without annealing of the wafer. However, to form an ohmic contact to the AlGaN:Si n-current spreading layer, the wafer must be annealed at 800 °C for 30 s in nitrogen ambient. A specific contact resistivity of $10^{-5}\ \Omega\text{cm}^2$ was obtained after annealing for a $Al_{0.3}Ga_{0.7}N$:Si n-current spreading layer.

Level 4: Deposition of a compensating layer

For the flip-chip mounting of the LEDs, it is necessary that the heights of the n- and the p-metal pads is the same. As the n-ohmic contact lies at a much lower level than the p-ohmic contact, a compensating layer consisting of a Ti/ Au metal stack was deposited on the n-ohmic contact.

Level 5: Deposition of an insulating layer

An insulating layer was deposited on the areas of the n-ohmic contact which lying around the mesa to prevent electrical shorting between the p-metal pad and the n-ohmic contact. In this work 300 nm SiN_x was used as an insulator. The SiN_x was deposited using plasma-enhanced chemical vapour deposition (PECVD) with NH_3 and SiH_4 diluted with Ar gas as input gases. A stack of 50 nm thick SiN*x* layers with alternative tensile and compressive strain was deposited to manage the stress in the layer and to ensure complete coverage over the wafer. The SiN_x structures were patterned using SF_6 plasma etching.

Level 6: Deposition of the metal pads

In the last level, both the n- and the p-metal pads were deposited for bonding of the UV LED chip to a submount. A layer stack consisting of Ti/Pt/Au/Ti/Pt/Au with a total thickness of 1 μm was used in this work for the metal pads. The metal stack was deposited using electron beam physical vapour deposition and patterned using the lift-off technique.

2.2.2 Fabrication of test UV LED structures

A simpler technological process was used for the fabrication of test LED structures which were used to obtain fast feedback for optimization of both the growth and the fabrication processes (Fig. 2.5). The test LED structures consisted of only four process levels. The processes for the deposition of the p-ohmic contact, definition of the mesa and deposition of the n-ohmic contact (Level 1 - Level 3) were the same as that for the flip-chip mountable LEDs. A metal reinforcement layer, consisting of Ti/Au layers with thickness of 10 nm and 400 nm respectively, was introduced due to the thinness of the p-ohmic contact (Level 4). As the LEDs were designed for on wafer measurements, no compensating layer, insulating layer or metal pads were included in the design.

2.3 Electrical and optical characterization of UV LEDs

The LED output power–current–voltage (L-I-V) characteristics were measured to investigate the device performance. A schematic of the set-up used for the measurement of on-wafer devices is shown in Fig. 2.6. The LED was contacted with the help of two micro positioners and a constant voltage source, Agilent 6614C, was used to drive the LEDs under forward and reverse bias. The current following through the forward biased LED was measured using

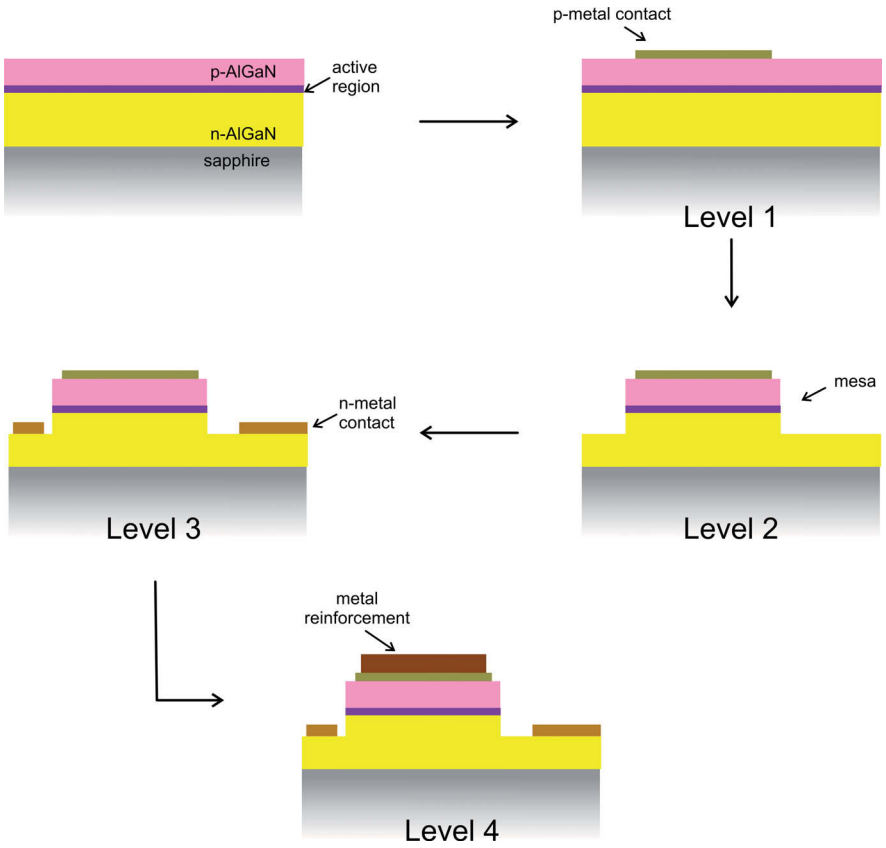

Figure 2.5: Schematic of the processing levels involved in the fabrication of a test UV LED structure.

a Keithley 2000 multimeter. For the reverse bias measurements, the set-up was shielded against electro-magnetic waves to ensure accurate measurements of small currents using a Keithley 6487 picoammeter. The current–voltage (I-V) characteristics of the diode were used to determine the turn-on voltage, the ideality factor (n_{ideal}) and the parasitic resistances, i.e. the resistance parallel to the diode (R_p) and the series resistance (R_s).

The light output power versus current (L-I) characteristics of on-wafer LEDs were measured by directly placing the wafers on a calibrated silicon photodetector, with an area of 100 mm^2. Only the light extracted through the substrate back-surface was measured and no active cooling of the device was used during the on-wafer measurements. The photocurrent of the silicon detector was measured using a Keithley 2000 ammeter. To measure the emission spectrum of the LED, the emitted light was coupled, with the help of an optical fiber, to a StellarNet EPP2000C spectrometer with resolution of 0.85 nm.

On-wafer pulsed measurements were conducted using an AVTEC AV-1010-B pulsed voltage source. The current flowing through the device was measured using a current clamp and a Textronix TDS 2024B digital storage oscilloscope. A fast calibrated silicon photodetector, with area of 63.6 mm^2, was used to measure the light output power of the LED. The photocurrent of the silicon detector was measured by monitoring the voltage drop produced across a 1 kΩ resistor with the help of an oscilloscope.

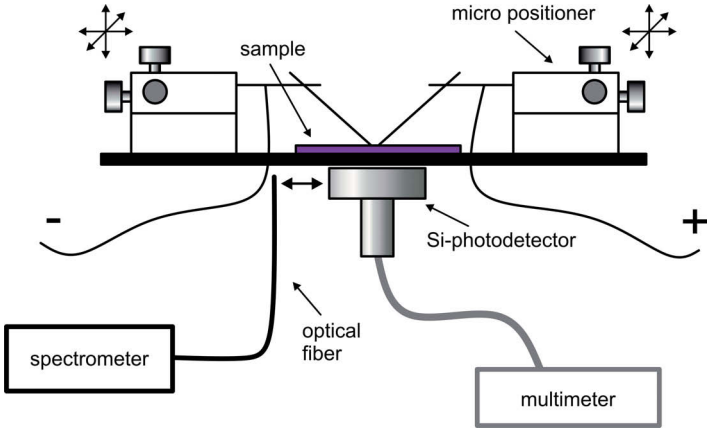

Figure 2.6: Schematic of the set-up used to measure, on wafer, the output power–current–voltage (L-I-V) characteristics of the LEDs.

The L-I characteristics of single LED chips, flip-chip mounted on AlN submounts, were measured in a calibrated OPTE-E-MA 18-inch integrating sphere (OL IS-1800) combined with an OPTE-E-MA double monochromator system for spectral measurements over the 200–800 nm wavelength range.

2.4 Measurement of the LED junction temperature

A direct measurement of the junction temperature of an LED during operation, with thermocouples or infrared cameras, is difficult due to the small size of the chips. However, indirect methods can be used to determine the diode junction temperature by monitoring a temperature dependent parameter of the LED. In this work the junction temperature of the LED during operation was determined by measuring the shift in the peak emission wavelength i.e. the electroluminescence of the band-to-band recombination.

The band-gap energy of semiconductors generally decreases with increasing temperature. This observation has two main contributing factors. The first contributing factor is a broadening of the energy levels, due to a temperature-dependent dilatation of the lattice, resulting in a decease of the band-gap energy [33]. The second and main contributing factor is a shift of the energy bands due to the interaction of the electrons with the vibrating lattice. Since the lattice vibrations are dependent on the temperature, the energy shift of the bands is also temperature dependent [34]. Varshni [35] proposed a semi-empirical formula to describe the temperature dependence of the band-gap energy of semiconductors (Eqn. 2.1).

$$E_g = E_0 - \frac{\alpha T^2}{T+\beta} \tag{2.1}$$

where E_g is the band-gap energy at the temperature T, E_0 is the band-gap energy at T = 0 K and α and β are fitting parameters. β is sometimes associated with the Debye temperature. For wurtzite AlN the Varshni parameters, α and β, were found to be 1.799 meV/K and 1462 K respectively for $T \leq 300\,K$ [36] while for wurtzite GaN they were found to be 7.7 meV/K and 600 K respectively for $T \leq 600\,K$ [37].

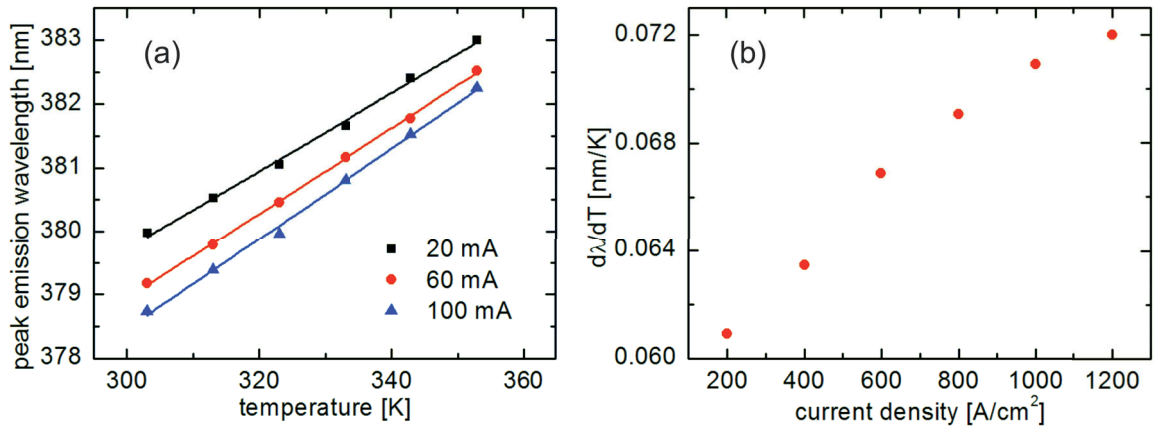

Figure 2.7: (a) Change in the peak emission wavelength with temperature measured at different pulsed operating currents for a 380 nm LED with an $In_{0.02}Ga_{0.98}N$ / $Al_{0.16}Ga_{0.84}N$ MQW active region. (b) Dependency of the temperature coefficient of the peak emission wavelength on the current density measured for a 380 nm LED with an $In_{0.02}Ga_{0.98}N$ / $Al_{0.16}Ga_{0.84}N$ MQW active region. All measurements were done on wafer.

To determine the junction temperature of the LED during operation from the shift in the peak emission wavelength method a two step approach is used. The first step is a calibration step in which the temperature dependence of the peak emission wavelength is determined. In the next step the change in the wavelength during operation is measured and the temperature is calculated.

For the calibration process, the LEDs were passively heated using a Peltier element, and the electroluminescence of the LEDs was measured at different currents under pulsed conditions (pulse width of 1 μs and a pulse repetition rate of 1 kHz) such that the junction temperature of the LED was the same as the ambient temperature. The temperature distribution in the device during the calibration measurements were simulated at thermal equilibrium[2]. The difference in the temperature of the Peltier element and the LED was found to be 0.06 % at 80° C. Even if a large air gap between the stage and the device and a low value for convection (20 W/m^{2}K) was considered, only a 0.46 % difference in temperature at 80° C was obtained. A room temperature pulsed measurement was also performed to obtain the room temperature peak emission wavelength of the LED at different currents. In Fig. 2.7 a the change in the peak emission wavelength with increasing temperature is shown for a 380 nm LED with an $In_{0.02}Ga_{0.98}N$ / $Al_{0.16}Ga_{0.84}N$ MQW active region. In the temperature range under consideration, the peak emission wavelength has a linear dependence on the junction temperature. Additionally, the temperature coefficient of the peak emission wavelength was found to be dependent on the current density (Fig. 2.7 b) which may be attributed to localization effects in the quantum wells.

[2]Simulations done by Christoph Stömacker.

In the next step the peak emission wavelength of the LED during operation was measured and the difference in the emission wavelength as compared to the room temperature pulsed measurement was calculated. The junction temperature was calculated using Eqn. 2.2.

$$T_{J_I} = \frac{\Delta\lambda}{d\lambda/dT_I} \tag{2.2}$$

where T_{J_I} is the junction temperature at the operating current I, $\Delta\lambda$ is the measured shift in the wavelength and $d\lambda/dT_I$ is the temperature coefficient of the peak emission wavelength at the current I.

2.5 Simulation of the performance of an LED chip

To investigate the current spreading and heat distribution in UV LED chips, 3-D simulations of the current distribution coupled with thermal analysis were performed using the SpeCLED commercial software package from STR [38]. The simulations of the light extraction from LED chips were done with the use of the RATRO commercial software package from STR [39] and the ZEMAX-EE commercial software package from ZEMAX Development Corporation [40].

2.5.1 Current spreading in an LED chip

For the simulation of the current spreading in an LED chip, the computation is simplified by using a 1-D/ 3-D hybrid approach. The SpeCLED software allows for the LED chip to be described by the following layers: substrate, thick n-type semiconductor layer, active region, thick p-type semiconductor layer, metallic electrodes and metallic pads. The simulation of the current spreading in the quasi-neutral p-and n-type semiconductor regions is considered within a 3-D approach (Fig 2.8). The quasi-neutral p-and n-type semiconductor regions are separated by the active region consisting of the MQWs and the space charge regions. In the simulation, the active region is considered to be a single layer with a distributed non-linear resistor like behaviour. The vertical current density (J_z) in this layer is locally controlled by the voltage (U_b) induced at the top and bottom interfaces of the layer.

Simulation of the active region

The dependence of J_z on U_b is calculated using the SiLENSe software package [41][3]. The band diagram for the active region at various biases is calculated using a 1-D approach and the distribution of electron and hole concentrations in the device structure is simulated considering both drift and diffusion. The radiative and non-radiative recombination rates of the carriers, including Auger recombination and recombination on threading dislocations, are calculated to determine the dependence of the IQE on J_z. Furthermore, the simulations can be carried out for various temperatures to determine the temperature dependent behaviour of

[3] Simulations of the active region done by Tim Kolbe.

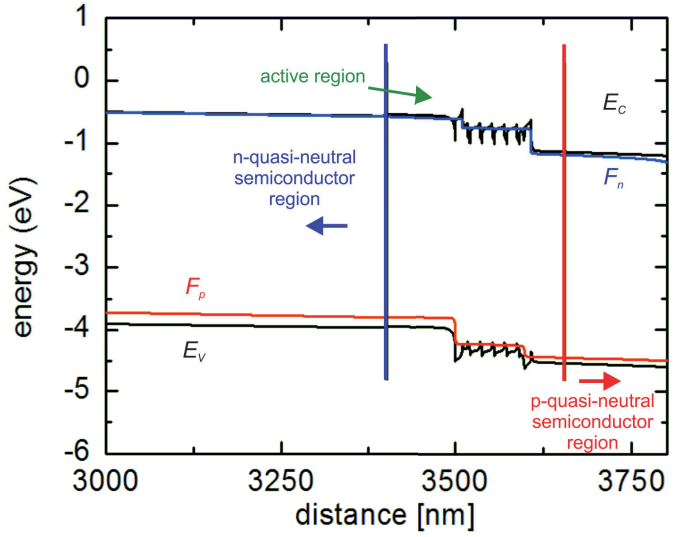

Figure 2.8: Calculated band structure diagram of an LED depicting the active region and the quasi-neutral semiconductor regions [38].

J_z and the IQE. Further details about the physics involved in the simulations is described in detail elsewhere [42].

Current spreading in the quasi-neutral semiconductor regions

In the quasi-neutral p-and n-type semiconductor regions, carrier drift is considered to be the dominant mode of transport and no electron-hole recombination is considered. In every semiconductor layer the current density ($\mathbf{J}$) is given by

$$\mathbf{J} = (\hat{\sigma}/q))\nabla F \tag{2.3}$$

$$\hat{\sigma}_n = q\hat{\mu}_n n_c \qquad \hat{\sigma}_p = q\hat{\mu}_p p_v \tag{2.4}$$

where q is the electron charge, F is the quasi-Fermi level of the electrons or the holes, $\hat{\sigma}_n$ ($\hat{\sigma}_p$) is the unipolar conductivity tensor of the n-semiconductor layer (p-semiconductor layer), $\hat{\mu}_n$ ($\hat{\mu}_p$) is the mobility tensor and n_c and p_v are the carrier concentrations in the n- and p-type semiconductor layers respectively. The introduction of a mobility tensor is useful for the description of superlattices in which the in-plane mobility ($\mu_\parallel$) of the carriers is different from the mobility normal to the plane of the active region ($\mu_\perp$). In the simulations, the value of $\hat{\mu}$ can be defined by the user.

As the layers are considered to be electrically neutral, the carrier concentration is equal to the ionized donor or acceptor concentration in the layer ($N_i^{\pm}$). The carrier concentrations in the semiconductor layers in the presence of an electric potential φ are given by

$$n_c(x,z,y) = N_c F_{1/2}\left(\frac{F(x,z,y) - E_s + q\varphi(x,z,y)}{kT}\right) \tag{2.5}$$

$$p_v(x,z,y) = N_v F_{1/2}(\frac{E_s - q\varphi(x,z,y) - F(x,z,y)}{kT}) \tag{2.6}$$

$$\Phi(x,z,y) = F(x,z,y) - E_s + q\varphi(x,z,y) \tag{2.7}$$

where $F_{(1/2)}$ is the Fermi-Dirac integral of the order of $1/2$, k is the Boltzmann constant, E_s is the conduction or valence band edge and N_c and N_v are the effective density of states in the conduction and the valence bands. N_c is given by

$$N_c = 2\left(\frac{m_e^{av} kT}{2\pi\hbar^2}\right)^{3/2} \tag{2.8}$$

where $\hbar$ is the reduced Planks constant and m_e^{av} is the average effective masses of the electron in the conduction band. For doubly degenerate valence subbands, as in the case of III-nitrides, N_v is given by

$$N_v = 2((m_{HH}^{av})^{3/2} + (m_{LL}^{av})^{3/2})\left(\frac{kT}{2\pi\hbar^2}\right)^{3/2} \tag{2.9}$$

where m_{HH}^{av} and m_{LH}^{av} are the average effective masses of the holes in the heavy hole and light hole valence subbands respectively. Due to electric neutrality, Φ is constant through out the semiconductor layer. Therefore $\nabla F = -q\nabla\varphi$. Using this expression in Eqn. 2.3 we get $\mathbf{J} = -\hat{\sigma}\nabla\varphi$ which is Ohm's law. Hence current spreading in the quasi-neutral p-and n-type semiconductor regions is described by Ohm's law.

The ionized impurity concentrations (N_D^+ or N_A^-) in the presence of an electric potential φ, considering incomplete ionization, are given by

$$N_D^+(x,y,z) = \frac{N_D(x,y,z)}{1 + g_D exp(\frac{\Phi(x,y,z) + E_D}{kT})} \tag{2.10}$$

$$N_A^-(x,y,z) = \frac{N_A(x,y,z)}{1 + g_A exp(\frac{E_A - \Phi(x,y,z)}{kT})} \tag{2.11}$$

where N_D and N_A are the doping concentrations, E_D and E_A are donor and acceptor ionization energies respectively and g_D and g_A are the degeneracy factors for the electrons and holes respectively. In this work the degeneracy factors were considered to be $g_D = 2$ and $g_A = 4$ because of the presence of doubly degenerate valence subbands in GaN and AlGaN alloys. Due to the electric neutrality condition, $n_c = N_D^+$ in the n-type semiconductor layer and $p_v = N_A^-$ in the p-type semiconductor layer. In the simulations, the values of N_D, N_A, E_D, E_A, N_c and N_v for the semiconductor layers can be specified as functions of both temperature and coordinate by the user. Hence Φ and the carrier concentrations are determined using Eqns. 2.5, 2.6, 2.10, 2.11 which are then used to calculate the electrical conductivity as a function of the doping level and the temperature.

In the simulations, electron-hole recombination is suppressed in the quasi-neutral p-and n-type semiconductor regions, i.e. $\nabla \cdot \mathbf{J} = 0$. Using this condition in Eqn. 2.3 we get

$$\nabla \cdot (\hat{\sigma} \nabla F) = 0 \tag{2.12}$$

The boundary conditions of the Eqn. 2.12 is dependent on the whether the layer is in contact with the active layer, substrate or a metal electrode and is descried as the following

1. The interface between the substrate and the n-type semiconductor layer is considered to have no resistance. The Fermi levels are considered to be aligned such that

$$F_n = F_s \tag{2.13}$$

$$\mathbf{n} \cdot (\hat{\sigma}_n \nabla F_n - \hat{\sigma}_s \nabla F_s) = 0 \tag{2.14}$$

   where F_n and F_s are the quasi-Fermi levels of the n-type semiconductor layer and the substrate respectively, $\hat{\sigma}_n$ and $\hat{\sigma}_s$ are the conductivities of the n-type semiconductor layer and the substrate respectively and $\mathbf{n}$ is the vector normal to the interface.

2. The active region, between the quasi-neutral p-and n-type semiconductor regions, is considered to be a single layer with a distributed non-linear resistor like behaviour. The non-linear dependence of J_z in the active region on U_b is used to produce the boundary conditions for the interfaces with the p-and n-type semiconductor layers. The quasi-Fermi levels and their gradients are related by the boundary condition

$$\mathbf{n} \cdot \hat{\sigma}_p \nabla F_p = \mathbf{n} \cdot \hat{\sigma}_n \nabla F_n = J_z(F_n - F_p) \tag{2.15}$$

   where F_n and F_p are the quasi-Fermi levels of the n- and p-type semiconductor layers respectively, $\mathbf{n}$ is the vector normal to the interface directed from the p- to the n-type semiconductor layer and $U_b = F_n - F_p$

3. The interface between the metal electrode and the n- or p-type semiconductor layer has a specific contact resistance ρ_c. Accounting for ρ_c, the boundary conditions at the interfaces are given by

$$\mathbf{n} \cdot \hat{\sigma} \nabla \varphi = (F_m - F)/\rho_c \tag{2.16}$$

   where F_m and F are the quasi-Fermi levels of the metal layer and the n- or p-type semiconductor layer respectively, $\hat{\sigma}$ is the conductivity of the semiconductor layer and $\mathbf{n}$ is the vector normal to the interface directed from the semiconductor layer to the metal layer. In the simulation the value of ρ_c can be determined by the user.

Current spreading in the metallic electrodes and pads

In the simulation model, it is assumed that the variation of the Fermi energy level across a thin metal layer is negligible. Furthermore the current is considered to flow mainly in the plane of the layer and hence a current density ($\mathbf{J}_m$) averaged over the layer cross-section is used in the simulations. Due to the conservation of charge we get, $h\nabla_2 \cdot \mathbf{J}_m = J_{out}$, where J_{out} is the current flowing out of the metal layer in the direction $\mathbf{n}$ from the semiconductor to the metal layer.

2.5.2 Distribution of temperature in an LED chip

The temperature distribution in an LED chip is simulated using self-consistent current spreading in a non-isothermal die and heat transfer simulations. The SpeCLED commercial software package from STR [38] was used for the simulations. First, the current spreading in the LED chip is simulated for a fixed temperature defined by the user. Next, the corresponding heat generated and temperature distribution in the chip is calculated for the given current density distribution. The material parameters of the layers are then adjusted according to the temperature distribution and once again the current spreading in the chip is simulated. This process is repeated until a self-consistent solution is reached. In the heat transfer simulations, only heat transfer by conduction is considered

Generation of heat in the LED chip

The main sources of heat, generated in the LED structure, were considered to the Joule heating of the quasi-neutral n- and p-type semiconductor layers and the metal electrodes, heating caused by non-radiative recombination in the active region and partial absorption of the emitted light in the LED structure.

The volumetric heat power generated in the quasi-neutral n- and p-type semiconductor layers and the metal electrodes, due to joule heating, is given by

$$Q_v(x,y,z) = J^2(x,y,z)/\sigma(x,y,z) \tag{2.17}$$

where $J(x,y,z)$ and $\sigma(x,y,z)$ are the 3-D current density and specific electrical conductivity of the layer.

In the active region, the difference between the total electrical power delivered to the active region and the optical power extracted from the LED is considered to be converted into heat. Hence the surface heat power generated in the active region is given by

$$q_a(x,y) = \{(J_z(x,y).U_b(x,y))\}_{electrical\ power} - \left\{\left(\frac{J_z(x,y)}{q}\cdot\hbar\omega\cdot\eta_{int}(x,y)\cdot\eta_{extraction}\right)\right\}_{optical\ power} \tag{2.18}$$

where q is the electron charge, $J_z(x,y)$ is the local density of current flowing through the active region, $U_b(x,y)$ is the local bias on the active region, $\eta_{int}(x,y)$ is the local IQE, and $\eta_{extraction}$ is the LEE. $\hbar\omega$ is the photon energy and is determined from the peak wavelength of the emitted LED spectrum. The $\eta_{extraction}$ is defined by the user in the simulations.

The heat generated due to joule heating at the contact resistances is given by

$$q_n(x,y) = \rho_{cn} \cdot J_z^2(x,y) \qquad q_p = \rho_{cp} \cdot J_z^2(x,y) \tag{2.19}$$

where q_n and q_p are the surface heat power generated at the n-electrode/ n-contact layer and p-electrode/ p-contact layer interfaces respectively, ρ_{cn} and ρ_{cp} are the n- and p-type contact resistances respectively and $J_z(x,y)$ is the local density of current flowing through the interfaces.

Analysis of the temperature distribution

The steady state heat equation is used to analyse the temperature distribution in the LED chip. The heat flux, $-\kappa\nabla T$, has divergence equal to the rate of heat generation

$$-\nabla(\kappa\nabla T) = q_{heat} \tag{2.20}$$

where T is the temperature, κ is the thermal conductivity and q_{heat} is the local heat source dependent on the current density. The boundary conditions to Eqn. 2.20 is dependent on the interface type. LED chips are surrounded by air or epoxies, which generally have a low thermal conductivity, hence all external surfaces of the chips are assumed to be adiabatic. Heat can only be transferred from the LED chip through the substrate backsurface or through the metal pads by way of conduction. The heat flux at the surface is given by

$$q_{heat} = \alpha_{heat}(T_a - T) \tag{2.21}$$

where α_{heat} is the heat transfer coefficient and T_a is the ambient temperature. α and T_a are assigned by the user in the simulations. The surface temperature is determined by balancing the external and internal heat fluxes. At an isothermal boundary $T = T_a$ ($\alpha_{heat} \to \infty$) while at an adiabatic boundary $q_{heat} = 0$ ($\alpha_{heat} = 0$)

2.5.3 Light extracted from an LED chip

The light extracted from an LED chip was simulated using the RATRO commercial software package from STR [39] and the ZEMAX-EE commercial software package from ZEMAX Development Corporation [40]. Rays with wavelength λ, which is defined by the user, are emitted from the active region of the LED chip. The optical path of a ray is traced using geometric optics till the ray is emitted into the immersion medium (air/ epoxy) or the intensity of the ray falls below a user defined fraction of the initial intensity i.e., the ray is absorbed in the medium.

The distribution of the emission intensity over the active region can either be obtained from the previously described current spreading simulations (Sec. 2.5.1 and Sec. 2.5.2) or

can be considered to be uniform across the active region. The angular distribution of the emission from the active region can be isotropic or can be manually defined by the user. Details about the angular distribution of the light emitted from the active region will be discussed in Sec. 5.2. The user defined absorption index, α_{abs}, of the active region is used to determine the re-absorption of the emitted light in the active region. The intensity of a ray, with direction θ with respect to the normal to the active region, decreases by a factor $exp(-d\alpha_{abs}/cos(\theta))$ each time it crosses the the active region with thickness d.

The wavelength dependent refraction index and absorption index of the n- and p-type semiconductor layers, metal electrodes, metal pads, substrate and immersion medium can be defined by the user. The optical models that can be used for the interfaces between the layers or the layer/ immersion medium interface are described below

Smooth Surface

The smooth surface optical model can be used for all the lateral chip interfaces, the heterostructure/substrate interface, n- and p-type semiconductor free surfaces, substrate free surfaces and the metal free surfaces. In this model the reflection (R) and transmission (T) coefficients for light intensity are determined from the Fresnel equations. If no light polarization is defined, the reflection and transmission coefficients of each ray are calculated as an average value of the TE and TM polarizations.

Mirror

The user can assign the reflection and transmission coefficients of the ray intensity in the mirror interface optical model. The absorption coefficient (A) is then given by $A = 1-R-T$. The reflection and refraction angles are determined by the law of reflection and Snell's law. The assigned values are used unless the incidence angle exceeds the total internal reflection angle. In case of total internal reflection $T = 0$, $R = 1-A$, while A is assumed to be constant in the whole angle range.

Multiple layers

The multiple layers optical model describes the behaviour of the interaction of a monochromatic plane wave of arbitrary incident angle with a stack of layers with given complex refractive index ($\tilde{n}$) assigned by the user. In this model the reflection, transmission and absorption in the layer stack is calculated using the transfer-matrix method [43].

3 Investigation of the physical parameters influencing the chip design of UV LEDs

When designing the chip layout of an LED it is necessary to consider all the factors that influence the electrical and optical characteristics of the device. Factors such as the dependence of the internal quantum efficiency (IQE) on the current density, temperature and current crowding can adversely affect the electrical and optical performance of LEDs. It is important to have a good understanding of the influence of these parameters on the LED characteristics to be able to design highly efficient LEDs. By intelligently designing the layout and geometry of LED chips, it is possible to minimize these detrimental effects. Therefore in this chapter, the influence of the current density dependence of the IQE as well as the temperature and current crowding on the chip design of UV LEDs will be presented.

3.1 Dependence of the IQE on the current density

The IQE of LEDs can be defined as the probability of radiative recombination of carriers in the active region and is given by:

$$\eta_{int} = \frac{R_{rad}}{R_{rad} + R_{non-rad}} \tag{3.1}$$

where η_{int} is the IQE of the LED and R_{rad} and $R_{non-rad}$ are the radiative and non-radiative recombination rates respectively. The radiative process in LEDs results in the emission of photons while the non-radiative processes result in the generation of heat and may be related to carrier losses inside the QWs, such as defect related recombination or Auger recombination, or losses due to recombination outside the QWs due to carrier leakage.

The dependence of the IQE on the current density is not completely understood. In particular, the reason for the observed reduction in the IQE of III-nitride LEDs at high injection currents (*efficiency droop*) is still under investigation. A number of different explanations, such as defect related recombination, Auger recombination and electron leakage have been proposed. Piprek [44] developed a unified model to describe the dependence of the IQE of III-nitride LEDs on the injection current density (Fig. 3.1). According to this model, the total current injected into the LED is divided into four sections

$$I = I_{def} + I_{rad} + I_{Auger} + I_{leak} \tag{3.2}$$

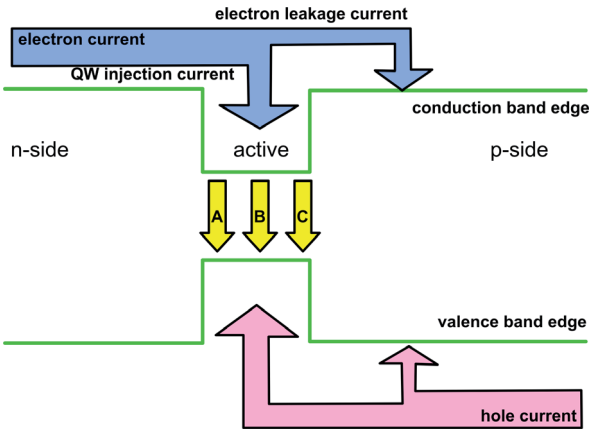

Figure 3.1: Schematic of the components of the current in an LED where A is the SRH recombination, B is the spontaneous recombination and C is the Auger recombination. [44].

where I_{def} is the defect recombination current, I_{rad} is the radiative recombination current, I_{Auger} is the Auger recombination current and I_{leak} is the leakage current. The current injected into the QWs (I_{QW}) is a combination of the first three terms of Eqn. 3.2.

Defect recombination current (I_{def})

The defect recombination current is given by

$$I_{def} = qV_{QW}An \tag{3.3}$$

where q is the electron charge, V_{QW} is the volume of all the quantum wells, n is the QW carrier density and A is the monomolecular non-radiative recombination coefficient. The A coefficient is determined from the Shockley-Read-Hall (SRH) recombination i.e., the non-radiative recombination of carriers via deep levels associated with dislocations and other defects. The SRH non-radiative recombination rate (R_{SRH}) for an undoped QW, assuming the deep level trap captures electrons and holes at the same rate, is given by [45]

$$R_{SRH} = \frac{\Delta n}{\tau_{NR}} = \frac{\Delta n}{\tau_0(1+cosh\frac{E_T-E_{Fi}}{kT})} \tag{3.4}$$

where Δn is the concentration of excess electrons injected into the active region, τ_{NR} is the non-radiative recombination lifetime, E_T and E_{Fi} are the trap energy and intrinsic Fermi level and τ_0 is dependent on the trap concentration and capture cross section. At low current densities the IQE of the LED is mainly dominated by the SRH recombination.

Hadar et al. [46] proposed that a density-activated defect recombination (DADR) may be responsible for the observed decrease in the IQE at high current densities. The physical model behind the proposal is that at densities higher than a critical value n_{DADR}, the carriers gradually escape from the local defect free potential minima in the QWs and start to fill the entire quantum well eventually reaching defects with lower recombination lifetime (τ_{DADR}). The total I_{def} would then be given by

$$\begin{aligned} I_{def} &= qV_{QW}An \qquad \text{for } n < n_{DADR} \\ &= qV_{QW}An + qV_{QW}(n - n_{DADR})^2/(2n_{DADR}\tau_{DADR}) \qquad \text{for } n > n_{DADR} \end{aligned} \tag{3.5}$$

For 410 nm InGaN LEDs n_{DADR} was determined to be 10^{12} cm^{-2} and τ_{DADR} was found to be 3.8 ns

Radiative recombination current (I_{rad})

The radiative recombination current is given by

$$I_{rad} = qV_{QW}Bn^2 \tag{3.6}$$

where q is the electron charge, V_{QW} is the volume of all the quantum wells, n is the QW carrier density and B is the bimolecular radiative recombination coefficient which in the case of III-nitride LEDs is also dependent on the spontaneous and piezoelectric polarization fields. The quadratic dependence of I_{rad} on the carrier density is only valid for low carrier densities where the carrier distributions can be described by Maxwell–Boltzmann distributions. At high carrier densities, due to phase-space filling, the carrier distributions are better described by step like Fermi distributions [47] and hence the radiative recombinations become monomolecular. To include the phase-space filling effect, David et al. [48] proposed the use of a carrier density dependent radiative coefficient. Based on this assumption the I_{rad} is expressed as

$$I_{rad} = qV_{QW}B_0n^2/(1 + n/n_0) \tag{3.7}$$

where B_0 and n_0 are fit parameters to calculate the radiative current. For a GaN/ InGaN LED emitting at 430 nm the fitted values of 7×10^{-11} cm^{3}s^{-1} and 0.5×10^{19} cm^{-3} were obtained for B_0 and n_0 respectively.

Leakage current (I_{leak})

Piprek [44] proposed that the leakage current is related to the I_{QW} by the equation

$$I_{leak} = a\,(I_{QW})^m \tag{3.8}$$

where a and m are fit parameters. Eqn. 3.8 can be used to describe carrier leakage by thermionic emission from QWs, carriers not captured by the QWs or defect assisted carrier tunnelling at a given temperature as no temperature dependence of the fitting parameters is defined.

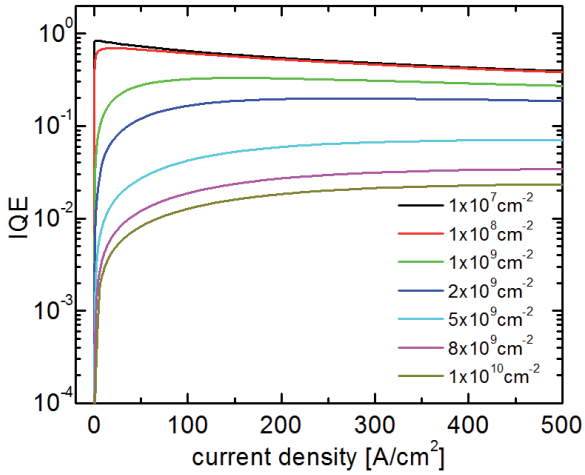

Figure 3.2: Simulation of the dependence of the IQE of a 320 nm LED, with a $5 \times Al_{0.20}In_{0.02}Ga_{0.78}N/\,Al_{0.30}In_{0.02}Ga_{0.68}N$ MQW active region, on the treading dislocation density of the template. Values are simulated for a temperature of 300 K [42].

Unified IQE model

The unified model for the IQE of III-nitride LEDs is given by

$$\eta_{IQE} = \frac{I_{rad}}{I_{QW} + aI_{QW}^{m}} \tag{3.9}$$

If the carrier concentration is considered to be less than n_{DADR}, B is considered independent of carrier density and no leakage current is assumed then Eqn. 3.9 reduces to a simplified IQE expression described by the well know ABC model for the recombination of carriers in the QWs.

$$\eta_{IQE} = \frac{Bn^2}{An + Bn^2 + Cn^3} \tag{3.10}$$

3.1.1 Dominance of the SRH recombination in UV LEDs

LEDs are typically operated at low current densities (< 500 A/cm^2). At these low current densities, the IQE is mainly dominated by the SRH recombination. In case of AlInGaN UV LEDs, due to the large dislocation densities which act as non-radiative recombination centres, the IQE is low at reduced currents. Kolbe [42] simulated the influence of the dislocation density on the IQE of 320 nm LEDs with $5 \times Al_{0.20}In_{0.02}Ga_{0.78}N/\,Al_{0.30}In_{0.02}Ga_{0.68}N$ MQW active region (Fig. 3.2). The radiative recombination coefficient and the Auger coefficient were considered to be 2.29×10^{-11} cm^{3}s^{-1} and 5×10^{-32} cm^{6}s^{-1} respectively. The simulations were based on the model by Karpov et al. [11] in which the treading dislocation density (TDD) forms acceptor like levels within the band-gap and the minority carrier diffusion lengths is a function of TDD. For a low TDD of 10^7 cm^{-2}, the IQE increased rapidly with the current density and a maximum of 84 % was obtained at a current density of 2 A/cm^2. With an increase in the TDD, the maximum in the IQE curve not only decreases but also shifts to higher current densities. For a TDD of 8×10^9 cm^{-2} which is typical for

LEDs grown on sapphire templates, the maximum IQE was only 3.4 % at 70 A/cm^2. Hence for UV LEDs grown on sapphire with TDDs in the order of 10^9 cm^{-2}, the IQE is mainly dominated by the SRH recombination at the typical operational current densities. The operating current is thus an important parameter in the design of the UV LED chip geometry and layout. To obtain a highly efficient device it is necessary to choose the area of the active region such as to ensure that the maximum in the IQE is achieved for the resulting operating current density.

3.2 Temperature effects in UV LEDs

The temperature of an LED can change during operation due to the self heating of the device and due to changes in the ambient temperature. Heat is generated in the LED due to the non-radiative recombination of the carriers and Joule heating in the ohmic contacts and the current spreading layers. The temperature of an LED during operation greatly influences not only the electrical and optical characteristics of the device but also the long term stability of the LED. In this section the detrimental effects of elevated temperatures in UV LEDs will be investigated.

3.2.1 Temperature droop in UV LEDs

The junction temperature of an LED has a tremendous influence on the electrical and optical characteristics of the device. In particular the output power of LEDs decreases at elevated temperatures which is referred to as the *temperature droop* [49]. The decrease in the emission power of LEDs with temperature can be described by the empirical formula [45]

$$I_{power}(T) = I_{power}(0K)exp(-T/T_c) \tag{3.11}$$

where $I_{power}(T)$ and $I_{power}(0K)$ are the emission powers of the LED at junction temperatures T K and 0 K and T_c is the characteristic temperature and a figure of merit of the temperature sensitivity of the device. A high value of T_c, indicating weak temperature dependence, is desired for many applications to minimize the impact of ambient changes on the device performance. Cao et al. [50] reported that III-nitride visible LEDs are relatively insensitive to the junction temperature with T_c in the range of 170 K to 270 K. However the T_c was found to decrease to 31–73 K for UV LEDs indicating that the efficiency of UV LEDs is extremely sensitive to small changes in the temperature.

To study the influence of the junction temperature on the efficiency of UV LEDs, the emission powers of 380 nm AlInGaN LEDs were measured at different temperatures and current densities under pulsed conditions to exclude the self heating of the device. The current density was determined from the ratio of the measured current to the p-contact area assuming uniform current injection. The layer-structures of the LEDs are given in Table. 3.1.

Due to the increase in the temperature, the following competing processes may occur in the LED leading to a change in the output power of the device.

1. Increased SRH recombination resulting in reduced output power. The SRH recombination rate is dependent on the temperature as seen in Eqn. 3.4. As the temperature rises, the non-radiative lifetime of the carriers decreases resulting in a higher probability of non-radiative recombination of the carriers and a reduction in the IQE of the LED.

2. Generation of carriers at high temperatures resulting in increased output power. Due to the elevated temperatures, a higher acceptor ionization is achieved in the p-current spreading layer which results in a higher injection efficiency of the device.

3. Temperature assisted carrier leakage from the QWs resulting in a decrease of the output power.

	substrate	MQW active region
Sample A	sapphire	$3 \times In_{0.01}Ga_{0.99}N/\ In_{0.05}Ga_{0.95}N$
Sample B	GaN	$3 \times In_{0.01}Ga_{0.99}N/\ In_{0.05}Ga_{0.95}N$
Sample C	sapphire	$3 \times In_{0.03}Ga_{0.97}N/\ GaN$
Sample D	sapphire	$3 \times In_{0.03}Ga_{0.97}N/\ Al_{0.16}In_{0.03}Ga_{0.81}N$
Sample E	sapphire	$3 \times In_{0.03}Ga_{0.97}N/\ Al_{0.16}Ga_{0.84}N$

Table 3.1: Structure of the 380 nm LEDs used for temperature droop investigations.The n- and p-current spreading layers of the LEDs were GaN:Si and GaN:Mg respectively while the electron and hole blocking layers were $Al_{0.23}Ga_{0.77}N$:Mg and $Al_{0.23}Ga_{0.77}N$:Si respectively.

The dependence of the emission power, of sample E, on the junction temperature and the current density is shown in Fig. 3.3 a. Based on Eqn. 3.11, the T_c of the LED was calculated for different current densities (Fig. 3.3 b). At low current densities the output power decreases exponentially with increasing temperature. At these low current densities the SRH recombination is dominant, hence the observed reduction in the output power may be attributed to the increase in the SRH recombination. As the current density increases, a smaller dependence of the output power on the temperature is observed. The increased temperature stability at a higher current density is reflected in the change of the value of T_c from 69 K at 50 A/cm^2 to 215 K at 1200 A/cm^2. This increase in stability can be attributed to a reduced contribution of the SRH recombination to the total carrier recombination due to saturation of the non-radiative recombination paths. A similar dependence of the T_c, of blue III-nitride LEDs, on the current density was reported by Chhajed et al. [51] and Meyaard et al. [52]. At high current densities, an initial increase in the output power is observed before the output power decreases at elevated temperatures. The measured increase in the output power can be explained by increased carrier activation resulting in a higher injection efficiency. The consequent decrease in the output power at elevated temperatures may arise due to carrier leakage from the QWs at high current densities and temperatures.

To distinguish the contributions of the SRH recombination and the carrier leakage to the temperature droop, the dependence of the temperature stability of the EQE of 380 nm LEDs on the defect densities of the templates and the barrier height of the quantum wells in the active region has been investigated.

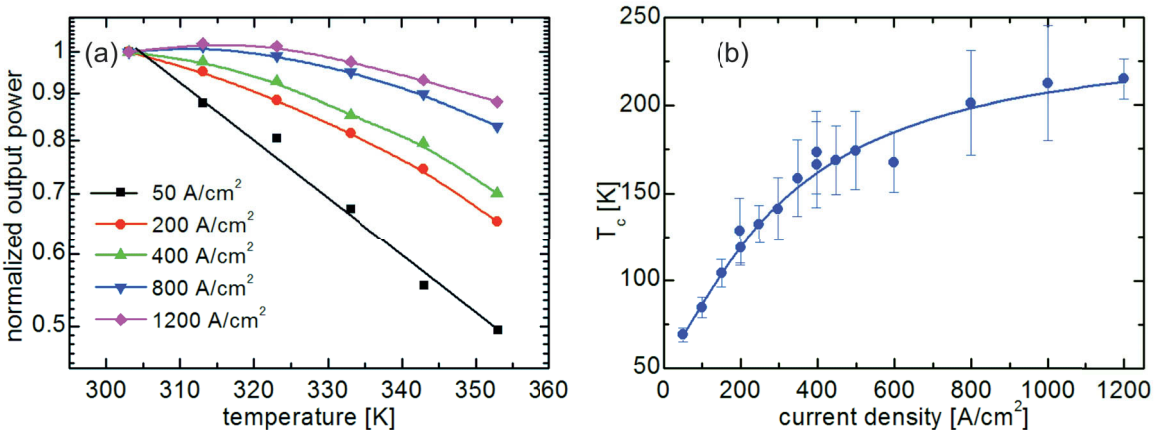

Figure 3.3: (a) Dependence of the normalized output power of a 380 nm AlInGaN LED on the ambient temperature measured on wafer under pulsed conditions to avoid self heating of the device. (b) Characteristic temperature (T_c) of the aforementioned LED plotted as a function of the current density. The T_c is determined from the region in the aforementioned plot where the output power decreases exponentially with the temperature. The curve is a guide to the eye and the error bars represent the accuracy of the fit for T_c.

Influence of the dislocation density

The dislocations in an LED are associated with deep levels which act as non-radiative recombination centres; hence LEDs with different TDD were compared to investigate the influence of the SRH recombination on the temperature dependence of the EQE. The output power-current characteristics of sample A, grown on a sapphire template with a TDD of $8 \times 10^9\,\mathrm{cm}^{-2}$, were compared to that of sample B, grown on a GaN template with a TDD of $4 \times 10^7\,\mathrm{cm}^{-2}$ (Fig. 3.4 a). Sample B has a five fold higher output power than sample A due to the higher IQE of the device resulting from a reduced non-radiative recombination rate [54].

To obtain a deeper understanding of the temperature dependence of the devices, their T_cs were derived at different current densities as shown in Fig. 3.4 b. At low current densities, where the SRH recombination is dominant, sample B has a weaker temperature dependence of the EQE with a T_c of 69 K at 9 A/cm^2 as compared to sample A with a T_c of 48 K. As the current density increases from 9 A/cm^2 to 100 A/cm^2, a significant increase in the T_c of sample A is observed in contrast to the small and more gradual increase observed for sample B. Hence at low current densities the TDD of the LED plays an important role in the temperature stability of the device.

Influence of the barrier height

To investigate the influence of the carrier-confining potentials in the quantum wells on the temperature stability of the EQE, 380 nm LEDs with GaN (sample C), $Al_{0.16}In_{0.03}Ga_{0.81}N$

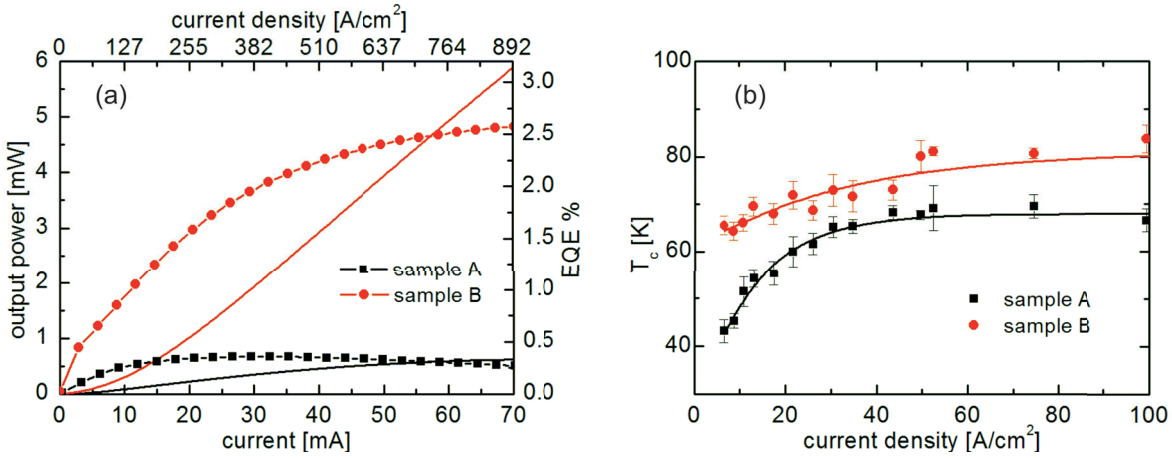

Figure 3.4: (a) Output power (solid lines) and EQE (symbols), measured on wafer, of 380 nm LEDs with TDD of 8×10^9 cm^{-2} (sample A) and 4×10^7 cm^{-2} (sample B) as a function of the operating current [53]. (b) Characteristic temperature T_c as a function of the current density for the aforementioned LEDs [53]. The curves are a guide to the eye and the error bars represent the accuracy of the fit for T_c.

(sample D), and $Al_{0.16}Ga_{0.84}N$ (sample E) quantum well barriers in the active region and having the same TDD were compared. The calculated band offsets for the GaN, $Al_{0.16}In_{0.03}Ga_{0.81}N$, and $Al_{0.16}Ga_{0.84}N$ barriers were 25 meV, 95 meV and 142 meV for the valence band and 54 meV, 205 meV and 308 meV for the conduction band, respectively [55]. The low carrier-confinement in sample C is reflected in the low output power of the LED as seen in Fig. 3.5 a. An approximately ten fold increase in the output power is observed in samples D and E. The highest output power is observed in sample D due to the presence of polarization matched barriers. Polarization matched barriers are quaternary barriers chosen such as to reduce the polarization sheet charges at the interface between QW and barrier resulting in a reduction of the quantum confined Stark effect and hence improved overlap of the electron and hole wave functions [18, 55]. The interface quality of the MQWs with different barriers is considered to be similar and hence no effect of the barriers on the crystal quality is expected [18].

The T_c extracted from the temperature dependence of the output power at different current densities for samples with different barrier heights is shown in Fig. 3.5 b. No essential link between the T_c and the room temperature output power of the device is observed. At low current densities, the temperature dependence of the output power is dominated by the SRH recombination and is weakly influenced by the barrier height. Even at these low current densities thermally assisted carrier leakage is possible for samples with low barrier potentials. Therefore at 50 A/cm^2, the LEDs have a similar temperature dependence which then begins to deviate, depending on the barrier height of the quantum wells, as the current density is increased. Sample E with the largest confining potential exhibits the weakest temperature dependence with a T_c of 207 K at 1 kA/cm^2 while sample C with the smallest confining potential showed the highest temperature sensitivity with a T_c of 103 K at 1 kA/cm^2. At

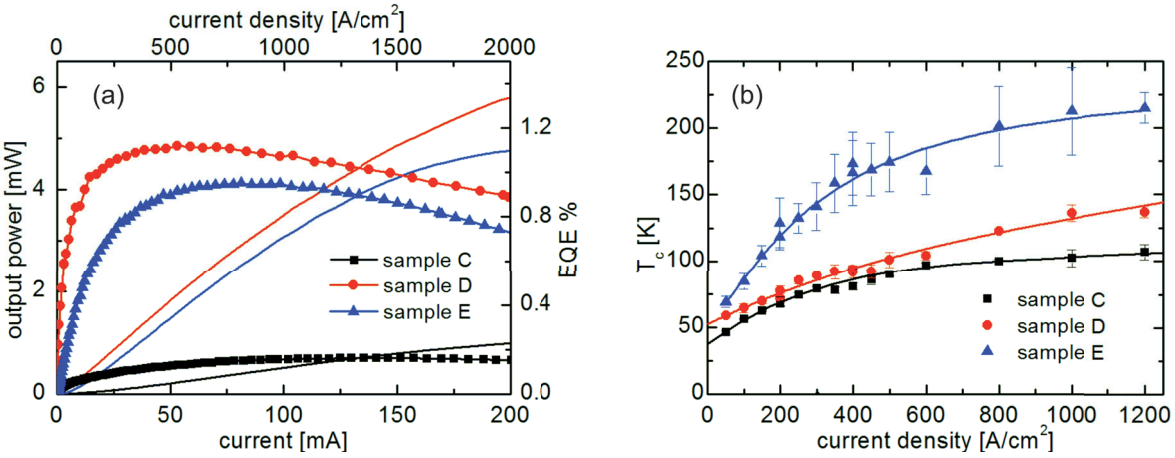

Figure 3.5: (a) Output power (lines) and EQE (symbols), measured on wafer, as a function of current for 380 nm LEDs with different quantum well barriers. Sample C: GaN barriers, sample D: $Al_{0.16}In_{0.03}Ga_{0.81}N$ barriers and sample E: $Al_{0.16}Ga_{0.84}N$ barriers [53]. (b) Characteristic temperature T_c as a function of current density for the aforementioned LEDs [53]. The curves are a guide to the eye and the error bars represent the accuracy of the fit for T_c.

high current densities, where the contribution of the SRH recombination to the total carrier recombination is reduced, the main factor influencing the reduction in the output power with ambient temperature should be thermionic emission resulting in carrier leakage from the quantum wells to the barriers. At elevated temperatures the carriers may obtain sufficient thermal energy to overcome the confining potentials and recombine non-radiatively in the barriers. An effect due to Auger recombination can be neglected due to the weak dependence of the Auger coefficient on temperature [56]. Hence, the improved temperature stability of LEDs with increasing barrier height at high current densities can be mainly attributed to a superior carrier confinement in the active region i.e. reduced thermally assisted carrier leakage from the quantum wells. An absolute correlation between the confinement potential and the T_c is difficult as the SRH recombination is not completely saturated.

Based on these investigations, the importance of the epitaxial design for the reduction of the temperature droop in UV LEDs is evident. When designing UV LEDs for applications with low operating current densities ($< 50\,A/cm^2$), it is essential that the crystalline perfection of the epitaxial heterostructure is high to fabricate devices with high temperature tolerance. On the other hand for LEDs with high operating current densities, it is necessary to design structures with large confining potentials, e.g. by increasing the Al content in the barriers.

3.2.2 Influence of temperature on the LED reliability

Temperature can significantly alter the electrical characteristics of the device and the long term reliability of the LEDs. Cao et al. [57] investigated the electrical and optical degradation of GaN/ InGaN SQW LEDs and proposed that the defect generation under high forward-

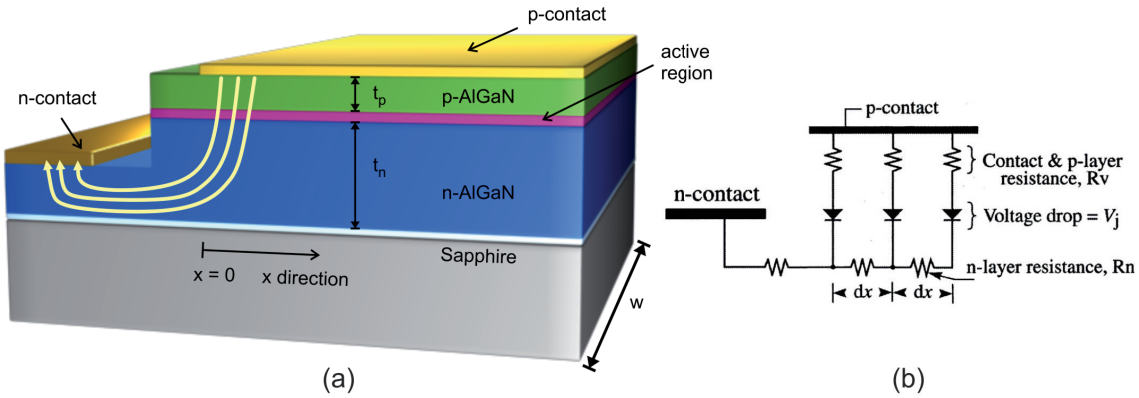

Figure 3.6: (a) Schematic of an UV LED with lateral geometry. (b) Equivalent circuit model developed by Xuo et al. [62].

current stress results from thermally assisted processes in the InGaN layer. Meneghini et al. [58] demonstrated a temperature induced morphological degradation of the ohmic contacts of GaN-based LEDs resulting in an increase in the series resistance of the device. For devices with non-optimized contact technology, detachment of the contact layers was observed due to thermal mismatch and/or poor adhesion between different metal layers. Furthermore, electrical contact metallurgical interdiffusion of LED packages, resulting in light output degradation, increase in parasitic series resistance and short circuit of LEDs, is also caused by high operational currents and large increases in temperature [59].

Temperature can also effect the stability of the LED packaging resulting in reduced lifetime of the device. Carbonization of the plastic LED encapsulant material may occur at the diode surface and bonding wires due to joule heating and high ambient temperatures which could contribute to optical power degradation and short circuit of the device [60]. Encapsulant delamination [61] and yellowing [59] may also occur due to repeated cyclic thermal stresses resulting in reduced mechanical toughness of the device and reduced output power.

Due to the various detrimental effects of temperature on the performance of LEDs, it is essential to design LED chips such that the heat generated within the device is efficiently dissipated from the device. Hence new LED chip layouts with low thermal resistances must be designed to enable low operational temperatures ensuring long term stable operation of the devices.

3.3 Current crowding in lateral geometry LEDs

The current crowding effect in III-nitride LEDs is an important factor in the chip designing process. Hence in this section the origin of current crowding in LEDs and its significance for UV LEDs will be presented.

3.3.1 Theory of current crowding

III-nitride LEDs fabricated on sapphire substrates, without substrate lift-off, have a lateral contact mesa geometry i.e., both the p and n contact lie side by side on the epitaxial side, due to the electrically insulating nature of the substrate (Fig. 3.6 a). The p-ohmic contact lies on the top of the mesa while the n-ohmic contact lies on the area surrounding the mesa. During operation, the current has to flow laterally through the n-current spreading layer. Due to the resistance of the n-current spreading layer, the current will crowd around the edges of the mesa which is called the *current crowding effect* [62]. Due to current crowding, there is a reduction of the effectively used area of the active region resulting in higher current densities. Localized over heating of the device may occur as a consequence of the high current densities. Current crowding will thus result in the saturation of the output power at lower currents. Additionally, the emission of light from the active region will be inhomogeneous across the mesa (Fig. 3.7) which may be a problem for some applications such as the use of LEDs in displays. Hence it is necessary that the current crowding effect is minimized to obtain efficient LEDs.

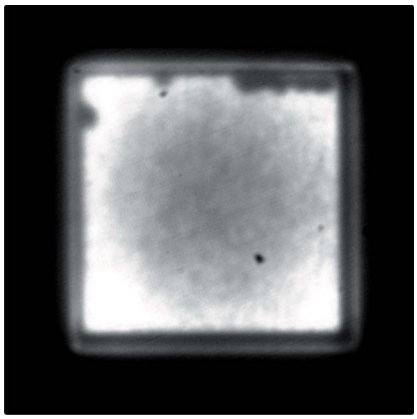

Figure 3.7: Optical microscope image showing inhomogeneous emission from a 350 nm AlInGaN LED measured at a current of 20 mA with ambient temperature of 300 K.

To study the distribution of the current injection in the active region across the mesa, Guo et al. [62] developed a model for the lateral current transport in LEDs using the equivalent circuit depicted in Fig. 3.6 b. Considering the potential to be uniform across the p-ohmic contact and the voltage drop across the p-type series resistance to be greater than kT/e, the current distribution in the active region can be described by the equation:

$$J(x) = J(0)exp(-x/L_s) \tag{3.12}$$

where x is the distance from the p-contact edge. Hence the current density will decrease exponentially as the distance from the p-contact edge increases. L_s, called the *current spreading length*, is the distance over which the current density will fall to $1/e$ of its maximum value at the edge of the p-contact. L_s is dependent on the specific contact resistance of the p-ohmic contact (ρ_{cp}), the resistivities of the p- and n-current spreading layers (ρ_p and ρ_n) and the thickness of the p- and n-current spreading layers (t_p and t_n) according to the equation:

$$L_s = \sqrt{(\rho_{cp} + \rho_p t_p)t_n/\rho_n} \tag{3.13}$$

Based on this model it can be seen that the current crowding in LEDs is minimal if the vertical resistance of the LED i.e, the resistivity of the p-current spreading layer and p-ohmic contact resistance, is large. However, an LED with a large vertical resistance is undesirable as the Joule heating in such a device will be considerable resulting in high operational temperatures. Contrastingly, the current crowding increases strongly as the sheet resistance of the n-current spreading layer increases.

3.3.2 Current crowding in UV LEDs

Current crowding is a severe problem for UV LEDs, which intensifies as the wavelength decreases, due to the difficulties in the growth of transparent n-doped AlGaN layers with low resistivities. The resistivity of the n-doped AlGaN layer is dependent on the carrier concentration and mobility. The commonly used n-type dopant in III-nitride layers is Si. Taniyasu et al. [63] reported that the n-type conductivity in AlGaN layers is limited due to the self compensation of the Si donors. The upper limit of uncompensated Si donors is dependent on the Al concentration in the layer and decreases as the Al concentration increases. For an Al concentration of 0.49, the upper limit of the Si concentration was found to be $6 \times 10^{19}\,\mathrm{cm}^{-3}$. Furthermore the ionization energy of the Si donors also increases with the Al concentration with a value of 8.1 meV for GaN layers [63] to (255 ± 11) meV for AlN layers [64]. Due to the self compensation effect of the Si donors and the increase in the activation energy, the carrier concentration in n-type AlGaN layers decreases with increasing Al concentration. Additionally, the mobility of the electrons in AlGaN layers is low due to alloy scattering and scattering at unidentified dislocation-related defects. The electron mobility was found to decrease from $\sim 100\ \mathrm{cm}^2/\mathrm{Vs}$ for $x \leq 0.1$ to $\sim 50\ \mathrm{cm}^2/\mathrm{Vs}$ for $x = 0.6$ [65] and then once again increases to $\sim 146\,\mathrm{cm}^2/\mathrm{Vs}$ for $x = 0.95$ [66]. Due to the low carrier concentrations and mobilities, the sheet resistance of the n-doped AlGaN layers is high ranging from $\sim$25 Ω/□ for low Al concentrations [64] to 15400 Ω/□ for $x = 0.95$ [66].

To study the current crowding effect in UV LEDs, the 3-D current spreading in an 320 nm LED die was simulated using the SpeCLED software package [38]. A simple stripe geometry was considered for the simulations. Keeping the area of the mesa constant at $0.5\,\mathrm{mm}^2$, the width was varied from 250 μm to 1000 μm. The LED structure consisted of a 200 nm thick $Al_{0.06}Ga_{0.94}N$:Mg p-current spreading layer with a resistivity of 10 Ωcm and an $Al_{0.33}Ga_{0.67}N$:Si n-current spreading layer with sheet resistance of 86 Ω/□. The p- and n-ohmic specific contact resistance was considered to be $0.01\,\Omega\mathrm{cm}^2$ and $10^{-5}\,\Omega\mathrm{cm}^2$ respectively. A current spreading length of 109 μm was obtained using Eqn. 3.12. For a mesa width of 1000 μm, the simulated distribution of the current density can be well described by the Eqn. 3.12 (Fig. 3.8 a). As the mesa width decreases and becomes comparable to the current spreading length, the simulated distribution of the current density begins to differ from the analytical model. Hence the analytical model for current crowding, which is based on the transfer line model, is valid only for the infinite mesa case.

The dependence of the current spreading length on the sheet resistance of the AlGaN:Si n-current spreading layer and the p-ohmic specific contact resistance was investigated for a fixed mesa area of $0.5\,\mathrm{mm}^2$ and width of 1000 μm (Fig. 3.8b). The sheet resistance of

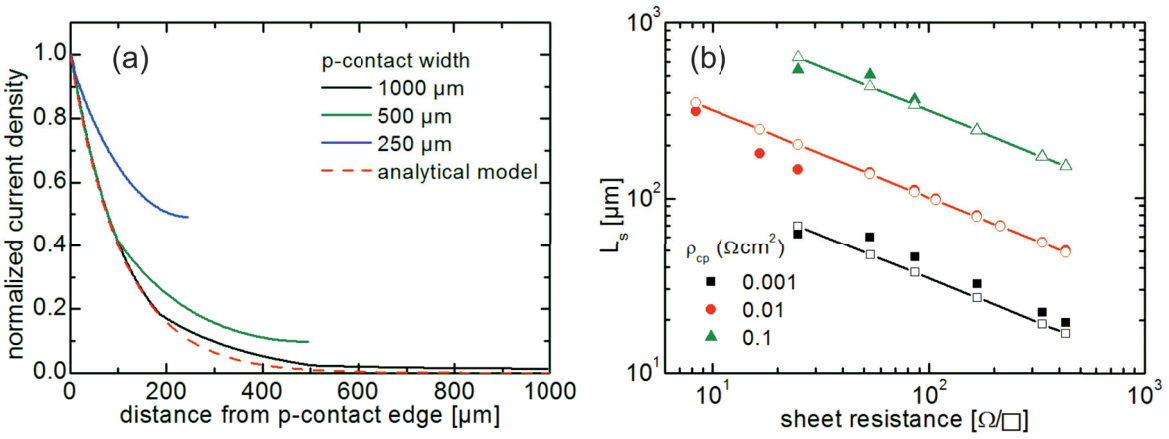

Figure 3.8: (a) Simulation of the current injection in the active region of a 320 nm LED as a function of the distance from the p-contact edge for LEDs with different p-contact widths using the 3-D current spreading model (solid lines) and the analytical model described by Eqn. 3.12 (dashed line). (b) Dependence of the current spreading length (distance from the p-contact at which the current density drops to $1/e$ times its initial value) on the sheet resistance of the n-current spreading layer and the p-ohmic specific contact resistance (ρ_{cp}) determined using the 3-D current spreading model (solid symbols) and the analytical model described by Eqn. 3.12 (open symbols).

the AlGaN:Si layer was varied from 25 $\Omega/\square$ to 430 $\Omega/\square$ while the p-ohmic specific contact resistance was varied from 0.1 Ωcm^2 to 0.001 Ωcm^2. For LEDs with high p-ohmic specific contact resistances, large current spreading lengths are obtained. A current spreading length as large as 154 μm was obtained even for LEDs with a sheet resistance of 430 $\Omega/\square$. A significantly smaller current spreading length is obtained for LEDs with low p-ohmic specific contact resistances. Even for an n-current spreading layer with 25 $\Omega/\square$ sheet resistance, the current spreading length is only 60 μm for a p-ohmic specific contact resistance of 0.001 Ωcm^2. No influence of the n-ohmic specific contact resistance on the current spreading length was observed in the case of isothermal simulations. The n-ohmic specific contact resistance will however add to the joule heating of the device which will in turn increase the current crowding effect.

To get uniform current injection in an LED, the width of the mesa should be approximately equal to twice the current spreading length. If the values of the p-ohmic specific contact resistance and the sheet resistance of the AlGaN:Si n-current spreading layer is known, Fig. 3.8 b can be used as a guide for designing the UV LED chip layout.

3.4 Summary

The dependence of the IQE on the current density, temperature effects and current crowding have been identified as the main factors that need to be taken into consideration when designing the chip layout of a UV LED. Based on the influence of these factors on the electrical

and optical properties of UV LEDs the following guidelines are obtained for the design of highly efficient and stable devices:

1. The size of the active region should be chosen to ensure that the maximum in the IQE is achieved for the operating current density due to the strong dependence of the IQE on the current density in the case of UV LEDs,

2. the thermal resistance of the LED chip should be minimized to enable low operational temperatures ensuring long term stable operation of the devices and

3. the width of the mesa in an LED should be less than twice the current spreading length to obtain uniform current injection in the UV LED.

4 Efficient UV LED chip designs for uniform current injection and heat management

The LED chip design is an essential part of the device fabrication process. For the production of highly efficient UV LEDs it is necessary to use novel LED chip layouts to ensure uniform current injection and good heat management. In this chapter, first an interdigitated finger contact geometry, in which the mesa area is reduced in one direction, will be introduced which results in an improvement of the uniformity of the current injection. The concept will then be extended to a reduction of the mesa area in two directions resulting in a micro-LED array geometry which not only improves the electrical performance of the LED but also reduces the self-heating and hence improves the thermal behaviour of the device.

4.1 Interdigitated finger contacts for homogeneous current injection in UV LEDs

In lateral geometry UV LEDs, current crowding is a serious issue which leads to detrimental effects such as a reduction in the effective area of the active region, localized over heating and non-homogeneous light emission as discussed in Sec. 3.3. To ensure a homogeneous current injection in the active region of the LED and hence avoid current crowding it is necessary to reduce the width of the mesa to less than twice the current spreading length. Gua et al. [67] proposed the use of interdigitated mesa patterns instead of conventional large area square contacts to prevent current crowding in lateral geometry III-nitride LEDs (Fig. 4.1). By reducing the width of the mesa in one direction, the distance from the centre of the mesa to the n-contact is reduced. In such a geometry the width of the p-type finger is chosen to be smaller than twice the current spreading length while the width of the n-type finger should not be larger than the contact transfer length (L_T). The contact transfer length can be determined from the transmission line model (TLM) and is given by

$$L_T = \sqrt{\frac{\rho_{cn}}{\rho_{sh_n}}} \tag{4.1}$$

where ρ_{cn} is the specific contact resistance of the n-ohmic contact and ρ_{sh_n} is the sheet resistance of the n-current spreading layer.

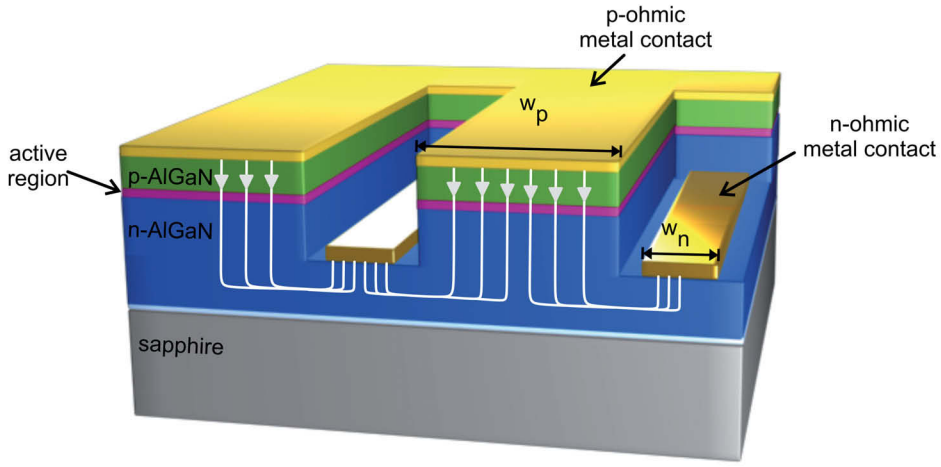

Figure 4.1: Schematic cross-sectional view of a nitride-based LED with interdigitated finger contact geometry. The width of the p-type finger is w_p while that of the n-type finger is w_n.

To investigate the influence of the finger width on the electrical, thermal and optical performance of UV LEDs, 380 nm AlInGaN LEDs with interdigitated finger contacts were fabricated. The structures were grown by MOVPE on (0001) oriented sapphire substrates and consisted of a 3.4 μm thick GaN:Si buffer layer, a 10 nm $Al_{0.23}Ga_{0.77}N$:Si hole blocking layer, an InGaN/AlInGaN MQW active region, followed by a 10 nm $Al_{0.23}Ga_{0.77}N$:Mg electron blocking layer and a 200 nm thick GaN:Mg contact layer. LEDs were fabricated using standard chip-processing technologies. Mesa structures were defined by ICP-etching in order to expose the n-GaN surface. A Ni/Au layer annealed in an oxygen ambient and reinforced with Ti/Au was used to form the p-ohmic metal contact. The n-current spreading layer was contacted using a Ti/Al/Mo/Au ohmic contact. Keeping the area of the p-contact constant at 0.0225 mm^2, LEDs with conventional square contacts and interdigitated fingers contacts were fabricated on the same wafer (Fig. 4.2). The footprint of all the different chips was kept constant. The different geometries fabricated were: (i) square contact, (ii) six interdigitated finger contact with finger width of 40 μm, (iii) ten interdigitated finger contact with finger width of 20 μm and (iv) fourteen interdigitated finger contact with finger width of 10 μm.

The L-I and V-I characteristic curves, measured under dc current operation, for the different contact geometries are shown in Fig. 4.3 a and Fig. 4.3 b, respectively. Below 70 mA, a linear increase in the output power with current is observed for all the devices. Above 70 mA, the curves become non linear and roll-over at different currents depending on the geometry of the device. The maximum output power is achieved for the LED with an interdigitated finger contact geometry with finger width of 10 μm.

The 3-D current and heat distribution in the devices was simulated, using the SpeCLED software package [38], to study the working of the LEDs. To simulate the heat distribution of the LEDs on wafer, all the external surfaces except the back-surface of the sapphire substrate

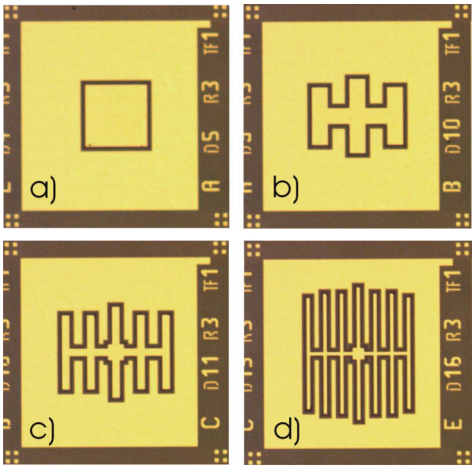

Figure 4.2: Optical microscope images of the UV LEDs with different design geometries: (a) Square contact and interdigitated finger contacts with p-type finger width of (b) 40 μm, (c) 20 μm and (d) 10 μm. The width of the n-type finger is the same as that of the p-type finger [68].

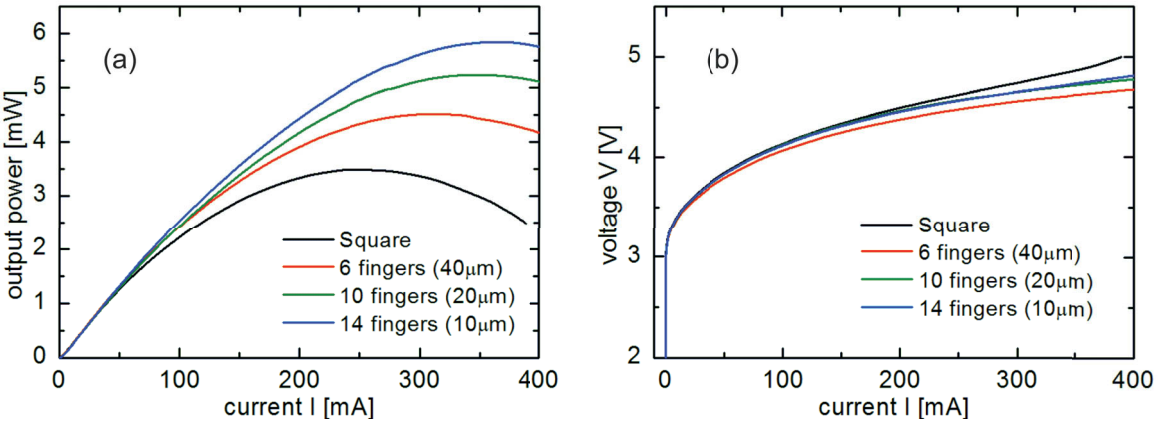

Figure 4.3: (a) Output power and (b) voltage measured on wafer as a function of current for 380 nm LEDs with a square contact and interdigitated finger contacts with p-type finger widths of 40 μm, 20 μm and 10 μm. The width of the n-type finger is the same as that of the p-type finger.

were considered to be adiabatic. In the case of the back-surface of the sapphire substrate the heat was transferred by conduction while no radiative heat transfer was considered. The lateral size of the sapphire substrate was taken to be large enough such that no further increase in the substrate size influenced the temperature of the device. The room temperature material properties used in the simulations were determined from hall and TLM measurements and are as follows: thicknesses of GaN:Mg and GaN:Si were $t_p = 0.2\,\mu$m and $t_n = 1.7\,\mu$m; electron and hole concentrations were $n = 4 \times 10^{18}\,\text{cm}^{-3}$ and $p = 1 \times 10^{17}\,\text{cm}^{-3}$; mobilities of holes and electrons were $\mu_p = 10\,\text{cm}^2/\text{Vs}$ and $\mu_n = 95\,\text{cm}^2/\text{Vs}$; specific contact resistances to GaN:Mg and GaN:Si were $7 \times 10^{-3}\,\Omega\text{cm}^2$ and $10^{-5}\,\Omega\text{cm}^2$. The thermal conductivities of the GaN and sapphire layers were considered to be 120 W/mK and 40 W/mK respectively. A heat transfer coefficient of 1×10^5 W/m^{2}K was used for the sapphire back-surface.

4.1.1 Current distribution in LEDs with interdigitated finger contacts

The current spreading length, for the 380 nm LEDs investigated, was estimated to be 87 μm using Eqn. 3.13 and assuming typical values for the contact and sheet resistances. The simulated distribution of the current injected into the active region is shown in Fig. 4.4. Although the length (150 μm) of the conventional square contact is less than twice the current spreading length, a significant current crowding is observed at the contact edges. A 20 % variation in the current density from the edge to the centre of the contact is calculated. When the square contact is replaced by an interdigitated finger contact, a more uniform current injection is obtained. With decreasing finger width, the non-uniformity in the current injection in the active region also decreases. For a finger width of 10 μm a less than 3 % variation in the current density was observed.

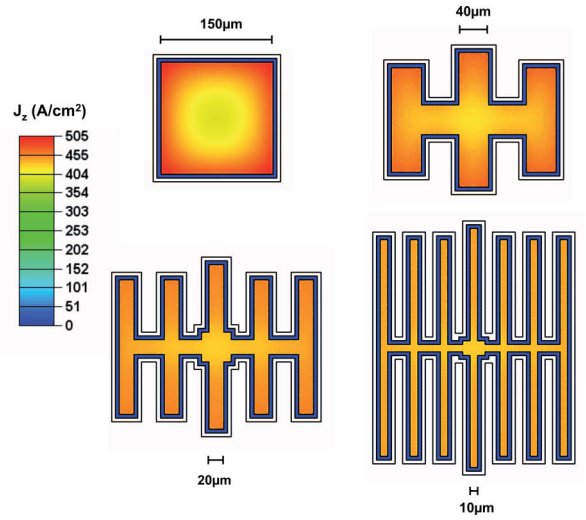

Figure 4.4: Simulation of the spatial distribution of the current injection in the active region of 380 nm LEDs with square and interdigitated finger contact geometries at a current of 100 mA. The operating voltage is 4.25 V, 4.19 V, 4.17 V and 4.15 V for the square contact and interdigitated finger contacts with p-type finger width of 40 μm, 20 μm and 10 μm respectively [68].

4.1.2 Electrical characteristics of LEDs with interdigitated finger contacts

For a better understanding of the electrical behaviour of the LEDs, the influence of the interdigitated finger contact geometry on the series resistance and the leakage currents in the device has been investigated.

Influence on the series resistance

The series resistance (R_s) in a lateral geometry LED can be divided into the p-ohmic contact resistance (R_{cp}), the resistances of the p- and n-current spreading layers (R_p and R_n respectively) and the n-ohmic contact resistance (R_{cn}) (Eqn. 4.2).

$$R_s = R_{cp} + R_p + R_n + R_{cn} \tag{4.2}$$

For a conventional square contact, if the length of the square (L) is larger than twice L_s then due to current crowding the components of R_s can be expressed as

$$R_{cp} = \frac{\rho_{cp}}{L^2 - (L - 2L_s)^2} \tag{4.3}$$

$$R_p = \frac{\rho_p t_p}{L^2 - (L - 2L_s)^2} \tag{4.4}$$

$$R_n = \frac{\rho_{sh_n}(L_s + d)}{4L} \tag{4.5}$$

$$R_{cn} = \frac{\rho_{cn}}{4LL_T} \tag{4.6}$$

where d is the distance between the edges of the p- and n-ohmic contacts and L^2 is the area of the p-contact. Since the current spreading in the p-current spreading layer is much smaller than the dimensions of the p-contact, it is not considered in the calculations. If the conventional square contact is replaced by an interdigitated finger contact with finger width w equal to $2L_s$ and keeping the p-ohmic contact area constant, the components of R_s are now given by

$$R_{cp} = \frac{\rho_{cp}}{L^2} \tag{4.7}$$

$$R_p = \frac{\rho_p t_p}{L^2} \tag{4.8}$$

$$R_n = \frac{\rho_{sh_n}(L_s + d)}{p} \tag{4.9}$$

$$R_{cn} = \frac{\rho_{cn}}{pL_T} \tag{4.10}$$

where p is the perimeter of the p-ohmic contact. Comparing Eqns. [4.3 - 4.6] to Eqns. [4.7 - 4.10], it can be seen that the use of intergitated finger contacts results in lower series resistance of the LED. Additionally, as the series resistance of the interdigited finger contact is influenced by the perimeter of the p-ohmic contact, the series resistance will decrease with decreasing finger width due to the increased perimeter of the device.

To experimentally study the influence of the contact geometry on the series resistance, the differential series resistance of the fabricated 380 nm LEDs was determined from the linear part of the measured I-V curves (Fig. 4.3 b). Differential series resistances of 2.5 Ω, 2.0 Ω, 1.4 Ω, and 1.5 Ω were obtained for the square contact and the interdigitated fingers contacts with finger widths of 40 μm, 20 μm, and 10 μm, respectively. Due to the large p-specific contact resistance of the LEDs, the series resistance is dominated by the resistance of the p-ohmic contact. Hence a large decrease in the differential series resistance is observed when moving from the conventional square contact to an interdigitated finger contact with finger width of 40 μm and then further to a finger width of 20 μm due to a more uniform current injection. The contribution of R_{cn} to the total series resistance vanishes due to the low resistance of the n-ohmic contact. Therefore reduction in the finger width to 10 μm does not strongly influence the differential series resistance as no change in the distribution of the current injection is expected.

Simulations of the devices show a decrease in the operating voltage at 100 mA from 4.25 V for the conventional square contact to 4.15 V for the contact with the narrowest finger width of 10 μm (Fig. 4.4). For an LED with emission of 380 nm, the voltage drop across the active region is 3.26 V. The remaining 0.99 V and 0.89 V, in the case of the square contact and the interdigitated finger contact with finger width of 10 μm respectively, is the voltage drop across the series resistance. The reduction in the operating voltage indicates a lowering of the series resistance, from the square contact to the contact with finger width of 10 μm, by 1 Ω which agrees well with the evaluation of the measured I-V curves.

Influence on the leakage current

The interdigitated finger contact geometry has an increased perimeter as compared to the conventional square contact with the same p-contact area. The use of reactive ion etching (RIE) for the definition of the mesa has been reported [69] to induce surface damage at the mesa edges resulting in leakage paths that bypass the active region. Hence an increased perimeter may result in larger leakage currents being observed in the case of LEDs with interdigitated finger contact geometries. An increase in the leakage current with the perimeter of the p-contact of 460 nm LEDs has been previously reported by Gua et al. [67]. To investigate the influence of the finger width on the leakage current of UV-LEDs, the reversed-biased I-V characteristics of the LEDs with different geometries were measured. At a reversed-bias voltage of 5 V, no clear dependence of the leakage current on the perimeter of the device was observed (Fig. 4.5). Furthermore a large scatter in the measurement was observed across the wafer. The results indicate that leakage through the volume of the device is dominant compared to the leakage current on the etched surface of the diode. Due to the large dislocation density (10^9 cm^{-2}) of the GaN/sapphire template on which the UV LEDs were grown, the

dominating mechanism is bulk leakage [70, 71]. The perimeter of the device will once again be an important factor for devices with low dislocation densities due to the reduction of the bulk leakage component to the total leakage current in the LED.

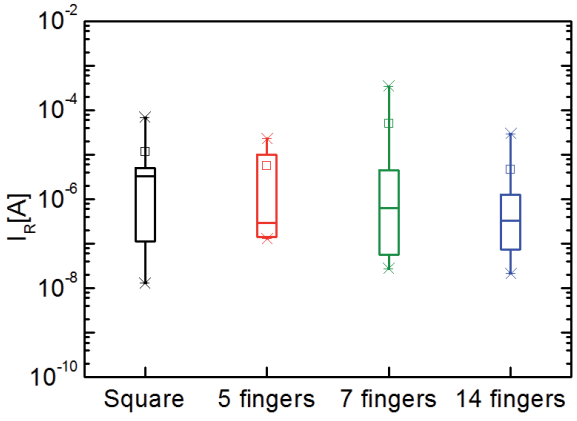

Figure 4.5: Boxplot of the leakage current measured at -5 V for 380 nm LEDs with square contact and interdigitated fingers contacts.

4.1.3 Self heating of LEDs during operation

The self heating of the LEDs can be studied by measuring the shift in the LED emission wavelength with the operating current (Fig. 4.6 a). With increasing current the emission wavelength is red shifted. At 300 mA dc current, a shift of 9.08 nm, w.r.t. the emission wavelength under pulsed conditions, is observed for the square contact corresponding to a 202°C increase in junction temperature. In comparison, the junction temperatures of the LEDs with interdigitated finger contacts increase by 139°C , 122°C and 104°C for the devices with finger widths of 40 μm, 20 μm and 10 μm respectively. The dependence of the self-heating of the LED on the contact geometry is also reflected in the thermal roll-over of the L-I curves shifting to higher currents as the width of the interdigitated fingers is decreased. The lower heating in the LEDs with interdigitated finger contacts as compared to the square contact may be attributed to the lower series resistances and/or a more efficient extraction of heat from the contact. The thermal resistance of the LEDs was determined from the shift in the emission wavelength (Fig. 4.6 b). The thermal resistance of the LED with the square contact was found to be 139 K/W while that of the LEDs with the interdigitated finger contacts decreased from 98 K/W to 76 K/W along with the finger width. The interdigitated finger contact geometry hence provides a better dissipation of the generated heat.

The simulated temperature distributions in the LEDs at 100 mA also show that the junction temperature is maximum for the LED with the square contact and decreases for the interdigitated finger contacts (Fig. 4.7 b). Furthermore the distribution of the temperature across the chip is more homogeneous for the LEDs with interdigitated finger contacts. Infrared camera images of the temperature distribution in the LEDs at 20 mA were found to be in good agreement qualitatively with the simulated temperature distributions (Fig. 4.7 a).

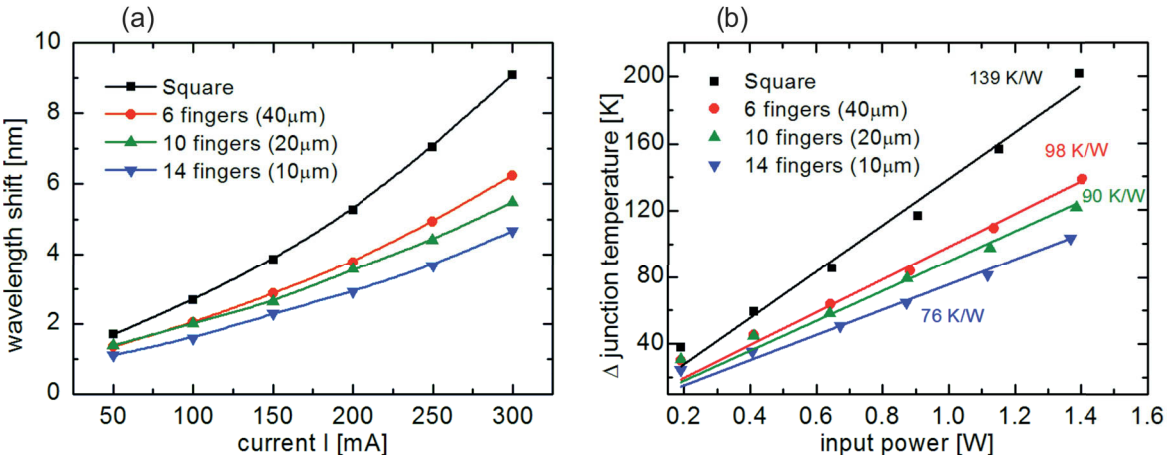

Figure 4.6: (a) Shift in emission wavelength as a function of current and (b) Junction temperature during dc operation as a function of input power, measured on wafer, for 380 nm LEDS with a square contact and interdigitated finger contacts with p-type finger widths of 40 μm, 20 μm and 10 μm.

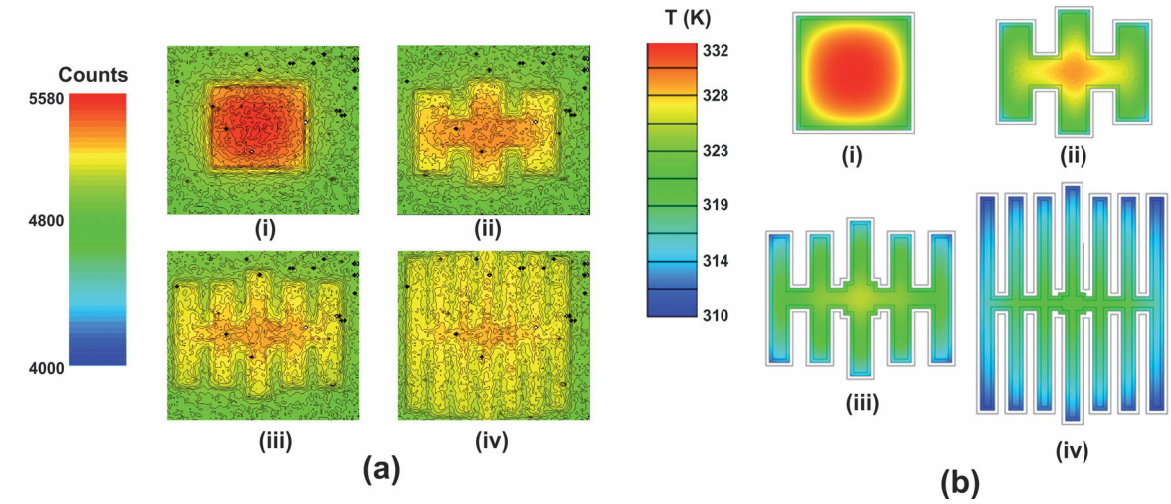

Figure 4.7: (a) Infra-red camera images of 380 nm LEDs with (i) square contact and interdigitated finger contacts with p-type finger widths of (ii) 40 μm, (iii) 20 μm and (iv) 10 μm measured at 20 mA. (b) Simulation of the temperature distribution in the active region of the LEDs. The total current is constant at 100 mA.

4.2 Micro-LED arrays for high power UV LEDs

In order for UV LEDs to be used in applications such as water purification, phototheraphy or UV-printing, devices with high output powers are required. High power LEDs are typically operated at currents greater that 100 mA. The low EQE and significant Joule heating, due to the high resistances of the ohmic contacts and the n-and p-current spreading layers, result in the self heating of UV LEDs at the necessary high currents. This self heating of the device is detrimental to its performance (Sec. 3.2). Hence for high power applications it is not only necessary to decrease the series resistance of the device but also to effectively extract the heat generated in the LEDs during operation by designing suitable contact geometries and heat sinks which will result in a low thermal resistance of the device.

An effective technique to improve the performance of high power lateral geometry LEDs is the use of micro-LED arrays [72–75]. In this geometry, a conventional large area single mesa LED is replaced by a matrix of interconnected micrometer size LEDs which are operated in parallel (Fig. 4.8). The use of micro-LED arrays results in reduced current crowding and a 2-D reduction in the LED access resistance as compared to the 1-D reduction obtained with the use of interdigitated finger contacts [74]. The thermal resistance of the device is also reduced due the segmentation of the area where heat is generated in the chip. Additionally the distance between the micro-LEDs allows the heat to be dissipated efficiently.

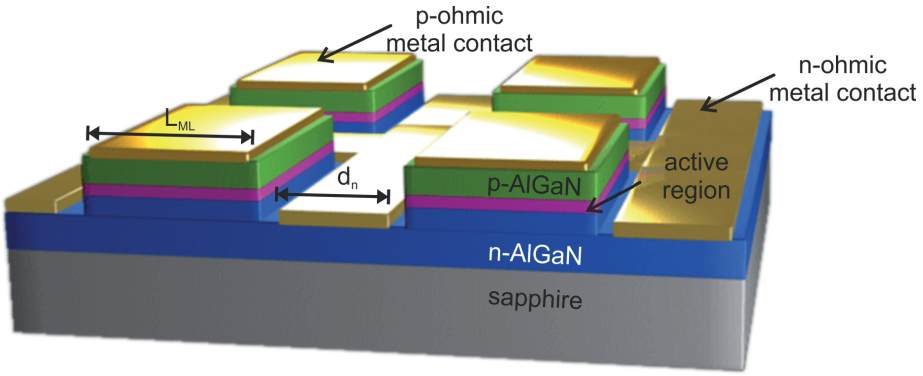

Figure 4.8: Schematic cross-sectional view of a nitride-based LED with micro-LED array geometry. The length of each micro-LED is L_{ML} and the width of the n-contact is d_n.

To study the influence of the micro-LED array geometry on the electrical, optical and thermal behaviour of UV LEDs, 380 nm and 327 nm LEDs with micro-LED arrays were fabricated. The LED layer structures were grown by MOVPE on (0001) oriented sapphire substrates. The LED emitting at 380 nm consisted of a 3.5 μm thick GaN:Si buffer layer, a 10 nm $Al_{0.23}Ga_{0.77}N$:Si hole blocking layer, an InGaN/InAlGaN MQW active region, followed by a 10 nm $Al_{0.23}Ga_{0.77}N$:Mg electron blocking layer and a 200 nm thick GaN:Mg contact layer. In the case of the LEDs emitting at 327 nm, the layer structure consisted of a 400 nm AlN base layer followed by a 7 μm thick transparent AlGaN:Si buffer layer, an InAlGaN/InAlGaN MQW active region, a 25 nm AlGaN:Mg electron blocking layer,a 500 nm thick GaN:Mg/$Al_{0.12}Ga_{0.88}N$:Mg short period superlattice and a 20 nm GaN:Mg

contact layer. After MOVPE growth the samples were annealed in nitrogen ambient in order to activate the p-type conductivity.

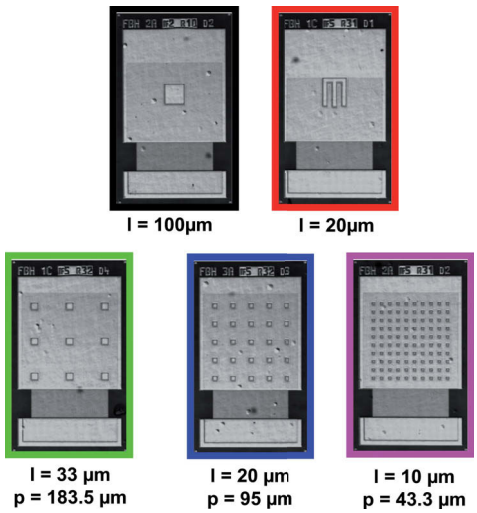

Figure 4.9: Optical microscope images of the UV LEDs with different design geometries where l is the length of the each individual micro-LED or finger width and p is the pitch of the array [76].

LEDs were fabricated using standard chip-processing technologies. Mesa structures were defined by ICP-etching in order to expose the n-(Al)GaN surface. A palladium based p-contact was deposited to form the p-electrode while an aluminium based contact was used to form the n-electrode. A SiN layer was used as an insulator and Ti/Au pads were fabricated for electrical contact. Keeping the area of the p-contact constant at 0.01 mm^2, LEDs with different design geometries were fabricated on the same wafer (Fig. 4.9). The footprint of all the different geometries was also kept constant. The different geometries fabricated were: (i) square contact, (ii) interdigitated fingers contact with finger width of 20 μm, (iii) micro-LED arrays with pixel sizes 10 μm, 20 μm, and 33 μm and pitch 43.3 μm, 95 μm and 183.5 μm, respectively.

To investigate the current spreading and heat distribution in LEDs with different geometries, 3-D simulations of the current distribution coupled with thermal analysis were performed using the SpeCLED software package [38]. The room temperature material properties used in the simulation of the LEDs emitting at 327 nm were as follows: thicknesses of $Al_{0.06}Ga_{0.94}N$:Mg and $Al_{0.35}Ga_{0.65}N$:Si were $t_p = 0.2\,\mu$m and $t_n = 6\,\mu$m; electron and hole concentrations were $n = 1.5 \times 10^{18}$ cm^{-3} and $p = 1 \times 10^{17}$ cm^{-3}; mobilities of holes and electrons were $\mu_p = 6$ cm^2/Vs and $\mu_n = 96$ cm^2/Vs; specific contact resistance to GaN:Mg and $Al_{0.35}Ga_{0.65}N$:Si were 10^{-2} Ωcm^2 and 10^{-4} Ωcm^2. For the electrical and thermal modelling, the 20 nm GaN:Mg layer was not taken into account. The thermal conductivities of the AlGaN and sapphire layers were considered to be 80 W/mK and 40 W/mK respectively. A heat transfer coefficient of 1×10^5 W/m^{2}K was used for the sapphire back surface.

4.2.1 Current distribution in micro-LED arrays

To study the influence of the contact design on the current injection into the active region, the thermally coupled 3-D current distribution in LEDs emitting at 327 nm with different device

geometries was simulated. Due to the high resistance of the p-contact and the thick n-current spreading layer, the current is almost uniformly injected into the active region of the LED (Fig. 4.10). In the case of the 0.01 mm^2 square contact, the current density varies by 7.2 % from the edge to the centre of the mesa at 100 mA. A uniform current injection is obtained across the finger width of the interdigitated finger contact and the micro-LED arrays. Current crowding will be an important issue when the resistance of the p-ohmic contact and p-current spreading layer is reduced. In addition, for LEDs emitting in the UV-B and UV-C regions, due to the high resistivity of the underlying n-AlGaN layers with high Al-contents, current spreading in the LED will be crucial. Consequently, the use of micro-LED arrays, where the pixel size is smaller than twice the current spreading length [62], will be beneficial for uniform current injection and hence improved device performance.

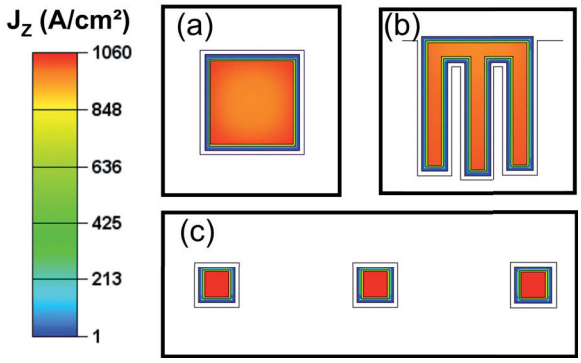

Figure 4.10: Simulation of the spatial distribution of the current density in the active region of 327 nm LEDs with (a) square (b) interdigitated fingercontact and (c) micro-LED array (zoomed in) with individual micro-LED size of 33 μm at a total current of 100 mA [76].

4.2.2 Influence of the micro-LED size on the operational voltage and series resistance

To analyse the influence of the contact geometry on the series resistance and the operational voltage, the I-V characteristics of the fabricated 380 nm and 327 nm LEDs were investigated. The operational voltages of the micro-LED arrays, emitting at 380 nm, were found to be lower than that of the interdigitated finger contact (Fig. 4.11 a). The series resistance, decreased from 2.9 Ω for the interdigitated finger contact to 2.0 Ω - 1.7 Ω for the micro-LED arrays. A 10 % variation in the series resistance was observed for each geometry across the wafer. As the p-contact resistance can be considered to be constant for all the devices, the decrease in the series resistance is attributed to a decrease in the resistance of the n-current spreading layer due to a one-dimensional reduction in the device geometry, as compared to the interdigitated finger contact. In the case of the LEDs emitting at 327 nm, due to the non-linearity of the p-contacts, the large p-contact resistance and the high resistivity of the $Al_{0.06}Ga_{0.94}N$:Mg cladding layer (3 Ωcm), large variations in the turn on voltages of the devices were observed across the wafer (Fig. 4.11 b). Despite this large variation, the series resistance decreased from 49 Ω for the square contact to 40 Ω for the interdigitated finger contact and further reduced to 37 Ω, 36 Ω and 32 Ω for the micro-LED arrays with pixel sizes 33 μm, 20 μm and 10 μm respectively.

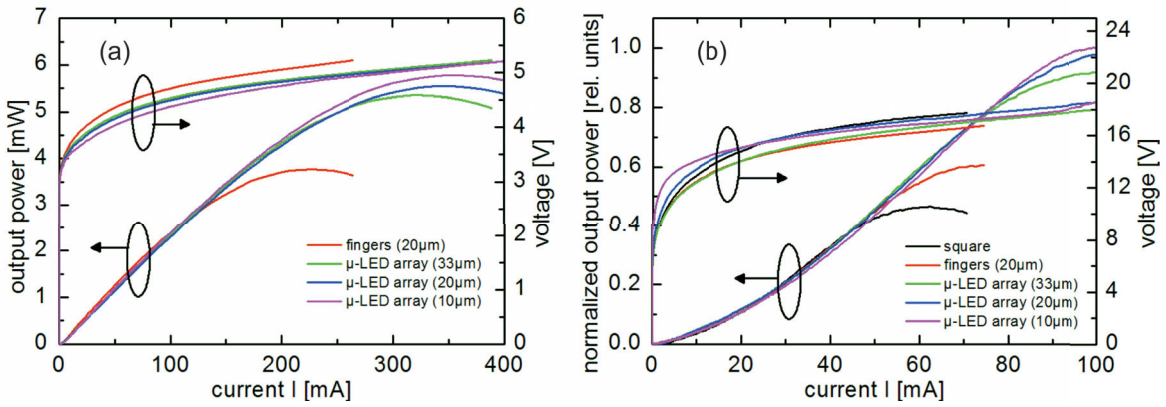

Figure 4.11: Emission power and operating voltage as a function of current, measured on wafer, for (a) 380 nm LEDs and (b) 327 nm LEDs with different design geometries [76].

To understand the observed decrease in the series resistance with the introduction of the micro-LED array geometry, the series resistance of a micro-LED array is compared to that of a conventional square contact when both devices have the same p-contact area. The series resistance of a conventional square contact, with length of the square (L) larger than twice L_s, is described by Eqns.[4.2 - 4.6]. To determine the series resistance of a square micro-LED array with p-contact area equal to that of the conventional square contact, we consider the resistance of each micro-LED. In the case of a square micro-LED array, with N micro-LEDs in a row, the length of each micro-LED is given by L/N. If d is the distance between the edges of the p- and n-ohmic contacts, the series resistance of a single micro-LED ($R_{s_{ML}}$), can be expressed as

- Case I: $L/N > 2L_s$

$$R_{s_{ML}} = \frac{\rho_{cp}}{(\frac{L}{N})^2 - ((\frac{L}{N}) - 2L_s)^2} + \frac{\rho_p t_p}{(\frac{L}{N})^2 - ((\frac{L}{N}) - 2L_s)^2} + \frac{\rho_{sh_n}(L_s + d)}{4(\frac{L}{N})} + \frac{\rho_{cn}}{4(\frac{L}{N})L_T} \quad (4.11)$$

- Case II: $L/N \leq 2L_s$

$$R_{s_{ML}} = \frac{\rho_{cp}}{(\frac{L}{N})^2} + \frac{\rho_p t_p}{(\frac{L}{N})^2} + \frac{\rho_{sh_n}(L_s + d)}{4(\frac{L}{N})} + \frac{\rho_{cn}}{4(\frac{L}{N})L_T} \quad (4.12)$$

The series resistance of the complete chip ($R_{s_{total}}$) is then given by the sum of the individual resistances in parallel.

$$R_{s_{total}} = R_{s_{ML}}/N^2 \quad (4.13)$$

Hence when $L/N > 2L_s$ the series resistance of the complete chip is given by

$$R_{s_{total}} = \frac{\rho_{cp}}{L^2-(L-2NL_s)^2} + \frac{\rho_p t_p}{L^2-(L-2NL_s)^2} + \frac{\rho_{sh_n}(L_s+d)}{4LN} + \frac{\rho_{cn}}{4LNL_T} \tag{4.14}$$

When $L/N \leq 2L_s$ the series resistance of the complete chip is given by

$$R_{s_{total}} = \frac{\rho_{cp}}{L^2} + \frac{\rho_p t_p}{L^2} + \frac{\rho_{sh_n}(L_s+d)}{4LN} + \frac{\rho_{cn}}{4LNL_T} \tag{4.15}$$

Comparing the Eqns.[4.2 - 4.6] to Eqns.[4.14 - 4.15], it can be seen that the use of micro-LED arrays results in lower series resistance. All the four contributions to the series resistance (R_{cp}, R_p, R_n and R_{cn}) will decrease with increasing number of micro-LEDs as long as the length of the micro-LED is greater than $2L_s$. For micro-LEDs with lengths equal to or smaller than $2L_s$, only R_n and R_{cn} will decrease with increasing number of micro-LEDs due to the longer perimeter. The number of micro-LEDs will influence the footprint of the device and hence it is necessary to determine the optimum number of micro-LEDs on a chip (Sec. 4.2.4).

4.2.3 Thermal resistance of LEDs with micro-LED arrays

The emission power of the micro-LED arrays at different currents was compared to that of a large area square contact and an interdigitated finger contact for LEDs emitting at 380 nm (Fig. 4.11 a) and 327 nm (Fig. 4.11 b). Initially the output power increases with the current and then rolls over at high currents. This rollover of the output power is attributed to the self-heating of the device which results in increased non-radiative recombination and carrier leakage [52]. The thermal rollover of the emission power shifts to higher currents as the device geometry is changed from a large area square contact into an interdigitated finger contact and then finally into micro-LED arrays. The increase in the maximum emission power is attributed to better heat dissipation and hence reduced self heating with the use of micro-LED arrays. Additionally, the larger perimeter of the mesas for the micro-LEDs could also increase the LEE of the device by deflecting guided light downwards towards the substrate.

To further investigate the influence of the device geometry on the self heating of the LED, the thermal resistances of the 380 nm LEDs with different device geometries were measured on wafer. As seen in Fig. 4.12 a, the thermal resistance of the interdigitated finger contact was determined to be 72 K/W. With the use of the micro-LED arrays, the thermal resistance reduced to 41 K/W for a pixel size of 33 μm and 36 K/W for a pixel size of 20 μm. No further decrease in the thermal resistance was observed with smaller pixel size.

The 327 nm LEDs were grown on an AlGaN:Si current spreading layer which has lower thermal conductivity as compared to GaN:Si layers [77]. Due to the reduced thermal conductivity of the underlying AlGaN:Si current spreading layer, the measured thermal resistance of the 327 nm LEDs are higher than that of the 380 nm LEDs (Fig. 4.12 b). A thermal resistance of 154 K/W was observed for the conventional square contact which reduced to

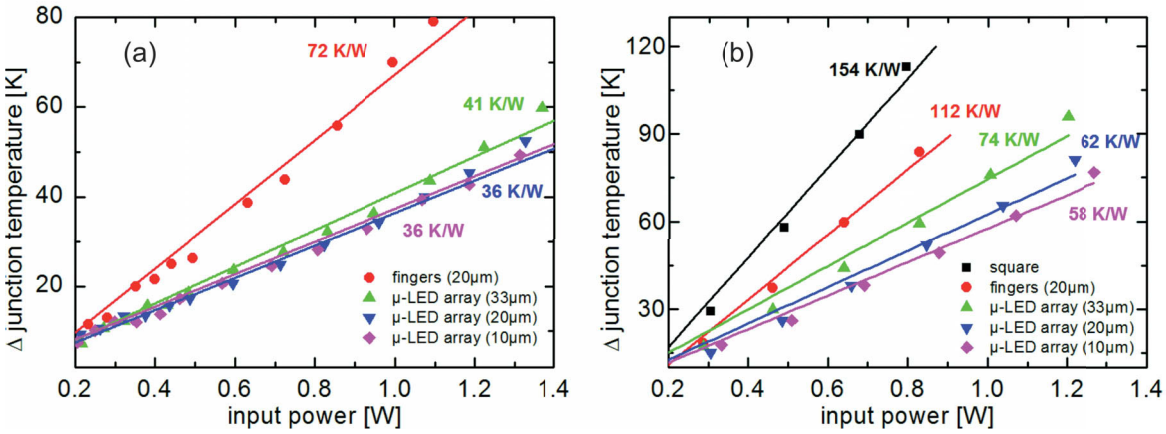

Figure 4.12: Junction temperature, measured on wafer, during dc operation as a function of input power for (a) 380 nm LEDs and (b) 327 nm LEDs with different design geometries [76].

112 K/W with the use of the interdigitated finger geometry. Thermal resistances as low as 58 K/W were obtained with micro-LED arrays. This corresponds to a factor of 2.6 decrease in the thermal resistance. The experimentally obtained results are in good agreement with the simulations of the current spreading and heat distribution in 327 nm LEDs. As seen in Fig. 4.13 b, the temperature of the active region decreases as we change the contact geometry from a square contact to micro-LED arrays at a fixed current of 50 mA. The thermal resistance of the LEDs, obtained from both simulations and experiments, was found to decrease linearly with the length of the pixels (Fig. 4.14) although the distance between the pixels also decreased correspondingly. In addition, the foot print of the device is the same for all the different geometries. This indicates that the improved heat dissipation is mainly due to the division of the heat source from one large area in the square contact into smaller pixels thus allowing sufficient area for the dissipation of the generated heat.

Infra-red camera images of the temperature distribution in 327 nm LEDs at 20 mA were found to be in good agreement with the simulated temperature distributions (Fig. 4.13 a). The conventional square contact showed the highest temperature and the most non-uniformity in the temperature distribution. With the introduction of the micro-LED arrays not only a drop in the peak temperature was observed but the temperature distribution across the chip becomes more uniform.

To show that the micro-LED array geometry will also be beneficial for flip-chip mounted LEDs, 3-D thermal distribution simulations[1] were done, using the Patran/ Nastran software package from MSC Software Corporation [78], of LEDs flip-chip mounted on AlN submounts to determine the thermal resistance of the entire device. The mounted LEDs were considered to be soldered on to a Cu-heatsink. The size of the LED chips was considered to be 600 μm x 1000 μm while that of the submount was 800 μm x 1500 μm. The thermal conductivities of the AlN submount, AlGaN p-cladding layer, solder, and the Cu-heatsink

[1] Simulations done by Christoph Stölmacker.

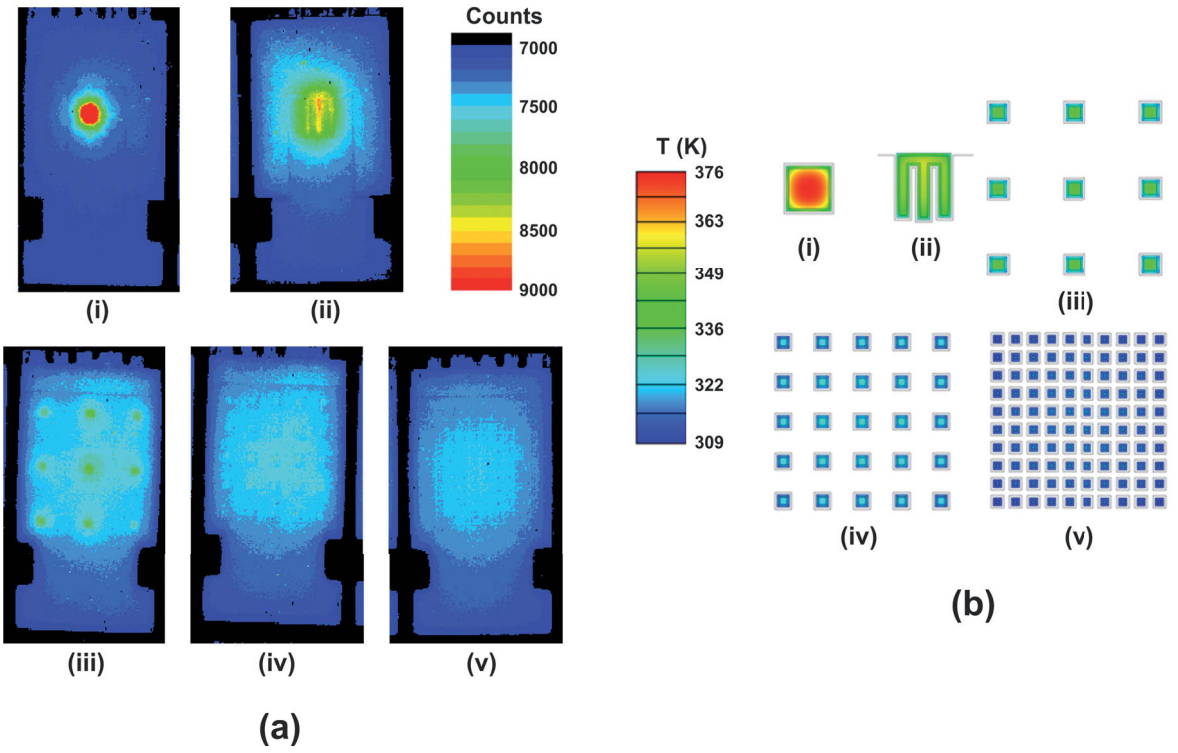

Figure 4.13: (a) Infra-red camera images of 327 nm LEDs with (i) square contact (l = 100 μm), (ii) interdigitated finger contact (l = 20 μm), (iii) micro-LED array (l = 33 μm, p = 183.5 μm), (iv) micro-LED array (l = 20 μm, p = 95 μm), and (v) micro-LED array (l = 10 μm, p = 43.3 μm) measured at 20 mA. (b) Simulation of the heat distribution in the active region of the LEDs. The total current is constant at 50 mA [76].

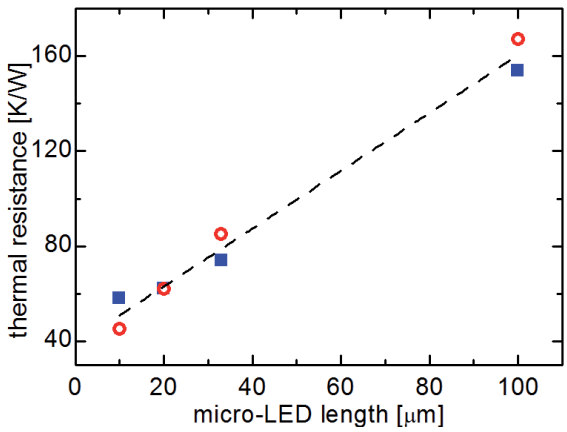

Figure 4.14: Experimental (solid squares) and theoretical (circles) thermal resistance of 327 nm LEDs as a function of the micro-LED length [76]. The dashed line is a guide to the eye.

were considered to be 170 W/mK, 20 W/mK, 57 W/mK, and 400 W/mK respectively. In the simulations the heat was generated in the active region and the back-surface of the Cu-heatsink was kept fixed at 300 K. Both conduction and convection modes of heat transfer were considered. For a conventional square p-contact with area 0.01 mm^2, the thermal resistance was determined to be 36 K/W which decreased to 13.5 K/W for a micro-LED array with individual micro-LED size of 10 μm, corresponding to a factor of 2.7 decrease in thermal resistance (Fig. 4.15). These results are consistent with the trends observed in the on-wafer measurements indicating that micro-LED arrays are an effective geometry for improved thermal management.

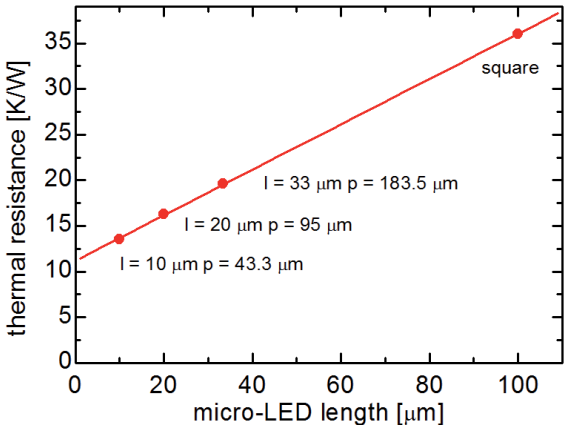

Figure 4.15: Simulated thermal resistance of flip-chip mounted 327 nm LEDs as a function of the micro-LED length [76].

4.2.4 Optimization of the number of micro-LEDs

The electrical, optical and thermal performance of UV LEDs with micro-LED arrays improves with decreasing size of the individual micro-LEDs, i.e. an increase in the number of micro-LEDs. However, an increase in the number of micro-LEDs is accompanied by an increase in the footprint of the chip due to the increased area of the n-contact. For a fixed LED chip footprint the number and size of the micro-LEDs will determine the effective die area (A_{eff}) i.e. the area of the LED chip emitting light. In order to efficiently use the chip area it is necessary maximize the ratio of the effective die area to the total area of the chip.

Consider a micro-LED array having a square footprint, with length L_{FP} and area (A_{FP}). If the number of micro-LEDs in a row is N and the width of the n-contact is d_n the length of each micro-LED (L_{ML}) is given by

$$L_{ML} = \frac{L_{FP} - [(N+1) \times d_n]}{N} \tag{4.16}$$

The effective area for the micro-LED array (A_{ML})can then be written as

- Case I: $L_{ML} > 2L_s$

$$A_{ML} = N^2(L_{ML}^2 - (L_{ML} - 2L_s)^2) \tag{4.17}$$

- Case II: $L_{ML} \leq 2L_s$

$$A_{ML} = N^2 L_{ML}^2 \tag{4.18}$$

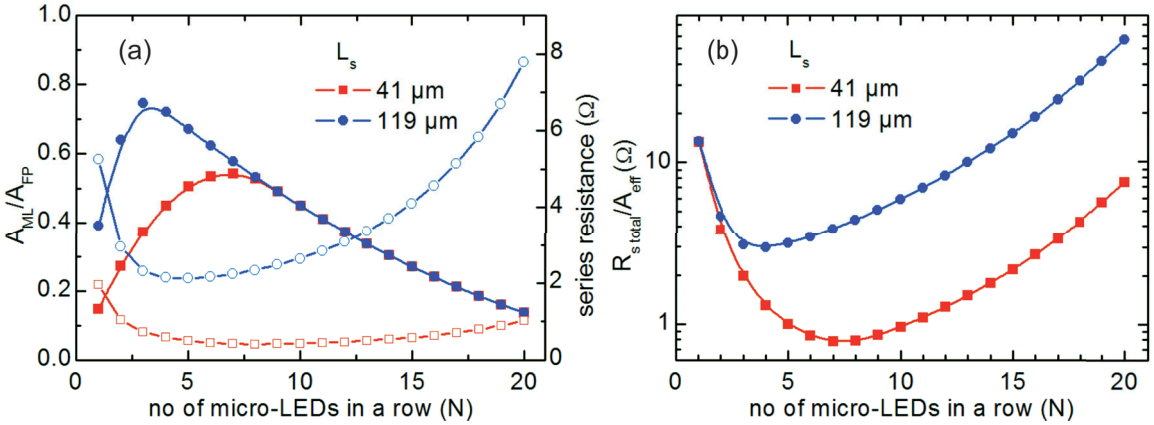

Figure 4.16: (a) Dependence of the effective useful die area and the series resistance on the number of micro-LEDs in a row for a fixed chip area of 1 mm^2 calculated for two current spreading lengths (L_s). (b) Determination of the optimum number of micro-LEDs in a row (minimum in the curve) for two current spreading lengths (L_s) and fixed chip area of 1 mm^2.

The ratio of the effective die area to the total area of the chip ($A_{eff} = A_{ML}/A_{FP}$), calculated for different current spreading lengths, is shown in Fig. 4.16 a. The area of the chip and the width of the n-contact was kept constant at 1 mm^2 and 20 μm respectively. The distance between the edges of the p- and n-ohmic contacts was considered to be 5 μm. The most efficient use of the LED chip is achieved when the size of the individual micro-LED is comparable to twice the current spreading length. Thus, it can be clearly seen that large current spreading lengths result in the maximum use of an LED chip area. To determine the optimum array for a fixed footprint, it is necessary to consider the series resistance ($R_{s_{total}}$) of the LED. In Fig. 4.16 a, the series resistance of the micro-LED arrays are calculated. The resistance initially decreases as the number of micro-LEDs increases but begins to rise as the total size of the p-contact is reduced in the case of large arrays. The optimum size of the micro-LED array can be determined from the minimum of the ratio $R_{s_{total}}/A_{eff}$ (Fig. 4.16 b). For a current spreading length of 41 μm, the optimized geometry is a 7×7 micro-LED array with the length of each individual micro-LED being 108 μm. On the other hand a 4×4 array is optimum for a current spreading length of 119 μm with individual micro-LED length of 212 μm.

4.3 Summary

The use of interdigitated finger contact geometry and micro-LED arrays to ensure uniform current injection in UV LEDs was demonstrated. Calculations and experiments show that these geometries have a lower series resistance as compared to conventional square contacts and improved heat management. The micro-LED arrays can be effectively used to reduce the self heating of UV LEDs due to improved temperature distribution resulting in a greater than two-fold decrease in the thermal resistance of the device as compared to a conventional large area square contact. Furthermore, even when the LEDs are flip-chip mounted, the micro-LED array geometry continues to be thermally advantageous. However, the use of this geometry greatly enhances the size of the chip thus reducing the useful die area. Hence a method to determine the optimum size of the micro-LED array for a fixed chip area was also presented. The use of this geometry will be essential for high power UV-B and UV-C LEDs due to its capabilities of ensuring uniform current injection, reduced series resistance and reduced self-heating of the device.

5 Extraction of light from light emitting diodes

Fabrication of UV LEDs is an emerging technology and hence research efforts are mainly being directed towards increasing the IQE of the devices while ignoring the LEE. Nevertheless, for the realization of high efficiency devices, methods to improve the LEE of UV LEDs are essential and therefore is a significant element of this thesis. In this chapter, the basic theory behind extraction of light from LEDs and the particular challenges faced in the outcoupling of light from UV LEDs will be discussed. Finally, an overview of the methods to increase the LEE of nitride-based LEDs will be presented.

5.1 Extraction of light from LEDs

For the realization of highly efficient LEDs it is necessary to extract all the light generated in the active region of the device into free space. Light extraction is a major challenge due to the high refractive index of the semiconductor/substrate which results in total internal reflection of the light at the semiconductor–air or substrate–air interface. The critical angle for total internal reflection (ϕ_c) can be determined from Snell's law and is given by Eqn. 5.1, where n_s is the refractive index of the semiconductor and n_{air} is the refractive index of air. Only light incident on the surface at an angle, w.r.t. the normal, smaller than the critical angle can escape thus defining a light escape cone.

$$\phi_c = sin^{-1}\frac{n_{air}}{n_s} \tag{5.1}$$

If the light emission is assumed to be from a point-like source in the semiconductor with a total power of P_{source}, then the fraction of light that is emitted into the escape cone is given by Eqn. 5.2 [45]. For semiconductors with a high refractive index like GaAs ($n_s \approx 3.4$) and GaN ($n_s \approx 2.56$) the critical angle is only 17.1° and 23° respectively. Due to the small critical angles only 2.21 % of the light can be extracted from a planar GaAs LED while 4.18 % of the emitted light can escape from a planar GaN LED.

$$\frac{P_{escape}}{P_{source}} \approx \frac{1}{4}\frac{n_{air}^2}{n_s^2} \tag{5.2}$$

LED structures are conventionally quadrangular parallelepipeds which have six light escape cones, two perpendicular and four parallel to the plane of the active layer. In the case of rectangular parallelepiped nitride-LEDs grown heteroepitaxially on sapphire substrates,

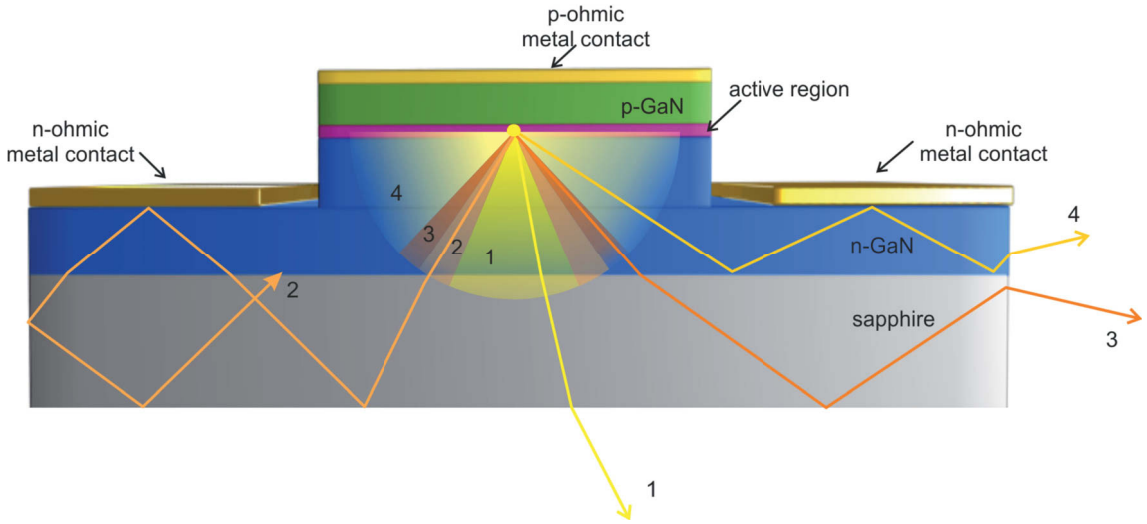

Figure 5.1: Schematic of the propagation of the emitted light in an LED

the photons will be outcoupled based on their angle of emission (θ) from the active region w.r.t. the normal to the plane of the active region (Fig. 5.1). The emission can be divided into various zones [79]:

1. Surface-emission zone: $0 \leq \theta < \theta_1 = \sin^{-1}(n_{air}/n_s)$
   The photons emitted within this zone will be extracted if the cladding layers and substrate are transparent and the ohmic contacts are transparent or reflective. For a GaN-based LED $\theta_1 \approx 23°$.

2. No escape zone: $\theta_1 \leq \theta < \theta_2 = \sin^{-1} \dfrac{n_{sub} \cos[\sin^{-1}(n_{air}/n_{sub})]}{n_s}$
   where n_{sub} is the refractive index of the substrate. These photons are totally internally reflected at both the surface and the edge of the LED. For GaN LEDs grown on sapphire substrates $\theta_2 \approx 35°$.

3. Substrate edge emission zone: $\theta_2 \leq \theta < \theta_3 = \sin^{-1}(n_{sub}/n_s)$
   Photon emitted within this angular region can be out coupled from the side walls of the substrate. For GaN LEDs grown on sapphire substrates $\theta_3 \approx 44°$. The light needs to undergo a number of reflections to reach the edge of the structure before being extracted.

4. Waveguide zone: $\theta_3 \leq \theta < 90°$. These photon are waveguided in the cladding layers and may be collected at the edge of the LED structure after multiple reflections.

The light which is guided within the LED structure may be re-absorbed by defects, contacts, the active region or other absorbing layers (Fig. 5.2). *Photon recycling* i.e., the re-emission of photons absorbed in the active region may occur which results in the randomization of the angular distribution of the photons. However, the probability of re-emission is

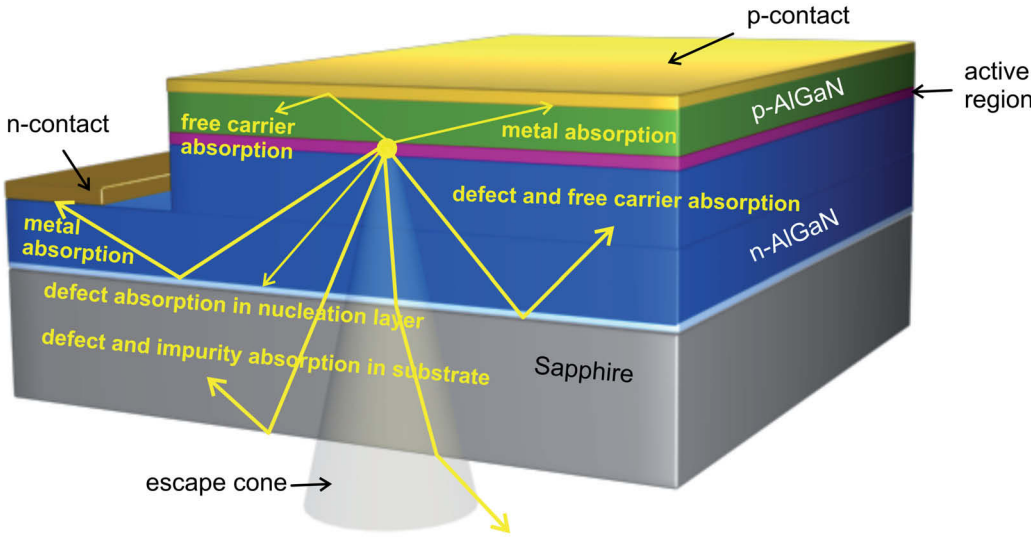

Figure 5.2: Schematic of the sources of losses in an LED

dependent on the IQE of the device and hence is not a viable method to improve the outcoupling of light. Therefore, to increase the efficiency of the LEDs, it is necessary to suitably modify the geometry of the LED to outcouple the light which is guided within the structure.

5.2 Effects of the polarization of the light emitted from UV LEDs

The wurtzite (WZ) phase of III-nitrides is mainly used in the fabrication of LEDs and optical devices. Hence in this section the band structure of the WZ phase of AlInGaN emitters will be discussed. The electrical and optical properties of WZ group III-nitrides are mainly determined by the band structure near the Brillouin zone centre (wave vector $k \approx 0$). At the Γ point, GaN and AlN have one conduction band (CB), Γ_7, with states having atomic s orbital like character. The valence subband (VB) states have atomic p_x, p_y and p_z character where the z-direction is defined parallel to the c-axis of the crystal. Transitions between the s and p_x, p_y and p_z like states involve x, y and z polarized light respectively. Due to the reduced symmetry of the wurtzite crystal structure, III-nitride materials are anisotropic along and perpendicular to the direction of the c-axis. This anisotropy results in a crystal-field splitting (Δ_{CF}) of the VBs. The top of the VB is split into twofold and single degenerate states [80]. The twofold degenerate state has atomic p_x and p_y like character (wave form $|X \pm iY\rangle$ like) while the single degenerate state has a predominant atomic p_z like character (wave form $|Z\rangle$ like). The order of the two energy levels depends on the kind of materials, the c/a ratio of the lattice constants and the relative displacement of the N sublattice with respect to the Al or Ga sublattice along the c-direction. If spin-orbit interaction Δ_{SO} is introduced, the degeneracy of the twofold degenerate state is lifted resulting in Γ_9 and Γ_7 states which are known as the

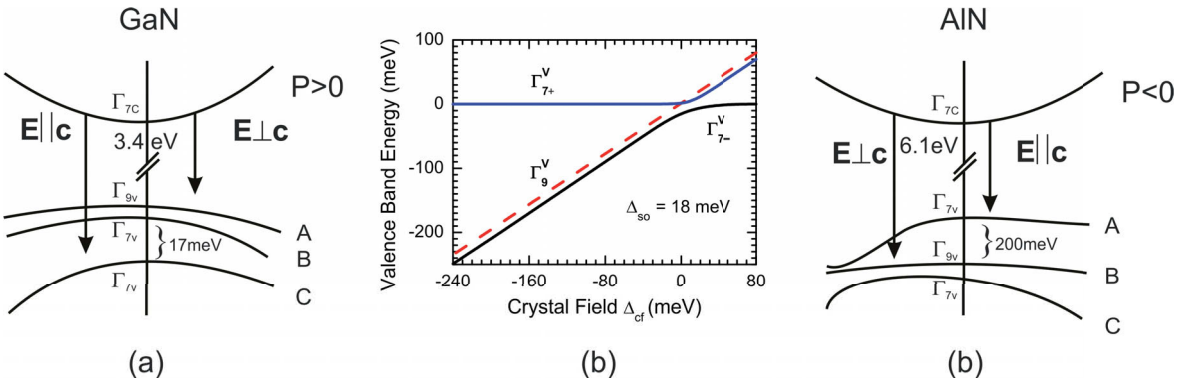

Figure 5.3: (a) Schematic of the band structure of WZ GaN at the Γ point [82, 84, 87]. (b) Relative valence band energies at the Γ point as a function of the crystal field for a spin-orbit energy of 18 meV [88]. (c) Schematic of the band structure of WZ AlN at the Γ point [85, 87].

heavy hole (HH) and light hole (LH) bands respectively. The single degenerate state (Γ_7) is called the crystal-field split off hole band (CH).

Based on the quasi-cubic model [81], at the Γ point the energetic position of the Γ_9 band with respect to the two (Γ_7) bands is given by

$$\Gamma_9 - \Gamma_{7\pm} = \frac{\Delta_{CF} + \Delta_{SO}}{2} \pm \frac{1}{2}\sqrt{(\Delta_{CF} + \Delta_{SO})^2 - \frac{8}{3}\Delta_{CF}\Delta_{SO}} \tag{5.3}$$

The spin-orbit splitting energies are positive for both GaN (17 meV) [82–84] and AlN (20 meV) [85]. However, the more ionic nature of AlN results in a crystal-field splitting Δ_{CF} which is negative (-206 meV) instead of positive as in the case of GaN (10 meV) [82–85]. Due to the difference in the crystal-field splitting, the order of the valence subbands at the Γ point in AlN is different from that in GaN (Fig. 5.3). In GaN, the HH (Γ_9) band is the topmost valence subband closely followed in energy by the LH (Γ_7) band and CH (Γ_7) band [86]. On the other hand, in AlN, the topmost valence subband is the CH band (Γ_7) followed by the HH band (Γ_9) and the LH band (Γ_7). The valence subbands are named A, B and C according to the order of their energetic positions from highest to the lowest.

Chen et al. [86] and Li et al. [89] calculated the square of the transition matrix element (I_V) for the band-to-band transition involving the three valence subbands, in GaN and AlN respectively, using the quasicubic model (Table 5.1). The square of the transition matrix element determines the polarization selection rules and is given by

$$I_V = \left|\left\langle \Psi_V \left| H_{dipole} \right| \Psi_C \right\rangle\right|^2 \tag{5.4}$$

where Ψ_V and Ψ_C are the hole and electron wave functions.

The dipole transition matrix calculations show that the recombination between the conduction band and the holes in the topmost valence subband Γ_7 in the case of AlN is almost prohibited for $E \perp c$ [89] i.e., the emitted light is TM polarized. On the contrary, for GaN, with the topmost valence subband Γ_9, the recombination is almost forbidden for $E||c$ [86] i.e., the emitted light is strongly TE polarized.

Table 5.1: Calculated values for the square of the transition matrix element (I_V) of WZ GaN [86] and WZ AlN [89] for light polarized parallel and perpendicular to the c-axis. For WZ GaN the values relative to E_A are listed.

GaN			AlN		
Transition	$E\|\|c$	$E\perp c$	Transition	$E\|\|c$	$E\perp c$
$E_A(\Gamma_{7C}\leftrightarrow\Gamma_{9V})$	0	1	$E_A(\Gamma_{7C}\leftrightarrow\Gamma_{7V})$	0.4580	0.0004
$E_B(\Gamma_{7C}\leftrightarrow\Gamma_{7V})$	0.053	0.974	$E_B(\Gamma_{7C}\leftrightarrow\Gamma_{9V})$	0	0.2315
$E_C(\Gamma_{7C}\leftrightarrow\Gamma_{7V})$	1.947	0.026	$E_c(\Gamma_{7C}\leftrightarrow\Gamma_{7V})$	0.0007	0.2310

In AlGaN alloys, as the concentration of Al increases Δ_{CF} changes from positive to negative. Neuschl et al. [90] proposed a crystal field bowing between 0 and -0.18 eV for AlGaN alloys while Coughlan et al. [91] proposed a crystal field bowing of -23 meV. As Δ_{CF} decreases the energy separation between the three valence subbands is reduced until the Γ_7 band becomes the uppermost band when Δ_{CF} becomes negative. Goldhahn et al. [88] calculated the relative positions of the three valence bands as a function of Δ_{CF} for $\Delta_{SO} = 18\,meV$ (Fig. 5.3b). Assuming a linear dependence of Δ_{CF} on the Al concentration in the alloy, a band crossing at 5 % Al concentration was predicted for strain-free AlGaN layers. Due to the dependence of the valence subband order on the Al concentration, the degree of polarization of light emitted from AlGaN layers is related to the composition of the alloy. The degree of polarization of the emitted light P (also denoted ρ) is defined as

$$P = \frac{I_{TE} - I_{TM}}{I_{TE} + I_{TM}} \tag{5.5}$$

where I_{TE} and I_{TM} are the integrated intensities of the in-plane emitted TE and TM polarized light respectively. At a critical Al concentration, the optical polarization of the emitted light from AlGaN layers will switch from predominantly TE polarization ($E\perp c$) to predominant TM ($E||c$) polarization. Light emitted from UV LEDs, grown along the c-axis, which is polarized with the electric field vector lying in the quantum well plane ($E\perp c$) can be efficiently extracted from an LED while the polarized light emitted with the electric field vector perpendicular to the plane of the quantum well ($E||c$) propagates within the LED and may be extracted from the die side walls or reabsorbed in the LED structure. The value of the critical Al concentration is therefore important for the extraction of the spontaneously emitted light in UV LEDs and hence has been widely investigated.

5.2.1 Factors influencing the light-polarization switching in AlGaN layers

In literature a large variation in the Al concentration, at which switching of polarization characteristics of light emitted from $Al_xGa_{1-x}N$ layers occurs, has been reported. Nam et al. [87] measured the change in the degree of polarization of the light emitted from 1 μm thick undoped $Al_xGa_{1-x}N$ layers grown on sapphire templates. The emitted light was found

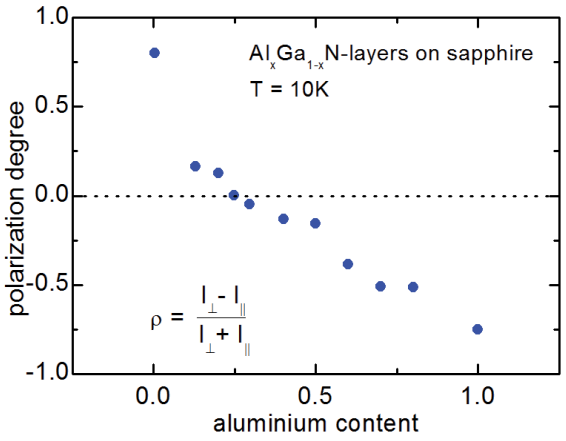

Figure 5.4: Dependence of the degree of polarization of the emitted light on the Al concentration (x) for 1 μm thick undoped $Al_xGa_{1-x}N$ layers grown on sapphire templates measured [87] by photoluminescence spectroscopy.

to switch from mainly TE polarized, for low values of x ($x < 0.25$), to dominantly TM polarized for higher values of x (Fig. 5.4). At $x = 0.25$ the degree of polarization was found to be zero as the three valence subbands become degenerate at the Γ point. Kolbe et al. [92] showed that for UV LEDs, the in-plane electroluminescence is polarized with the intensity of TE polarized light to TM polarized light reducing with decreasing wavelength. The cross over from mainly TE polarized light to dominantly TM polarized light was found to be at a wavelength of 300 nm (Fig. 5.5). Basal et al. [93] reported polarization switching at an Al composition $x \approx 0.83$ for $Al_xGa_{1-x}N$/ AlN MQWs grown on sapphire (0001) substrates. For AlGaN MQW lasers built on free-standing AlN templates grown on SiC substrates, Kawanishi et al. [94] estimated a change in the lasing polarization from the TM mode to the TE mode at an Al concentration $x \approx 0.36 - 0.41$ based on experimental results. Netzel et al. [95] reported an optical polarization switching at an Al concentration of 8 % for AlGaN layers grown pseudo-morphically on top of 4.4 μm GaN buffer layers on c-plane sapphire substrates.

To understand the discrepancies in the reported values of the critical Al concentration i.e., the wavelength at which the polarization switching of the emitted light takes place, the influence of many factors such as the strain in the quantum well, quantum well thickness and the internal electric fields have been investigated.

Strain state of the AlGaN layers

The strain state of the quantum well strongly influences the critical Al concentration, i.e. the wavelength, at which the polarization switching of the emitted light takes place [93, 96, 97]. The strain in the $Al_xGa_{1-x}N$ quantum well layers grown epitaxially on substrates such as SiC, sapphire, GaN and AlN is dependent on the substrate or the underlying $Al_yGa_{1-y}N$ template ($x < y$).

In strained layers due to the deformation of the crystal, the crystal field splitting differs from that in an unstrained bulk crystal. Chuang et al. [98] derived analytical expressions for the ordering of the valence subbands in strained wurtzite semiconductors using the $k \cdot p$

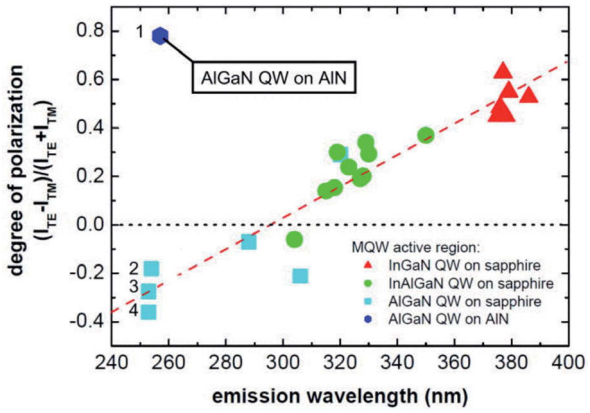

Figure 5.5: Degree of polarization of emission from LEDs fabricated on sapphire or AlN substrates. Device 1, in the upper left hand corner, was grown on AlN and emits highly polarized TE light at 253 nm. The quantum wells in devices 2, 3, and 4 are identical in design to device 1 but are grown on sapphire. The long dashed line illustrates the trend for LEDs grown on sapphire [96].

approach with the cubic approximation. In the case of strained $Al_xGa_{1-x}N$ layers, with isotropic in-plane strain, the energetic position of the Γ_9 band with respect to the Γ_7 band is given by

$$\Gamma_9 - \Gamma_7 = -\frac{\Delta' + \Delta_{SO}}{2} + \sqrt{\left(\frac{\Delta' + \Delta_{SO}}{2}\right)^2 - \frac{2}{3}\Delta'\Delta_{SO}}$$
$$\Delta' = \Delta_{CF} + [D_3 - D_4\,(C_{33}/C_{13})]\,\varepsilon_{zz}$$

where Δ_{SO} is the split-off energy, Δ_{CF} is the crystal field splitting energy, D_i are the deformation potentials, C_i are the elastic stiffness constants, and ε_{zz} is the strain tensor element along the c-direction [93, 98].

The polarization switching of the light, emitted from $Al_xGa_{1-x}N$ layers, occurs at the Al concentration at which $\Delta' = 0$. Hence, the Al concentration at which polarization switching occurs can be shifted to higher or lower values depending on the strain in the layer. Theoretical calculations reveal that for AlGaN layers grown along the c-direction, compressive in-plane strain pushes the $|X \pm iY\rangle$ like bands (Γ_9 and Γ_7) upward and tensile strain along the c direction pushes the $|Z\rangle$ like band (Γ_7) downward [93, 96, 99]. Therefore, compressive in-plane strain moves the Al concentration at which polarization switching occurs to higher values while tensile in-plane strain moves the Al concentration to lower values. Sharma et al. [97] calculated the relative oscillator strength of the lowest excitonic transition under strain for light polarized along the z direction in $Al_xGa_{1-x}N$ layers grown on $Al_yGa_{1-y}N$ templates ($x < y$) (Fig. 5.6). The critical Al concentration at which polarization switching occurs was found to increase linearly with the Al content in the $Al_yGa_{1-y}N$ template or substrate. Northrup et al. [96] have shown that the critical Al concentration can be controlled by changing the strain in the quantum well. Using this method 253 nm LEDs with strongly TE emission have been demonstrated (Fig. 5.5). Tim Kolbe et al. [100] demonstrated a dependence of the in-plane light polarization of 380 nm LEDs on the in-plane strain of the active region. The TM polarized part of the in-plane emitted light was found to become more dominant as compared to the TE polarized part for MQWs with decreasing tensile in-plane strain of the MQW barriers.

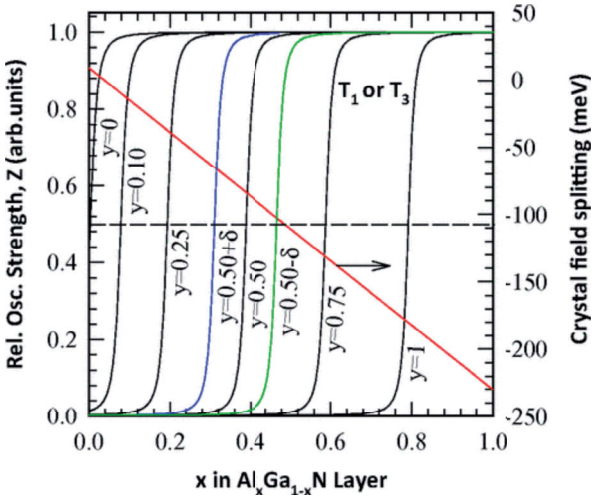

Figure 5.6: Relative oscillator strength of the lowest excitonic transition, $\Gamma_7 \rightarrow \Gamma_9$ (T_1) or $\Gamma_7 \rightarrow \Gamma_7$ (T_3), under strain for light polarized along the z-direction plotted as functions of Al compositions of $Al_xGa_{1-x}N$ layers grown on $Al_yGa_{1-y}N$ templates. The dashed line defines the critical Al composition at which polarization switching occurs. The residual strain in $Al_{0.50}Ga_{0.50}N$ templates is considered to be $\delta = 0.4\,\%$. The interpolated values of the crystal field splitting of the $Al_xGa_{1-x}N$ layers are also shown in the same graph (right axis) [97].

Quantum confinement

Quantum confinement in $Al_xGa_{1-x}N/\,Al_yGa_{1-y}N$ MQWs affects the ordering of the valence subbands in the quantum well and hence the optical polarization of the emitted light [93, 96, 97, 101]. The QW thickness, the barrier composition and the internal electric fields (due to spontaneous and piezoelectric polarization) influence the quantum confinement of the carriers in the QW. Banal et al. [93] proposed a simple qualitative model to describe the effect of quantum confinement on the ordering of the valence subbands in $Al_xGa_{1-x}N/\,AlN$ single quantum wells. Since the hole effective mass in the top most $|Z\rangle$ like band (Γ_7) is much lighter than that in the $|X \pm iY\rangle$ like bands (Γ_9 and Γ_7), the quantum confinement lowers the energy of the $|Z\rangle$ like band (Γ_7) in the $Al_xGa_{1-x}N$ layer. Under sufficiently strong quantum confinement, cross over of the Γ_7 and the Γ_9 bands will occur causing a switch in the optical polarization. For thin quantum wells (< 3 nm), the well width dominates the quantum confinement effect and the critical Al concentration at which polarization switching of the emitted light takes place is shifted to higher values as the well width decreases (Fig. 5.7). For thick quantum wells (> 3 nm), the critical Al concentration is dependent on the internal electric field and independent of the well width. Sharma et al. [97] reported that the switching of the valence subbands due to quantum confinement only occurs when the three valence subbands are in close proximity. Al tahtamouni et al. [102] investigated the optical polarization of $Al_{0.65}Ga_{0.35}N/\,AlN$ single quantum wells using photoluminescence spectroscopy. At a well width of 2 nm the dominant polarization component of the band-edge emission switched from $E||c$ to $E\perp c$. Wierer et al. [103] reported a decrease in the degree of polarization with increasing quantum well thickness for UV LEDs with $Al_xGa_{1-x}N/\,Al_yGa_{1-y}N$ MQWs.

Northrup et al. [96] investigated the influence of the barrier composition on critical Al concentration for $Al_xGa_{1-x}N/\,Al_yGa_{1-y}N$ MQWs. Due to the lighter effective mass in the CH band, as compared to the HH band, the hole wavefunction is less localized than that for the HH state. The energy of the CH band is thus more sensitive to the barrier potential as compared to the HH band. For a fixed quantum well thickness of 3 nm, the critical wave-

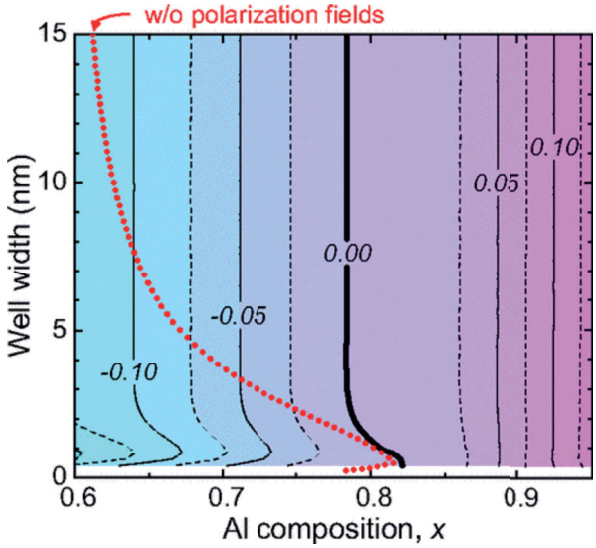

Figure 5.7: Contour plot of the calculated energy difference of $E(\Gamma_7)-E(\Gamma_9)$ in the unit of electron volts for $Al_xGa_{1-x}N$/ AlN single quantum wells grown on unstrained AlN. Red/ gray dotted thick line is the $E(\Gamma_7)-E(\Gamma_9)$=0 line for flat-band QWs without a polarization field, while (black) thick and thin lines are for QWs with polarization fields. The assumed spontaneous polarization was $-0.040\,C/m^2$ [93].

length, at which polarization switching of the emitted light takes place, could be shifted by 15 nm by increasing the Al concentration in the barrier from $y = 0.7$ to $y = 1.0$.

The critical Al concentration, at which polarization switching of the emitted light takes place, decreases gradually with increasing carrier density [103–105]. This can be explained by the fact that at high carrier densities, carriers will occupy higher states above $k = 0$ in the conduction and valence subbands which allows more transitions to the second and third highest valence subbands. The light emission characteristics will thus be affected by transition matrix elements far from $k = 0$. The matrix elements for TM-polarization above the band-edge are much larger than those for TE-polarization. Hence the light emission for TM-polarization becomes larger than that for TE-polarization at higher carrier densities.

5.2.2 Optical polarization dependence on substrate orientation

The optical polarization properties of the spontaneous light emitted from AlGaN quantum wells grown on semipolar and nonpolar substrates have been investigated to improve the performance of UV LEDs [101, 106–108]. Using a 6×6 k·p Hamiltonian under the quasi cubic approximation, Yamaguchi [106] calculated the transition matrix elements for light polarized in the substrate plane and perpendicular to the substrate plane in the case of 1.5 nm thick $Al_xGa_{1-x}N$/ AlN quantum wells grown on AlN substrates with orientation θ w.r.t. the c-plane (Fig. 5.8). In the c-plane case due to the 6-fold symmetry there is only a minor interaction between the three valence subbands through the spin-orbit interaction. Hence an abrupt change from TE to TM polarization is observed at an Al concentration of 76 % (Fig. 5.8 a). Additionally, the in plane optical properties are isotropic. For substrates with orientation $\theta > 0$, the symmetry in the quantum wells is broken resulting in a mixing of the three valence subbands. Accordingly, a gradual polarization switching occurs as the Al concentration increases. Furthermore a large in-plane optical anisotropy appears due to the break down of the 6-fold symmetry and the presence of anisotropic in-plane strain.

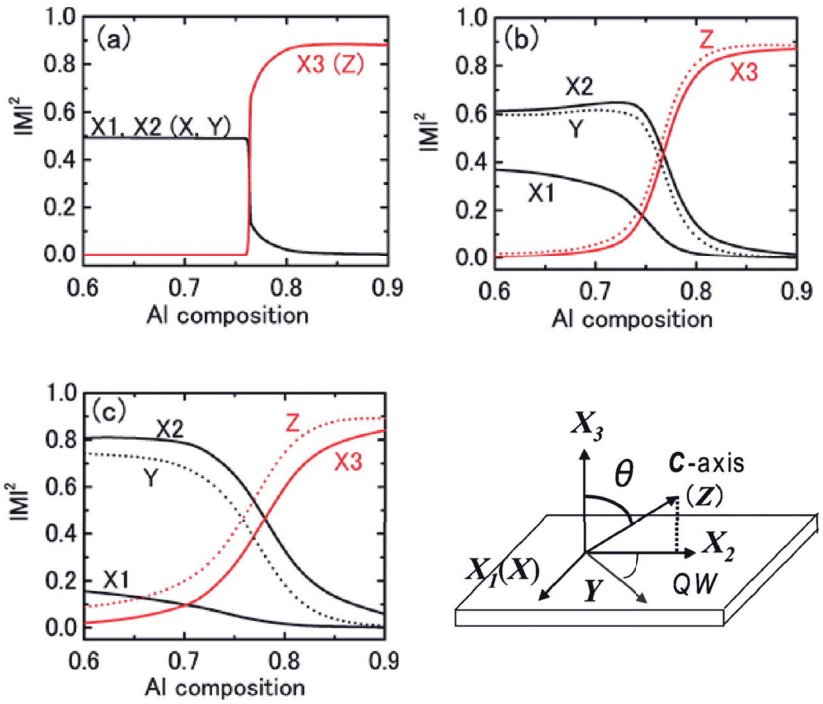

Figure 5.8: SQW-layer Al composition dependence of optical matrix elements for X1, X2, and X3 polarizations (solid lines) and Y and Z polarizations (broken line) in 1.5 nm AlGaN quantum wells on (a) exact, (b) 5°-misoriented, and (c) 10°-misoriented c-plane AlN substrates [106].

In the case of $Al_xGa_{1-x}N$ thin films grown on m-plane AlN substrates ($\theta = 90°$), the valence band ordering is affected by the in-plane strain which is compressive and anisotropic [107]. Transition matrix calculations show that the emitted light is mainly polarized in the z-direction ($E||c$) which lies in the plane of the substrate and hence can be easily extracted from the top/ bottom surface [107, 108]. LEDs grown on m-plane AlN can thus be used for the fabrication of efficient surface emitting LEDs. Banal et al. [109] showed experimentally that the band-edge photoluminescence from m-plane AlGaN quantum wells grown on partially relaxed AlGaN templates has a strong polarization in the direction $E||c$ (Fig. 5.9). Theoretical investigations reveal that although semipolar AlGaN quantum wells show stronger in-plane polarization of the emitted light as compared to c-plane AlGaN quantum wells, they show weaker in-plane polarization as compared to the non-polar case [106, 108]. Wang et al. [108] reported that $(11\bar{2}2)$-plane AlGaN quantum wells grown on AlN substrates show a weaker in-plane polarization of the emitted light as compared to $(20\bar{2}1)$-plane AlGaN quantum wells.

For the InGaN material system, Schade et al. [110, 111] conducted both experimental studies and analytical calculations on polarization properties of InGaN layers and LEDs on polar, semipolar and nonpolar crystal orientations. It was confirmed that both the inclination angle between the c-plane and the plane of growth as well as the indium composition and thus the anisotropic strain state influence the transition point between dominant optical polariza-

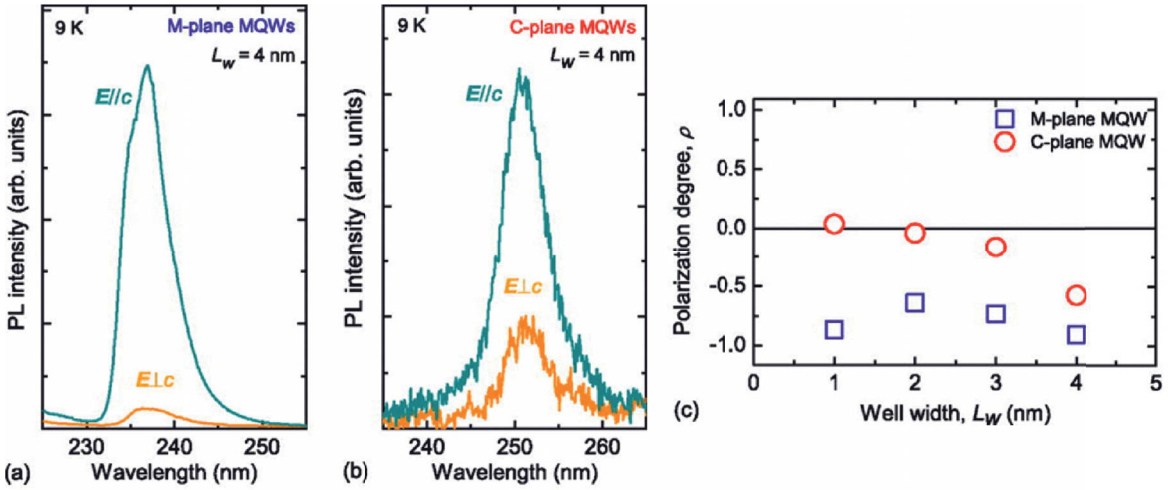

Figure 5.9: Polarization PL spectra, measured at 9 K, from (a) m- and (b) c-plane AlGaN MQWs with quantum well width (L_w) = 4 nm. (c) Polarization degree (ρ) of the PL from the m- and c-plane AlGaN MQWs as a function of L_w. The wavelength of the LEDs varied from 225 nm to 250 nm [109].

tion states. While the main difference of the InGaN system in comparison to AlGaN is the negative crystal-field splitting Δ_{CF}, the model itself is valid for the entire AlInGaN system.

5.2.3 Influence of the optical polarization on the light extraction efficiency

The polarization of the emitted light is an important issue for the extraction of light from UV LEDs grown along the c-axis as the angular distribution of the light emitted from the active region of the LED is dependent on the degree of polarization. A model based on the basis states of the bulk Hamiltonian [98] can be used to determine the angular distribution of the light emitted from the active region of III-nitride LEDs [111, 112]. In this model all emitters are considered to be dipoles where the electric field vector **E** of the emitted wave lies in the plane defined by the orientation of the dipole and the photon vector **k**. For electromagnetic waves $\mathbf{E} \perp \mathbf{k}$ is required.

In III-nitride LEDs, the conduction band has states with atomic *s* orbital like character while the three valence subbands have states with atomic p_x, p_y and p_z character where the z-direction is defined parallel to the c-axis of the crystal. The p_x and p_y orbitals combine to form the HH and LH valence subbands (wave form $|X \pm iY\rangle$ like) which have a rotational symmetric distribution around the c-axis (Fig. 5.10). Hence transitions into these subbands will result in the emission of TE polarized light. The CH valence subband has a predominant atomic p_z like character (wave form $|Z\rangle$ like) which is aligned along the c-axis. Therefore transitions into the CH valence subband will result in the emission of TM polarized light.

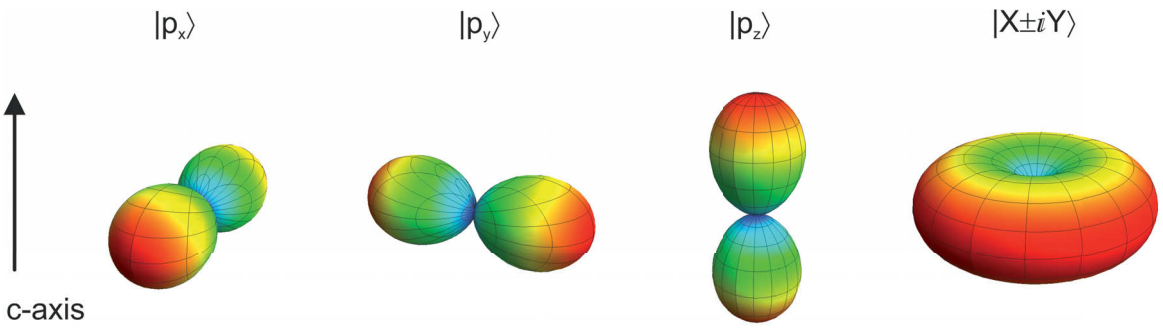

Figure 5.10: Dipole orientation of the $|p_x\rangle$, $|p_y\rangle$, $|p_z\rangle$, and the $|X \pm iY\rangle$ orbitals [112]

In spherical coordinates the angular dependence of the wavefunctions of the p-orbitals are given by

$$\begin{aligned} |p_x\rangle &= sin\theta cos\phi \\ |p_y\rangle &= sin\theta sin\phi \\ |p_z\rangle &= cos\theta \end{aligned} \tag{5.6}$$

and the intensity distribution for the radiation emitted by each dipole is given by

$$\begin{aligned} I_x &= I_{x0}\left(sin^2\theta sin^2\phi + cos^2\theta\right) \\ I_y &= I_{y0}\left(sin^2\theta cos^2\phi + cos^2\theta\right) \\ I_z &= I_{z0} sin^2\theta \end{aligned} \tag{5.7}$$

where I_{x0}, I_{y0} and I_{z0} are the ratios of the contributions from each valence subband. I_{x0}, I_{y0} and I_{z0} are dependent on the energy separation between the subbands and the thermal occupancy of the holes which is described by the Fermi-Dirac distribution. In the case of LEDs grown along the c-axis, $I_{x0} = I_{y0}$. Using Eqns. 5.5 and 5.7, the angular distribution of the emission from the active region of an LED can be determined from the measured polarization degree (P). If the polarization degree is measured along the y-axis then

$$I_{x0} = \frac{I_{z0}(1+P)}{(1-P)} \tag{5.8}$$

In Fig. 5.11 the angular distribution of the emission from the active region of an LED is depicted for different polarization degrees. In the case of mainly TE polarized light, most of the light is emitted at small angles with respect to the c-axis i.e., more light is emitted within the top surface and bottom substrate light escape cones. This results in a high LEE of the device. As the degree of polarization decreases, the light emitted at higher angles increases and at zero polarization degree the light emission is isotropic. Further decrease in the degree of polarization results in the emission being mainly TM polarized with most of the light emitted at large angles w.r.t. the c-axis. As described in Sec. 5.1 light emitted at

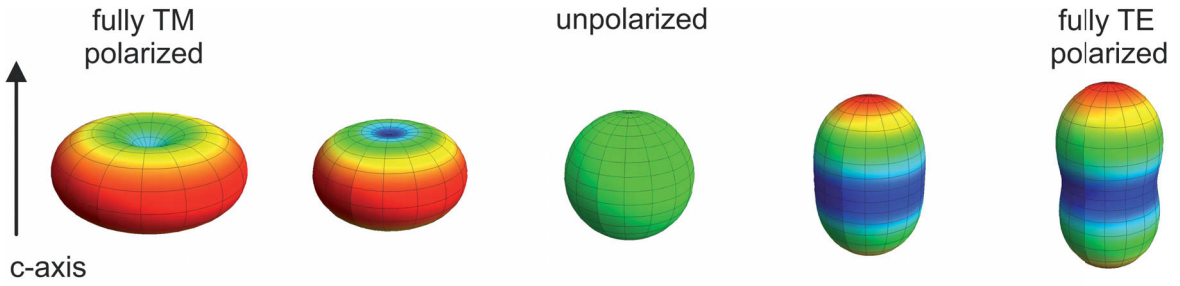

Figure 5.11: Calculated emission distribution inside the semiconductor of polarized light with different polarization states from fully TM- to fully TE polarized [112].

these large angles is trapped and finally absorbed in the LED structure resulting in devices with low LEEs.

To study the influence of the polarization degree of the emitted light on the LEE, the light extracted from a 320 nm InAlGaN LED was simulated using a non-sequential ray tracing software package *ZEMAX-EE* [40]. A 400 μm x 400 μm chip was considered for the simulations with a 100 μm x 100 μm square p-ohmic metal contact (Fig. 5.12). All surfaces and interfaces were considered to be smooth and hence no light scattering was assumed in the simulations. The optical parameters used for the simulations were obtained from literature and are given in Table 5.2. The degree of polarization of the light emitted from the active region was varied from P = 1 i.e., completely TE polarized emission, to P = -1 i.e., completely TM polarized emission. The distributions shown in Fig. 5.11 where used to describe the angular distribution of the emission from the active region.

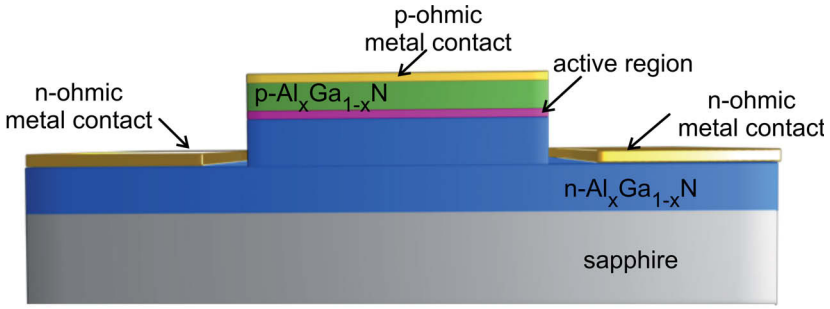

Figure 5.12: Schematic of the LED structure used for the simulation of light extraction.

For TE polarized emission, 12 % of the emitted light is outcoupled from the LED (Fig. 5.13 a). The LEE was found to decrease as the light emission from the active region becomes more TM polarized. For completely TM polarized emission, only 3 % of the emitted light can be outcoupled. The rest of the light is lost due to absorption in the LED. The degree of polarization of the light emitted from the active region of the LED also impacts the far field radiation pattern of the device (Fig. 5.13 b). For P = 1, the light is mainly directed perpendicular to the surface. As the polarization degree decreases the emergence of *rabbit ears* is seen due to outcoupling of light from the sidewalls of the sapphire substrate. For P = -1,

Table 5.2: 320 nm LED material parameters used for simulations. Values of refractive index of AlInGaN layers determined by a model from [113] based on experimental values from [114–120]. R, T and A are the reflection, transmission and absorption coefficients respectively.

Layer	Thickness	Refractive index	
p-$Al_{0.06}Ga_{0.94}N$	200 nm	2.637	A = 1
p-$Al_{0.25}Ga_{0.75}N$	200 nm		T = 1
n-$Al_{0.35}Ga_{0.65}N$	3.5μm	2.554	T = 1
sapphire	430μm	1.806 [121]	
p-ohmic metal contact	500 nm		R = 0.4
n-ohmic metal contact	500 nm		R = 0.65

almost no light is emitted perpendicular to the surface. The light can only be extracted from the sidewalls of the chip which results in a low LEE. In applications where the LED needs to be coupled to external optical components, this dependence of the far field radiation pattern of UV LEDs on the polarization degree is an important issue.

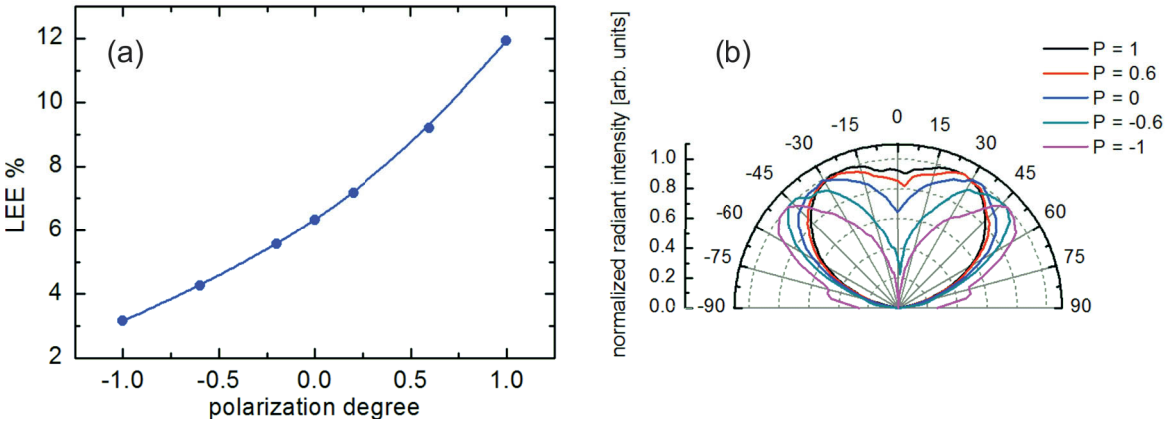

Figure 5.13: Simulated dependence of the (a) light extraction efficiency of a 320 nm UV LED chip and (b) farfield radiation pattern of a 320 nm UV LED chip on the degree of polarization (P) of the light emitted from the active region.

The simulation results clearly show that the extraction of light will be a severe problem for LEDs with mainly TM polarized light emitted from the active region. This indicates that for LEDs emitting in the UV-B and UV-C region, with large concentrations of Al in the QWs, the LEE will be very low. Hence to achieve highly efficient UV LEDs it is necessary to either shift the wavelength at which switching of the polarization occurs to shorter wavelengths or to develop novel methods to extract the light emitted at large angles w.r.t. the c axis.

5.3 Methods to increase the extraction of light

Various techniques have been implemented to increase the light extraction from nitride-based LEDs. An overview of a few of the popular methods to increase the LEE of the devices will be presented in this section.

5.3.1 Modification of the LED geometry

One of the most intuitive methods to increase the LEE of LEDs is to change the shape of the device from a quadrangular parallelepiped to a geometric structure that enables more light to be extracted from the side walls of the LED. The ideal LED shape would be a sphere with a point-like active region in the centre of the sphere. In this case, all the light would be emitted normal to the surface and hence outcoupled efficiently. The fabrication of a spherical LED is however technically impractical. A more technologically viable method to increase the LEE of the LED is to consider a cylindrical structure where the four in plane escape cones are replaced by an escape ring. A 10 % increase in the output power of blue GaN circular disc LEDs, as compared to cubic LED structures, was demonstrated by Wang et al [122] with the use of laser micro-machining to dice the sapphire substrate.

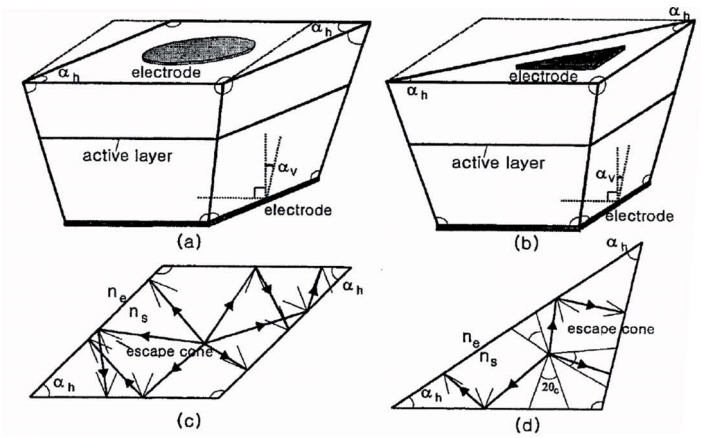

Figure 5.14: Schematic of geometrically deformed (a) rhomboidal and (b) triangular LED chips. Depiction of the photon trajectories in the horizontal planes of (c) rhomboidal and (b) triangular LED chips [123].

Lee et al. [123] proposed the use of geometrically deformed LED chips, in which the horizontal cross section of the LED is either rhomboidal or triangular and the side walls slanted, to increase the LEE of LEDs (Figs. 5.14 a and b). Due to the deformation of the horizontal and vertical planes, the photon trajectory is changed after each reflection off the wall resulting in the photons, regardless of their travelling directions, finding the escape cone after multiple reflections (Figs. 5.14 c and d). Based on this design, truncated inverted pyramid [124, 125], triangular [126] and lozenge-shaped [127] GaN-based LED chips have been fabricated which exhibit higher LEEs as compared to a quadrangular device. Kim et al. [126] demonstrated a 48 % increase in the output power of a 455 nm InGaN LED with the use of an equilateral triangular LED chip as compared to a quadrangular device. A 88.6 % increase in the output power of a InGaN truncated inverted pyramidal LED, with side walls inclined at 50°, was reported by Fu et al. [124]. The InGaN LEDs which were grown on

sapphire substrates were diced and shaped by applying four consecutive oblique laser cuts onto the sides of the LEDs. To determine the optimized polygonal geometry to maximize the side wall light extraction, Wang et al. [128] fabricated 470 nm InGaN LEDs of different geometries ranging from triangular to heptagonal chips (Fig. 5.15 a). With the help of both simulations and experiments they showed that the extraction of light from LEDs with odd number of side walls is higher than that from LEDs with an even number of side walls (Fig. 5.15 b).

The shaping of LED dies, although beneficial to the LEE of the LED, is a tedious and expensive procedure due to the hardness of the sapphire substrate. To reduce costs, shaping of the LED at the wafer level has been investigated [129–131]. A nearly two-fold increase in the output power of blue GaN-based LEDs has been demonstrated with the use of deep etched angled mesa side walls [130, 131]. The angled side walls deflect the laterally guided photons to a direction normal to the surface after total internal reflection which results in increased outcoupling of the light. Micro-LED arrays [129] have also been used to increase the LEE of LEDs due to the increased side wall area as compared to a conventional large area LEDs. Also, due to the shorter photon flight distances to the side walls, reduced optical absorption in the cladding layers is expected.

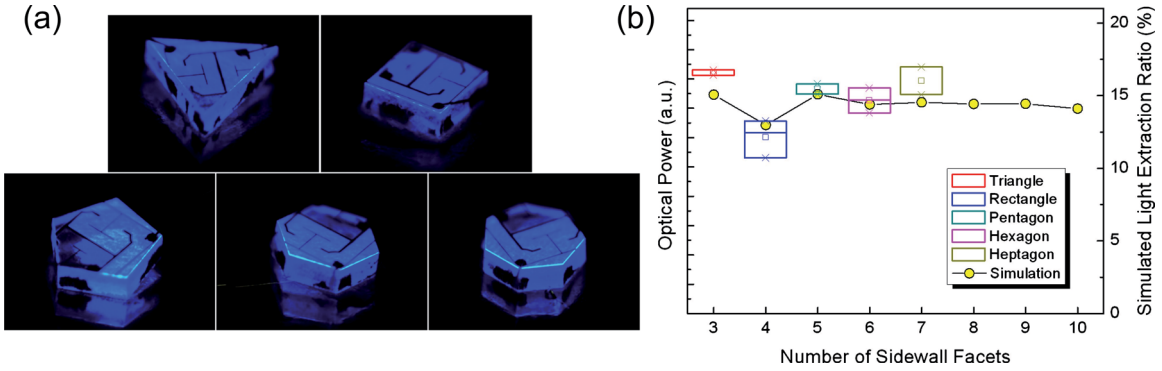

Figure 5.15: (a) Optical microscopy images of polygonal 470 nm LED chips fabricated using laser micro-machining [128]. (b) Measured and simulated light output from the polygonal LEDs at an operating current of 20 mA [128].

The LED geometry can be further modified by texturing the surfaces of the semiconductor and substrate layers. The use of textured surfaces has proved to be the most efficient and cost effective method to increase the LEE of blue nitride-based LEDs. The physics behind the observed increase in the LEE with texturing of surfaces and its impact on UV LEDs will be discussed in detail in Chap. 6.

5.3.2 Modification of the spontaneous emission

Advanced techniques such as photonic crystals, resonant cavity LEDs and surface plasmons have been used to increase not only the LEE of LEDs but also to enhance the IQE and modify the direction of spontaneous emission from the LED.

The spontaneous emission decay constant τ for radiating dipoles is given by Fermi's golden rule as

$$\frac{1}{\tau} = \frac{2\pi}{\hbar} \left| \left\langle f \left| H_{dipole} \right| i \right\rangle \right|^2 \rho(\hbar\omega) \tag{5.9}$$

where $\rho(\hbar\omega)$ is the photon density of states and $\left\langle f \left| H_{dipole} \right| i \right\rangle$ is the dipole transition matrix element. The enhancement of spontaneous emission by altering the photon density of states is called the Purcell effect [132]. Several techniques based on the Purcell effect have been used to increase the LEE of LEDs by increasing or modifying the spontaneous emission of light from the active region of the LED.

Photonic crystals

Photonic crystals (PCs), which are artificial materials with two or three dimensional periodic refractive index distributions on the scale of the wavelength of light [133], have been intensively investigated for the extraction of light from LEDs. The behaviour of photons in a PC is analogous to that of electrons in an atomic crystal. By suitably designing the structure it is possible to obtain a photonic bandgap where no photonic modes exist for certain directions of propagation. If a point defect is introduced in the PC, an emission channel can be created in the photonic bandgap. Due to the point defect, the PC now behaves like a nanocavity and the LED emission, if coupled to the cavity mode, can be greatly enhanced by the Purcell effect. Fujita et al. [134] demonstrated the inhibition and redistribution of spontaneous light emission using 2-D PCs formed in a GaInAsP slab. They showed that with the use of a 2-D PC it is possible to prevent the spontaneous in-plane emission of light while redistributing the saved energy to enable enhanced spontaneous emission in the vertical direction. However, for the PCs to be effective it is necessary for the structures to penetrate the active layer making it difficult to achieve an electrically pumped device. Additionally, the short wavelength and low refractive index of III-nitride semiconductors, make the use of PCs to modify the spontaneous emission of LEDs even more challenging [135].

Another method in which PCs can increase the LEE of LEDs is by Bragg scattering of the guided light out of the device. Using this technique, Order et al. [137] demonstrated a 20 fold increase in the emission light intensity of optically pumped InGaN/GaN MQWs using a triangular lattice 2-D array of PCs. Wierer et al. [135] reported an $\sim 73\,\%$ increase in the LEE for 450 nm III-nitride thin-film LEDs with a 2-D PC layer formed in the n-GaN layer. Shakya et al. [136] demonstrated a factor of 2.5 enhancement in the output power of 333 nm III-nitride UV LEDs with the use of triangular lattice 2-D PCs (Fig. 5.16). They showed that separation of the light generation and extraction area i.e., light is generated in an injection region and guided modes are extracted when reaching the PC region, results in enhanced light extraction.

Resonant cavity LEDs

Resonant cavity LEDs (RCLEDs) or microcavity LEDs [138], in which the active region is placed into an optical cavity, have been used to increase the output power of LEDs. The

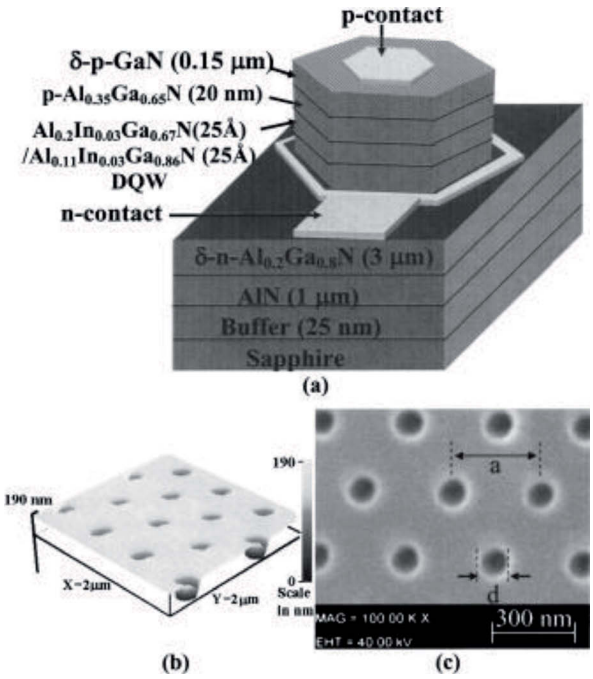

Figure 5.16: (a)Schematic of a 333 nm LED with a 2-D triangular PC etched on the free p-GaN layer surrounding the p-metal contact. (b) AFM image of the PC with lattice constant a = 600 nm, diameter of holes d = 200 nm and depth $\sim$ 190 nm. (c) SEM image of the PC with lattice constant a = 300 nm and diameter of holes d = 100 nm [136]

cavity is defined by a highly reflective mirror placed a few wavelengths away from the active region and a moderately reflective distributed Bragg reflector (DBR) to allow the extraction of light. In such a Fabry-Perot resonator, the density of the optical modes is enhanced for resonance wavelengths. Since the probability of radiative recombination is proportional to the photon density of states, enhanced spontaneous emission will be achieved if the optical cavity mode is in resonance with the LED emission wavelength. Enhanced directionality and spectral purity can also be obtained with the use of RCLEDs. Shen et al. [139] investigated the optical cavity effects in flip-chip InGaN/GaN LEDs where the QWs were placed at a few wavelengths distance from a highly reflective metallic p-ohmic contact. A change in the LEE was observed when the distance between the QWs and the metal reflector was changed. The ratio of the maximum to the minimum of the LEE was determined to be 2.3 indicating that microcavity effects can greatly influence the LEE of the device. Moudakir et al. [140] demonstrated a 390 nm nitride-based RCLED with the vertical cavity formed between a bottom AlGaN/GaN DBR and a top dielectric SiO_2/ZrO_2 mirror. Output powers of 0.6 mW were reported for the devices. As we move towards shorter wavelengths, the fabrication of RCLEDs becomes challenging due to difficulties in the growth of DBRs consisting of III-nitride semiconductor layers with a sufficiently large refractive index contrast and the fabrication of highly reflective p-ohmic contacts.

Surface plasmons

Resonant surface plasmon (SP) coupling can also be used to increase the output power of LEDs [141, 142]. If the active region of the LED is placed within the SP fringing field penetration depth of a thin metallic layer, the QW can be strongly quantum electrodynamically

coupled to the SP mode. In this case when an electron and hole recombine, a SP is created instead of a photon being emitted into free space. At the SP resonant energy, the SP density of states is very high. If the emission wavelength of the LED matches the SP resonant energy, the spontaneous emission will be greatly enhanced due to the Purcell effect. To extract the light from the SP mode it is necessary to scatter the SPs which can be effectively achieved if the metal layer is rough and has imperfections [143]. Okamoto et al. [143] demonstrated a 6.8 fold enhancement in the η_{int} of 470 nm optically pumped LEDs with an Ag coating and a 3 fold enhancement for LEDs with an Al coating. However for the coupling of the QW with the SP it is necessary that the distance between the QW and the metal layer is within the SP fringing field penetration depth which is only 47 nm for Ag and 77 nm for Al on GaN. An exponential increase in the luminescence intensity was found as the distance between the QW and the metal layer decreased. This becomes an issue for the fabrication of electrically pumped III-nitride LEDs where a thickness of at least 100 nm is needed to obtain a high quality p-current spreading layer.

Even if coupling between the QW and the SPs is not possible, they can still be used to enhance the LEE by SP-TM wave coupling. Gao et al. [144] reported a 217 % increase in the peak photoluminescence intensity at 294 nm for AlGaN-based UV LEDs with an 5 nm thick Al layer placed at a distance of 90 nm from the active region. No increase in the IQE was observed indicating that the QWs do not couple to the SPs. They also showed that the enhancement increased as the wavelength decreased which might be attributed to the increased TM emission from the LEDs at shorter wavelengths and stronger coupling as the photon energy approaches the SP resonant energy.

5.3.3 Packaging of LEDs

Optimization of the packaging technology can significantly increase the LEE of LEDs. In this section the advantages of flip-chip mounting and LED encapsulation for UV LEDs will be discussed. In addition the use of polydimethylsiloxane (PDMS) as an encapsulant for UV LEDs will be proposed and its influence on the LEE of UV LEDs will be investigated.

Flip-chip mounting of UV LEDs

Nitride-based LEDs grown on transparent substrates can be packaged as top-emitters (epitaxially up) i.e., the light is mainly collected from the epitaxial surface or bottom-emitters (epitaxially down) i.e., the light is mainly collected from the transparent substrate. In the case of LEDs grown on insulating sapphire substrates, both the p and the n contacts lie on the epitaxial surface of the device. Hence for top-emitters the light must be extracted through the ohmic contacts. The LEE of such devices is greatly reduced due to absorption at the ohmic p-contact, bonding pads and the bonding wires. The issue is even more critical for UV LEDs since at these short wavelengths it is difficult to find contacts which are both electrically conductive and transparent (Chap. 7). Furthermore due to the difficulty in growing highly conductive p-AlGaN layers, most UV-LEDs are capped with a thin absorbing p-GaN layer to obtain an ohmic p-contact with a low contact resistance. To circumvent this

problem a flip-chip bonding scheme is used for LEDs [145] in which the LED die is inverted and mounted on the submount with the epitaxial side down (Fig. 5.17).

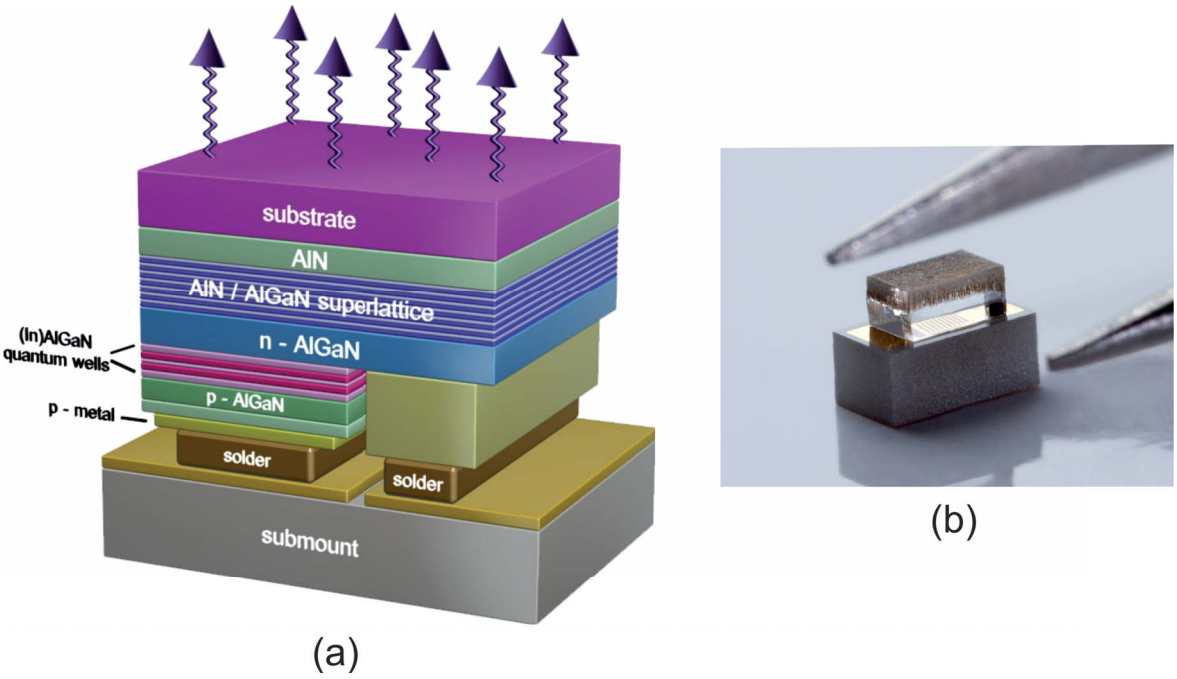

Figure 5.17: (a) Schematic of a UV LED flip-chip mounted on a submount. The light is collected from the transparent substrate [146]. (b) Photograph of a 320 nm LED flip-chip mounted on an AlN submount

Although flip-chip mounting is a challenging technological process, flip-chip LEDs (FCLEDs) have a number of advantages over the traditional top emitter LEDs which include:

- reduced thermal resistance of the device due to efficient transfer of heat through the metal bonding pads. In the case of top-emitter LEDs grown on sapphire substrates, the thermal resistance of the device is high due to the low thermal conductivity and thickness of the sapphire substrate. The low thermal resistance of FCLEDs results in good thermal performance of the devices and subsequently increased lifetimes.
- good current spreading because of the presence of thick p-ohmic contacts as the contacts no longer have to be semi-transparent. Hence FCLEDs can be manufactured with large emission areas.
- compatibility with wafer scale packaging.
- no distortion of the radiation pattern due to the absence of bonding wires.
- enhanced LEE as the light is extracted from the transparent sapphire substrate avoiding absorption at the ohmic p-contact, bonding pads and the bonding wires. Furthermore if the contacts are replaced by highly reflective mirrors, light propagating downwards can be redirected up and extracted through the substrate increasing the LEE.

In Fig. 5.18, the output power of 305 nm AlInGaN LED measured on wafer is compared to the output power of the same LED after dicing and flip-chip mounting on an AlN submount. The FCLED was measured in an integrating sphere under dc conditions. Due to the enhancement of the heat and light extraction, a maximum output power of 3 mW at 200 mA was achieved.

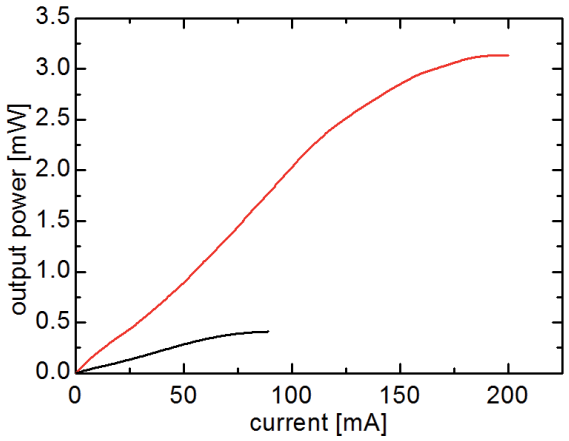

Figure 5.18: Emission characteristics of a LED emitting at 305 nm with micro-LED array contact geometry (l = 33 μm, p = 183.5 μm) measured on wafer (black line) and after flip-chip bonding (red/ gray line) [76].

Encapsulation of UV LEDs

The chip-encapsulating material is another factor of the packaging technology that can greatly influence the LEE of the LEDs. In order to increase the LEE an optically transparent encapsulant should be used, which decreases the index contrast at the semiconductor/ substrate–air interface thus opening the escape cone [45]. Given that the geometry of the encapsulant is chosen such (e.g. hemispherical dome structure) that the light is always incident normal to the encapsulant–air interface, the LEE can be increased by a factor of two or three. For UV LEDs the chosen encapsulant should be optically transparent in the UV region, stable under UV exposure and high temperatures, chemically inert, hermetic, moldable and have a refractive index similar or close to that of the semiconductor material or the substrate. However, the transparency of epoxy resins or silicones, presently used as encapsulants for visible and IR LEDs, decreases drastically at wavelengths shorter than 350 nm. Prolonged exposure to UV light and heat also degrades the encapsulant which results in a further decrease in the transparency [147]. As most commercial silicones are either strongly absorbing or degrade rapidly in the deep UV region, they are not used in the packaging of UV LEDs below 350 nm. Currently, for the packaging of deep UV LEDs, UV transparent quartz windows or lenses are used. However, the fabrication of quartz lenses and their integration with LEDs is tedious and very expensive. Recently Yamada et al presented results on 265 nm and 285 nm UVC LEDs encapsulated with polymerized perfluoro(4-vinyloxy-1-butene) [148]. The stable end (s-type) version of the encapsulant was reported to have a transparency level above 90% down to 200 nm and no visible ageing or degradation of the encapsulant was found after more than 3000 hours of operation.

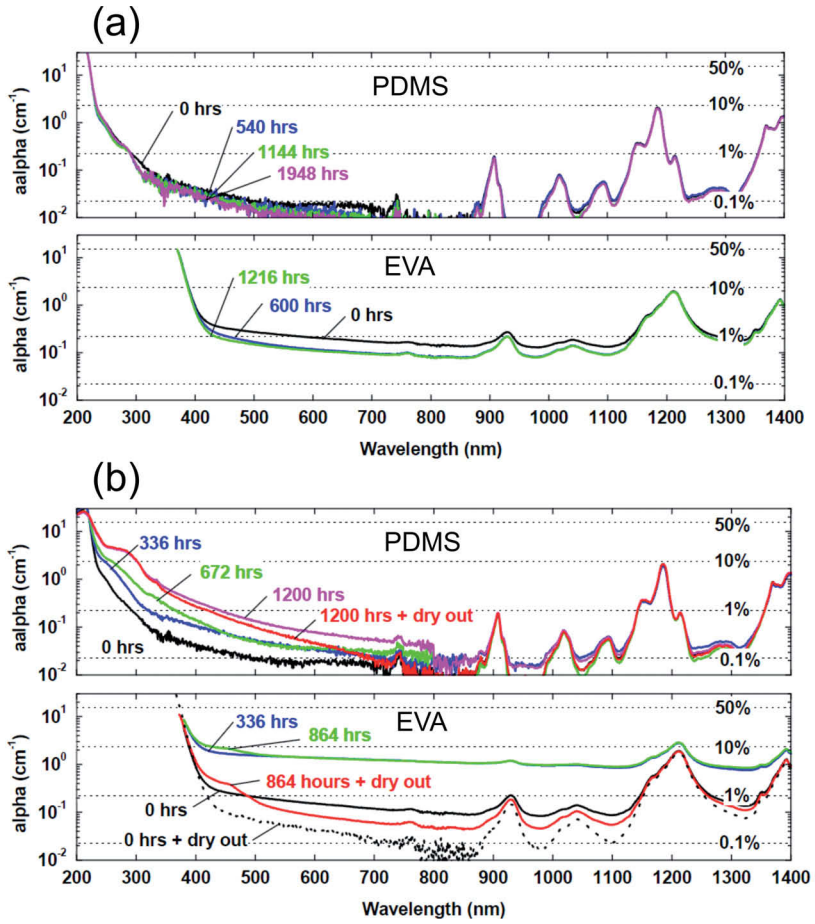

Figure 5.19: Absorption coefficient of PDMS and ethylene vinyl acetate (EVA) as a function of wavelength and time spent (a) under a Xe arc lamp at room temperature in air (b) at 85°C and 85% relative humidity [149].

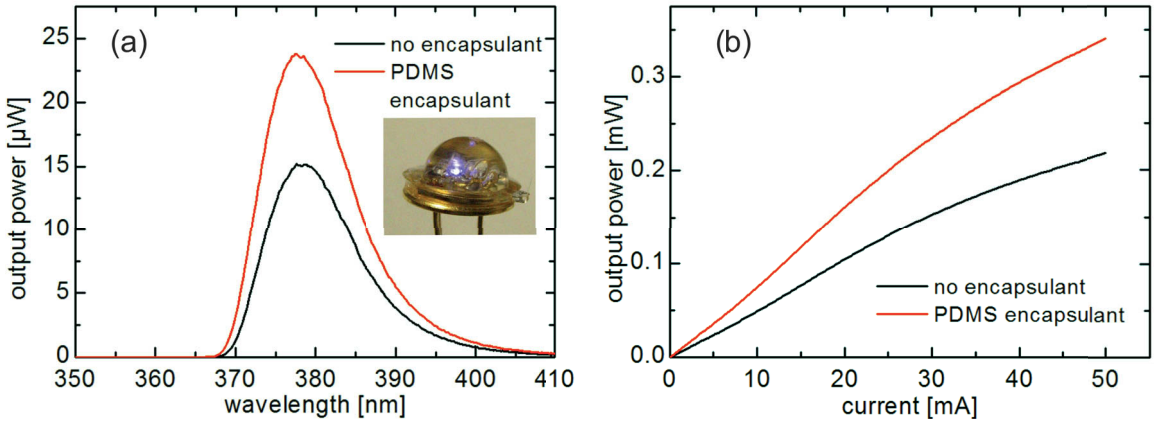

Figure 5.20: (a) Comparison of the spectrum of a 390 nm InAlGaN LED chip without an encapsulant to an LED chip with PDMS as an encapsulant. Inset: Photograph of the encapsulated LED. (b) Integrating sphere measurements of the output power of 390 nm InAlGaN LED chips with and without a PDMS encapsulant.

In this work the use of polydimethylsiloxane (PDMS), with refractive index of 1.54 - 1.55 [150], as an encapsulant for UV LEDs was investigated. PDMS is an elastomeric material and belongs to the group of polymeric organosilicon compounds or silicones. It is extensively used as a master mould for soft lithography due to its ease of use (easily moldable), low cost and high transparency in the UV region [151]. However, it has never before been used as an encapsulant for UV LEDs. McIntosh et al. [149] demonstrated that PDMS is stable under 1948 hours of exposure to a Xenon arc lamp (5.6 kWh/m^2) at room temperature (Fig. 5.19 a). Additionally, they showed after exposure to damp heat (85% relative humidity and 85°C) for 1200 hours, the absorption in a 1.6 mm thick PDMS layer increased from less than 1% to 10% at 300 nm (Fig. 5.19 b). The stability of PDMS to UV exposure and its reasonable stability to heat and high humidity make it ideal for UV LED encapsulation.

To study the influence of PDMS, used as an encapsulant, on the LEE of UV LEDs, the change in the output power of a 380 nm LED after encapsulation with PDMS was measured. The encapsulant was moulded into a hemispherical dome using an aluminium master mould. No change in the emission spectrum of the LED was observed indicating no absorption of light in the PDMS layer or secondary emission of light from the layer (Fig. 5.20 a). A two-fold increase in the output power of the LED was obtained indicating a two-fold increase in the LEE of the LED with the use of a hemispherical PDMS encapsulant (Fig. 5.20 b). Hence PDMS, with its high UV transparency, UV and thermal stability and easy handling, can be used as an effective and low cost option as an UV and visible LED encapsulant and for the fabrication of integrated optical components to increase the LEE of LEDs.

5.4 Summary

The challenges in extracting light from LEDs have been presented and in particular the new challenges arising due to the polarization of the emitted light, in the case of UV LEDs, has been discussed. Simulations were used to investigate the influence of the polarization degree on the LEE and the far field radiation pattern of UV LEDs. A strong decrease in the LEE was observed for LEDs with mainly TM polarized light emission. Furthermore the light is emitted at large angles making it difficult to couple the LEDs to external optical systems. The simulation results clearly show that it is necessary to apply novel techniques to increase the LEE of LEDs to obtain highly efficient devices. Techniques currently used to increase the LEE of visible III-nitride LEDs were presented and their possible application to UV LEDs were discussed. To increase the LEE of UV LEDs, the use of PDMS as an encapsulant for UV LEDs was studied and a 2 fold increase in the LEE of UV-A LEDs was demonstrated. In the next chapters, two more techniques to increase the LEE of UV LEDs i.e., use of textured surfaces and a novel nanopixel contact LED design will be presented.

6 Texturing of the substrate back-surface for the enhancement of light extraction from UV LEDs

Texturing of the semiconductor/ substrate surfaces is a very efficient method to increase the LEE of LEDs. Due to the cost effectiveness of this process, it is one of the most commonly used techniques to enhance the light output power of commercial visible LEDs. In this chapter, the mechanism behind the enhanced outcoupling of the light will be discussed and the concept will be applied to nitride-based UV-A and UV-B LEDs grown on sapphire substrates. With the help of simulations and experiments, the influence of a patterned substrate surface on the LEE of UV LEDs will be investigated and optimized patterns will be presented.

6.1 Texturing of surfaces to increase light extraction

The use of textured semiconductor/ substrate surfaces, which not only increases the one bounce extraction of light but also randomizes the angular distribution of the photons in the LED, results in better outcoupling of the light generated in the LED. A detailed explanation of the mechanism behind the process will be presented in Sec. 6.2. This approach was first proposed in 1973 by Bergh et al. [152] and later demonstrated in 1999 by Schnitzer et al. [153] on GaAs LEDs. The EQE of the thin film GaAs LEDs, with large area dielectric coated Au mirrors, was found to increase from 9 % for a planar surface to 30 % for an LED with a semiconductor surface textured using natural lithography, i.e. the etching of the semiconductor layer using randomly distributed spherical colloidal particles as a mask [153].

In 2003, first reports on the use of surface texturing of GaN to increase the LEE of blue LEDs were published by Huh et al. [155] and Haerle et al. [156]. Using Pt clusters as an etch mask for the wet chemical etching of the top p-GaN layer, Huh et al. demonstrated a 52.4 % increase in the light output power [155]. Haerle et al. achieved EQEs as high as 35 % (LEE of 75 %) for thin film FC blue LEDs with a highly reflective p-mirror metallization and efficient roughening of the n-GaN layer [156]. Fujji et al. [157] demonstrated a twofold to threefold increase in the output power of FC GaN LEDs with a hexagonal cone like n-GaN surface coupled with a Ag-based highly reflective p-contact. Huang et al. [158] used Ni-nanoclusters to nano-roughen the p-GaN surface resulting in a 55 % increase in the output power.

For GaN-based LEDs grown on sapphire substrates, complex surface processing such as ICP etching have been used to fabricate patterned arrays on the surface of the sapphire

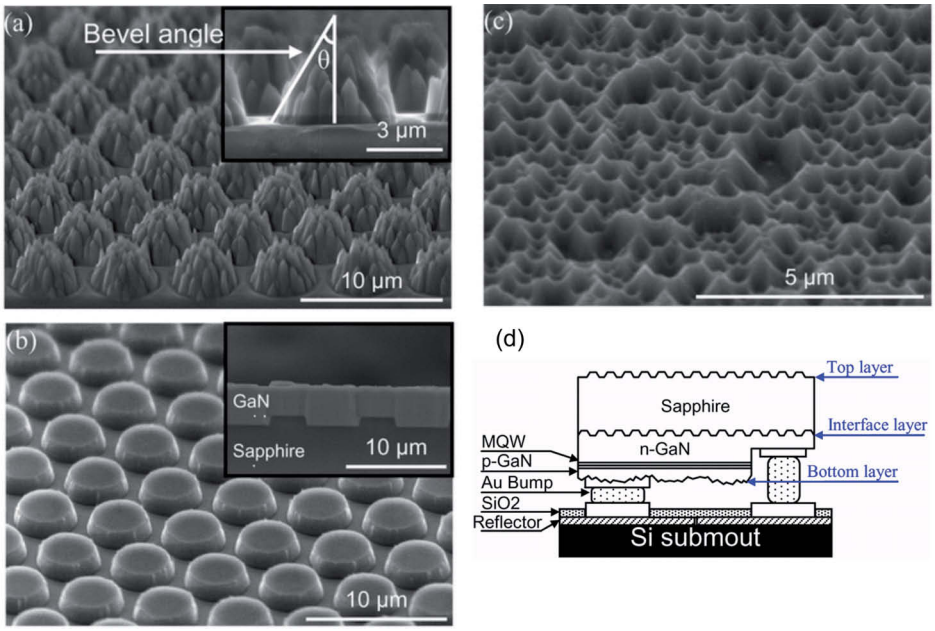

Figure 6.1: SEM image of the surface morphology of (a) top surface sapphire textured layer, (b) interface pattern sapphire layer, and (c) bottom naturally textured p-GaN layer. (d) Schematic of the FC-LEDs with triple-light scattering layers [154].

substrate. A 40.2 % increase in the output power of FC GaN-based LEDs, by the use of a mesh type textured sapphire back-surface along with a Ni/Ag p-pad reflector electrode, was demonstrated by Han et al. [159]. A technique to reduce the dislocation density in the epitaxial layers is the epitaxial growth on patterned sapphire substrates (pss) [160]. These structures at the GaN-sapphire interface scatter the light resulting in higher output powers [161]. In 2008, Lee et al. fabricated LEDs with triple-light scattering layers (Fig. 6.1) i.e., patterned sapphire back-surface and interface along with a naturally textured p-GaN surface, which resulted in a 60 % increase of the output power [154]. The technique of surface roughening coupled with a rear mirror, to increase the LEE, has been extensively explored for LEDs emitting in the blue wavelength region and has proven to be a viable solution for the commercial fabrication of LEDs. However, its impact on near and deep UV LEDs still requires to be investigated.

6.2 Modelling the influence of textured surfaces on the LEE of LEDs

A statistical approach in which the behaviour of light is considered to be ergodic was proposed by Yablonovitch [162] and Schnitzer [153] to understand the observed increase in the LEE with the use of textured surfaces. In this photon gas model, light rays incident on a surface with irregular shape lose all memory of the incident angle after the first or second

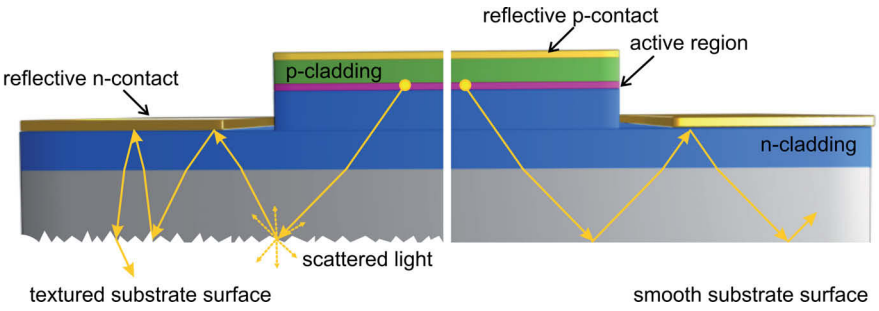

Figure 6.2: Schematic of the propagation of light in an LED with a textured substrate back-surface and a smooth substrate back-surface. The incident angle of propagation is randomized in the case of a textured surface.

scattering from the surface i.e., the angle of incidence will be totally lost after total internal reflection, leading to complete randomization of the photon trajectories with respect to internal angles in the semiconductor. Consequently photons which were originally emitted out of the escape cone can be redirected into the escape cone after reflection (Fig. 6.2). An equivalent wave-optical description is the mixing of waveguide modes confined in the cavity, formed between the LED surface and reflector, and modes which are not confined in the LED [163]. Schnitzer et al. [153] did not consider any increase in the one bounce transmission due to the rough surface.

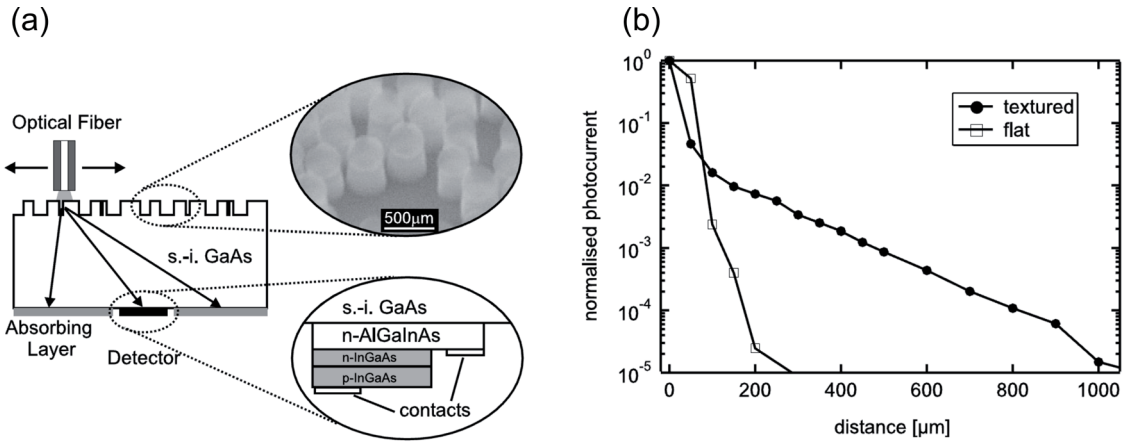

Figure 6.3: (a) Schematic of the setup for the measurement of the light transmitted through a textured GaAs surface. Upper inset: SEM image of the textured surface. Lower inset: structure of the integrated detector [164]. (b) Comparison of the light detected by the detector, placed at different distances from the optical fiber, for a flat and a textured GaAs layer with an integrated InGaAs detector of $50 \times 50\,\mu\text{m}^2$ in size. The light detected at different distances of the detector from the optical fiber is related to the angular distribution of the light. The surface is roughened using natural lithography with polystyrene spheres with size 300 nm [164].

For a quantitative assessment of the behaviour of LEDs with textured surfaces, Windisch et al. published a series of papers studying the behaviour of light propagation through tex-

tured GaAs surfaces [163–166]. Using an integrated detector (Fig 6.3 a), they showed that 72 % of the light incident normally on a textured GaAs surface is transmitted through the surface without being scattered (Fig 6.3 b) [164]. The rest of the light is not scattered into random directions but is dispersed preferentially into small angles described by a scattering function with angular distribution $cos(\theta)^{2.8}$ where θ is the angle w.r.t. the normal. To measure the angular dependence of the transmission coefficient for GaAs textured surfaces, transmission of light incident on a bevelled GaAs plane was measured (Fig 6.4) [166]. Contradictory to the assumption of Schnitzer et al., transmission of light was observed for angles greater than the critical angle for textured surfaces although a reduction in the transmission was observed for incident angles within the escape cone. An angle averaged transmission $\bar{T}$ of 1.35 % was observed for flat samples and increased to 2.6 % for samples textured with pillars of diameter 350 nm and height 180 nm. Windisch et al. compared the EQE of LEDs with textured surfaces to those with flat surfaces both with and without a rear mirror. An EQE of 2.15 % was measured for GaAs LEDs with flat surfaces which increased to 18.5 % with the addition of a rear mirror. In the case of LEDs with textured surfaces a greater increase in the EQE, from 3.2 % to 46 %, was observed with the use of a rear mirror indicating internal scattering of the light reflected from the textured surface is the major cause of the observed enhancement [166].

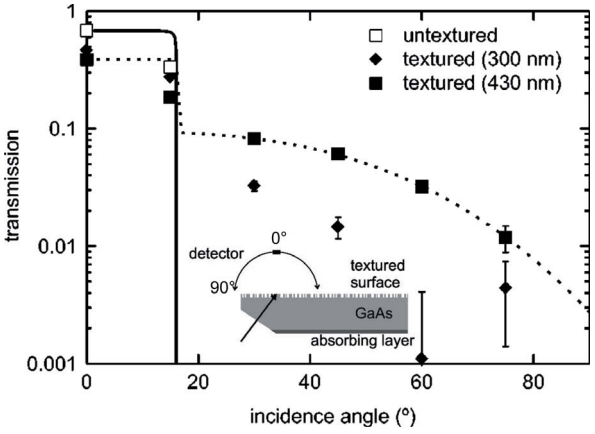

Figure 6.4: Total transmission through a naturally textured GaAs surface versus incidence angle. Solid line: theorectical transmission according to Fresnel's formulas. Inset: Schematic of the sample geometry [166].

A. David used a numerical model based on solving the Maxwell's equations to describe scattering of light by a roughened semiconductor interface [167]. The period of the structures considered were 0.8 to 2 times the wavelength of the emitted light. The scattering efficiency was found to be dependent on the incoming angle. The backscattering is diffused at normal incidence and specular at glancing angles while the transmission on the other hand is specular near normal incidence and diffused at large angles (Fig 6.5). A large number of round trips of the light rays in the LED is required for the outcoupling of the light and the ergodicity was found to decrease with successive bounces. Due to the requirement of multiple bounces, the presence of any lossy features can significantly impact the LEE of the devices. A. David also showed that for large feature sizes i.e., greater than 4.5 times the wavelength of the generated light, the results obtained from wave-optics calculations slowly converges to the results obtained using geometric optics.

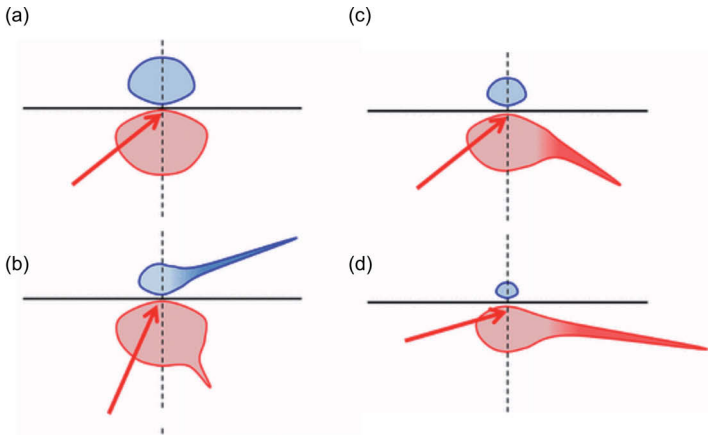

Figure 6.5: Sketches of scattering profiles for various cases. The horizontal line represents the rough surface, and the clouds are the backward and forward-scattered intensities. (a) Ideal diffuser, with no specular peaks in the scattering profiles. (b)–(d) Realistic scattering at various angles of incidence. (b) near normal incidence T is mostly specular and R is mostly diffuse. (c) At intermediate angles T is diffuse and the specular component of R increases. (d) At glancing angle T vanishes, and R is mostly specular [167].

The models discussed show that the use of scattering structures increases the one bounce extraction efficiency of the light only by a small amount. The main increase in the LEE with the use of textured surfaces is due to the randomization of the light rays after reflection allowing the light to obtain multiple chances to enter the escape cone.

6.3 Influence of a mechanically textured sapphire substrate on the LEE of UV LEDs

In flip-chip mounted UV LEDs grown on sapphire substrates, the light is extracted from the sapphire back-surface. As in the case of the visible LEDs, texturing of the sapphire back-surface could be used to increase the LEE of the devices. The simplest method to texture the surface is mechanical polishing. Hence, to study the influence of surface texturing on the LEE of UV LEDs, the light output power of LEDs with a polished substrate back-surface was compared to the output power of the same LED after the substrate back-surface of the LED was mechanically roughened. Assuming that the texturing process does not affect the contacts or the IQE of the device, the observed change in the output power would correspond to a change in the LEE of the device. To obtain a smooth surface, the sapphire substrate was mechanically polished using a paste of B_4C particles with particle size 9 μm followed by diamond particles of particle size 3 μm. The substrate was roughened using a paste of diamond particles with particle size 30 μm. The roughness of the sapphire was determined using scanning white light interferometry (SWLI) (Fig. 6.6). Mechanical texturing of the surface results in a non-uniform surface roughness as seen in Fig. 6.7. The angles of the roughened surface varies across the surface and hence no typical angles can be determined. In the case of the polished surface, scratching of the surface is observed.

A comparison of the electric and optical performance of an LED emitting at 391 nm with different surface roughnesses of the sapphire substrate back-surface is shown in Fig. 6.8 a.

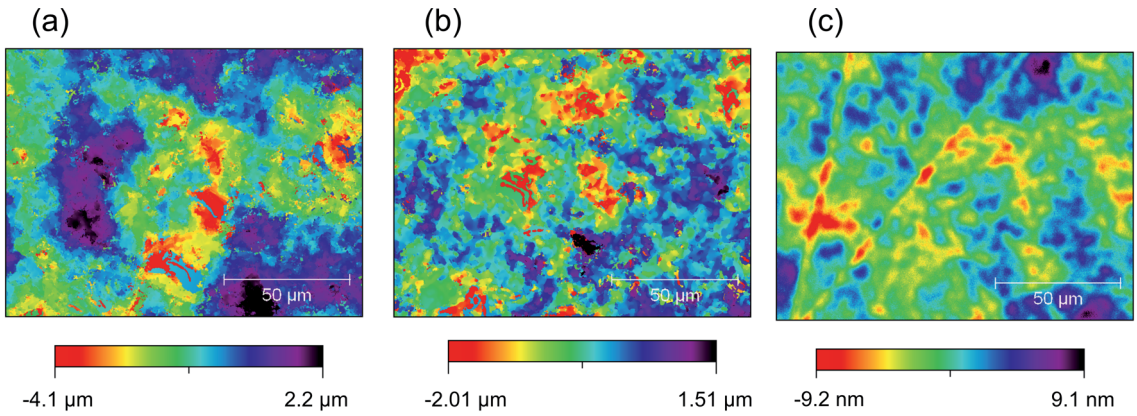

Figure 6.6: Roughness of sapphire substrate back-surface measured by SWLI (a) rough surface as bought from manufacturer (rms surface roughness = 1.4 μm) (b) roughened using 30 μm diamond particles (rms suface roughness = 0.75 μm) (c) polished (rms surface roughness = 2.71 nm)

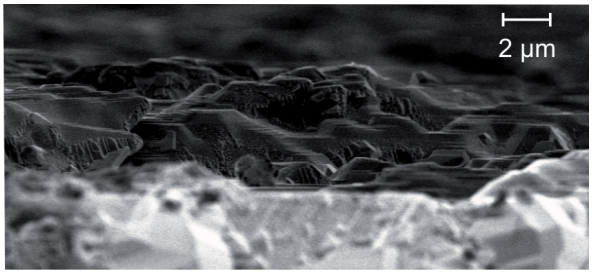

Figure 6.7: Cross-sectional SEM image of the back-surface of the sapphire substrate as purchased from the manufacturer.

The emission power of the LED is found to increase with the surface roughness as in the case of the blue and arsenide based LEDs. No change in the operating voltage was observed, indicating that no damage to the ohmic contacts or the LED heterostructure is caused during the polishing process.

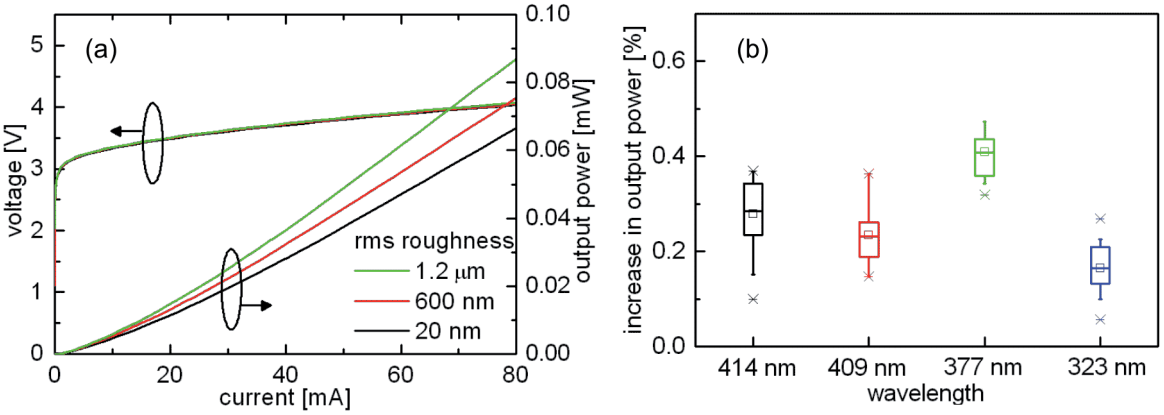

Figure 6.8: (a) Comparison of the L-I-V characteristics, measured on wafer, of a 391 nm LED with different roughnesses of the sapphire substrate back-surface. (b) Box plot of the increase in the output power of LEDs measured on wafer, emitting at different wavelengths, after roughening the sapphire substrate back-surface from 2.71 nm to 1.4 μm measured at various points across the wafer.

For a quantitative assessment of the behaviour of the LEDs with mechanically roughed surfaces, the change in the emission power of the device after mechanical roughening of the substrate to 1.4 μm was investigated for LEDs emitting in the UV-A and UV-B wavelength region. The parameters of the samples studied are listed in Table 6.1. The large variation in the change of the output power of the LEDs, from the same sample, is due to the differences in the surface roughness across the wafer. In the case of all samples an increase in the output power was observed after roughening of the sapphire substrate (Fig. 6.8 b). This indicates that surface texturing can increase the LEE of LEDs even in the UV wavelength region. The enhancement may be attributed to an increase in the one bounce extraction of light and/ or to the randomization of the incident angular distribution of the photons after multiple reflections (Sec. 6.2). Due to the requirement of multiple reflections, even at the same wavelength, the change in the output power is dependent on the reflectivity of the ohmic contacts. Absorption in the LED heterostructure, owing to the presence of absorbing p-cladding layers, layers with large number of defects and devices with low IQEs, would also influence the enhancement of the LEE. This is reflected in the experimental results where although a large variation in the data is observed the measured increase in the LEE tends to decrease with the emission wavelength of the LED due to the lack of reflective contacts and lower IQE of LEDs at shorter wavelengths. The large improvement in the LEE of the 377 nm LEDs may be attributed to the high reflectivity of the ITO/Ti/Pt/Au p-contact due to the transparency of the ITO layer coupled with the presence of untreated Ti/Pt/Au layers.

Table 6.1: Parameters of the LEDs used for the investigation of mechanical roughening of the substrate on the LEE of the device

	Substrate	Wavelength (nm)	p-metal contact	n-metal contact
Sample A	sapphire	414	Ni/Au/Ti/Au	Ti/Al/Mo/Au
Sample B	sapphire	409	Ni/Au/Ti/Au	Ti/Al/Mo/Au
Sample C	sapphire	377	ITO/Ti/Pt/Au	Ti/Al/Mo/Au
Sample D	sapphire	323	Pd/Ti/Au	Ti/Al/Mo/Au (annealed)

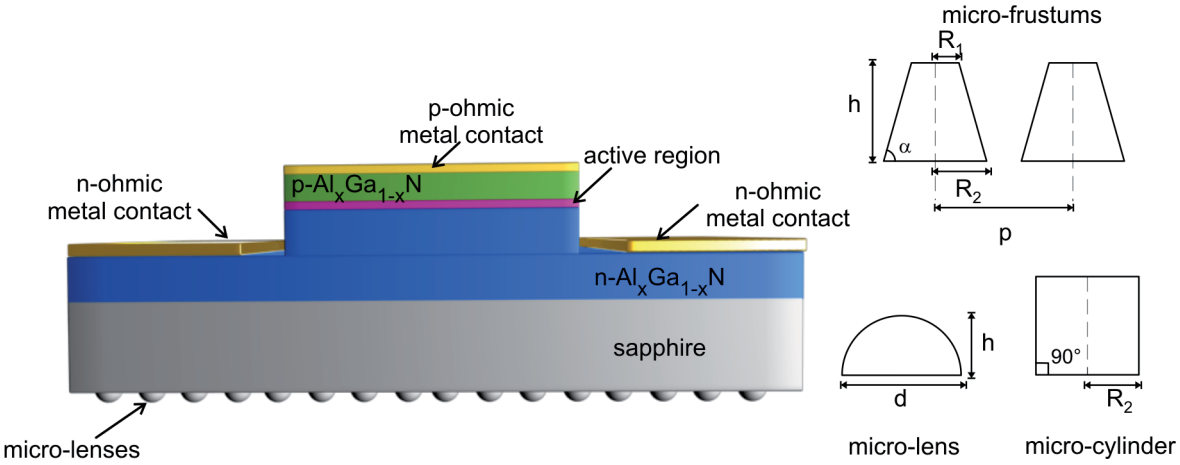

Figure 6.9: Schematic of the LED structure and micro-structures used for the simulation of the light extraction

6.4 Modelling the influence of sapphire micro-structures on the LEE of UV LEDs

Simulations were used to obtain a deeper understanding of the influence of the sapphire substrate texturing on the LEE of UV LEDs. Arrays of etched micro-structures were considered for a controlled, systematic investigation as the optical description of a random interface is difficult. The light extracted from 320 nm LEDs with and without etched sapphire micro-structures on the substrate back-surface was simulated using a non-sequential ray tracing software package *ZEMAX-EE* [40]. The optical parameters used for the simulations were obtained from literature and are given in Table 6.2. A simplified conventional square p-contact LED structure (Fig. 6.9) was considered for the simulations of the LEE measured on wafer i.e. no emission from the sides of the substrate. The light emission from the 100 μm x 100 μm active region was considered to be isotropic i.e. no polarization effects were considered. No scattering of light was assumed in the simulations as the dimensions of the micro-structures are much larger than the wavelength of the emitted light and all surfaces and interfaces were considered to be smooth.

Table 6.2: 320 nm LED material parameters used for simulations. Values of the refractive index of the AlInGaN layers determined by a model from [113] based on experimental values from [114–120]. R, T and A are the reflection, transmission and absorption coefficients respectively.

Layer	Thickness	Refractive index	
p-$Al_{0.06}Ga_{0.94}N$	200 nm	2.637	A = 1
p-$Al_{0.25}Ga_{0.75}N$	200 nm	2.701	T = 1
n-$Al_{0.35}Ga_{0.65}N$	3.5μm	2.554	T = 1
sapphire	430μm	1.806 [121]	
p-ohmic metal contact	500 nm		R = 0.4
n-ohmic metal contact	500 nm		R = 0.65

6.4.1 Influence of the parameters of the micro-structures on the LEE

An array of micro-structures etched in the sapphire back-surface was introduced in the simulation model and its impact on the LEE was studied. The different micro-structures simulated were arrays of micro-cylinders, micro-frustums and micro-lenses (Fig. 6.9). An absorbing p-$Al_{0.06}Ga_{0.94}N$ layer was considered for the simulations. The simulated LEE was 3.45 % for a 320 nm LED measured on-wafer, with an n-ohmic metal contact with reflectivity 0.65 and a smooth sapphire substrate back-surface. If the LED wafer is replaced by an individual 0.16 mm^2 LED chip with a smooth sapphire substrate in the simulation model, the LEE of the device increases to 6.2 %. The observed increase is due to collection of light from the side walls. In this work, only the change in the LEE of LEDs measured on-wafer is considered.

The influence of the coverage area, i.e. the area of the substrate covered by the microstructures, on the LEE was investigated. The coverage area is defined in Eqn. 6.1, where p is the pitch and R_2 is the radius of the base of the microstructure.

$$\text{coverage area} = \frac{\pi R_2^2}{p^2} \tag{6.1}$$

In Fig 6.10 a the increase in the output power, with the use of micro–structures as compared to a smooth sapphire back-surface, is calculated for different coverage areas. A more than 50 % increase in the output power can be obtained with the use of micro-structures. Due to the micro-structures, the incident angle of the light is changed at the micro-structure-air interface as compared to a flat surface. Hence light initially emitted outside the escape cone may now lie in the escape cone or after multiple reflections find the escape cone and be extracted. For both the micro-lenses and the micro-frustums the enhancement of the LEE strongly depends on the percentage of the surface area etched with micro-structures. The observed dependence is anticipated since as the coverage area decreases, a flat, smooth surface is approached which results in a decrease in the output power and consequently, reduced enhancement of the light extraction.

The dependence of the LEE on the parameters of etched micro-lenses, micro-frustums and micro-cylinders was systematically analysed. In the case of the micro-frustums, the influ-

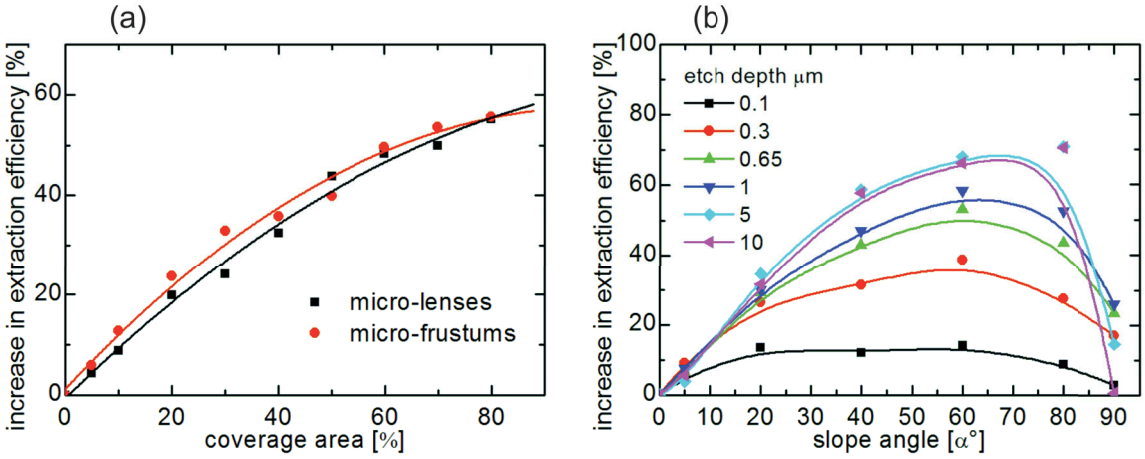

Figure 6.10: Simulation of the dependence of the increase in the extraction efficiency of 320 nm LEDs on (a) the coverage area for micro-lenses ($h = 650nm$, $R_1 = 1.38\,\mu m$) and micro-frustums ($h = 650nm$, $R_1 = 1\,\mu m$, $\alpha = 60^\circ$) and (b) the slope angle (α) and the etch depth (h) of the micro-frustums etched in the sapphire substrate back-surface with a coverage area of 65 %. The p-contact is considered to be absorbing and reflectivity of n-ohmic metal contact is 0.65.

ence of the slope angle (α) and the etch depth on the light extraction is shown in Fig. 6.10 b. For $\alpha = 90^\circ$ the micro-frustum corresponds to a micro-cylinder. An increase of only 26 % is obtained with the use of micro-cylinders for on wafer LEDs. This increase is due to out-coupling of light, emitted at large angles, at the edges of the microcylinders. At a constant coverage area, initially a steep increase in the output power is observed when the etch depth of the structures increases from 0.1 μm to 1 μm which begins to saturate for etch depths greater than 1 μm. A broad maximum is observed in the curve of enhancement of LEE versus the slope angle for the shallow etched structures. The peak in the LEE shifts towards larger slope angles as the etch depth increases.

To understand the observed behaviour we consider a ray of light incident at an angle θ on a flat substrate–air interface. If the flat surface is replaced by a micro-frustum with slope angle α then the angle θ' at which the ray impinges on the surface is given by $(\alpha - \theta)$ for $\theta \leq \alpha$ or $(\theta - \alpha)$ for $\theta > \alpha$ (Fig. 6.11). The light will be extracted if: $|\alpha - \theta| \leq \phi_c$, where ϕ_c is the critical angle given by Eqn. 5.1

We consider two cases

Case I $\alpha \leq \phi_c$

The light is extracted, with a transmission dependent on the Fresnel coefficients for the interface, if θ satisfies the equation

$$0^\circ \leq \theta \leq \alpha + \phi_c < 90^\circ \tag{6.2}$$

Case II $\alpha \geq \phi_c$

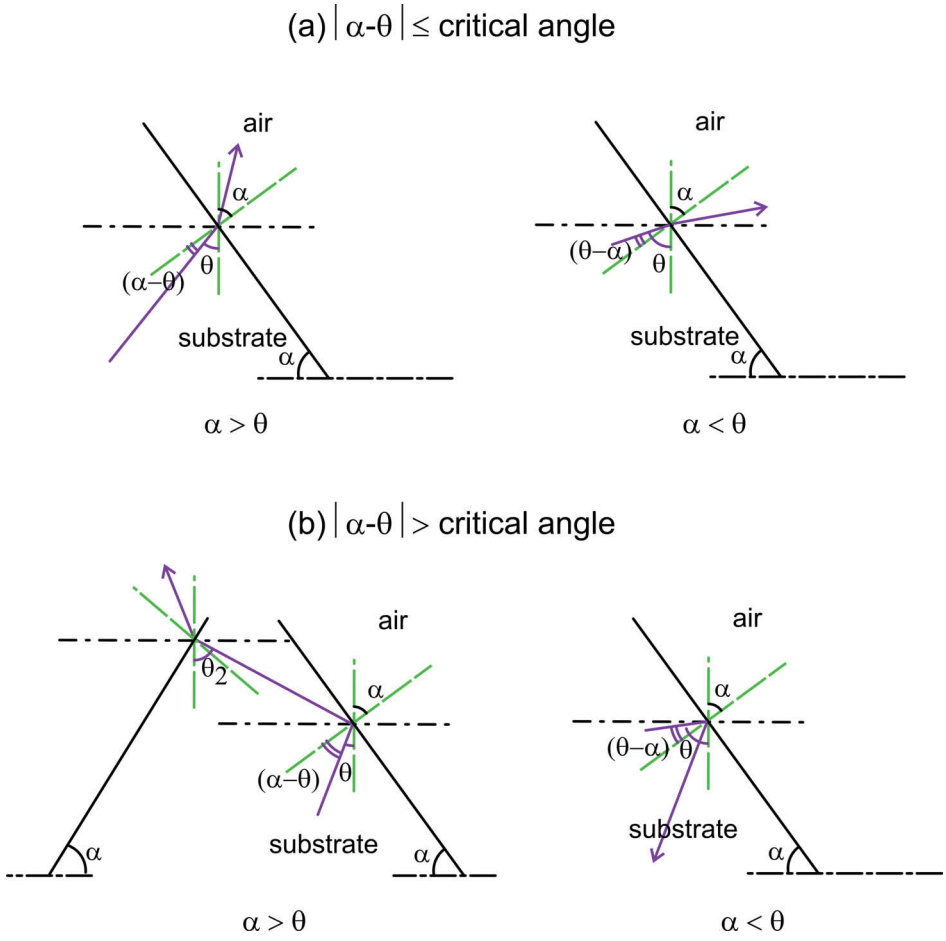

Figure 6.11: Schematic of the possible paths of a ray of light incident on the surface of a micro-frustum etched in the substrate back-surface

The light is extracted if θ satisfies the equation

$$\alpha - \phi_c \leq \theta \leq \alpha + \phi_c < 90^\circ \tag{6.3}$$

Accordingly if we consider only the one bounce extraction of light, the maximum efficiency is obtained for slope angles ranging from (ϕ_c) to $(90 - \phi_c)$. In the case of a sapphire substrate this would correspond to angles ranging from 33.7° to 56.3° which agrees well with the simulation results for the shallow etched micro-frustums.

In the case of the deep etched structures, the reflected light must also be considered. Let θ_2 be the angle at which the reflected ray is incident on a flat substrate-air interface. For slope angles greater than the critical angle, rays with $\theta < \alpha - \phi_c$ will be reflected forward towards the opposite side of the frustum with the angle of incidence, w.r.t. a flat surface, increased by $(180 - 2\alpha)$. After multiple reflections the ray can satisfy the condition of Eqn. 6.3 and escape the device. The greater the etch depth, the more reflections are possible

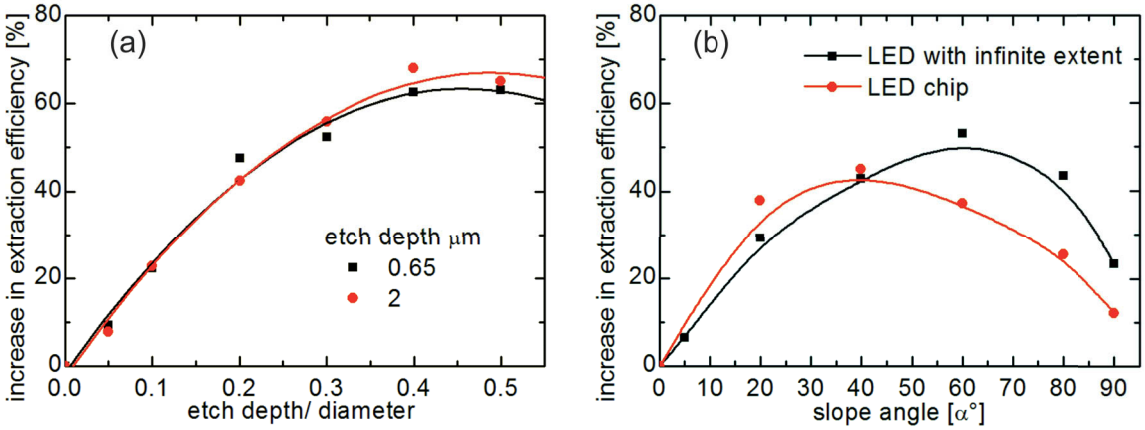

Figure 6.12: (a) Simulation of the dependence of the increase in the LEE of 320 nm LEDs on the etch depth and diameter of the micro-lenses etched in the sapphire substrate back-surface. (b) Simulation of the dependence of the increase in the LEE of 320 nm LEDs with infinite extent and LED chips on the slope angle (α) of micro-frustums ($h = 650\,nm$, $R_1 = 1\,\mu m$, coverage area = 65 %) etched in the sapphire substrate back-surface. The p-contact is considered to be absorbing and reflectivity of n-ohmic metal contact is 0.65.

before intersection of the ray with the top flat of the frustum and hence the maximum of the LEE versus slope angle curve moves towards larger values of the slope angle.

If $\alpha < \theta$ and $(\theta - \alpha) > \phi_c$ then the ray will be reflected back towards the active region of the device and depending on the reflectivity of the metal ohmic contacts may receive additional opportunities to find the light escape cone.

In Fig. 6.12 a, the simulated increase in the output power with the use of micro-lenses etched in the sapphire substrate back-surface is shown. The amount of light extracted strongly depends on the ratio of the etch depth to the diameter of the lens i.e., the solid angle suspended by the lens. The maximum power was obtained with hemispherical domes. As the angle suspended by the lens decreases, the surface morphology moves towards that of a flat surface and hence a reduced enhancement of the light extraction is observed. Since the enhancement of light extraction is only dependent on the solid angle and is independent of the etch depth, shallow etched structures with correspondingly small diameters can be used to increase the LEE of UV LEDs.

If the idealized LED with an infinite extent is replaced by an LED chip with dimensions 1 mm^2, an enhancement of the LEE, with the use of micro-structures etched in the substrate back-surface, is still achieved (Fig. 6.12 b). The maximum enhancement is obtained for smaller micro-frustum slope angles as compared to the infinite extent case. The obtained shift in the maximum is due to efficient outcoupling of the light, emitted at large angles, from the LED sidewalls even for a smooth surface. Therfore, the main benefit of the use of micro-structures is the extraction of light emitted in the no escape zone (Sec. 5.1).

To determine the most efficient micro-structures, the maximum simulated increase in the LEE of 320 nm LEDs with the use of optimized micro-cylinders, micro-frustums and micro-

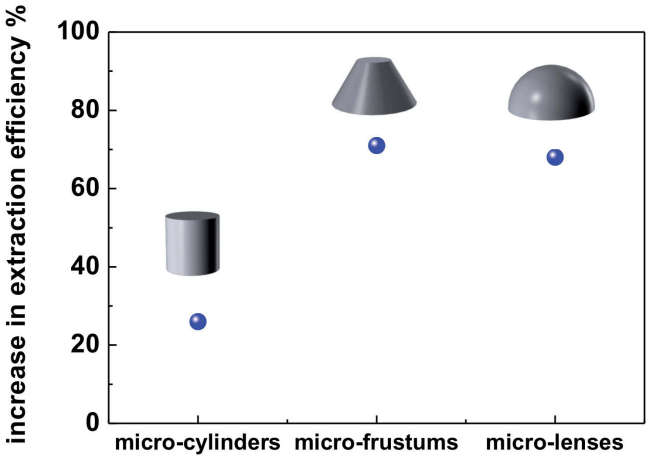

Figure 6.13: Simulated dependence of the LEE of 320 nm LEDs on the shape of the microstructure etched in the sapphire substrate back-surface. The p-contact is considered to be absorbing and reflectivity of n-ohmic metal contact is 0.65.

lenses etched in the sapphire substrate back-surface is shown in (Fig.6.13). The LEE of the LEDs can be most effectively increased with the use of micro-frustums or micro-lenses due to a change of the surface morphology.

6.4.2 Influence of the reflectivity of the metal contacts on the LEE

The impact of the reflectivity of the metal ohmic contacts on the LEE of LEDs, with smooth sapphire substrate back-surfaces, was investigated. A transparent p-$Al_{0.25}Ga_{0.75}N$ layer was considered for the simulations. For a 320 nm LED with an absorbing p-ohmic metal contact and a n-ohmic metal contact with reflectivity 0.65, the simulated LEE was 7.25 %. In Fig. 6.14 a, the increase in the LEE is shown for different reflectivites of the ohmic metal contacts. For a p-ohmic metal contact reflectivity of 0.4, a mere 11 % increase in the output power was observed when an absorbing n-ohmic metal contact was replaced by a contact with reflectivity 0.9. Only a minor influence of the n-ohmic metal contact reflectivity on the output power was observed. On the other hand, an increase in the reflectivity of the p-ohmic metal contact greatly enhanced the output power. Up to 84 % increase in the LEE was obtained by using a p-ohmic metal contact with reflectivity of 0.9 as compared to an absorbing contact. Light emitted towards the p-contact, with an incident angle less than the critical angle, can be extracted after specular reflection at the p-ohmic metal contact. At the same time light emitted within the escape cone reflected at the substrate-air interface, due to fresnel reflections, will also have multiple opportunities to escape due to reflections at the p-ohmic metal contact. Therefore, a reflective p-ohmic contact can greatly enhance the performance of the LEDs. For an LED with a smooth sapphire back-surface, the reflectivity of the n-contact does not greatly influence the LEE as the propagation angle of the light incident on the n-ohmic metal contact surface would be much larger than the critical angle and would be internally guided after specular reflection at the contact.

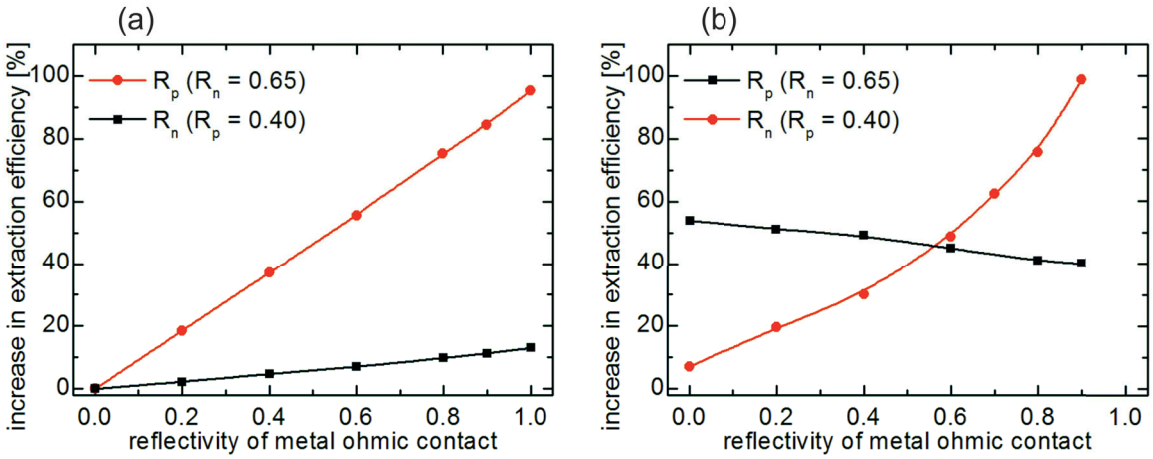

Figure 6.14: Simulation of the increase in the LEE, of 320 nm LEDs, with the reflectivity of the ohmic metal contacts for (a) a smooth sapphire substrate back-surface as compared to an absorbing ohmic metal contact. (b) micro-frustums with $h = 650\,nm$, $R_1 = 1\,\mu m$, $\alpha = 60°$ and 65 % coverage area etched in the sapphire substrate back-surface as compared to a smooth surface.

The influence of the reflectivity of the metal ohmic contacts on the LEE of the LEDs in combination with the use of etched micro-structures is shown in Fig. 6.14 b. The structures considered for the simulations were micro-frustums with $h = 650\,nm$, $R_1 = 1\,\mu m$, $\alpha = 60°$ and 65 % coverage area. For a given n-metal ohmic contact reflectivity, there is no significant impact of the reflectivity of the p-ohmic metal contact. The slight decrease in the enhancement of the LEE observed with higher reflectivity is due to the initially higher LEE of the LED with a smooth surface and a highly reflective p-ohmic metal contact. Light emitted directly under the p-metal ohmic contact would mainly lie within the escape cone and hence be extracted from the LED even in the absence of the micro-structures. Therefore, no significant influence of the p-ohmic metal contact reflectivity is observed. In contrast, the LEE of the LED is strongly influenced by the reflectivity of the n-ohmic metal contact. Nearly 100 % improvement in the LEE is obtained with the use of contacts with 90 % reflectivity. The enhancement in LEE can be attributed to reflection, at the n-ohmic metal contact, of the light redirected back into the LED by the microstructures with incident angles different from the initial angle of propagation. After multiple reflections the light initially outside the escape cone can be directed into the escape cone. In conclusion, for a highly efficient LED with a large LEE, it is necessary to have not only a highly reflective p-ohmic metal contact but also the reflectivity of the n-ohmic metal contact should be large.

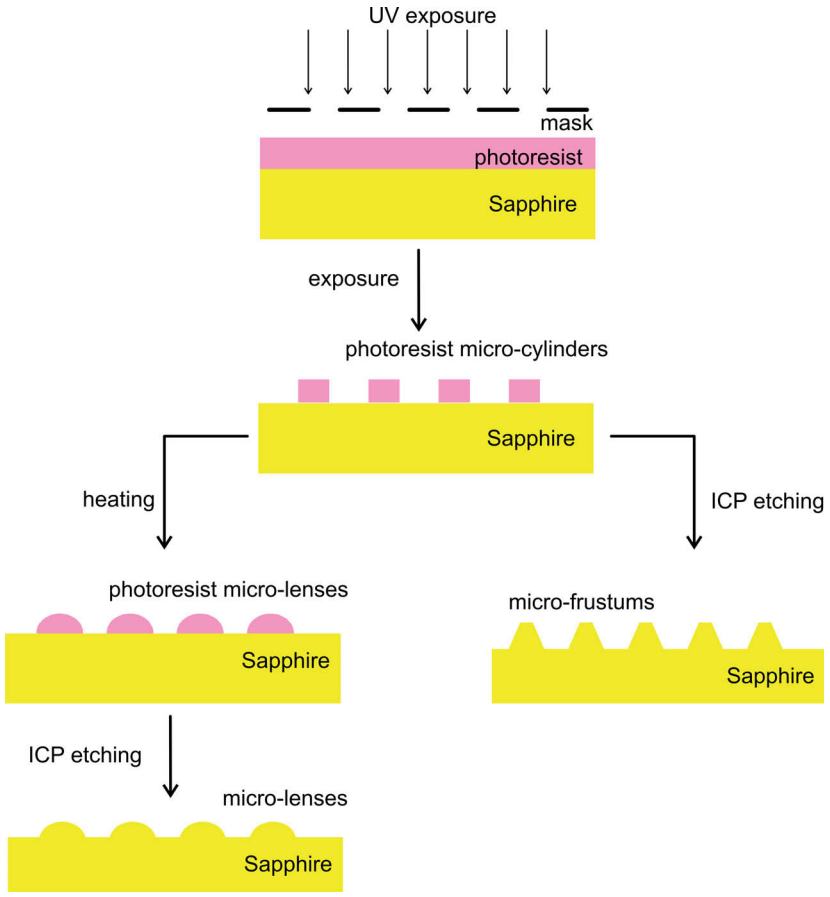

Figure 6.15: Schematic of the processing steps involved in the fabrication of micro-structures etched in a sapphire substrate

6.5 Experimental determination of the influence of micro-frustums on the LEE of UV LEDs

To experimentally determine the influence of micro-structures etched in the sapphire back-surface on the LEE of UV LEDs, the emission powers of LEDs with polished sapphire back-surfaces were compared to its emission power after the etching of the micro-structures on the sapphire back-surface. The micro-frustums and micro-lenses were found to be the structures that provide the highest enhancment of the LEE (Sec. 6.4.1) and consequently the fabrication of these structures was investigated.

6.5.1 Fabrication of micro-structures etched in sapphire

The process flow for the fabrication of the micro-structures is shown in Fig. 6.15.

A mask consisting of a hexagonal array of circles with diameter 2 μm and distance 1 μm was used for the fabrication of the micro-structures. The pattern was transferred to a 2 μm

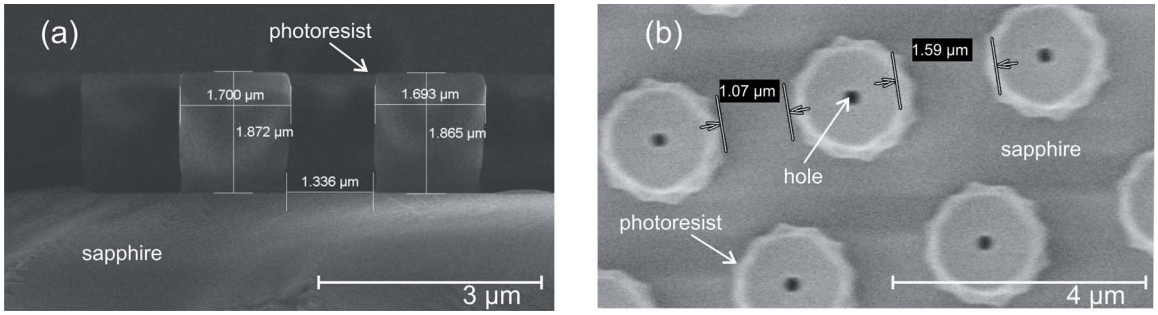

Figure 6.16: (a) Cross-sectional SEM image of the photoresist mask consisting of micro-cylinders used for the etching of micro-frustums and micro-lenses in the sapphire substrate back-surface. (b) top view SEM image of photoresist micro-cylinders with holes in the center of the structures arising from the interference fringes generated during exposure due to the transparency of the sapphire substrate.

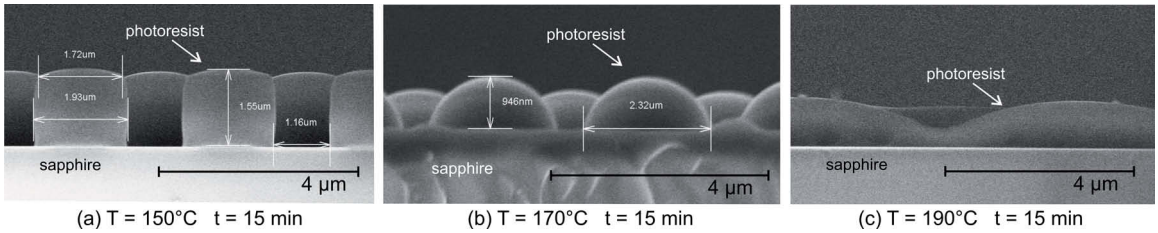

Figure 6.17: Cross-sectional SEM image of the thermal reflow of the photoresist micro-cylinders after heating at different temperatures for 15 min (a) T = 150°C, (b) T = 170°C and (c) T = 190°C.

thick photoresist layer (SPR 995–CM1.1[1]) using contact photolithography (Fig. 6.16 a). Due to the transparency of the substrate, interference fringes may be generated, during the exposure of the photoresist, resulting in the formation of a pit in the center of the micro-cylinders (Fig. 6.16 b). This pit formation can be avoided with the use of an absorbing foil under the samples. For the patterning of the micro-frustums, the photoresist micro-cylinders were directly used as a mask for the etching of sapphire. To fabricate the micro-lenses, the photoresist cylinders were transformed first into micro-lenses using thermal reflow. In Fig. 6.17, SEM images of the photoresist micro-cylinders after reflow at different temperatures is presented. The photoresist micro-cylinders were converted to micro-lenses by reflowing them at 165°C for 30 min or 170°C for 15 min.

The next step in the fabrication process is the transfer of the pattern from the photoresist mask to the sapphire substrate. Patterning of sapphire is technically challenging due to its resistance to most chemical etching processes and a value of 9 on the Mohs scale of mineral hardness [168]. ICP-etching using BCl_3 and Cl_2 as reagents was used to pattern sapphire with an etch rate of 175 nm/min and an etch selectivity ratio of the photoresist to sapphire of 2:1[2]. During the etching of sapphire, temperatures higher than 200°C are reached as a result

[1] produced by Dow (Rohm and Haas Electronic Materials)
[2] etching of sapphire done at SENTECH Instruments GmbH

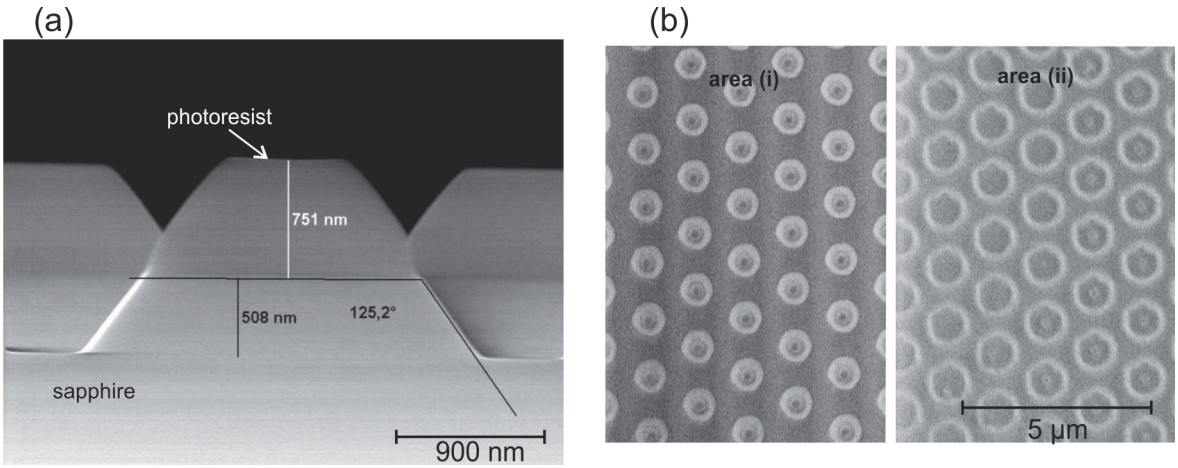

Figure 6.18: (a) Cross-sectional SEM image of the micro-frustum etched in the sapphire substrate using ICP etching. (b) SEM image of arrays of micro-frustums etched in the sapphire substrate back-surface at the edge (area (i)) and the centre (area (ii)) of the wafer.

of its high chemical resistance and low thermal conductivity coefficient of 40.06 W/mK at 273 K [168]. Therefore, the samples were cooled, using He gas, during the etching process to prevent damage to the etching mask and the LED. Photoresist micro-cylinders could be successfully used as a mask for the patterning of micro-frustums in sapphire. By controlling the etch time, micro-frustums with slope angles ranging from 50° to 65° and etch depths ranging from 500 nm to 960 nm were obtained (Fig. 6.18 a). For the successful transfer of the micro-lenses to the sapphire substrate, an etch selectivity ratio of the photoresist to sapphire of 1:1 is required. Due to the high etch selectivity ratio obtained for the process, the fabrication of optimized micro-lenses with etch depth to diameter ratios close to 0.5 was not possible. Consequently, only the influence of the micro-frustums was investigated in this work.

6.5.2 Investigation of the influence of the micro-frustums on the extraction efficiency

The structures of the LEDs investigated and the parameters of the micro-frustums patterned on the substrate back-surface are shown in Table 6.3. The measured change in the output power of the LEDs after the patterning of the micro-frustums, compared to a smooth substrate back-surface, is presented in Fig. 6.19. The large scatter in the measurements is due to the in-homogeneity of the micro-frustums across the wafer. Due to the bowing of the wafer, the temperature distribution across the wafer is non-uniform. This leads to in-homogeneous etching conditions resulting in different dimensions of the micro-frustums across the wafer (Fig. 6.18 b). At 10 mA a (19 ± 14) % increase in the output power of LEDs was obtained for sample C (Fig. 6.19). The measured enhancement is less than the 54 % increase expected from the simulations. After the etching process the operating voltage at 10 mA increases from (3.95 ± 0.11) V to (4.06 ± 0.16) V, indicating that the etching process degrades the

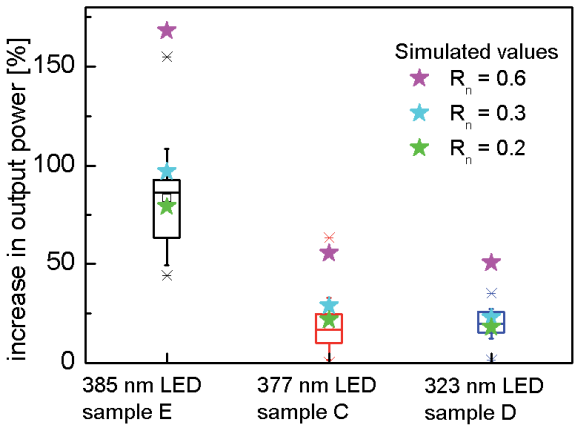

Figure 6.19: Box plot of the increase in the output power of UV LEDs, measured on wafer, after etching micro-frustums in the substrate back-surface. The simulated increase in the output power is plotted (stars) for different reflectivities of the n-ohmic metal contact.

ohmic metal contacts. Increased absorption in the ITO layer could result from the degradation of the contact during the patterning of the substrate. In the case of Ti/Al/Mo/Au contacts on n-GaN, it has been shown that a Ti-N compound is formed at the metal-GaN interface even without annealing of the contact [169, 170]. On annealing the contacts at 800°C, intermixing of the metal layers is observed and a surface morphology with rms roughness of 48 nm has been reported [169, 170]. The presence of a Ti-N interlayer, in the case of the not annealed contacts, and the intermixing of the metal layers, in the case of the annealed contacts, could decrease the reflectivity of the n-ohmic metal contact from the theoretical value of 0.6 used in the simulations. Therefore, the difference in the simulated and the measured values in the enhancement of the LEE could be attributed to the degradation of the contacts i.e., increased absorption in the ITO layer after etching, and the reduced reflectivity of the n-ohmic metal contact. As seen in in Fig. 6.19, by adjusting the reflectivity of the n-ohmic metal contact a good agreement between simulations and experiments can be obtained.

A (20 ± 7) % increase in the output power, as compared to a smooth substrate surface, is observed for sample D emitting at 323 nm with the use of micro-frustums with slope angle 58° and height 650 nm (Fig. 6.19). The measured increase in the extraction efficiency is greater than the (16 ± 7) % increase in the output power obtained by mechanically roughening the sapphire back-surface. This is one of the first reports of the enhancement of the LEE of UV-B LEDs using a patterned sapphire substrate back-surface.

To study the influence of micro-structures etched in the substrate back-surface on the enhancement of the LEE of LEDs grown homo-epitaxially on GaN bulk substrates, micro-frustums with slope angle 58° and height 650 nm were etched in the GaN substrate back-surface of sample E. An (83 ± 26) % increase in the extraction efficiency of the LEDs was observed with the use of etched micro-frustums (Fig. 6.19). In the case of LEDs grown on sapphire substrates, even with the patterned substrate back-surface, a large fraction of the light is waveguided in the n-$Al_xGa_{1-x}N$ layer and can not be extracted. However, for LEDs grown on GaN substrates, patterning of the surface can be effectively used to extract all the light as the light is no longer waveguided within the LED structure. Therefore, a much

Table 6.3: Structure of the LEDs investigated and parameters of the micro-frustums etched in the substrate back-surface.

	Substrate	Wavelength (nm)	p-cladding layer	p-ohmic metal contact	n-cladding layer	n-ohmic metal contact	Micro-frustum etch depth (nm)	Micro-frustum slope angle	Micro-frustum coverage %
Sample C	sapphire	377	$Al_{0.07}Ga_{0.93}N$ (45 nm) GaN (15 nm)	ITO/Ti/PT/Au	GaN (2.5μm)	Ti/Al/Mo/Au	950	50°	55
Sample D	sapphire	323	GaN (60 nm)	Pd/Ti/Au	$Al_{0.4}Ga_{0.6}N$/ $Al_{0.3}Ga_{0.7}N$ SL (7.2μm)	Ti/Al/Mo/Au (annealed)	650	58.5°	59
Sample E	GaN	385	GaN (200 nm)	Ni/Au/Ti/Au	GaN (6.4μm)	Ti/Al/Mo/Au	650	58.5°	59

greater enhancement of the LEE, with the use of micro-structures etched in the substrate back-surface, is observed for homo-epitaxially grown LEDs.

6.6 Summary

The use of a textured substrate back-surface to enhance the LEE of UV LEDs was systematically investigated using simulations and experiments. A simple technique of mechanical polishing with diamond particles, to roughen the sapphire substrate back-surface, was successfully used to increase the output power of 323 nm LEDs by (16 ± 7) % as compared to a smooth surface.

For a even greater enhancement of the LEE, the use of patterned arrays of micro-cylinders, micro-frustums and micro-lenses etched in the substrate back-surface was proposed. Simulations were used to determine the parameters of the microstructures that influence the enhancement of the LEE of UV LEDs. The increase in the LEE with the use of microstructures was found to be strongly dependent on the coverage area of the structures and a greater than 50 % increase in the output power can be achieved with high coverage areas. Furthermore, shallow etched micro-structures i.e., etch depths less than 5 μm, were found to be sufficient to maximize the LEE. The maximum increase in the LEE with the use of micro-cylinders, micro-frustums and micro-lenses, for 320 nm LEDs with an absorbing p-side and and n-ohmic metal contact reflectivity of 0.65, was calculated to be 26 %, 71 % and 68 % respectively. Using ICP etching, micro-frustums were patterned on the sapphire/ GaN substrate back-surface of LEDs emitting in the UV A and UV B region. A (20 ± 7) % increase in the output power of LEDs emitting at 323 nm was obtained with the use of micro-frustums. As a result, the use of micro-frustums to enhance the LEE of UV LEDs was successfully demonstrated.

Simulations were further used to investigate the influence of the reflectivity of the ohmic metal contacts on the LEE of UV LEDs. For an LED with smooth surfaces, the LEE was greatly increased with the use of reflective p-ohmic metal contacts. The reflectivity of the n-ohmic metal contact was found to have only a minor influence on the LEE of the LED. In contrast, for LEDs with micro-structures etched in the substrate back-surface, the reflectivity of the n-ohmic metal contact greatly influenced the observed enhancement in the LEE of the LEDs. Thus to fabricate UV LEDs with high LEEs it is important that the p-side is transparent and both the p- and n-ohmic contacts are highly reflective.

7 Nanopixel contact LED design for enhanced light extraction from UV LEDs

One of the major sources of losses of the light generated in nitride-based LEDs grown on sapphire substrates is light absorption at the electrical contacts. For the efficient outcoupling of light from FCLEDs, light that is emitted towards the metal contacts needs to be reflected to the transparent substrate. The immense influence of the reflectivity of the ohmic metal contacts on the LEE of LEDs has been previously discussed in Sec. 6.4. In the case of UV LEDs, obtaining p-contacts which are both ohmic and reflective is challenging due to the large bandgap of AlGaN, the limits in p-doping of AlGaN layers and the low reflectivity of metals in the UV wavelength range. To overcome this challenge, a novel nanopixel contact LED design, consisting of an array of nanopixel p-contacts combined with a metallic reflector, will be presented in this chapter.

7.1 State of the art reflective p-contacts for nitride-based UV and visible LEDs

To enhance light extraction, the reflectivity of electrical contacts needs to be increased without compromising the contact resistance. Increase in the contact resistance would result in higher operating voltages and resistive electrical losses which would lower the wall plug efficiency of the device. In the absence of suitable reflective ohmic contacts, an alternative approach to increase the LEE is to integrate a reflector into the LED. For the reflector to be effective, it should have a high reflectivity with a weak angular dependence in the wavelength range of interest.

Al, Rh and Ag metal reflectors have the highest reflectivity in UV wavelength region (Fig. 7.1). Ag, which is one of the most frequently used reflector for the visible region, becomes absorbing in the UV-B region due to $4d \rightarrow 5s$ interband transitions. Accordingly, Ag can only be used as a reflector in the UV-A wavelength range. The work functions of Al, Rh and Ag are 4.28 eV [172], 5 eV [173] and 4.26 eV [174] respectively. Due to their low work functions, they do not produce good ohmic contacts to p-$Al_xGa_{1-x}N$. One method to circumvent this problem is the use of semi-transparent interlayers between the reflector and the p-$Al_xGa_{1-x}N$ to obtain a low specific contact resistance. For the blue and near-UV region, the use of thin semi-transparent interlayers such as Ni/Au [175] [176], Zn-Ni

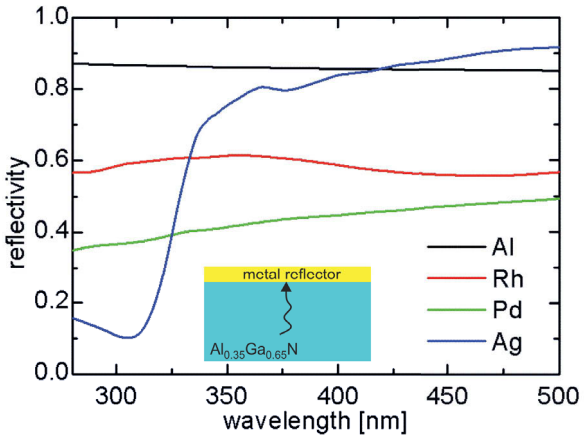

Figure 7.1: Calculated reflectance of 500 nm thick metallic reflectors on an $Al_{0.35}Ga_{0.65}N$ layer for normal incidence. Values of refractive index of metal layers obtained from [171]. Refractive index values of the $Al_{0.35}Ga_{0.65}N$ layer determined by a model from [113] based on experimental values from [114–120]

solid solution [177], indium-doped ZnO [178], Ir [179], indium-tin-oxide (ITO) [180] and Ag/ITO [181] have been extensively investigated. However, when moving deeper into the UV region, the absorption of light in these interlayers increases drastically.

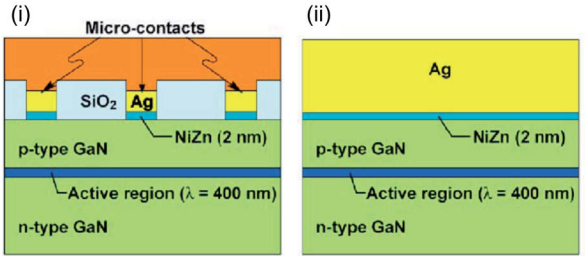

Figure 7.2: Schematic cross-sectional view of GaInN LED with a (i) GaN/SiO_2 /Al ODR with NiZn/Ag microcontacts and (ii) Ag reflector with thin NiZn (2 nm) interlayer [182].

Another approach to increase the LEE is the use of multilayer mirrors such as distributed Bragg reflectors (DBR) or omni-directional reflectors (ODRs). One of the major drawbacks of using such reflectors is that, unlike metallic mirrors, they are electrically insulating and hence no current can flow through the reflector. In order to provide electrical conductivity, it is necessary to perforate the mirror with arrays of microcontacts. Kim et. al. utilized an ODR consisting of GaN, a quarter-wave thick SiO_2 low-refractive-index layer perforated by an array of NiZn/Ag microcontacts and an Al layer to enhance the light extraction efficiency of 400 nm LEDs (Fig. 7.2) [182]. A 38 % higher output power was obtained for LEDs with a GaN/SiO_2/Al ODR as compared to LEDs with a Ag reflector. The size of the microcontacts ranged from $4 \times 4\,\mu m^2$ to $10 \times 10\,\mu m^2$ with minimum interval between the microcontacts of 15 μm. Due to the large distance between the microcontacts no current is injected in the region between the contacts and hence light is generated only in the active region below the microcontacts. Jeong et. al. [183] used a DBR consisting of 11 layers of alternating quarter-wave thick Ti_3O_5 and Al_2O_3 along with an p-ohmic contact ITO interlayer to increase the output power of 385 nm LEDs by 15 % compared to LEDs with a Ag reflector. Nakashima et. al. demonstrated a 1.6 times higher output power for 350 nm LEDs with the use of a perforated SiO_2/AlN dielectric multilayer coupled with an ITO interlayer as compared to Ni/Au p-contacts [184].

In the case of all the LEDs with reflective p-contacts discussed above, light is generated under the low contact resistance interlayer or microcontacts which are absorbing in the UV-B and UV-C wavelength range. Noticeably, in most commercial UV-LEDs due to the difficulties in growing highly doped p-$Al_xGa_{1-x}N$ layers, the LED structure is capped with an absorbing p-GaN layer for the formation of low resistivity p-ohmic contacts. For an efficient outcoupling of the light, with the use of reflective contacts, in UV LEDs, new contact layouts need to be designed such that light absorption in the p-GaN layer is avoided and the light is also generated in the region below the exposed mirror.

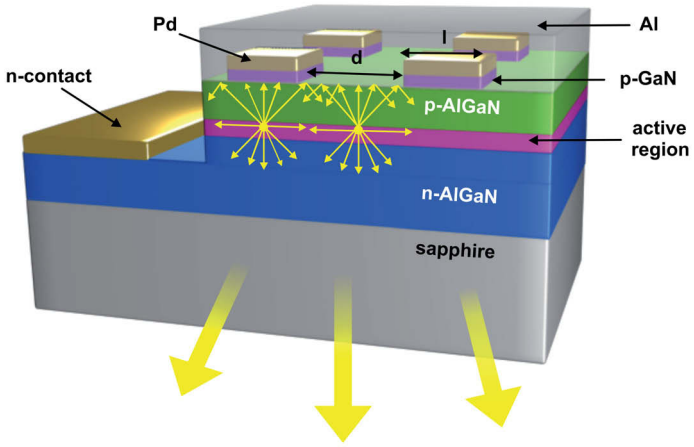

Figure 7.3: Schematic cross-sectional view of nitride-based nanopixel UV LED with Pd contacts and Al reflector layer.

7.2 Description of the nanopixel contact LED design

In this work a novel nanopixel contact LED design, consisting of nanopixel contacts of Pd (or any other low resistivity ohmic contact to p-GaN / p-AlGaN) combined with an Al reflector (metal reflector), is proposed to enhance light extraction in UV LEDs. A schematic cross-sectional view of the structure is shown in Fig. 7.3. The structure consists of a two dimensional array of Pd nanopixel contacts or any other low resistivity ohmic contact, with dimensions less than $4 \times 4\ \mu m^2$ and spaced less than $4\ \mu m$ apart. The Pd nanopixels form an ohmic contact to the p-GaN cap layer or the p-AlGaN cladding layer. If an absorbing p-GaN layer is implemented in the LED structure for the formation of low resistivity ohmic contacts, it can be etched off in the area between the nanopixels. Next, the entire p-side is covered with an Al reflector which also acts as a current spreading layer. If the spacing (d) between the nanopixels is sufficiently small, a large portion of the current will flow into the region between the nanopixels due to current spreading in the p-cladding layer. This results in the almost homogenous injection of current throughout the entire active region of the mesa structure. Light emitted in the region just below the nanopixels, towards the p-side of the diode, will be absorbed or poorly reflected by the Pd nanopixel contacts, while the light

emitted in the region between the nanopixels will be highly reflected by the Al layer. The LEE of the device can thus be increased if current overlap is obtained in the region between the nanopixels i.e. the nanopixel spacing is in the order of the current spreading length in the p-AlGaN cladding layer. To maximize the outcoupling of the generated light, the ratio of the area covered by the nanopixel contacts to the total mesa area (fill factor) should be minimal. Hence, optimization of both the size (l) and spacing (d) between the nanopixels is necessary to maximize the light extraction.

7.3 Theorectical impact of the nanopixel contact size and spacing

To maximize the LEE, with the use of nanopixel contact LED design, it is necessary to minimize the fill factor i.e. majority of the light should be generated under the Al reflector. The minimum fill factor is limited by:

1. the desired operational voltage. For fixed device dimensions, the voltage drop across the p-ohmic contact will increase by a factor *(100/fill factor)* for a LED with nanopixel contacts as compared to a large area contact LED. Therefore, the operational voltage will increase with reduced fill factor.

2. the minimum size of the nanopixel contacts which is determined by the fabrication technique.

3. the distance between the pixels which is governed by the current spreading in the p-cladding layer.

Current spreading in the p-cladding layer is necessary for the injection of current in the region between the nanopixel contacts. A minimum current density is required for the generation of light and additionally the IQE also depends on the current density (Sec. 3.1). When the lateral flow of current in an LED is considered, depending on the sheet resistance of the cladding layers, the current will prefer to flow in the layer with lower resistance. In the case of nitride-based UV LEDs, due to the difficulties in growing thick, highly doped p-AlGaN layers, the sheet resistance of the p-cladding layer is much higher than that of the n-cladding layer. Therefore, the junction current will tend to crowd around the nanopixel contact.

Thompson [185] proposed a model to describe the current spreading under a linear stripe top contact with the current spreading layer lying just above the p-n junction (Fig 7.4). In this model, the potential and current density (J_0) under the top metal contact is considered to be constant. Due to the high conductivity of the n-cladding layer, the n-side boundary of the active region is assumed to be a plane of equipotential V_{n0}. The equipotentials in the p-cladding layer are taken to be perpendicular to the p-n junction, in the region outside the contact, with purely transverse current flow. If ρ_p and t_p are the resistivity and thickness of

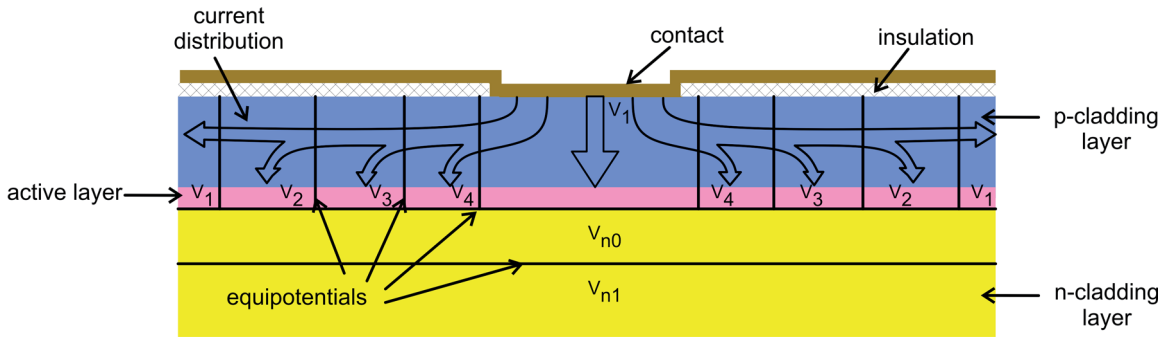

Figure 7.4: Schematic of equipotentials and current distribution between contact and active layer in structures with linear stripe contact geometry [185].

the p-current spreading layer and n_{ideal} is the diode ideality factor, then the current density $J(x)$ through the active region at a distance x from the edge of the contact is given by Eqn. 7.1

$$J(x) = 2\frac{J_0}{(x/L_{s_p} + 2^{1/2})^2} \tag{7.1}$$

where L_{s_p} is the current spreading length given by Eqn. 7.2.

$$L_{s_p} = \sqrt{\frac{t_p n_{ideal} kT}{\rho_p J_0 e}} \tag{7.2}$$

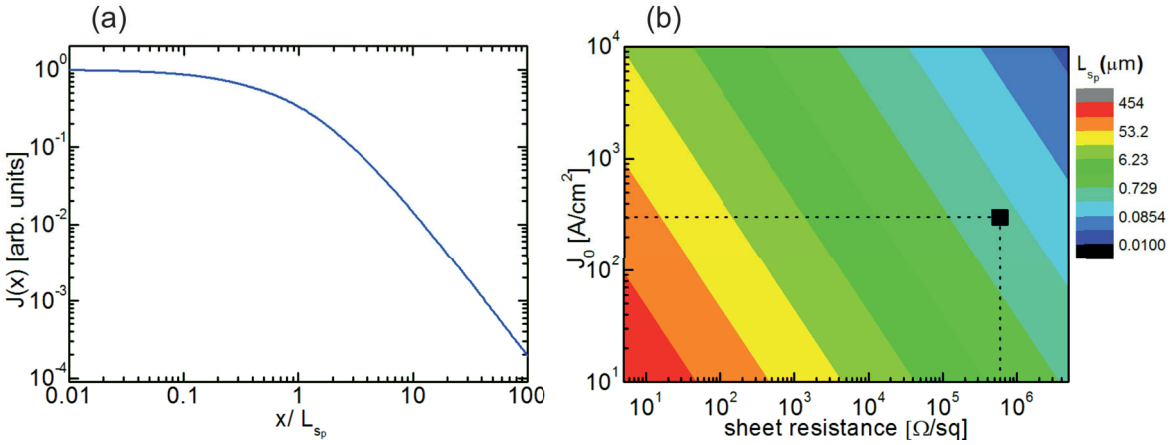

Figure 7.5: (a) Current density in the active region at a distance x from the edge of the contact as a function of the ratio x/L_{s_p}. (b) Calculated values for L_{s_p} as a function of the current density under the contact J_0 and the sheet resistance of the p-cladding layer. The n_{ideal} for UV AlInGaN LEDs is assumed to be 4.

Fig. 7.5 a shows the current density as a function of the ratio of the distance from the nanopixel contact edge (x) to L_{s_p}. A drastic decrease in the current density is observed

when the ratio $x/L_{s_p} \gg 1$. Consequently for the generation of light in the region between the nanopixel contacts, the spacing between the contacts (d) should follow the design rule $d \leq 2L_{s_p}$. As seen in Eqn. 7.2, L_{s_p} can be increased by reducing the resistivity or increasing the thickness of the p-cladding layer. The dependence of L_{s_p} on the current density further implies that the current injection in the region between the contacts and hence the efficiency with which the light is generated between the contacts will be dependent on the operational current. Therefore, the LEE of LEDs with nanopixel contacts design will be a function of the operational current. In Fig. 7.5 b, the current spreading length is calculated for different current densities under the contacts and sheet resistances of the p-cladding layer. For typical values of $\rho_p = 10\,\Omega$cm and $t_p = 200$ nm of the p-cladding layer, the distance between the nanopixel contacts should be around 1 μm at a current density of 200 A/cm^2. This implies that nanopixel contact sizes of less than $1 \times 1\ \mu m^2$ are required to obtain a fill factor ≤ 25 %.

7.4 Optical and electrical investigation of LEDs with nanopixel contact geometry

To demonstrate the viability of the nanopixel contact LED design experimentally, AlInGaN LEDs emitting from 390 nm to 400 nm with Pd nanopixel contacts and an Al reflector layer were fabricated. The layer structures were grown by MOVPE on (0001) oriented 2-inch sapphire substrates [186]. The structure consists of a GaN:Si buffer layer, a 5-period InGaN/InAlGaN MQW active region, a 10 nm thick $Al_{0.23}$GaN:Mg electron blocking layer, and a 200 nm thick GaN:Mg current spreading layer [55]. LEDs were fabricated using standard chip processing technology. Mesa structures were etched using inductively-coupled plasma in a chlorine atmosphere down to the n-GaN current spreading layer. An array of 30 nm thick nanopixel Pd contacts was fabricated on the mesa structure and annealed in nitrogen ambient at 530°C to form ohmic contacts. Arrays with nanopixel contact sizes from 4×4, to $1 \times 1\ \mu$m^2 and spacings of 4 to 0.5 μm along with conventional large-area square contacts (conventional LED contact) were fabricated on the same wafer for comparison. Ti/Al/Mo/Au layers were then deposited on the n-GaN surface. Finally Al/Pt/Au layers were deposited on the mesa structures. Transfer length measurements (TLM) were carried out to determine whether current is injected into the p-cladding layer by the Al reflector layer. As seen in Fig. 7.6, current is injected into the LED only through the Pd nanopixel contacts. For a systematic study of the influence of the nanopixel contact geometry on the LEE of the LEDs, two cases were considered:

1. the p-ohmic contact area was kept constant for all the LED structures i.e. the mesa area varied according to the fill factor and

2. the mesa area was kept constant for all the LED structures i.e. the p-ohmic contact area varied according to the fill factor.

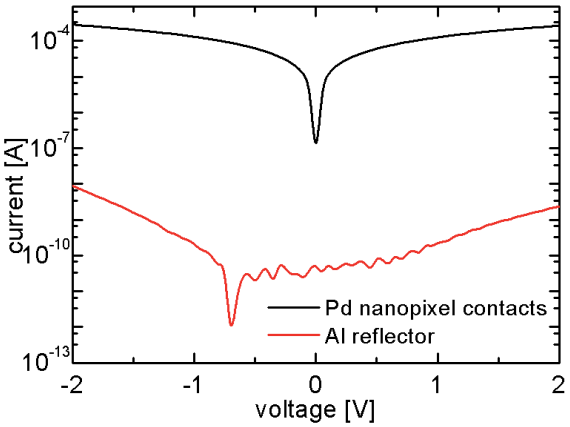

Figure 7.6: Two point I-V measurements on Pd and Al contacts depicting no current injection into the p-GaN cladding layer through the Al reflector. Current is only injected into the LED through the Pd nanopixel contacts.

7.4.1 LEDs with constant p-ohmic contact area: mesa area reduces with increase in fill factor

For the comparison of LEDs with identical p-ohmic contact area but varied nanopixel contact geometries, the Pd area was kept constant at $100 \times 100\,\mu m^2$. Nanopixel contact LEDs with a fixed nanopixel size of $1 \times 1\,\mu m^2$ and with nanopixel spacing 1.5, 1 and 0.5 μm along with a conventional $100 \times 100\,\mu m^2$ square contact LED were compared. This corresponds to filling factors of 16, 25, 44 and 100 % respectively. A similar operating voltage is obtained for all the LEDs confirming that the p-ohmic area is the same in all the devices (Fig. 7.7 a). Typical L-I characteristics of the different LED structures are shown in Fig. 7.7 b. At low currents, the output power of the large area contact is greater than that for the LEDs with nanopixel contact geometry. As the current increases the output power of the nanopixel contact LEDs becomes larger than that of the conventional LED. The crossover in the L-I curves occur at higher currents as the fill factor of the LEDs with nanopixel contacts decreases.

If no current spreading between the nanopixel contacts is assumed, the L-I characteristics of all the LEDs at low currents should be the same due to the identical current density in the LEDs. At high currents due to reduced heating, in the case of the LEDs with nanopixel contacts, the thermal roll-over of the output power occurs at larger currents as the fill factor decreases (Sec. 4.2.3). One factor that could decrease the output power is leakage currents. The mesa lengths of the LEDs with nanopixel spacing 1.5, 1 and 0.5 μm and the conventional LED are 260, 210, 160 and 110 μm respectively. If the main source of leakage was along the mesa side walls, the leakage current would increase with reducing fill factor. The increased leakage would result in lower output powers for the LEDs with nanopixel contact geometry. In Fig. 7.8 a, the measured reverse-biased current is plotted against the length of the mesa of the LEDs. The reverse current is found to increase linearly with the square of the mesa length i.e., the reverse current increases with the area of the mesa and not the perimeter. This implies that the bulk of the LED is the dominant source of the leakage current. Under the assumption of no current spreading, all the LEDs have the same contact area and consequently should have the same volume of leakage. The observed difference in the L-I characteristics of the

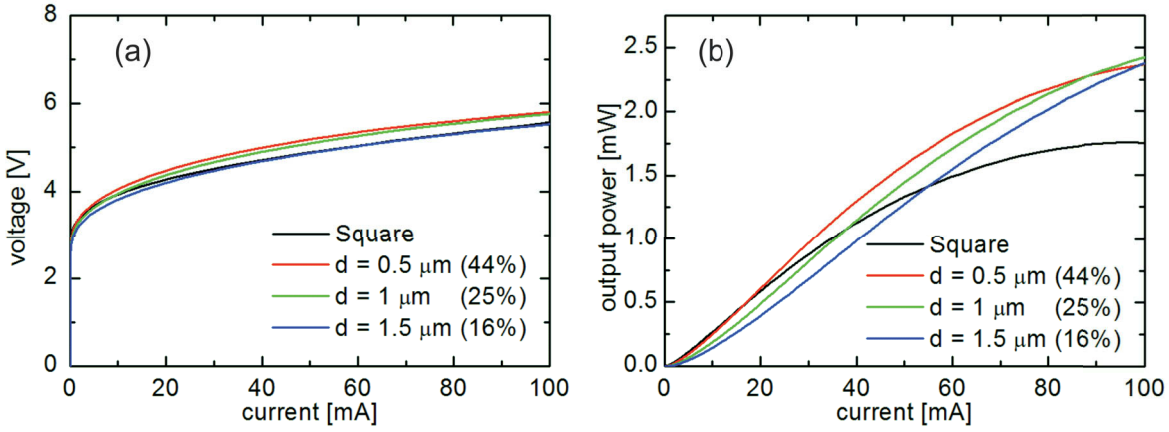

Figure 7.7: (a) V-I characteristics, measured on wafer, of nanopixel 400 nm AlInGaN LEDs with (i) square contact ($100 \times 100\,\mu m^2$) and nanopixel contact LEDs with nanopixel size = $1 \times 1\,\mu m^2$ and nanopixel spacing (ii) $0.5\,\mu m$ (iii) $1\,\mu m$ and (iv) $1.5\,\mu m$. The Pd area is kept constant at $100 \times 100\,\mu m^2$. (b) L-I characteristics, measured on wafer, for the structures (i-iv).

LEDs at low currents can therefore not be explained by variation in the leakage current. Hence current spreading in the p-cladding layer must be considered to understand the L-I characteristics of the devices.

If current spreading in the p-cladding layer and consequently current overlap in the region between the nanopixels is considered, the average current density in the LED would decrease with the fill factor. In Fig. 7.8 b, the measured dependence of the EQE of the conventional large area contact LED on the current density is depicted. A maximum in the EQE curve is obtained at a current density of 200 A/cm^2. In the case of the conventional LED, the LEE should be independent of the current density and thus the IQE of the LED should mirror the observed dependence of the EQE on the current density. At low operating currents, the nanopixel contact LEDs have a lower current density as compared to the conventional LED which in turn results in lower IQE in the nanopixel contact LEDs and hence a reduced output power. As the current increases, due to current spreading in the p-cladding layer and current overlap in the region between the nanopixels, the current density in the region between the nanopixel contacts increases resulting in more efficient generation of light in the region between the contacts. The light generated between the nanopixel contacts will be reflected by the Al-mirror and efficiently extracted from the LED which will result in a higher output power as compared to the conventional LED. The current at which the current density is sufficiently large to enable efficient generation of light between the pixels will depend on the nanopixel spacing. Correspondingly, the current at which the output power of the nanopixel contact LED becomes greater than that of the conventional LED will increase as the fill factor of the device decreases (Fig. 7.7 b).

The experimental data clearly demonstrates that current spreading in the p-cladding layer can be effectively used to inject current in the region between the nanopixels. By the op-

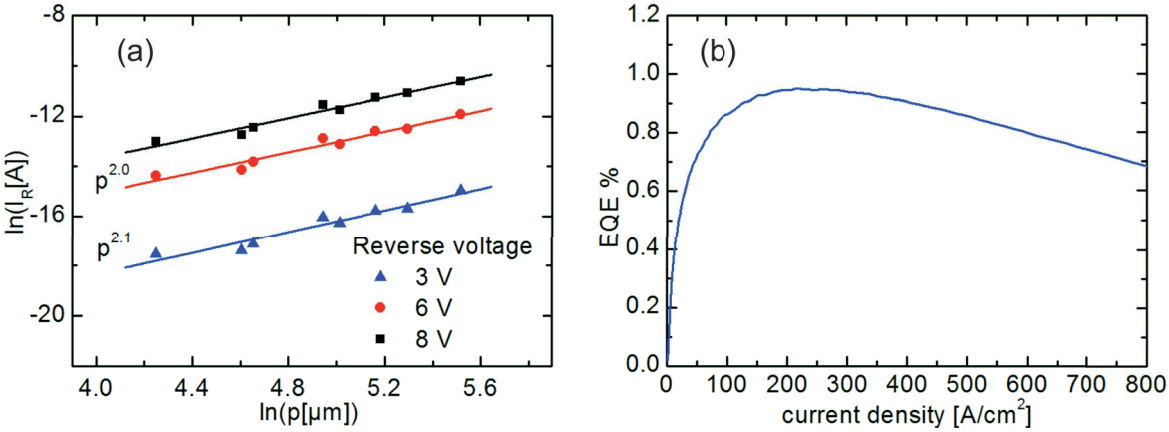

Figure 7.8: (a) Dependence of the reverse current (I_R) on the mesa length (p), measured at different bias voltages, of 400 nm AlInGaN LEDs with conventional large area square contacts and nanopixel contacts. (b) Dependence of EQE % on the operating current density, measured on wafer, for a 400 nm AlInGaN LED with large area $100 \times 100\,\mu m^2$ square contact.

timization of the nanopixel spacing, for the required operational current, it is possible to increase the LEE of UV LEDs with the use of the nanopixel contact LED design.

7.4.2 LEDs with constant mesa area: p-ohmic contact area reduces with decrease in fill factor

The mesa area was kept constant at $160 \times 160\,\mu m^2$ for the comparison of LEDs with identical mesa area but varied nanopixel contact geometry. Typical L-I characteristics for nanopixel LEDs, with different nanopixel sizes 4×4, 2×2 and $1 \times 1\,\mu m^2$ and spacing 4, 2, and 1 μm respectively but identical fill factor of 25 %, along with a conventional $150 \times 150\,\mu m^2$ square contact LED (100 % fill factor) are shown in Fig. 7.9 a. It can be clearly observed that the light output increases with decreasing nanopixel size and spacing. At 20 mA, the nanopixel LEDs with nanopixel sizes 4×4, 2×2 and $1 \times 1\,\mu m^2$ show a 55, 78 and 90 % increase in the light output power respectively compared to the conventional square contact. From the V-I characteristics shown in Fig. 7.9 b, it can be seen that at 20 mA the forward voltage for the nanopixel LEDs is much larger than that for the conventional square contact LED. This is mainly attributed to the decrease in the effective total p-ohmic contact area. Increase in contact resistance due to structural imperfections arising from the fabrication of contacts with small dimensions may also contribute to the observed increase in the operational voltage. The challenges in the fabrication of the nanopixel contacts with small dimensions will be discussed in detail in Sec. 7.5. Maximum wall plug efficiencies of 0.44 %, 0.51 %, 0.46 % and 0.34 % are obtained for the nanopixel LEDs, with different nanopixel sizes 4×4, 2×2 and $1 \times 1\,\mu m^2$ and the $150 \times 150\,\mu m^2$ square contact LED respectively.

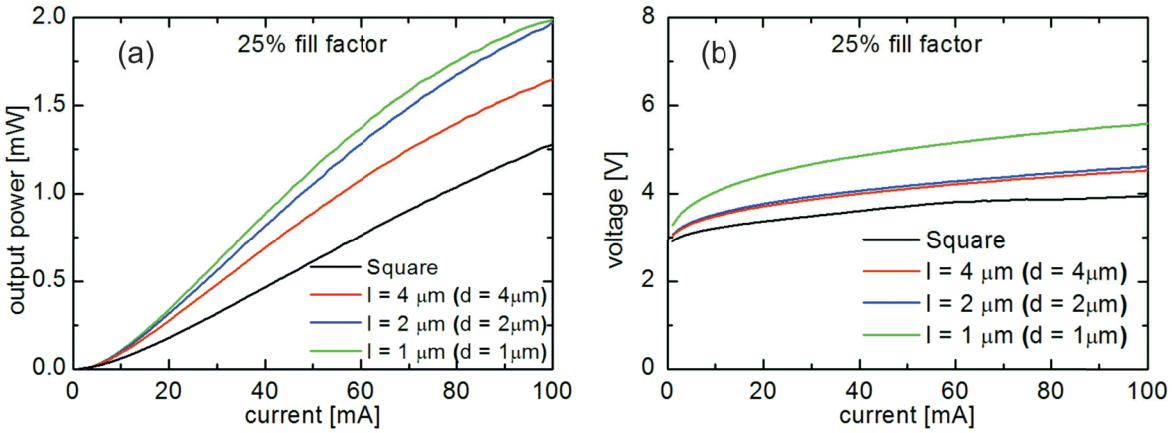

Figure 7.9: (a) L-I characteristics, measured on wafer, of nanopixel 390 nm AlInGaN LEDs with (i) square contact ($150 \times 150\,\mu m^2$) (ii) nanopixel size = $4 \times 4\,\mu m^2$, nanopixel spacing $4\,\mu m$ (iii) nanopixel size = $2 \times 2\,\mu m^2$, nanopixel spacing $2\,\mu m$ and (iv) nanopixel size = $1 \times 1\,\mu m^2$, nanopixel spacing $1\,\mu m$ [187]. Mesa area is kept constant at $160 \times 160\,\mu m^2$. (b) V-I characteristics, measured on wafer, for the structures (i-iv) [187].

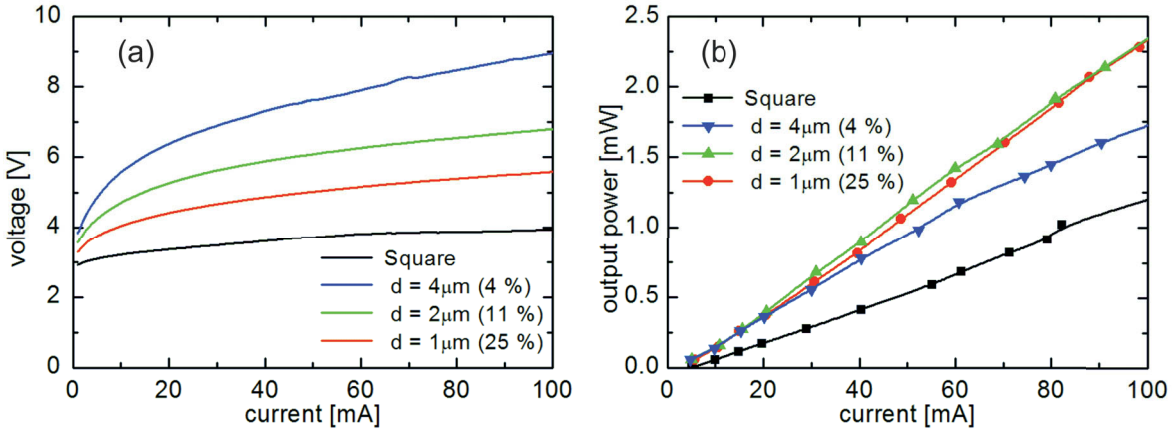

Figure 7.10: (a) DC V-I characteristics, measured on wafer, of nanopixel 390 nm AlInGaN LEDs with nanopixel size of $1 \times 1\,\mu m^2$ and nanopixel spacing (i) $4\,\mu m$ (ii) $2\,\mu m$ (iii) $1\,\mu m$ and (iv) square contact ($150 \times 150\,\mu m^2$) [187]. Mesa area is kept constant at $160 \times 160\,\mu m^2$. (b) Pulsed L-I characteristics, measured on wafer, for the structures (i-iv) [187]. Pulse width of $1.5\,\mu s$ and a 0.15 % duty cycle.

To study the influence of the fill factor on the output power of the LEDs, nanopixel LEDs with a fixed nanopixel size of $1 \times 1\,\mu\text{m}^2$ and with nanopixel spacing 4, 2 and 1 μm along with a conventional $150 \times 150\,\mu\text{m}^2$ square contact LED were compared. This corresponds to filling factors of 4, 11, 25 and 100 % respectively. The forward voltage increases as the spacing between the nanopixels increases due to the decrease in the effective total p-ohmic contact area (Fig. 7.10 a) resulting in dissimilar levels of heating in the different LEDs. Hence, for comparison between the devices, L-I characteristics were measured under pulsed conditions as shown in Fig. 7.10 b. For a pulse width of 1.5 μs and a 0.15 % duty cycle, at 20 mA, the nanopixel LEDs with fill factors 4, 11 and 25 % show a 101, 114 and 103 % increase in the output power respectively compared to the conventional square contact. For nanopixel LEDs with different fill factors, the light output could increase due to the following reasons:

1. increase in current density (at low currents) resulting in higher IQE,
2. enhanced reflection at the Al reflector along the increased perimeter of the p-contact and
3. enhanced reflection at the Al reflector due to current overlap in the region between the nanopixels.

At high currents the nanopixel LEDs with spacing of 2 and 1 μm show a larger output than the LED with spacing of 4 μm. This effect could be an indication that current overlap and concurrently enhanced light reflection at the Al reflector occurs for the LEDs with smaller nanopixel spacing at high currents. It can be seen from Fig. 7.10, that the nanopixel LED with spacing of 1 μm results in the highest conversion efficiency considering that its operating voltage is the lowest of all nanopixel LEDs. The maximum wall plug efficiencies of the nanopixel LEDs with fill factors 4, 11 and 25 % and the large area square contact are determined to be 0.25 %, 0.39 %, 0.46 % and 0.34 % respectively.

The three-dimensional current spreading in an UV LED, emitting at 380 nm, was simulated, using the SpeCLED software package [38], to get a deeper understanding of the working of the LEDs with nanopixel contacts. The room temperature material properties used in the simulation of the LEDs emitting at 380 nm were as follows: thicknesses of GaN:Mg and GaN:Si were $t_p = 0.2\,\mu$m and $t_n = 1.7\,\mu$m; electron and hole concentrations were $n = 1.5 \times 10^{18}\,\text{cm}^{-3}$ and $p = 1 \times 10^{17}\,\text{cm}^{-3}$; mobilities of holes and electrons were $\mu_p = 10\,\text{cm}^2/\text{Vs}$ and $\mu_n = 263\,\text{cm}^2/\text{Vs}$; specific contact resistance to GaN:Mg and GaN:Si were $10^{-2}\,\Omega\text{cm}^2$ and $10^{-4}\,\Omega\text{cm}^2$. Keeping the nanopixel size constant at $1 \times 1\,\mu\text{m}^2$ and varying the nanopixel spacing from 1 to 4 μm, current spreading in the 200 nm thick p-GaN layer was investigated. Fig. 7.11 shows the simulated current density injected in the active region. For a nanopixel spacing of 4 μm, the density of the current injected in the region exactly in the middle of the imaginary line joining two neighboring pixels is 13 A/cm^2, indicating that there is no current overlap in the region between the pixels. The injected current between the nanopixels is too low for efficient light emission. The ratio (r) of the current density injected in the middle of two neighboring pixels to that in the center of the nanopixel

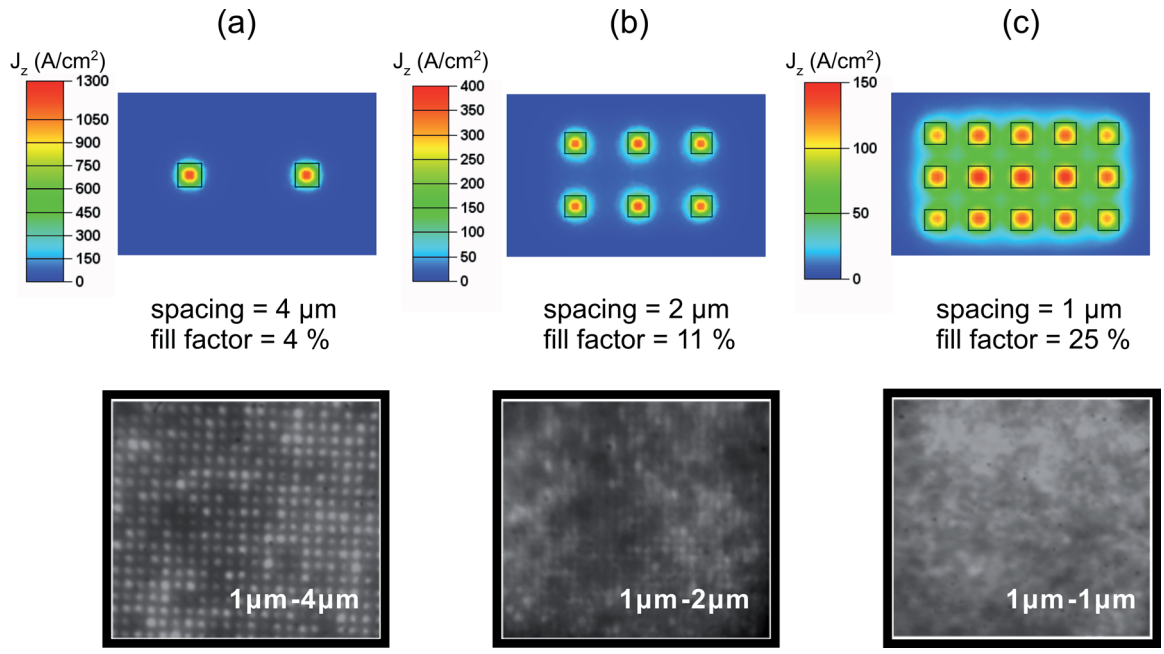

Figure 7.11: Above: Simulation of the current injection in the active region for nanopixel contacts 380 nm AlInGaN LEDs with nanopixel size $1 \times 1\,\mu m^2$ and nanopixel spacing (a) $4\,\mu$m, (b) $2\,\mu$m and (c) $1\,\mu$m. The total current is constant at 20 mA. Below: Optical microphotographs of the nanopixel AlInGaN LEDs with nanopixel size $1 \times 1\,\mu m^2$ and nanopixel spacing (a) $4\,\mu$m, (b) $2\,\mu$m and (c) $1\,\mu$m at 15 mA total current. Mesa area is kept constant at $160 \times 160\,\mu m^2$.

is ~ 0.01. As the spacing is decreased to $2\,\mu$m some current overlap can be observed. The minimum current density injected in the region between the nanopixels is $36\,A/cm^2$ while r increases to ~ 0.1. For a nanopixel spacing of $1\,\mu$m, the minimum current injected in the region between the nanopixels is $73\,A/cm^2$ and r is ~ 0.53. This strong overlap of the current in the region between the nanopixels results in emission from the entire active region. Hence a $1\,\mu$m or less spacing between nanopixels is required to obtain light emission from the entire region.

Optical microphotographs of the nanopixel LEDs, at a total current of 15 mA, were taken from the polished back surface of the sapphire (Fig. 7.11 – 7.12). The resolution of the setup was 420 nm. For the LED with nanopixel size of $4 \times 4\,\mu m^2$, no light is emitted in the region between the contacts demonstrating that a distance of $4\,\mu$m is too large for significant current overlap. In addition, the area from which light is emitted is larger than that of the nanopixels indicating that due to current spreading in the p-GaN layer, light is also emitted in the region surrounding the nanopixels. Reflection from the Al layer results in increased intensity observed at the edges of the nanopixels Fig. 7.12. The emission images (Fig. 7.11) of the LEDs with constant nanopixel size of $1 \times 1\,\mu m^2$ and varying the nanopixel spacing from 1 to $4\,\mu$m show that for nanopixel spacing of 4 and $2\,\mu$m no light is emitted in the area between the nanopixels while for the LED with nanopixel spacing of $1\,\mu$m, the entire active

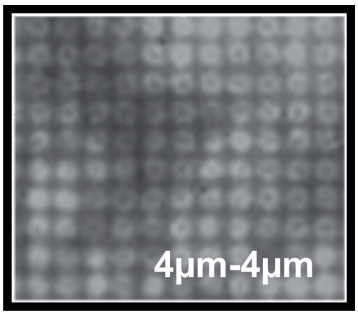

Figure 7.12: Optical microphotographs of a nanopixel contact AlInGaN LED with nanopixel size $4 \times 4\,\mu\text{m}^2$ and nanopixel spacing $4\,\mu\text{m}$ at 15 mA total current. The bright ring around the nanopixel contact is a result of the increased light extraction at the edges due to reflection at the Al reflector.

region appears to emit light. This compares well with the result obtained from simulations, that nanopixel spacing (d) of 1 μm or less is necessary for current overlap.

The experimental data confirms that the nanopixel contact LED design can be used to enhance the LEE of UV LEDs. For the design to be efficient, i.e. current is injected homogeneously in the entire active region, it is necessary for the spacing between the pixels to be less than 1 μm.

7.5 Fabrication of nanometer size contacts

To maximize the LEE of UV LEDs with the use of nanopixel contact LED design, it is necessary to minimize the fill factor. From both theoretical predictions and experimental results, a maximum spacing of 1 μm between the nanopixels contacts is required for light to be generated in the region between the contacts. Hence to obtain a fill factor of less than 25 %, nanopixel contacts smaller than $1 \times 1\,\mu\text{m}^2$ are required. The crucial step in the fabrication of LEDs with nanopixel contacts is the structuring of the contacts. Due to the nanometer dimensions of the contacts, the fabrication process becomes complex and care must be taken to ensure that the contacts can be electrically connected. In this work a method to fabricate 30 nm thick Pd nanopixel contacts with sizes $500 \times 500\,\text{nm}^2$ and less was developed. The process flow for the fabrication of Pd nanopixel contacts is shown in Fig. 7.13.

The use of e-beam lithography was investigated for the fabrication of Pd nanopixel contacts with sizes ranging from 100×100 to $500 \times 500\,\text{nm}^2$ and a constant spacing of 500 nm. A spacing of 500 nm was taken to ensure that current overlap between the pixels is obtained even at low operational currents. A 100 nm thick resist layer (AZ nLOF 2035[1]) was used as a mask and the e-beam doses required for the patterning of the nanostructures are shown in Table 7.1. Rounding of the edges were observed for the small contacts of size $100 \times 100\,\text{nm}^2$ (Fig. 7.14 a). As the nanopixels have a spacing of only 500 nm, the proximity effect must be taken into consideration during e-beam direct writing. Proximity effect in e-beam lithography is the phenomenon in which blurring of the energy distribution takes place mainly due to forward and backward electron scattering in the resist and substrate. Due to the proxim-

[1] produced by MicroChemicals GmbH

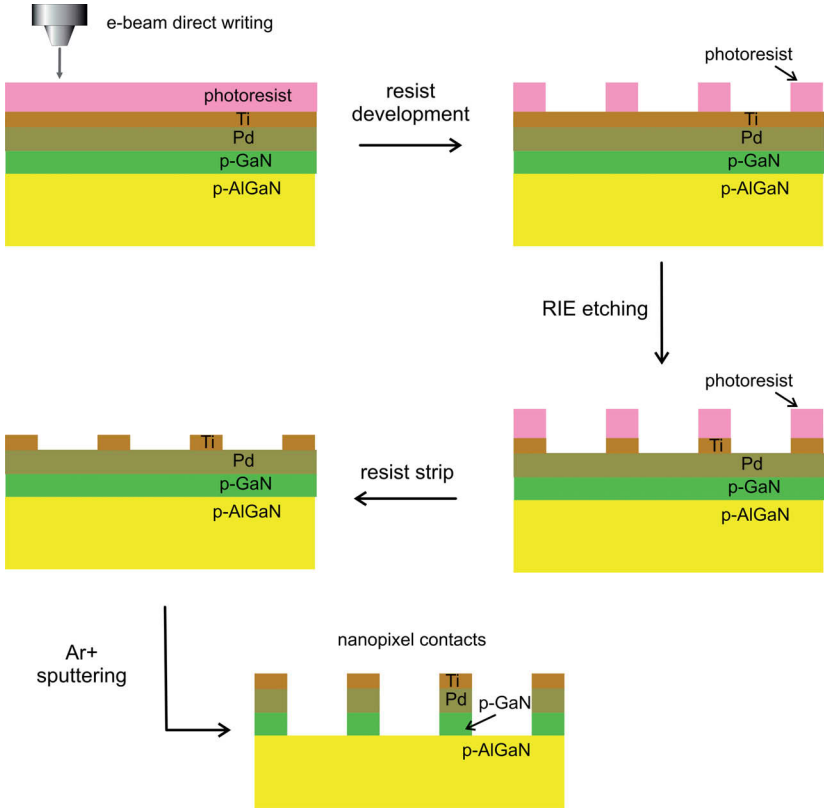

Figure 7.13: Schematic of fabrication of Pd nanopixel LED contacts using e-beam lithography.

Table 7.1: Required e-beam doses for the transfer of a nanopixel contact layout to a 100 nm thick AZ nLOF 2035 photoresist layer. The size of the structures obtained after e-beam lithography are compared to the size defined in the CAD mask layout.

Length of nanopixel in mask layout	Electron dose	Measured length of nanopixel
100 nm	150 μC	113 nm
200 nm	130 μC	205 nm
300 nm	110 μC	308 nm
400 nm	90 μC	405 nm
500 nm	80 μC	509 nm

ity effect, the pixels at the edges of the mesa structure are weakly defined as compared to those in the center (Fig. 7.14 b). To obtain a homogeneous pattern across the entire mesa structure, the proximity effect can be precompensated with the use a proximity correction scheme based on the modification of the e-beam dose. In this scheme a different dose is applied to each pixel to compensate for the proximity effect. The correction requires an accurate knowledge of the energy deposited in the resist by the e-beam writer which is described by the proximity function. The function is modelled as a sum of two Gaussian terms; one representing the short range effect due to forward scattering and the other representing the long range effect due to backscattered electrons (Eqn. 7.3).

$$f(r) = \frac{1}{\pi(1+\eta)}\frac{1}{\alpha^2}e^{-\frac{r^2}{\alpha^2}} + \frac{\eta}{\beta^2}e^{-\frac{r^2}{\beta^2}} \tag{7.3}$$

α is the forward scattering range parameter, β is the backscattering range parameter, η is the ratio of backscattered energy to forward scattered energy and r is the distance from the point of electron incidence. The parameters α, β and η are dependent on the resist–substrate system and the energy of the beam. The proximity correction is related to the deconvolution of the desired result and the proximity function [188]. For the system under investigation, the values for α, β and η were found to be 450, 3600 and 5 respectively [189].The commercial software package *PROXECCO*[2] was used to calculate the required doses for proximity correction. A homogeneous nanopixel contact pattern was obtained across the entire mesa structure with the use of the proximity correction during e.beam writing (Fig. 7.14 b).

Wet chemical etching using a solution of *Aqua regia*[3] or sputtering by bombardment with Ar+ ions can be used for the structuring of the 30 nm thick Pd layer. Due to strong underetching and the small dimensions of the nanopixels, wet etching results in the complete removal of the Pd layer. Hence the Pd layer was patterned by sputtering using Ar+ ions. It is also possible to etch off the thin (40 nm), absorbing p-GaN contact layer between the nanopixel contacts by increasing the sputtering time. During the sputtering process, the sputtered Pd and p-GaN material is redeposited on the sides of the etching mask (Fig 7.15) forming insulating side walls, i.e. no current could be injected into the contacts. The height

[2]Proximity Effect Correction Software by *Vistec Electron Beam GmBH*, Jena, Germany

[3]also know as nitric acid hydrochloride (HNO_3 + 3 HCl (1:3)) which is a highly corrosive mixture of acids

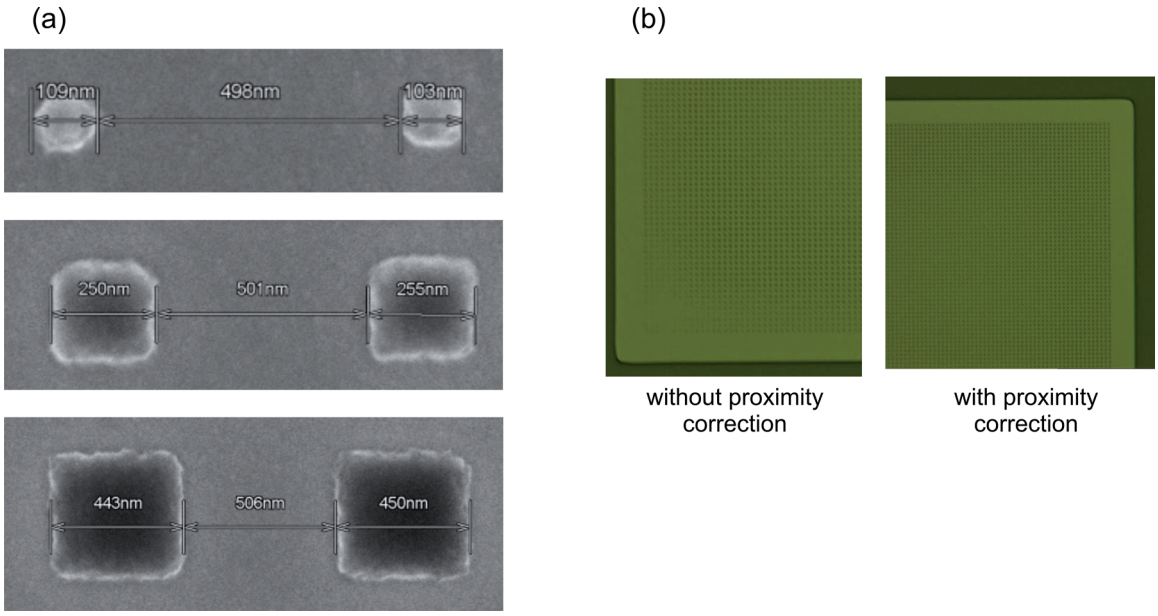

Figure 7.14: (a) SEM images of a 100 nm AZ nLOF 2035 photoresist layer patterned into nanopixel contacts using e-beam lithography. (b) Comparison of the transfer, using e-beam lithography, of the nanopixel contact layout to a 100 nm AZ nLOF 2035 photoresist layer with and without the use of e-beam proximity correction. With the use of the proximity correction a homogeneous array of nanopixel contacts are obtained even at the edges of the mesa structure.

of these redeposition walls was found to be proportional to the height of the etch mask. Further more the side walls impede the complete removal of the etch mask preventing electrical contact to the nanopixels in the case of an insulating mask (e.g. photoresist, SiN). To circumvent this problem, the use of Ti as a mask for the sputtering of Pd was investigated. As the sputter rate for Ti is 2 nm/min as compared to 8 nm/min for Pd and 6 nm/min for GaN, a 20 nm thick Ti layer is sufficient as a hard mask for the patterning of a 30 nm Pd and 40 nm p-GaN layer. Due to the electrical conductivity of the Ti mask, removal of the mask after etching is not necessary for the electrical contact to the nanopixels. The 20 nm Ti layer was structured using e-beam lithography and reactive ion etching (RIE) with an SF_6 based recipe. SEM images show that with the use of the Ti hard mask, for the patterning of the Pd nanopixels, no redeposition wall formation is observed (Fig 7.15). The Pd nanopixel contacts, which are electrically connectable, can thus be successfully fabricated using a Ti hard mask.

Using the process described above, it is possible to fabricate nanopixel contacts with sizes less than $500 \times 500\,\mathrm{nm}^2$. The complete LED fabrication can be achieved by integrating the nanopixel contacts fabrication step in the standard LED processing technology (Sec. 2.2). The fabrication of the complete LED structure was out of the scope of this thesis.

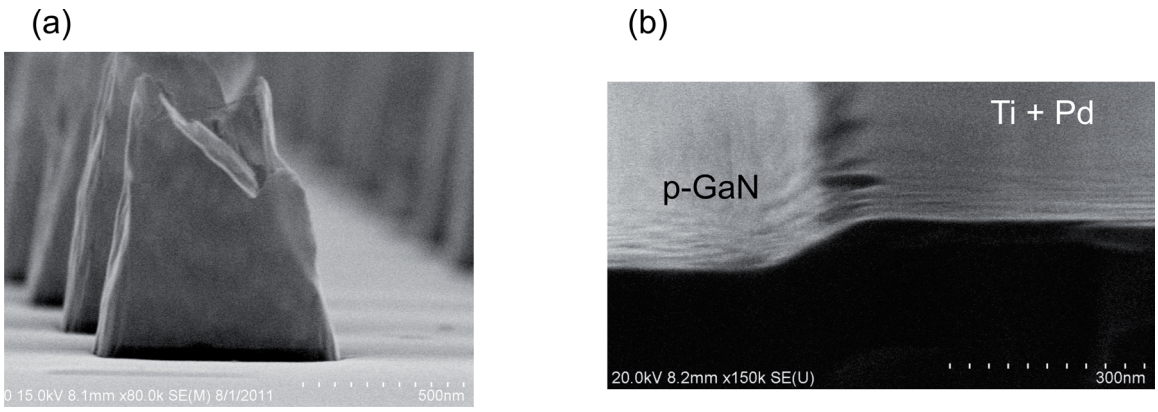

Figure 7.15: Cross-sectional SEM images of a Pd nanopixel contact, after resist stripping, patterned using sputtering by bombardment with Ar+ ions and (a) a 1.1 μm photoresist mask and (b) a 20 nm thick Ti hard mask. Electrically insulating redeposition walls are observed when using a thick photoresist mask. No walls were observed in the case of a Ti mask.

7.6 Summary

A novel nanopixel contact LED design, consisting of nanopixel contacts of a low resistivity ohmic p-contact material combined with a metal reflector, which results in enhanced light extraction in UV LEDs was demonstrated. A 90 % increase in the light output power of a 390 nm AlInGaN LED was shown for nanopixel LEDs with a nanopixel size of $1 \times 1\,\mu\text{m}^2$ and spacing of 1 μm as compared to the conventional square contact geometry under dc conditions. To optimize the efficiency of the nanopixel contact design

1. the spacing between the nanopixels should be less than twice the current spreading length of the p-cladding layer

2. and the width of the nanopixel contact should be less than the nanopixel spacing.

In the case of a 200 nm thick p-AlGaN layer, due to the large sheet resistance of the layer, a nanopixel spacing of less than 1 μm is required. Accordingly, for AlInGaN UV LEDs the nanopixel contact size should be less than $1 \times 1\,\mu\text{m}^2$. To achieve these small dimensions, a method using e-beam lithography to fabricate Pd nanopixel contacts with dimensions done to 100 nm has been presented. In the deep UV region, where transparent or reflective ohmic contacts are difficult to fabricate, the nanopixel contact design will be an excellent technique to enhance light extraction.

8 Summary and outlook

The goal of this work was the design and fabrication of highly efficient III-nitride based UV LEDs to be used in various applications such as water disinfection, sensors and UV printing. As a result, this work focussed on the designing of chip geometries that not only improved the electrical characteristics of the LED but also increased the light extraction efficiency (LEE) of the devices.

The first step in designing an efficient LED chip geometry is identifying the physical parameters that affect the performance of the device. Three factors, namely the current density dependence of the IQE, the temperature of the device and the phenomenon of current crowding in lateral geometry LEDs, were determined to be the key parameters that should be considered when designing the LED chip layout. In the case of UV LEDs, a strong dependence of the IQE on the current density was observed. Due to the high defect densities of the structure, the Shockley-Read-Hall (SRH) non-radiative recombination of carriers is dominant at low current densities resulting in low IQE values. On the other hand, at high current densities an efficiency droop was observed which may be attributed to the Auger recombination of carriers or the leakage of carriers from the quantum wells. When designing an LED chip it is necessary to consider the current at which the LED will be operated for the desired application. The size of the active region must then be chosen to ensure that the maximum in the IQE is achieved for the resulting current density.

The temperature of the LED during operation was identified as the second critical factor for the device performance. A *temperature droop* i.e. a strong decrease in the output power at high temperatures was observed for UV LEDs. This temperature sensitivity of the device was defined by the characteristic temperature (T_c). The T_c of a UV LED was found to be dependent on the current density. The output power was very sensitive to the temperature at low current densities with T_c ranging between 48 K and 69 K at 9 A/cm^2 for 380 nm LEDs. At these low current densities the defect density of the template plays an important role in the temperature stability of the device due to the increased SRH recombination at elevated temperatures. As the current density increased, a smaller dependence of the output power on the temperature was observed which was attributed to the saturation of the SRH recombination channels. T_cs as high as 207 K were obtained for 380 nm LEDs with a current density of 1 kA/cm^2. Thermally activated carrier leakage from the quantum wells was identified as the main reason for the decrease in the output power at these high current densities. Hence improved confinement of the carriers with the use of barriers with larger Al content is necessary to improve the temperature stability of the LED at high current densities. The investigation of the temperature dependence of the LED performance further emphasized the importance of designing UV LED chips with minimal self heating and low thermal resistances.

Finally, the current crowding in lateral geometry UV LEDs was investigated to determine the effectively used area of the active region. With the help of simulations, it was shown that current crowding is a serious issue for UV LEDs due to the high sheet resistance of the n-current spreading layer. To obtain uniform current injection in the active region, the width of the mesa should be less than twice the current spreading length. In this work the current spreading length was calculated for different combinations of the n-current spreading layer sheet resistance and the specific contact resistance of the p-ohmic contact to be used as a guideline for designing UV LED chip layouts.

The use of interdigitated finger contacts and micro-LED arrays as efficient UV LED chip geometries was proposed and investigated based on the previous results. These geometries provide uniform current injection when the finger width or the micro-LED size is chosen to be less than twice the current spreading length. This not only ensures a lower current density but also decreases the series resistance of the device as compared to a conventional large area square contact. The increased mesa perimeter also contributes to a reduction in the series resistance of the LED. UV LEDs with these geometries were shown to have a higher wall plug efficiency as well as reduced self heating due to the lower series resistance of the device. In the case of high power UV LEDs the benefits of using micro-LED arrays was investigated. Due to the distribution of the heat source across the chip and the presence of free area for heat dissipation, a greater than two-fold decrease in the thermal resistance of UV LEDs with micro-LED arrays as compared to conventional large area square contacts was obtained. However, the use of this geometry reduces the useful die area. Hence a method to determine the optimum size of the micro-LED array for a fixed chip area was presented in this work.

The second part of this thesis focussed on the issue of light extraction from UV LEDs. The main reasons for the difficulties in exacting the light generated in the LED are the high refractive indices of the semiconductors and the sapphire substrate, the absence of transparent or reflective p-ohmic contacts and the polarization of the light emitted from the active region.

Due to the anisotropy along and perpendicular to the c-axis of the wurtzite crystal structure of III-nitrides, a crystal field splitting of the three valence subbands occurs at the Γ point. The more ionic nature of AlN results in a negative crystal field splitting instead of positive as in the case of GaN. The different ordering of the valence subbands gives rise to polarization of the optical emission along the direction of $E \perp c$ ($E||c$) in GaN (AlN) layers grown along the c-axis. In AlGaN alloys as the concentration of Al increases, the polarization of the emitted light changes from mainly TE polarized to mainly TM polarized. The critical Al concentration at which the switch in polarization occurs can be controlled by changing the strain, quantum confinement and the orientation of the substrate. TE polarized light can be easily extracted from the top or bottom surfaces of an LED as the light is emitted at small angles w.r.t. the c-axis. On the other hand, TM polarized light is trapped in the LED as most of the light is emitted at large angles w.r.t. the c-axis. Simulations showed that the LEE of a UV LED decreased from 12 % for TE polarized light to 3 % for TM polarized light. Thus, in the case of deep UV LEDs, with large Al contents in the quantum wells, it is necessary to develop techniques to extract the light with is emitted at large angles.

To enhance the LEE of UV LEDs, the encapsulation of the devices, the texturing of the substrate back-surface and the use of nanopixel LED contacts was investigated in this work.

UV LEDs were flip-chip mounted on AlN submounts to improve the LEE and to reduce the thermal resistance of the devices. To complete the package, the use of Polydimethylsiloxane (PDMS) as an efficient and stable encapsulatant for UV LEDs was proposed and demonstrated. A 2-fold increase in the output power of 380 nm LEDs was obtained with the use of PDMS as an encapsulant.

Texturing the back-surface of the substrate was show, with the help of simulations and experiments, to increase the LEE of UV LEDs. A (16±7) % increase in the output power of 323 nm LEDs was demonstrated by mechanically roughening the smooth sapphire substrate back-surface. To further enhance the LEE, the use of patterned arrays of micro-cylinders, micro-frustums and micro-lenses etched in the substrate back-surface was proposed. Simulations showed that a greater than 50 % increase in the output power can be achieved with high coverage areas of shallow etched ($<5\,\mu$m) micro-structures on the substrate back-surface. The maximum increase in the LEE with the use of micro-cylinders, micro-frustums and micro-lenses, for 320 nm LEDs with an absorbing p-side and an n-ohmic metal contact reflectivity of 0.65, was calculated to be 26 %, 71 % and 68 % respectively. A technique to fabricate these structures in sapphire or GaN, using ICP etching, was developed in this work. A (20 ±7) % increase in the output power of LEDs emitting at 323 nm was obtained with the use of micro-frustums.

Simulations were further used to investigate the influence of the reflectivity of the ohmic metal contacts on the LEE of UV LEDs. For a LED with smooth surfaces, the LEE was greatly increased with the use of reflective p-ohmic metal contacts. The reflectivity of the n-ohmic metal contact was found to have only a minor influence on the LEE of the LED. In contrast, for LEDs with micro-structures etched in the substrate back-surface, the reflectivity of the n-ohmic metal contact greatly influenced the observed enhancement in the LEE of the LEDs. Hence to fabricate UV LEDs with high LEEs it is crucial that the p-side is transparent and both the p- and n-ohmic contacts are highly reflective.

A novel nanopixel contact LED design, consisting of nanopixel contacts of a low resistivity ohmic p-contact material combined with a metal reflector, was proposed to circumvent the problems in obtaining highly reflective or transparent p-ohmic contacts to p-doped AlGaN layers. A 90 % increase in the light output power of a 390 nm AlInGaN LED was demonstrated for nanopixel LEDs with a nanopixel size of $1 \times 1\,\mu\text{m}^2$ and spacing of $1\,\mu$m as compared to the conventional square contact geometry under dc conditions. To optimize the efficiency of the nanopixel contact design the spacing between the nanopixels should be less than twice the current spreading length of the p-cladding layer and the width of the nanopixel contact should be less than the nanopixel spacing. In the case of a 200 nm thick p-AlGaN layer, due to the large sheet resistance of the layer, a nanopixel spacing of less than $1\,\mu$m is required. Hence, for AlInGaN UV LEDs the nanopixel contact size should be less than $1 \times 1\,\mu\text{m}^2$. To achieve these small dimensions, a method using e-beam lithography to fabricate Pd nanopixel contacts with dimensions down to 100 nm was developed. The use of the nanopixel contact LED design can also be extended to fabricate reflective n-contacts to increase the LEE of UV LEDs.

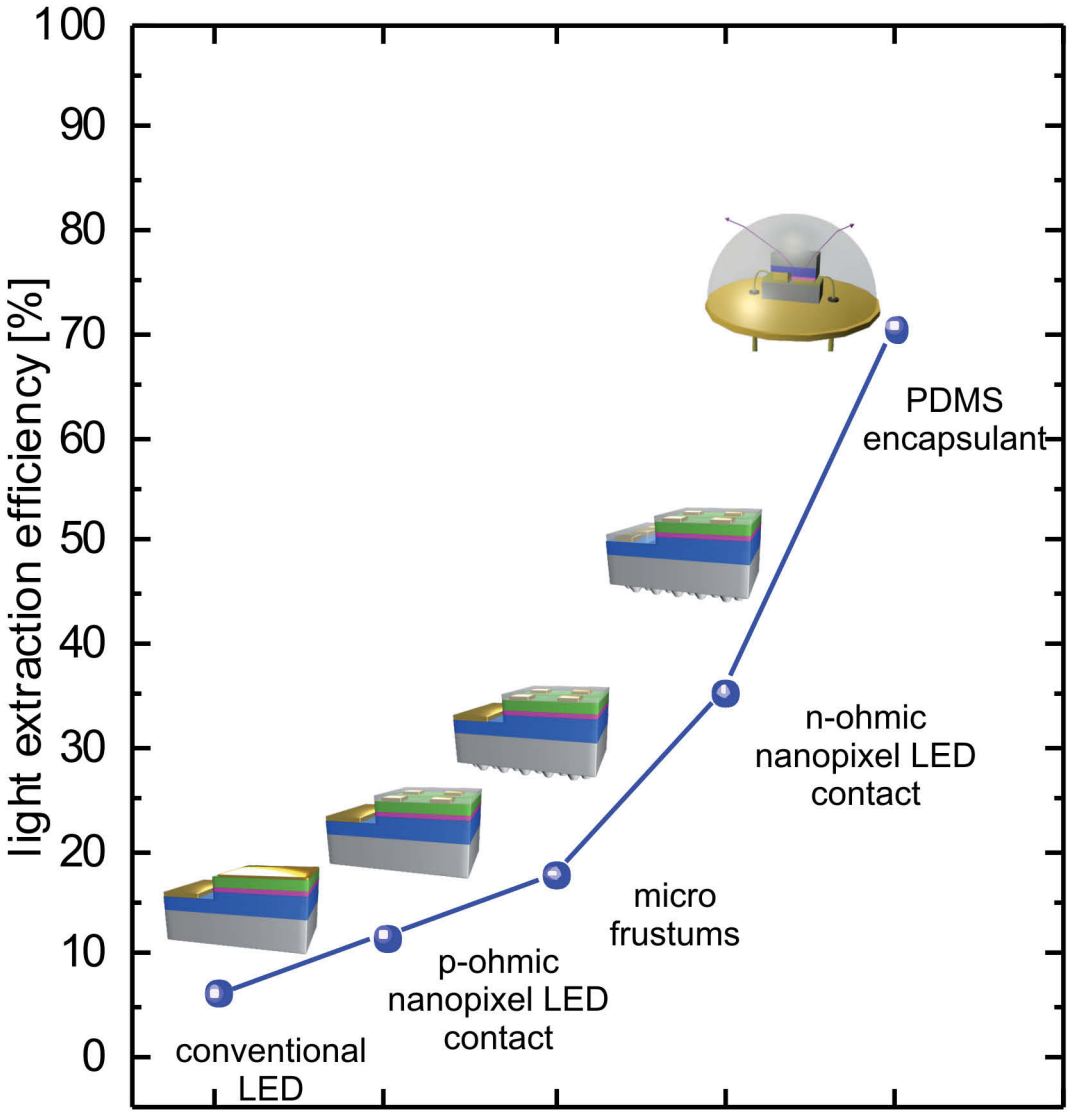

Figure 8.1: Estimated light extraction efficiency of a 320 nm LED with the use of the techniques investigated in this thesis.

All the techniques to increase the LEE of UV LEDs investigated in this work can be technologically combined to realise highly efficient UV LEDs. In the case of a 320 nm LED with micro-LED array geometry flip-chip mounted on an AlN submount, a LEE of 70 % can be achieved with the use of reflective nanopixel contacts for the both the p- and n-ohmic contacts, patterning of the substrate back-surface and encapsulation using PDMS (Fig. 8.1).

While a number of techniques to increase the efficiency of UV LEDs have been discussed in this work, many more techniques need to be investigated for further development of the devices. One of the very important technologies that needs to be developed is the laser lift-off of the sapphire substrate. This technique will not only increase the LEE of the LEDs, as now shaping of the LED geometry will be easier, but will also allow the fabrication of vertical UV LEDs which are less tedious to package. Another promising technique, is the growth of UV LEDs on patterned sapphire substrates (pss). The growth on pss is expected to reduce the defect densities and hence increase in the IQE of the LEDs. Furthermore, the patterned sapphire at the heterostructure–substrate interface will scatter the light resulting in an increase in the LEE of the UV LEDs. Similarly the growth of UV-C LEDs on free standing AlN substrates will improve the overall efficiency of the LEDs. In particular due to the strain in the active layers grown on AlN substrates, the light emitted from the active region will still be mainly TE polarized even at short wavelengths resulting in higher LEE of the LEDs. In the future, in order for UV LEDs to enter the market, the packaging of the devices will also be an important research topic. AlN heat sinks capable of handling the large amounts of heat generated in UV LEDs need to be developed. Understandably, the development of UV encapsulants and UV transparent packaging optics will also be a focus of research and development.

The work done in this thesis has contributed to the development of highly efficient UV-B LEDs with one of the highest EQEs (2 %) and lifetimes ($L_{50} > 10000$ hours) worldwide. Due to the large potential market for these devices, the Technische Universität Berlin and the Ferdinand-Braun-Institut Leibniz-Institut für Höchstfrequenztechnik received the *EXIST Transfer of Research* grant[1] in April 2014 to commercialize the UV LEDs through the establishment of the spin-off *UVphotonics*.

[1] Federal Ministry of Economics and Energy (BMWi)

Bibliography

[1] LEDinside, "2015 LED Demand and Supply Market Outlook." http://www.ledinside.com, Dec. 2014.

[2] N. Tansu and L. J. Mawst, "Current injection efficiency of InGaAsN quantum-well lasers," *Journal of Applied Physics*, vol. 97, no. 5, p. 054502, 2005.

[3] Y. Muramoto, M. Kimura, and S. Nouda, "Development and future of ultraviolet light-emitting diodes: UV-LED will replace the UV lamp," *Semiconductor Science and Technology*, vol. 29, no. 8, p. 084004, 2014.

[4] H. Hirayama, N. Maeda, S. Fujikawa, S. Toyoda, and N. Kamata, "Recent progress and future prospects of AlGaN-based high-efficiency deep-ultraviolet light-emitting diodes," *Japanese Journal of Applied Physics*, vol. 53, no. 10, p. 100209, 2014.

[5] J. Rass, T. Kolbe, N. Lobo-Ploch, T. Wernicke, F. Mehnke, C. Kuhn, J. Enslin, M. Guttmann, C. Reich, A. Mogilatenko, J. Glaab, C. Stölmacker, M. Lapeyrade, S. Einfeldt, M. Weyers, and M. Kneissl, "High-power UV-B LEDs with long lifetime," *Proc. SPIE*, vol. 9363, pp. 93631K–93631K–13, 2015.

[6] M. Kneissl, F. Mehnke, C. Kuhn, C. Reich, M. Guttmann, J. Enslin, T. Wernicke, A. Knauer, V. Kueller, U. Zeimer, M. Lapeyrade, J. Raß, N. Lobo-Ploch, T. Kolbe, J. Glaab, S. Einfeldt, and M. Weyers, "Deep Ultraviolet LEDs: from materials research to real-world applications." IEEE Photonics Society Summer Topical Meeting Series, 2015. Accepted for publication.

[7] I. Akasaki, H. Amano, Y. Koide, K. Hiramatsu, and N. Sawaki, "Effects of AlN buffer layer on crystallographic structure and on electrical and optical properties of GaN and $Ga_{1-x}Al_xN$ ($0<x\leq 0.4$) films grown on sapphire substrate by MOVPE ," *Journal of Crystal Growth*, vol. 98, no. 1-2, pp. 209 – 219, 1989.

[8] S. Nakamura, "GaN Growth Using GaN Buffer Layer," *Japanese Journal of Applied Physics*, vol. 30, no. 10A, p. L1705, 1991.

[9] T. Mukai, S. Nagahama, N. Iwasa, M. Senoh, and T. Yamada, "Nitride light-emitting diodes," *Journal of Physics: Condensed Matter*, vol. 13, no. 32, p. 7089, 2001.

[10] H. Hirayama, S. Fujikawa, N. Noguchi, J. Norimatsu, T. Takano, K. Tsubaki, and N. Kamata, "222-282 nm AlGaN and InAlGaN-based deep-UV LEDs fabricated on

high-quality AlN on sapphire," *physica status solidi (a)*, vol. 206, no. 6, pp. 1176–1182, 2009.

[11] S. Y. Karpov and Y. N. Makarov, "Dislocation effect on light emission efficiency in gallium nitride," *Applied Physics Letters*, vol. 81, no. 25, pp. 4721–4723, 2002.

[12] M. Kneissl, T. Kolbe, C. Chua, V. Kueller, N. Lobo, J. Stellmach, A. Knauer, H. Rodriguez, S. Einfeldt, Z. Yang, N. M. Johnson, and M. Weyers, "Advances in group III-nitride-based deep UV light-emitting diode technology," *Semiconductor Science and Technology*, vol. 26, no. 1, p. 014036, 2011.

[13] Z. Yu, M. Johnson, J. Brown, N. El-Masry, J. Cook-Jr, and J. Schetzina, "Study of the epitaxial-lateral-overgrowth (ELO) process for GaN on sapphire ," *Journal of Crystal Growth*, vol. 195, no. 1-4, pp. 333 – 339, 1998.

[14] J. P. Zhang, H. M. Wang, M. E. Gaevski, C. Q. Chen, Q. Fareed, J. W. Yang, G. Simin, and M. A. Khan, "Crack-free thick AlGaN grown on sapphire using AlN/AlGaN superlattices for strain management," *Applied Physics Letters*, vol. 80, no. 19, pp. 3542–3544, 2002.

[15] V. Kueller, A. Knauer, C. Reich, A. Mogilatenko, M. Weyers, J. Stellmach, T. Wernicke, M. Kneissl, Z. Yang, C. Chua, and N. Johnson, "Modulated Epitaxial Lateral Overgrowth of AlN for Efficient UV LEDs," *Photonics Technology Letters, IEEE*, vol. 24, no. 18, pp. 1603–1605, 2012.

[16] T. Takano, Y. Narita, A. Horiuchi, and H. Kawanishi, "Room-temperature deep-ultraviolet lasing at 241.5 nm of AlGaN multiple-quantum-well laser," *Applied Physics Letters*, vol. 84, no. 18, pp. 3567–3569, 2004.

[17] O. Ambacher, J. Majewski, C. Miskys, A. Link, M. Hermann, M. Eickhoff, M. Stutzmann, F. Bernardini, V. Fiorentini, V. Tilak, B. Schaff, and L. F. Eastman, "Pyroelectric properties of Al(In)GaN/GaN hetero- and quantum well structures," *Journal of Physics: Condensed Matter*, vol. 14, no. 13, p. 3399, 2002.

[18] A. Knauer, H. Wenzel, T. Kolbe, S. Einfeldt, M. Weyers, M. Kneissl, and G. Tränkle, "Effect of the barrier composition on the polarization fields in near UV InGaN light emitting diodes," *Applied Physics Letters*, vol. 92, no. 19, p. 191912, 2008.

[19] M. Katsuragawa, S. Sota, M. Komori, C. Anbe, T. Takeuchi, H. Sakai, H. Amano, and I. Akasaki, "Thermal ionization energy of Si and Mg in AlGaN," *Journal of Crystal Growth*, vol. 189-190, no. 0, pp. 528 – 531, 1998.

[20] K. B. Nam, M. L. Nakarmi, J. Li, J. Y. Lin, and H. X. Jiang, "Mg acceptor level in AlN probed by deep ultraviolet photoluminescence," *Applied Physics Letters*, vol. 83, no. 5, pp. 878–880, 2003.

[21] T. Kinoshita, T. Obata, H. Yanagi, and S. Inoue, "High p-type conduction in high-Al content Mg-doped AlGaN," *Applied Physics Letters*, vol. 102, no. 1, p. 012105, 2013.

[22] F. Mehnke, C. Kuhn, J. Stellmach, T. Kolbe, N. Lobo-Ploch, J. Rass, M.-A. Rothe, C. Reich, N. Ledentsov, M. Pristovsek, T. Wernicke, and M. Kneissl, "Effect of heterostructure design on carrier injection and emission characteristics of 295 nm light emitting diodes," *Journal of Applied Physics*, vol. 117, no. 19, p. 195704, 2015.

[23] S. Sumiya, Y. Zhu, J. Zhang, K. Kosaka, M. Miyoshi, T. Shibata, M. Tanaka, and T. Egawa, "AlGaN-Based Deep Ultraviolet Light-Emitting Diodes Grown on Epitaxial AlN/Sapphire Templates," *Japanese Journal of Applied Physics*, vol. 47, no. 1R, p. 43, 2008.

[24] Z. Gong, M. Gaevski, V. Adivarahan, W. Sun, M. Shatalov, and M. Asif Khan, "Optical power degradation mechanisms in AlGaN-based 280nm deep ultraviolet light-emitting diodes on sapphire," *Applied Physics Letters*, vol. 88, no. 12, p. 121106, 2006.

[25] M. Meneghini, D. Barbisan, L. Rodighiero, G. Meneghesso, and E. Zanoni, "Analysis of the physical processes responsible for the degradation of deep-ultraviolet light emitting diodes," *Applied Physics Letters*, vol. 97, no. 14, p. 143506, 2010.

[26] A. Fujioka, K. Asada, H. Yamada, T. Ohtsuka, T. Ogawa, T. Kosugi, D. Kishikawa, and T. Mukai, "High-output-power 255/280/310 nm deep ultraviolet light-emitting diodes and their lifetime characteristics," *Semiconductor Science and Technology*, vol. 29, no. 8, p. 084005, 2014.

[27] S. Nakamura and S. F. Chichibu, *Introduction to nitride semiconductor blue lasers and light emitting diodes*. London New York: Taylor & Francis, 2000.

[28] F. Mehnke and T. Kolbe. private communication, Technische Universität Berlin, Institut für Festkörperphysik.

[29] F. Brunner, H. Protzmann, M. Heuken, A. Knauer, M. Weyers, and M. Kneissl, "High-temperature growth of AlN in a production scale 11×2' MOVPE reactor," *physica status solidi (c)*, vol. 5, no. 6, pp. 1799–1801, 2008.

[30] Y. Ohba, H. Yoshida, and R. Sato, "Growth of High-Quality AlN, GaN and AlGaN with Atomically Smooth Surfaces on Sapphire Substrates," *Japanese Journal of Applied Physics*, vol. 36, no. 12A, p. L1565, 1997.

[31] J. E. Northrup and C. G. Van de Walle, "Indium versus hydrogen-terminated GaN(0001) surfaces: Surfactant effect of indium in a chemical vapor deposition environment," *Applied Physics Letters*, vol. 84, no. 21, pp. 4322–4324, 2004.

[32] S. Keller, S. Heikman, I. Ben-Yaacov, L. Shen, S. P. DenBaars, and U. K. Mishra, "Indium-surfactant-assisted growth of high-mobility AlN/GaN multilayer structures by metalorganic chemical vapor deposition," *Applied Physics Letters*, vol. 79, no. 21, pp. 3449–3451, 2001.

[33] J. Bardeen and W. Shockley, "Deformation Potentials and Mobilities in Non-Polar Crystals," *Phys. Rev.*, vol. 80, pp. 72–80, 1950.

[34] H. Y. Fan, "Temperature Dependence of the Energy Gap in Monatomic Semiconductors," *Phys. Rev.*, vol. 78, pp. 808–809, 1950.

[35] Y. Varshni, "Temperature dependence of the energy gap in semiconductors," *Physica*, vol. 34, no. 1, pp. 149 – 154, 1967.

[36] Q. Guo and A. Yoshida, "Temperature Dependence of Band Gap Change in InN and AlN," *Japanese Journal of Applied Physics*, vol. 33, no. 5R, p. 2453, 1994.

[37] M. E. Levinshtein, S. L. Rumyantsev, and M. Shur, *Properties of advanced semiconductor materials : GaN, AlN, InN, BN, SiC, SiGe*. Wiley, 2001.

[38] "SpeCLED: Physics summary." `http://www.str-soft.com`. STR, Inc., 10404 Patterson Ave., Suite 108, Richmond, VA 23238, USA.

[39] "SpeCLED & RATRO Graphical User Interface Manual." `http://www.str-soft.com`. STR, Inc., 10404 Patterson Ave., Suite 108, Richmond, VA 23238, USA.

[40] "ZEMAX EE." `http://www.zemax.com/`. Zemax, LLC, 22908 NE Alder Crest Drive, Suite 100, Redmond, WA 98053 USA.

[41] "SiLENSe." `http://www.str-soft.com`. STR, Inc., 10404 Patterson Ave., Suite 108, Richmond, VA 23238, USA.

[42] T. Kolbe, *Einuss des Heterostrukturdesigns auf die Effizienz und die optische Polarisation von (In)AlGaN-basierten Leuchtdioden im ultravioletten Spektralbereich*. PhD thesis, Technische Universität Berlin, 2012.

[43] M. Born and E. Wolf, *Principles of Optics: Electromagnetic Theory of Propagation, Interference and Diffraction of Light*. Cambridge University Press, 7th ed., 1999.

[44] J. Piprek, "Efficiency droop in nitride-based light-emitting diodes," *physica status solidi (a)*, vol. 207, no. 10, pp. 2217–2225, 2010.

[45] E. F. Schubert, *Light-Emitting Diodes*. Cambridge University Press, 2006.

[46] J. Hader, J. V. Moloney, and S. W. Koch, "Density-activated defect recombination as a possible explanation for the efficiency droop in GaN-based diodes," *Applied Physics Letters*, vol. 96, no. 22, p. 221106, 2010.

[47] J. Hader, J. V. Moloney, and S. W. Koch, "Supression of carrier recombination in semiconductor lasers by phase-space filling," *Applied Physics Letters*, vol. 87, no. 20, p. 201112, 2005.

[48] A. David and M. J. Grundmann, "Droop in InGaN light-emitting diodes: A differential carrier lifetime analysis," *Applied Physics Letters*, vol. 96, no. 10, p. 103504, 2010.

[49] D. S. Meyaard, Q. Shan, J. Cho, E. F. Schubert, S.-H. Han, M.-H. Kim, C. Sone, S. J. Oh, and J. K. Kim, "Temperature dependent efficiency droop in GaInN light-emitting diodes with different current densities," *Applied Physics Letters*, vol. 100, no. 8, p. 081106, 2012.

[50] X. Cao, S. LeBoeuf, and T. E. Stecher, "Temperature-dependent electroluminescence of AlGaN-based UV LEDs," *Electron Device Letters, IEEE*, vol. 27, no. 5, pp. 329–331, 2006.

[51] S. Chhajed, J. Cho, E. F. Schubert, J. K. Kim, D. D. Koleske, and M. H. Crawford, "Temperature-dependent light-output characteristics of GaInN light-emitting diodes with different dislocation densities," *physica status solidi (a)*, vol. 208, no. 4, pp. 947–950, 2011.

[52] D. S. Meyaard, Q. Shan, Q. Dai, J. Cho, E. F. Schubert, M.-H. Kim, and C. Sone, "On the temperature dependence of electron leakage from the active region of GaInN/GaN light-emitting diodes," *Applied Physics Letters*, vol. 99, no. 4, pp. 041112–041112–3, 2011.

[53] N. Lobo Ploch, S. Einfeldt, M. Frentrup, J. Rass, T. Wernicke, A. Knauer, V. Kueller, M. Weyers, and M. Kneissl, "Investigation of the temperature dependent efficiency droop in UV LEDs," *Semiconductor Science and Technology*, vol. 28, no. 12, p. 125021, 2013.

[54] M. F. Schubert, S. Chhajed, J. K. Kim, E. F. Schubert, D. D. Koleske, M. H. Crawford, S. R. Lee, A. J. Fischer, G. Thaler, and M. A. Banas, "Effect of dislocation density on efficiency droop in GaInN/GaN light-emitting diodes," *Applied Physics Letters*, vol. 91, no. 23, p. 231114, 2007.

[55] T. Kolbe, A. Knauer, H. Wenzel, S. Einfeldt, V. Kueller, P. Vogt, M. Weyers, and M. Kneissl, "Emission characteristics of InGaN multi quantum well light emitting diodes with differently strained InAlGaN barriers," *physica status solidi (c)*, vol. 6, no. S2, pp. S889–S892, 2009.

[56] A. Laubsch, M. Sabathil, J. Baur, M. Peter, and B. Hahn, "High-Power and High-Efficiency InGaN-Based Light Emitters," *Electron Devices, IEEE Transactions on*, vol. 57, no. 1, pp. 79–87, 2010.

[57] X. Cao, P. Sandvik, S. LeBoeuf, and S. Arthur, "Defect generation in InGaN/GaN light-emitting diodes under forward and reverse electrical stresses ," *Microelectronics Reliability*, vol. 43, no. 12, pp. 1987 – 1991, 2003.

[58] M. Meneghini, A. Tazzoli, G. Mura, G. Meneghesso, and E. Zanoni, "A Review on the Physical Mechanisms That Limit the Reliability of GaN-Based LEDs," *Electron Devices, IEEE Transactions on*, vol. 57, no. 1, pp. 108–118, 2010.

[59] M.-H. Chang, D. Das, P. Varde, and M. Pecht, "Light emitting diodes reliability review ," *Microelectronics Reliability*, vol. 52, no. 5, pp. 762 – 782, 2012. Reliability of High-Power {LED} Packaging and Assembly.

[60] M. Meneghini, L. Trevisanello, C. Sanna, G. Mura, M. Vanzi, G. Meneghesso, and E. Zanoni, "High temperature electro-optical degradation of InGaN/GaN {HBLEDs}," *Microelectronics Reliability*, vol. 47, no. 9-11, pp. 1625 – 1629, 2007. 18th European Symposium on Reliability of Electron Devices, Failure Physics and Analysis.

[61] J. Hu, L. Yang, and M. W. Shin, "Mechanism and thermal effect of delamination in light-emitting diode packages," *Microelectronics Journal*, vol. 38, no. 2, pp. 157 – 163, 2007. 2005 Workshop on Thermal Investigations of {ICs} and Systems (THERMINIC).

[62] X. Guo and E. Schubert, "Current crowding and optical saturation effects in GaInN/GaN light-emitting diodes grown on insulating substrates," *Applied Physics Letters*, vol. 78, no. 21, pp. 3337–3339, 2001.

[63] Y. Taniyasu, M. Kasu, and N. Kobayashi, "Intentional control of n-type conduction for Si-doped AlN and $Al_XGa_{1-X}N$ ($0.42 \leq x < 1$)," *Applied Physics Letters*, vol. 81, no. 7, pp. 1255–1257, 2002.

[64] R. Collazo, S. Mita, J. Xie, A. Rice, J. Tweedie, R. Dalmau, and Z. Sitar, "Progress on n-type doping of AlGaN alloys on AlN single crystal substrates for UV optoelectronic applications," *physica status solidi (c)*, vol. 8, no. 7-8, pp. 2031–2033, 2011.

[65] A. Allerman, M. Crawford, A. Fischer, K. Bogart, S. Lee, D. Follstaedt, P. Provencio, and D. Koleske, "Growth and design of deep-UV (240-290 nm) light emitting diodes using AlGaN alloys ," *Journal of Crystal Growth*, vol. 272, no. 1-4, pp. 227 – 241, 2004.

[66] F. Mehnke, T. Wernicke, H. Pingel, C. Kuhn, C. Reich, V. Kueller, A. Knauer, M. Lapeyrade, M. Weyers, and M. Kneissl, "Highly conductive n-$Al_xGa_{1-x}N$ layers with aluminum mole fractions above 80%," *Applied Physics Letters*, vol. 103, no. 21, p. 212109, 2013.

[67] X. Guo, Y.-L. Li, and E. F. Schubert, "Efficiency of GaN/InGaN light-emitting diodes with interdigitated mesa geometry," *Applied Physics Letters*, vol. 79, no. 13, pp. 1936–1938, 2001.

[68] H. Rodríguez, N. Lobo, S. Einfeldt, A. Knauer, M. Weyers, and M. Kneissl, "GaN-based ultraviolet light-emitting diodes with multifinger contacts," *physica status solidi (a)*, vol. 207, no. 11, pp. 2585–2588, 2010.

[69] C. Pernot, A. Hirano, H. Amano, and I. Akasaki, "Investigation of the Leakage Current in GaN P-N Junctions," *Japanese Journal of Applied Physics*, vol. 37, no. 10B, p. L1202, 1998.

[70] D. S. Li, H. Chen, H. B. Yu, H. Q. Jia, Q. Huang, and J. M. Zhou, "Dependence of leakage current on dislocations in GaN-based light-emitting diodes," *Journal of Applied Physics*, vol. 96, no. 2, pp. 1111–1114, 2004.

[71] J. W. P. Hsu, M. J. Manfra, R. J. Molnar, B. Heying, and J. S. Speck, "Direct imaging of reverse-bias leakage through pure screw dislocations in GaN films grown by molecular beam epitaxy on GaN templates," *Applied Physics Letters*, vol. 81, no. 1, pp. 79–81, 2002.

[72] S. X. Jin, J. Li, J. Z. Li, J. Y. Lin, and H. X. Jiang, "GaN microdisk light emitting diodes," *Applied Physics Letters*, vol. 76, no. 5, pp. 631–633, 2000.

[73] H. Choi, C. Jeon, M. Dawson, P. Edwards, and R. Martin, "Fabrication and performance of parallel-addressed InGaN micro-LED arrays," *Photonics Technology Letters, IEEE*, vol. 15, no. 4, pp. 510–512, 2003.

[74] V. Adivarahan, S. Wu, W. Sun, V. Mandavilli, M. Shatalov, G. Simin, J. W. Yang, H. Maruska, and M. A. Khan, "High-power deep ultraviolet light-emitting diodes based on a micro-pixel design," *Applied Physics Letters*, vol. 85, no. 10, pp. 1838–1840, 2004.

[75] A. Chakraborty, L. Shen, and U. K. Mishra, "Interdigitated Multipixel Arrays for the Fabrication of High-Power Light-Emitting Diodes With Very Low Series Resistances, Reduced Current Crowding, and Improved Heat Sinking," *Electron Devices, IEEE Transactions on*, vol. 54, no. 5, pp. 1083–1090, 2007.

[76] N. Lobo Ploch, H. Rodriguez, C. Stolmacker, M. Hoppe, M. Lapeyrade, J. Stellmach, F. Mehnke, T. Wernicke, A. Knauer, V. Kueller, M. Weyers, S. Einfeldt, and M. Kneissl, "Effective Thermal Management in Ultraviolet Light-Emitting Diodes With Micro-LED Arrays," *Electron Devices, IEEE Transactions on*, vol. 60, no. 2, pp. 782–786, 2013.

[77] W. Liu and A. A. Balandin, "Thermal conduction in $Al_xGa_{1-x}N$ alloys and thin films," *Journal of Applied Physics*, vol. 97, no. 7, pp. 073710–073710–6, 2005.

[78] "Patran/ Nastran." `www.mscsoftware.com`. MSC Software GmbH., Am Moosfeld 13, 81829 Munich, Germany.

[79] J.-S. Kim, P. K. H. Ho, N. C. Greenham, and R. H. Friend, "Electroluminescence emission pattern of organic light-emitting diodes: Implications for device efficiency calculations," *Journal of Applied Physics*, vol. 88, no. 2, pp. 1073–1081, 2000.

[80] M. Suzuki, T. Uenoyama, and A. Yanase, "First-principles calculations of effective-mass parameters of AlN and GaN," *Phys. Rev. B*, vol. 52, pp. 8132–8139, 1995.

[81] J. Hopfdeld, "Fine structure in the optical absorption edge of anisotropic crystals ," *Journal of Physics and Chemistry of Solids*, vol. 15, no. 1-2, pp. 97–107, 1960.

[82] N. V. Edwards, S. D. Yoo, M. D. Bremser, T. W. Weeks, O. H. Nam, R. F. Davis, H. Liu, R. A. Stall, M. N. Horton, N. R. Perkins, T. F. Kuech, and D. E. Aspnes, "Variation of GaN valence bands with biaxial stress and quantification of residual stress," *Applied Physics Letters*, vol. 70, no. 15, pp. 2001–2003, 1997.

[83] I. Vurgaftman and J. R. Meyer, "Band parameters for nitrogen-containing semiconductors," *Journal of Applied Physics*, vol. 94, no. 6, pp. 3675–3696, 2003.

[84] A. A. Yamaguchi, Y. Mochizuki, H. Sunakawa, and A. Usui, "Determination of valence band splitting parameters in GaN," *Journal of Applied Physics*, vol. 83, no. 8, pp. 4542–4544, 1998.

[85] A. Sedhain, J. Y. Lin, and H. X. Jiang, "Valence band structure of AlN probed by photoluminescenc," *Applied Physics Letters*, vol. 92, no. 4, p. 041114, 2008.

[86] G. D. Chen, M. Smith, J. Y. Lin, H. X. Jiang, S. H. Wei, M. Asif Khan, and C. J. Sun, "Fundamental optical transitions in GaN," *Applied Physics Letters*, vol. 68, no. 20, pp. 2784–2786, 1996.

[87] K. B. Nam, J. Li, M. L. Nakarmi, J. Y. Lin, and H. X. Jiang, "Unique optical properties of AlGaN alloys and related ultraviolet emitters," *Applied Physics Letters*, vol. 84, no. 25, pp. 5264–5266, 2004.

[88] R. Goldhahn, C. Buchheim, P. Schley, A. T. Winzer, and H. Wenzel, *Optical Constants of Bulk Nitrides*. Wiley-VCH Verlag GmbH & Co. KGaA, 2007.

[89] J. Li, K. B. Nam, M. L. Nakarmi, J. Y. Lin, H. X. Jiang, P. Carrier, and S.-H. Wei, "Band structure and fundamental optical transitions in wurtzite AlN," *Applied Physics Letters*, vol. 83, no. 25, pp. 5163–5165, 2003.

[90] B. Neuschl, J. Helbing, M. Knab, H. Lauer, M. Madel, K. Thonke, T. Meisch, K. Forghani, F. Scholz, and M. Feneberg, "Composition dependent valence band order in c-oriented wurtzite AlGaN layers," *Journal of Applied Physics*, vol. 116, no. 11, p. 113506, 2014.

[91] C. Coughlan, S. Schulz, M. A. Caro, and E. P. O'Reilly, "Band gap bowing and optical polarization switching in $Al_{1-x}Ga_xN$ alloys," *physica status solidi (b)*, pp. –, 2015.

[92] T. Kolbe, A. Knauer, C. Chua, Z. Yang, S. Einfeldt, P. Vogt, N. M. Johnson, M. Weyers, and M. Kneissl, "Optical polarization characteristics of ultraviolet (In)(Al)GaN multiple quantum well light emitting diodes," *Applied Physics Letters*, vol. 97, no. 17, p. 171105, 2010.

[93] R. G. Banal, M. Funato, and Y. Kawakami, "Optical anisotropy in [0001]-oriented $Al_xGa_{1-x}N$/AlN quantum wells (x >0.69)," *Phys. Rev. B*, vol. 79, p. 121308, 2009.

[94] H. Kawanishi, M. Senuma, and T. Nukui, "Anisotropic polarization characteristics of lasing and spontaneous surface and edge emissions from deep-ultraviolet ($\lambda \approx 240nm$) AlGaN multiple-quantum-well lasers," *Applied Physics Letters*, vol. 89, no. 4, p. 041126, 2006.

[95] C. Netzel, A. Knauer, and M. Weyers, "Impact of light polarization on photoluminescence intensity and quantum efficiency in AlGaN and AlInGaN layers," *Applied Physics Letters*, vol. 101, no. 24, p. 242102, 2012.

[96] J. E. Northrup, C. L. Chua, Z. Yang, T. Wunderer, M. Kneissl, N. M. Johnson, and T. Kolbe, "Effect of strain and barrier composition on the polarization of light emission from AlGaN/AlN quantum wells," *Applied Physics Letters*, vol. 100, no. 2, p. 021101, 2012.

[97] T. K. Sharma, D. Naveh, and E. Towe, "Strain-driven light-polarization switching in deep ultraviolet nitride emitters," *Phys. Rev. B*, vol. 84, p. 035305, 2011.

[98] S. L. Chuang and C. S. Chang, "k·p method for strained wurtzite semiconductors," *Phys. Rev. B*, vol. 54, pp. 2491–2504, 1996.

[99] D. Fu, R. Zhang, B. Liu, Z. L. Xie, X. Q. Xiu, H. Lu, Y. D. Zheng, and G. Edwards, "Exploring optimal UV emission windows for AlGaN and AlInN alloys grown on different templates," *physica status solidi (b)*, vol. 248, no. 12, pp. 2816–2820, 2011.

[100] T. Kolbe, A. Knauer, C. Chua, Z. Yang, V. Kueller, S. Einfeldt, P. Vogt, N. M. Johnson, M. Weyers, and M. Kneissl, "Effect of temperature and strain on the optical polarization of (In)(Al)GaN ultraviolet light emitting diodes," *Applied Physics Letters*, vol. 99, no. 26, p. 261105, 2011.

[101] A. Atsushi Yamaguchi, "Valence band engineering for remarkable enhancement of surface emission in AlGaN deep-ultraviolet light emitting diodes," *physica status solidi (c)*, vol. 5, no. 6, pp. 2364–2366, 2008.

[102] T. M. Al tahtamouni, J. Y. Lin, and H. X. Jiang, "Optical polarization in c-plane Al-rich AlN/$Al_xGa_{1-x}N$ single quantum wells," *Applied Physics Letters*, vol. 101, no. 4, p. 042103, 2012.

[103] J. J. Wierer, I. Montaño, M. H. Crawford, and A. A. Allerman, "Effect of thickness and carrier density on the optical polarization of $Al_{0.44}Ga_{0.56}N/Al_{0.55}Ga_{0.45}N$ quantum well layers," *Journal of Applied Physics*, vol. 115, no. 17, p. 174501, 2014.

[104] S.-H. Park and J.-I. Shim, "Carrier density dependence of polarization switching characteristics of light emission in deep-ultraviolet AlGaN/AlN quantum well structures," *Applied Physics Letters*, vol. 102, no. 22, p. 221109, 2013.

[105] S. Wieczorek, W. W. Chow, S. R. Lee, A. J. Fischer, A. A. Allerman, and M. H. Crawford, "Analysis of optical emission from high-aluminum AlGaN quantum-well structures," *Applied Physics Letters*, vol. 84, no. 24, pp. 4899–4901, 2004.

[106] A. A. Yamaguchi, "Theoretical investigation of optical polarization properties in Al-rich AlGaN quantum wells with various substrate orientations," *Applied Physics Letters*, vol. 96, no. 15, p. 151911, 2010.

[107] J. Bhattacharyya, S. Ghosh, and H. T. Grahn, "Are AlN and GaN substrates useful for the growth of non-polar nitride films for UV emission? The oscillator strength perspective," *physica status solidi (b)*, vol. 246, no. 6, pp. 1184–1187, 2009.

[108] C.-P. Wang and Y.-R. Wu, "Study of optical anisotropy in nonpolar and semipolar AlGaN quantum well deep ultraviolet light emission diode," *Journal of Applied Physics*, vol. 112, no. 3, p. 033104, 2012.

[109] R. G. Banal, Y. Taniyasu, and H. Yamamoto, "Deep-ultraviolet light emission properties of nonpolar M-plane AlGaN quantum wells," *Applied Physics Letters*, vol. 105, no. 5, p. 053104, 2014.

[110] L. Schade, U. T. Schwarz, T. Wernicke, J. Rass, S. Ploch, M. Weyers, and M. Kneissl, "On the optical polarization properties of semipolar InGaN quantum wells," *Applied Physics Letters*, vol. 99, no. 5, p. 051103, 2011.

[111] L. Schade, U. T. Schwarz, T. Wernicke, M. Weyers, and M. Kneissl, "Impact of band structure and transition matrix elements on polarization properties of the photoluminescence of semipolar and nonpolar InGaN quantum wells," *physica status solidi (b)*, vol. 248, no. 3, pp. 638–646, 2011.

[112] J. Rass. private communication, Technische Universität Berlin, Institut für Festkörperphysik.

[113] H. Wenzel. private communication, Ferdinand-Braun-Institut Leibniz-Institut für Höchstfrequenztechnik.

[114] R. Goldhahn, S. Shokhovets, J. Scheiner, G. Gobsch, T. Cheng, C. Foxon, U. Kaiser, G. Kipshidze, and W. Richter, "Determination of Group III Nitride Film Properties by Reflectance and Spectroscopic Ellipsometry Studies," *physica status solidi (a)*, vol. 177, no. 1, pp. 107–115, 2000.

[115] R. Goldhahn, P. Schley, A. T. Winzer, G. Gobsch, V. Cimalla, O. Ambacher, M. Rakel, C. Cobet, N. Esser, H. Lu, and W. J. Schaff, "Detailed analysis of the dielectric function for wurtzite InN and In-rich InAlN alloys," *physica status solidi (a)*, vol. 203, no. 1, pp. 42–49, 2006.

[116] P. Schley, R. Goldhahn, A. T. Winzer, G. Gobsch, V. Cimalla, O. Ambacher, M. Rakel, C. Cobet, N. Esser, H. Lu, and W. J. Schaff, "Transition energies and Stokes shift analysis for In-rich InGaN alloys," *physica status solidi (b)*, vol. 243, no. 7, pp. 1572–1576, 2006.

[117] N. A. Sanford, A. Munkholm, M. R. Krames, A. Shapiro, I. Levin, A. V. Davydov, S. Sayan, L. S. Wielunski, and T. E. Madey, "Refractive index and birefringence of $In_xGa_{1-x}N$ films grown by MOCVD," *physica status solidi (c)*, vol. 2, no. 7, pp. 2783–2786, 2005.

[118] S. Shokhovets, R. Goldhahn, G. Gobsch, S. Piekh, R. Lantier, A. Rizzi, V. Lebedev, and W. Richter, "Determination of the anisotropic dielectric function for wurtzite AlN and GaN by spectroscopic ellipsometry," *Journal of Applied Physics*, vol. 94, no. 1, pp. 307–312, 2003.

[119] N. A. Sanford, L. H. Robins, A. V. Davydov, A. Shapiro, D. V. Tsvetkov, A. V. Dmitriev, S. Keller, U. K. Mishra, and S. P. DenBaars, "Refractive index study of $Al_xGa_{1-x}N$ films grown on sapphire substrates," *Journal of Applied Physics*, vol. 94, no. 5, pp. 2980–2991, 2003.

[120] R. Goldhahn, A. Winzer, V. Cimalla, O. Ambacher, C. Cobet, W. Richter, N. Esser, J. Furthmüller, F. Bechstedt, H. Lu, and W. Schaff, "Anisotropy of the dielectric function for wurtzite InN," *Superlattices and Microstructures*, vol. 36, no. 4-6, pp. 591–597, 2004. European Materials Research Society 2004, Symposium L. InN, GaN, AlN and Related Materials, their Heterostructures and Devices.

[121] W. D. Rogatto, *The Infrared and Electro-Optical Systems Handbook. Vol. 3 Electro-Optical Components*. SPIE Optical Engineering, 1993.

[122] X. H. Wang, W. Y. Fu, P. T. Lai, and H. W. Choi, "Evaluation of InGaN/GaN light-emitting diodes of circular geometry," *Opt. Express*, vol. 17, no. 25, pp. 22311–22319, 2009.

[123] S. J. Lee and S. W. Song, "Efficiency improvement in light-emitting diodes based on geometrically deformed chips," *Proc. SPIE*, vol. 3621, pp. 237–248, 1999.

[124] W. Y. Fu, K. N. Hui, X. H. Wang, K. Wong, P. Lai, and H. Choi, "Geometrical Shaping of InGaN Light-Emitting Diodes by Laser Micromachining," *Photonics Technology Letters, IEEE*, vol. 21, no. 15, pp. 1078–1080, 2009.

[125] B. Sun, L. Zhao, T. Wei, X. Yi, Z. Liu, G. Wang, and J. Li, "Shape designing for light extraction enhancement bulk-GaN light-emitting diodes," *Journal of Applied Physics*, vol. 113, no. 24, p. 243104, 2013.

[126] J.-Y. Kim, M.-K. Kwon, J.-P. Kim, and S.-J. Park, "Enhanced Light Extraction From Triangular GaN-Based Light-Emitting Diodes," *Photonics Technology Letters, IEEE*, vol. 19, no. 23, pp. 1865–1867, 2007.

[127] D.-H. Jang, J.-I. Shim, and D.-S. Shin, "Enhancement of Light Extraction Efficiency Using Lozenge-Shaped GaN-Based Light-Emitting Diodes," *Photonics Technology Letters, IEEE*, vol. 21, no. 12, pp. 760–762, 2009.

[128] X. H. Wang, P. T. Lai, and H. W. Choi, "The contribution of sidewall light extraction to efficiencies of polygonal light-emitting diodes shaped with laser micromachining," *Journal of Applied Physics*, vol. 108, no. 2, p. 023110, 2010.

[129] M. Shatalov, W. Sun, A. Lunev, X. Hu, A. Dobrinsky, Y. Bilenko, J. Yang, M. Shur, R. Gaska, C. Moe, G. Garrett, and M. Wraback, "AlGaN Deep-Ultraviolet Light-Emitting Diodes with External Quantum Efficiency above 10%," *Applied Physics Express*, vol. 5, no. 8, p. 082101, 2012.

[130] C.-C. Kao, H.-C. Kuo, H.-W. Huang, J.-T. Chu, Y.-C. Peng, Y.-L. Hsieh, C. Y. Luo, S.-C. Wang, C.-C. Yu, and C.-F. Lin, "Light-output enhancement in a nitride-based light-emitting diode with 22° undercut sidewalls," *Photonics Technology Letters, IEEE*, vol. 17, no. 1, pp. 19–21, 2005.

[131] J.-S. Lee, J. Lee, S. Kim, and H. Jeon, "GaN Light-Emitting Diode with Deep-Angled Mesa Sidewalls for Enhanced Light Emission in the Surface-Normal Direction," *Electron Devices, IEEE Transactions on*, vol. 55, no. 2, pp. 523–526, 2008.

[132] E. M. Purcell, "Spontaneous emission probabilities at radio frequencies," *Physical Review*, vol. 69, p. 681, 1946.

[133] E. Yablonovitch, "Inhibited Spontaneous Emission in Solid-State Physics and Electronics," *Phys. Rev. Lett.*, vol. 58, pp. 2059–2062, 1987.

[134] M. Fujita, S. Takahashi, Y. Tanaka, T. Asano, and S. Noda, "Simultaneous inhibition and redistribution of spontaneous light emission in photonic crystals," *Science*, vol. 308, no. 5726, pp. 1296–1298, 2005.

[135] J. J. Wierer, A. David, and M. M. Megens, " III-nitride photonic-crystal light-emitting diodes with high extraction efficiency," *Nat Photon*, vol. 3, no. 3, pp. 163–169, 2009.

[136] J. Shakya, K. H. Kim, J. Y. Lin, and H. X. Jiang, "Enhanced light extraction in III-nitride ultraviolet photonic crystal light-emitting diodes," *Applied Physics Letters*, vol. 85, no. 1, pp. 142–144, 2004.

[137] T. N. Oder, J. Shakya, J. Y. Lin, and H. X. Jiang, "III-nitride photonic crystals," *Applied Physics Letters*, vol. 83, no. 6, pp. 1231–1233, 2003.

[138] E. F. Schubert, Y. Wang, A. Y. Cho, L. Tu, and G. J. Zydzik, "Resonant cavity light emitting diode," *Applied Physics Letters*, vol. 60, no. 8, pp. 921–923, 1992.

[139] Y. C. Shen, J. J. Wierer, M. R. Krames, M. J. Ludowise, M. S. Misra, F. Ahmed, A. Y. Kim, G. O. Mueller, J. C. Bhat, S. A. Stockman, and P. S. Martin, "Optical cavity effects in InGaN/GaN quantum-well-heterostructure flip-chip light-emitting diodes," *Applied Physics Letters*, vol. 82, no. 14, pp. 2221–2223, 2003.

[140] T. Moudakir, F. Genty, M. Kunzer, P. Borner, T. Passow, S. Suresh, G. Patriarche, K. Kohler, W. Pletschen, J. Wagner, and A. Ougazzaden, "Design, Fabrication, and Characterization of Near-Milliwatt-Power RCLEDs Emitting at 390 nm," *Photonics Journal, IEEE*, vol. 5, no. 6, pp. 8400709–8400709, 2013.

[141] A. Köck, E. Gornik, M. Hauser, and W. Beinstingl, "Strongly directional emission from AlGaAs/ GaAs light emitting diodes," *Applied Physics Letters*, vol. 57, no. 22, pp. 2327–2329, 1990.

[142] A. Neogi, C.-W. Lee, H. O. Everitt, T. Kuroda, A. Tackeuchi, and E. Yablonovitch, "Enhancement of spontaneous recombination rate in a quantum well by resonant surface plasmon coupling," *Phys. Rev. B*, vol. 66, p. 153305, 2002.

[143] K. Okamoto, I. Niki, A. Shvartser, Y. Narukawa, T. Mukai, and A. Scherer, "Surface-plasmon-enhanced light emitters based on InGaN quantum wells," *Nature Materials*, vol. 3, no. 9, pp. 601–605, 2004.

[144] N. Gao, K. Huang, J. Li, S. Li, X. Yang, and J. Kang, "Surface-plasmon-enhanced deep-UV light emitting diodes based on AlGaN multi-quantum wells," *Scientific Reports*, vol. 2, no. 816, 2012.

[145] J. J. Wierer, D. A. Steigerwald, M. R. Krames, J. J. O'Shea, M. J. Ludowise, G. Christenson, Y.-C. Shen, C. Lowery, P. S. Martin, S. Subramanya, W. Götz, N. F. Gardner, R. S. Kern, and S. A. Stockman, "High-power AlGaInN flip-chip light-emitting diodes," *Applied Physics Letters*, vol. 78, no. 22, pp. 3379–3381, 2001.

[146] R. Kremzow. private communication, Technische Universität Berlin, Institut für Festkörperphysik.

[147] D. L. Barton, M. Osinski, P. Perlin, C. Helms, and N. Berg, "Life tests and failure mechanisms of GaN/AlGaN/InGaN light emitting diodes," in *Reliability Physics Symposium, 1997. 35th Annual Proceedings., IEEE International*, pp. 276–281, 1997.

[148] K. Yamada, Y. Furusawa, S. Nagai, A. Hirano, M. Ippommatsu, K. Aosaki, N. Morishima, H. Amano, and I. Akasaki, "Development of underfilling and encapsulation for deep-ultraviolet LEDs," *Applied Physics Express*, vol. 8, no. 1, p. 012101, 2015.

[149] K. R. McIntosh, J. N. Cotsell, J. Cumpston, A. Norris, N. E. Powell, and B. M. Ketola, "The Effect of Accelerated Aging Tests on the Optical Properties of Silicone and EVA Encapsulants," *Proceedings of the 24th EU PVSEC: Hamburg*, 2009.

[150] J. Brandrup and E. H. I. (editors), *Polymer handbook. 3rd edition*. Akademie Verlag GmbH, 1990.

[151] D. C. Duffy, J. C. McDonald, O. J. A. Schueller, and G. M. Whitesides, "Rapid prototyping of microfluidic systems in poly(dimethylsiloxane)," *Analytical Chemistry*, vol. 70, no. 23, pp. 4974–4984, 1998.

[152] A. Bergh and H. Saul, "Surface roughening of electroluminescent diodes," *US. Patent*, no. 3739217, 1973.

[153] I. Schnitzer, E. Yablonovitch, C. Caneau, T. J. Gmitter, and A. Scherer, "30% external quantum efficiency from surface textured, thin-film light-emitting diodes," *Applied Physics Letters*, vol. 63, no. 16, pp. 2174–2176, 1993.

[154] C.-E. Lee, Y.-C. Lee, H.-C. Kuo, T. chang Lu, and S.-C. Wang, "High-Brightness InGaN-GaN Flip-Chip Light-Emitting Diodes With Triple-Light Scattering Layers," *Photonics Technology Letters, IEEE*, vol. 20, no. 8, pp. 659–661, 2008.

[155] C. Huh, K.-S. Lee, E.-J. Kang, and S.-J. Park, "Improved light-output and electrical performance of InGaN-based light-emitting diode by microroughening of the p-GaN surface," *Journal of Applied Physics*, vol. 93, no. 11, pp. 9383–9385, 2003.

[156] V. Haerle, B. Hahn, S. Kaiser, A. Weimar, D. Eisert, S. Bader, A. Ploessl, and F. Eberhard, "Light extraction technologies for high-efficiency GaInN-LED devices," *Proc. SPIE*, vol. 4996, pp. 133–138, 2003.

[157] T. Fujii, Y. Gao, R. Sharma, E. Hu, S. DenBaars, and S. Nakamura, "Increase in the extraction efficiency of gan-based light-emitting diodes via surface roughening," *Applied Physics Letters*, vol. 84, no. 6, pp. 855–857, 2004.

[158] H.-W. Huang, J. T. Chu, C. C. Kao, T. H. Hseuh, T. C. Lu, H. C. Kuo, S. C. Wang, and C. C. Yu, "Enhanced light output of an InGaN/GaN light emitting diode with a nano-roughened p-GaN surface," *Nanotechnology*, vol. 16, no. 9, p. 1844, 2005.

[159] D.-S. Han, J.-Y. Kim, S.-I. Na, S.-H. Kim, K.-D. Lee, B. Kim, and S.-J. Park, "Improvement of light extraction efficiency of flip-chip light-emitting diode by texturing the bottom side surface of sapphire substrate," *Photonics Technology Letters, IEEE*, vol. 18, no. 13, pp. 1406–1408, 2006.

[160] C. I. H. Ashby, C. C. Mitchell, J. Han, N. A. Missert, P. P. Provencio, D. M. Follstaedt, G. M. Peake, and L. Griego, "Low-dislocation-density GaN from a single growth on a textured substrate," *Applied Physics Letters*, vol. 77, no. 20, pp. 3233–3235, 2000.

[161] M. Yamada, T. Mitani, Y. Narukawa, S. Shioji, I. Niki, S. Sonobe, K. Deguchi, M. Sano, and T. Mukai, "InGaN-Based Near-Ultraviolet and Blue-Light-Emitting Diodes with High External Quantum Efficiency Using a Patterned Sapphire Substrate and a Mesh Electrode," *Japanese Journal of Applied Physics*, vol. 41, no. Part 2, No. 12B, pp. L1431–L1433, 2002.

[162] E. Yablonovitch, "Statistical ray optics," *J. Opt. Soc. Am.*, vol. 72, no. 7, pp. 899–907, 1982.

[163] R. Windisch, C. Rooman, B. Dutta, A. Knobloch, G. Borghs, G. Dohler, and P. Heremans, "Light-extraction mechanisms in high-efficiency surface-textured light-emitting diodes," *Selected Topics in Quantum Electronics, IEEE Journal of*, vol. 8, no. 2, pp. 248–255, 2002.

[164] R. Windisch, S. Schoberth, S. Meinlschmidt, P. Kiesel, A. Knobloch, P. Heremans, B. Dutta, G. Borghs, and G. H. Döhler, "Light propagation through textured surfaces," *Journal of Optics A: Pure and Applied Optics*, vol. 1, no. 4, p. 512, 1999.

[165] R. Windisch, P. Heremans, A. Knobloch, P. Kiesel, G. Dohler, B. Dutta, and G. Borghs, "Light-emitting diodes with 31% external quantum efficiency by outcoupling of lateral waveguide modes," *Applied Physics Letters*, vol. 74, no. 16, pp. 2256–2258, 1999.

[166] R. Windisch, C. Rooman, S. Meinlschmidt, P. Kiesel, D. Zipperer, G. Dohler, B. Dutta, M. Kuijk, G. Borghs, and P. Heremans, "Impact of texture-enhanced transmission on high-efficiency surface-textured light-emitting diodes," *Applied Physics Letters*, vol. 79, no. 15, pp. 2315–2317, 2001.

[167] A. David, "Surface-roughened light-emitting diodes: An accurate model," *Display Technology, Journal of*, vol. 9, no. 5, pp. 301–316, 2013.

[168] E. Dobrovinskaya, L. Lytvynov, and V. Pishchik, "Properties of sapphire," in *Sapphire*, Micro- and Opto-Electronic Materials, Structures, and Systems, pp. 55–176, Springer US, 2009.

[169] D. Selvanathan, L. Zhou, V. Kumar, I. Adesida, and N. Finnegan, "Long-term thermal stability of Ti/Al/Mo/Au ohmic contacts on n-GaN," *Journal of Electronic Materials*, vol. 32, no. 5, pp. 335–340, 2003.

[170] D. Selvanathan, F. M. Mohammed, A. Tesfayesus, and I. Adesida, "Comparative study of Ti/Al/Mo/Au, Mo/Al/Mo/Au, and V/Al/Mo/Au ohmic contacts to AlGaN/GaN heterostructures," *Journal of Vacuum Science & Technology B*, vol. 22, no. 5, pp. 2409–2416, 2004.

[171] E. D. Palik, *Handbook of Optical Constants of Solids*. Academic Press, San Diego, 1998.

[172] R. M. Eastment and C. H. B. Mee, "Work function measurements on (100), (110) and (111) surfaces of aluminium," *Journal of Physics F: Metal Physics*, vol. 3, no. 9, p. 1738, 1973.

[173] B. Nieuwenhuys, R. Bouwman, and W. Sachtler, "The changes in work function of group Ib and {VIII} metals on xenon adsorption, determined by field electron and photoelectron emission ," *Thin Solid Films*, vol. 21, no. 1, pp. 51 – 58, 1974.

[174] A. W. Dweydari and C. H. B. Mee, "Work function measurements on (100) and (110) surfaces of silver," *physica status solidi (a)*, vol. 27, no. 1, pp. 223–230, 1975.

[175] D. L. Hibbard, S. P. Jung, C. Wang, D. Ullery, Y. S. Zhao, H. P. Lee, W. So, and H. Liu, "Low resistance high reflectance contacts to p-GaN using oxidized Ni/Au and Al or Ag," *Applied Physics Letters*, vol. 83, no. 2, pp. 311–313, 2003.

[176] J.-W. Park, J.-O. Song, D.-S. Leem, and T.-Y. Seong, "Low-Resistance and Reflective Ni/Rh and Ni/Au/Rh Contacts to p-GaN for Flip-Chip LEDs," *Electrochemical and Solid-State Letters*, vol. 8, no. 1, pp. G17–G19, 2005.

[177] J.-O. Song, D.-S. Leem, J. S. Kwak, O. H. Nam, Y. Park, and T.-Y. Seong, "Low-resistance and highly-reflective Zn-Ni solid solution/Ag ohmic contacts for flip-chip light-emitting diodes," *Applied Physics Letters*, vol. 83, no. 24, pp. 4990–4992, 2003.

[178] K.-Y. Ban, H.-G. Hong, D. Y. Noh, T.-Y. Seong, J.-O. Song, and D. Kim, "Use of an indium zinc oxide interlayer for forming Ag-based Ohmic contacts to p-type GaN for UV-light-emitting diodes," *Semiconductor Science and Technology*, vol. 20, no. 9, p. 921, 2005.

[179] K.-Y. Ban, H.-G. Hong, D.-Y. Noh, J. I. Sohn, D.-J. Kang, and T.-Y. Seong, "Ir/Ag reflector for high-performance GaN-based near UV light emitting diodes ," *Materials Science and Engineering: B*, vol. 133, no. 1-3, pp. 26 – 29, 2006.

[180] K. Takehara, K. Takeda, S. Ito, H. Aoshima, M. Iwaya, T. Takeuchi, S. Kamiyama, I. Akasaki, and H. Amano, "Indium–Tin Oxide/Al Reflective Electrodes for Ultraviolet Light-Emitting Diodes," *Japanese Journal of Applied Physics*, vol. 51, p. 042101, 2012.

[181] J.-O. Song, W.-K. Hong, Y. Park, J. S. Kwak, and T.-Y. Seong, "Low-resistance Al-based reflectors for high-power GaN-based flip-chip light-emitting diodes," *Applied Physics Letters*, vol. 86, no. 13, p. 133503, 2005.

[182] J. K. Kim, J.-Q. Xi, H. Luo, E. F. Schubert, J. Cho, C. Sone, and Y. Park, "Enhanced light-extraction in GaInN near-ultraviolet light-emitting diode with Al-based omnidirectional reflector having NiZn/Ag microcontacts," *Applied Physics Letters*, vol. 89, no. 14, p. 141123, 2006.

[183] T. Jeong, H. H. Lee, S.-H. Park, J. H. Baek, and J. K. Lee, "InGaN/AlGaN Ultraviolet Light-Emitting Diode with a Ti_3O_5/Al_2O_3 Distributed Bragg Reflector," *Japanese Journal of Applied Physics*, vol. 47, no. 12, pp. 8811–8814, 2008.

[184] T. Nakashima, K. Takeda, H. Shinzato, M. Iwaya, S. Kamiyama, T. Takeuchi, I. Akasaki, and H. Amano, "Combination of Indium-Tin Oxide and SiO_2 /AlN Dielectric Multilayer Reflective Electrodes for Ultraviolet-Light-Emitting Diodes," *Japanese Journal of Applied Physics*, vol. 52, no. 8S, p. 08JG07, 2013.

[185] G. H. B. Thompson, *Physics of Semiconductor Laser Devices*. John Wiley and Sons, New York, 1980.

[186] A. Knauer, F. Brunner, T. Kolbe, V. Küller, H. Rodriguez, S. Einfeldt, M. Weyers, and M. Kneissl, "MOVPE growth for UV-LEDs," *Light-Emitting Diodes: Materials, Devices, and Applications for Solid State Lighting XIII*, vol. 7231, no. 1, p. 72310G, 2009.

[187] N. Lobo, H. Rodriguez, A. Knauer, M. Hoppe, S. Einfeldt, P. Vogt, M. Weyers, and M. Kneissl, "Enhancement of light extraction in ultraviolet light-emitting diodes using nanopixel contact design with Al reflector," *Applied Physics Letters*, vol. 96, no. 8, p. 081109, 2010.

[188] H. Eisenmann, T. Waas, and H. Hartmann, "PROXECCO-Proximity effect correction by convolution," *Journal of Vacuum Science & Technology B*, vol. 11, no. 6, pp. 2741–2745, 1993.

[189] J. M. Bilbao Torresl, "Proximity Effect Correction in Electron Beam Lithography," 2011. Intership report, Ferdinand-Braun-Institut, Leibniz-Institut für Höchstfrequenztechnik.

Appendix 1: Heterostructures of UV LEDs

Heterostructure of a 320 nm LED

		Layer	Thickness (nm)
	p-contact layer	GaN:Mg	20
100 ×	p-current spreading layer	$Al_{0.12}Ga_{0.88}N$:Mg / GaN:Mg (SL)	500
	EBL	$Al_{0.40}Ga_{0.60}N$:Mg	23
	interlayer	$Al_{0.60}Ga_{0.40}N$:Mg	1.0
	barrier	$Al_{0.30}In_{0.02}Ga_{0.68}N$	5.0
5 × MQW		$Al_{0.20}In_{0.02}Ga_{0.78}N$	2.5
	first barrier	$l_{0.30}In_{0.01}Ga_{0.69}N$	20
100 ×		$Al_{0.30}Ga_{0.70}N$:Si / $Al_{0.40}Ga_{0.60}N$:Si (SL)	660
	n-current spreading layers	$Al_{0.35}Ga_{0.65}N$:Si	600
100 ×		$Al_{0.30}Ga_{0.70}N$:Si / $Al_{0.40}Ga_{0.60}N$:Si (SL)	660
		$Al_{0.35}Ga_{0.65}N$:Si	5000
		$Al_{0.35}Ga_{0.65}N$	800
80 ×	strain compensation layers	AlN / GaN (SL)	150
	buffer	AlN	500
	substrate	sapphire	430 μm

Heterostructure of a 380 nm LED

		Layer	Thickness (nm)
	p-current spreading layer	GaN:Mg	200
	EBL	$Al_{0.23}Ga_{0.77}N$:Mg	10
	barrier	$Al_{0.16}In_{0.04}Ga_{0.80}N$	2.8
	barrier	$Al_{0.16}In_{0.04}Ga_{0.80}N$:Si	1.4
	barrier	$Al_{0.16}In_{0.04}Ga_{0.80}N$	2.8
$5 \times$ MQW		$In_{0.03}Ga_{0.97}N$	3.0
	barrier	$Al_{0.16}In_{0.04}Ga_{0.80}N$	2.8
	barrier	$Al_{0.16}In_{0.04}Ga_{0.80}N$:Si	1.4
	barrier	$Al_{0.16}In_{0.04}Ga_{0.80}N$	2.8
	HBL	$Al_{0.23}Ga_{0.77}N$:Si	10
	n-current spreading layer	GaN:Si	3500
	buffer	GaN	1700
	substrate	sapphire	430 μm

Appendix 2: List of samples

	Sample number	Process number
Fig. 2.7 a	B2524	Z1 3934 GAL
Fig. 2.7 b	B2524	Z1 3934 GAL
Fig. 3.3 a	B2524	Z1 3934 GAL
Fig. 3.3 b	B2524	Z1 3934 GAL
Fig. 3.4 a	TS1653-6	
	TS1653-3	
Fig. 3.4 b	TS1653-6	
	TS1653-3	
Fig. 3.5 a	B2522	Z1 3934 GAL
	B2533	Z1 3934 GAL
	B2524	Z1 3934 GAL
Fig. 3.5 b	B2522	Z1 3934 GAL
	B2533	Z1 3934 GAL
	B2524	Z1 3934 GAL
Fig. 3.7	B3080	Z1 4487 UVL
Fig. 4.3 a	B2945	Z1 4458 UVL
Fig. 4.3 b	B2945	Z1 4458 UVL
Fig. 4.5	B2945	Z1 4458 UVL
Fig. 4.6 a	B2945	Z1 4458 UVL
Fig. 4.6 b	B2945	Z1 4458 UVL
Fig. 4.7 a	B2945	Z1 4458 UVL
Fig. 4.11 a	B2956	Z1 5320 UVL
Fig. 4.11 b	TS0518-2	Z1 5338 UVL
Fig. 4.12 a	B2956	Z1 5320 UVL
Fig. 4.12 b	TS0518-2	Z1 5338 UVL
Fig. 4.13	TS0518-2	Z1 5338 UVL
Fig. 4.14	TS0518-2	Z1 5338 UVL

	Sample number	Process number
Fig. 5.18	TS1428-D	Z1 6067 LED
Fig. 5.20	B3920-C	Z1 5728 UVL
Fig. 6.8 a	B2134	Z1 3851 GAL
Fig. 6.8 b	B2132	Z1 3851 GAL
	B2134	Z1 3851 GAL
	B4383	Z1 5827 LAT
	TS0637	Z1 5364 UVL
Fig. 6.19	B2701	Z1 4161 GAL
	B4383	Z1 5827 LAT
	TS0637	Z1 5364 UVL
Fig. 7.6	B4225	PT 2188 LED
Fig. 7.7 a	B4225	PT 2188 LED
Fig. 7.7 b	B4225	PT 2188 LED
Fig. 7.8 a	B4225	PT 2188 LED
Fig. 7.8 b	B4225	PT 2188 LED
Fig. 7.9 a	B3280	Z1 4829 UVL
Fig. 7.9 b	B3280	Z1 4829 UVL
Fig. 7.10 a	B3280	Z1 4829 UVL
Fig. 7.10 b	B3280	Z1 4829 UVL
Fig. 7.11 a	B3280	Z1 4829 UVL
Fig. 7.11 b	B3280	Z1 4829 UVL
Fig. 7.12	B3280	Z1 4829 UVL

Appendix 3: List of abbreviations

Ag	silver
Al	aluminium
AlN	aluminium nitride
AlGaN	aluminium gallium nitride
AlInGaN	aluminium indium gallium nitride
Al_2O_3	aluminium oxide
Ar	argon
Au	gold
B_4C	boron carbide
BCl_3	boron trichloride
CB	conduction band
CH	crystal field split-off hole band
Cl_2	chlorine
Cp_2Mg	cyclopentadienylmagnesium
DADR	density-activated defect recombination
DBR	distributed Bragg reflector
EBL	electron blocking layer
ELO	epitaxial lateral-overgrowth
EQE	external quantum efficiency
FC	flip-chip
FCLEDs	flip-chip LEDs
Ga	gallium
GaN	gallium nitride
H_2	hydrogen gas
HCl	hydrogen chloride
HH	heavey hole
HF	hydrogen fluoride
HNO_3	nitric acid
H_20	water
ICP	inductively coupled plasma
InGaN	indium gallium nitride
InN	indium nitride
IQE	internal quantum efficiency
Ir	iridium
ITO	indium tin oxide

I-V	current–voltage characteristics
LED	light emitting diodes
LEE	light extraction efficiency
LH	light hole
L-I	output power–current characteristics
L-I-V	output power–current–voltage characteristics
MEMOCVD	migration-enhanced metalorganic chemical vapour deposition
Mg	magnesium
Mo	molybdenum
MOVPE	metalorganic vapour phase epitaxy
MQB	multiple quantum barriers
MQW	multiple quantum wells
N	nitrogen
N_2	nitrogen gas
Ni	nickel
NH_3	ammonia
NH_4F	ammonium fluoride
ODR	omni-directional reflector
PCs	photonic crystals
Pd	palladium
PDMS	polydimethylsiloxane
PECVD	plasma enhanced chemical vapour deposition
pss	patterned sapphire substrates
Pt	platinum
QCSE	quantum confined Stark effect
QW	quantum well
RCLEDs	resonant cavity LEDs or microcavity LEDs
Rh	rhodium
RIE	reactive ion etching
rms	root mean square
SEM	scanning electron microscope
SF_6	sulfur hexafluoride
Si	silicon
SiO_2	silicon dioxide
SiN_x	silicon nitride phase
SiH_4	silane
Si_2H_4	disilane
SL	superlattice
SP	surface plasmon
SRH	Shockley-Read-Hall
SWLI	scanning white light interferometry
TDD	treading dislocation density
TE	transverse–electric

TLM	transmission line model
TM	transverse–magnetic
Ti	titanium
Ti_3O_5	trititanium pentoxide
TMAl	trimethylaluminium
TMGa	trimethylgallium
TMIn	trimethylindium
UV	ultraviolet
VB	valence band
WPE	wall plug efficiency
WZ	wurtzite
Zn	zinc
ZnO	zinc oxide
ZrO_2	zirconium dioxide

List of publications

Parts of this work have been published as listed below:

Articles

- **N. Lobo**, H. Rodriguez, A. Knauer, M. Hoppe, S. Einfeldt, P. Vogt , M. Weyers and M. Kneissl, "Enhancement of light extraction in UV LEDs using nanopixel contact design with Al reflector", *Applied Physics Letters*, vol. 96, no. 8, p. 081109, 2010.

- **N. Lobo Ploch**, H. Rodriguez, C. Stölmacker, M. Hoppe, M. Lapeyrade, J. Stellmach, F. Mehnke, Tim Wernicke, A. Knauer, V. Kueller, M. Weyers, S. Einfeldt, M. Kneissl, "Effective Thermal Management in Ultraviolet Light Emitting Diodes with Micro-LED Arrays", *Electron Devices*, *IEEE Transactions on*, vol. 60, no. 2, pp. 782-786, 2013.

- **N. Lobo Ploch**, S. Einfeldt, M. Frentrup, J. Rass, T. Wernicke, A. Knauer, V. Küller, M. Weyers and M. Kneissl, "Investigation of the temperature dependent efficiency droop in UV LEDs", *Semiconductor Science and Technology*, vol. 28, no. 12, p. 125021, 2013.

- M. Kneissl, T. Kolbe, **N. Lobo**, J. Stellmach, A. Knauer, V. Küller, H. Rodriguez, S. Einfeldt, Markus Weyers, "Deep UV nitride-based light emitting diodes-applications and challenges", *Proceedings of China SSL2009, 6th China International Forum on Solid State Lighting*, 2009.

- H. Rodriguez, **N. Lobo**, S. Einfeldt, A. Knauer, M. Weyers and M. Kneissl, "GaN-based Ultraviolet Light-Emitting Diodes with Multifinger Contacts", *physica status solidi (a)*, vol. 207, no. 11, pp. 2585-2588, 2010.

- M. Kneissl, T. Kolbe, **N. Lobo**, J. Stellmach, A. Knauer, V. Kueller, H. Rodriguez, S. Einfeldt, M. Weyers, "Advances in InAlGaN-based deep UV light emitting diode technologies", *Proceedings of the 12th International Symposium on the Science and Technology of Light Sources and the 3rd International Conference on White LEDs and Solid State Lighting, LS-WLED 2010*, pp.265-268, 2010.

- M. Kneissl, T. Kolbe, C. Chua, V. Kueller, **N. Lobo**, J. Stellmach, A. Knauer, H. Rodriguez, S. Einfeldt, Z. Yang, N. M. Johnson, M. Weyers, "Advances in group III-nitride based deep UV light emitting diode technology", *Semiconductor Science and Technology*, vol. 26, no. 1, p. 014036, 2011.

- M. Lapeyrade, F. Eberspach, **N. Lobo-Ploch**, C. Reich, M. Guttmann, T. Wernicke, F. Mehnke, S. Einfeldt, A. Knauer, M. Weyers, M. Kneissl, "Current spreading study in UV-C LED emitting around 235 nm", *Proc. SPIE*, vol. 9363, pp. 93631P-93631P-15, 2015.

- J. Rass, T. Kolbe, **N. Lobo-Ploch**, T. Wernicke, F. Mehnke, C. Kuhn, J. Enslin, M. Guttmann, C. Reich, J. Glaab, C. Stoelmacker, M. Lapeyrade, S. Einfeldt, M. Weyers, M. Kneissl, "High power UV-B LEDs with long lifetime", *Proc. SPIE*, vol. 9363, pp. 93631K-93631K-13, 2015.

- F. Mehnke, C. Kuhn, J. Stellmach, T. Kolbe, **N. Lobo-Ploch**, J. Rass, M.-A. Rothe, C. Reich, N. Ledentsov Jr., M. Pristovsek, T. Wernicke, and M. Kneissl, "Effect of heterostructure design on carrier injection and emission characteristics 295 nm LEDs", *Journal of Applied Physics*, vol. 117, no. 19, p. 195704, 2015.

- J. Glaab, C. Ploch, R. Kelz, C. Stoelmacker, M. Lapeyrade, **N. Lobo Ploch**, J. Rass, T. Kolbe, S. Einfeldt, F. Mehnke, C. Kuhn, T. Wernicke, M. Weyers, M. Kneissl, "Temperature induced degradation of InAlGaN multiple-quantum well UV-B LEDs", *Proceedings of MRS Spring Meeting*, vol. 1792, mrss15-2102646, 2015.

- M. Kneissl, F. Mehnke, C. Kuhn, C. Reich, M. Guttmann, J. Enslin, T. Wernicke, A. Knauer, V. Kueller, U. Zeimer, M. Lapeyrade, J. Raß, **N. Lobo-Ploch**, T. Kolbe, J. Glaab, S. Einfeldt, M. Weyers, "Deep Ultraviolet LEDs: from materials research to real-world applications", *IEEE Photonics Society Summer Topical Meeting Series*, 2015.

- J. Rass, **N. Lobo Ploch**, M. Kneissl, "Optical polarization and light extraction from UV LEDs", *III-Nitride Ultraviolet Emitters- Technologies & Applications*, Ed. J. Rass and M. Kneissl, Springer, 2015 (in publication).

Patent application

- Michael Kneissl, Neysha Lobo, "Light emitting diode", EP2587560 A1, 2011.

International conferences

- N. Lobo, H. Rodriguez, A. Knauer, S. Einfeldt, W. John, P. Vogt, M. Weyers, M. Kneissl, "Enhanced light extraction from nitride based ultraviolet LEDs", *iNOW-Konferenz Stockholm / Berlin*, 2009, Stockholm / Berlin (poster presentation).

- N. Lobo, H. Rodriguez, A. Knauer, M. Hoppe, S. Einfeldt, P. Vogt, M. Weyers, M. Kneissl, "Novel nanopixel contact design for enhanced light extraction from ultraviolet light-emitting diodes", *IWN 2010*, 2010, Tampa, FL, USA (oral presentation).

- N. Lobo, H. Rodriguez, M. Hoppe, A. Knauer, J. Stellmach, V. Küller, P. Vogt, S. Einfeldt, M. Weyers, M. Kneissl, "Investigation and comparison of nanopixel contact LEDs and micro-LED arrays for enhanced light extraction from ultraviolet light-emitting diodes", *E-MRS spring meeting*, Congress Center, 2011, Nice, France (oral presentation).
- N. Lobo Ploch, S. Einfeldt, T. Kolbe, A. Knauer, M. Frentrup, V. Kueller, M. Weyers, M. Kneissl, "Influence of temperature on the optical properties of near-UV LEDs", *IWN 2012*, 2012, Sapporo, Japan (poster presentation).

Acknowledgements

My time as a doctorate student has been a wonderful experience which has seen me grow into a confident scientist and person. This would not have been possible without the help of a number of people and so I would like to put my gratitude into writing.

First and foremost I would like to thank my doctoral supervisor Prof. Dr. Kneissl for always being willing to discuss new ideas, for challenging me with interesting research questions and for believing in my capabilities. I would also like to thank Prof. Dr. Gottfried Dölher for being my examiner and Prof. Dr. Lehmann for being the chairperson of the doctoral examination committee.

I would like to thank Dr. Sven Einfeldt who was the first person I went to when I needed any advice or feed back. I am grateful to Prof. Dr. Günther Tränkle, Prof. Dr. Markus Weyers, Dr. Patrick Vogt and Dr. Tim Wernicke for the many scientific discussions and their invaluable advice. This work would not be possible without the availability of UV LED wafers and for that I am thankful to Dr. Martin Frentrup, Dr. Veit Hoffman, Dr. Arne Knauer, Dr. Viola Küller, Frank Mehnke und Joachim Stellmach for growing the LEDs. I would like to thank Dr. Hernán Rodrígues and Dr. Mickael Lapeyrade for the processing of the LEDs and for always being willing to help with any processing issues I faced. I am grateful to Mr. Mattias Matala and Dr. Wilfred John who worked with me on the fabrication of the nanopixel contact LEDs and Mr. Deepak Prasai and Dr. Ralph-Stephan Unger who worked with me on the fabrication of the sapphire micro-structures. I am especially grateful to Mr. Christoph Stölmacker for the mounting of the LED chips, the thermal simulations of mounted LED chips and for the long scientific discussions. I am thankful to Dr. Tim Kolbe for the simulations of the LED active region and Dr. Jens Rass for the calculation of the polarized emission distribution in the semiconductor structure.

I am extremely thankful to the entire process technology department in FBH. It was indeed a privilege to be given a chance to work in the FBH clean room and I am grateful for all the support I received from the technicians. I would like to thank all my colleagues in both FBH and TUB. I really enjoyed all our long discussions about physics and life in general. I am sure that many of the friendships that I have formed during this time will remain with me through life.

I would like to thank my family who have always been my support system. I am grateful to my mother, Yvette, and my sisters, Yolynd, Charise and Noellene, for their constant encouragement and also for providing me with a reality check when I needed one. In particular I would like to thank Noellene for proof reading my thesis. I my thankful to my parents-in-law Cecylia and Joseph Ploch for the many hours of baby-sitting that gave me the time to write my thesis. I believe I am truly blessed because of my daughter Rhea. Each smile from her makes me feel like the most loved and important person in the world. I would like to

thank my husband Simon without whom this thesis would not be possible. Thank you for pushing me to carry on when things got overwhelming, for taking on much more than your own share of tasks so that I would be able to work on my thesis, for believing in me and even more for making me believe in myself. Finally I would like to thank God. I can definitely say that His plans for my life have been better than my dreams.